Heat transport mechanisms in silica-based core materials for thermal superinsulations

Zur Erlangung des akademischen Grades eines

DOKTORS DER INGENIEURWISSENSCHAFTEN

von der KIT-Fakultät für Chemieingenieurwesen und Verfahrenstechnik des
Karlsruher Instituts für Technologie (KIT)
genehmigte

DISSERTATION

von

Sebastian Sonnick, M.Sc.

Tag der mündlichen Prüfung: 05. Dezember 2022

Erstgutachter: Prof. Dr. rer. nat. Matthias Rädle

Zweitgutachter: Prof. Dr. Ing. Hermann Nirschl

Acknowledgment

Abstract

This thesis explores heat transfer in silica-based superinsulation. Four peer-reviewed publications on this topic are presented in a systematic series. The focus is on analytical calculation methods for different heat transfer mechanisms. These methods are compared with numerous measurements of gas pressure-dependent thermal conductivity and evaluated accordingly. A special guarded hot plate apparatus is developed and set up to perform the thermal conductivity measurements. This apparatus is suitable for measuring the gas pressure-dependent thermal conductivity of fragile powder compacts in a pressure range from <0.01 mbar to atmospheric pressure. Various precipitated silicas, fumed silicas, silica gels, and glass sphere beads are investigated. The known heat transfer mechanisms in these materials can only be studied separately to a limited extent because they tend to couple. In particular, an interaction between the heat conduction of the solid skeleton and the heat conduction of the gas phase can be observed. This coupling effect depends on the solid structure of the different materials. Therefore, as an essential element of this work, the coupling effect in different materials is quantified, and heuristic models for its calculation are found.

The first publication deals with gas–solid coupling in precipitated silicas. It investigates whether various commercially available precipitated silicas differ in their tendency to couple, and which material properties are responsible for the coupling. The coupling effect factor f is introduced for evaluation. The results indicate no significant differences between the products. Instead, a clear, almost linear relationship was found between porosity and the coupling effect factor. It can be concluded that the precipitated silicas studied do not exhibit structural differences on the size scale, which is crucial for heat flow. The gas–solid coupling is mainly attributed to the regions around the contact points of the particles. The coupling effect factor thus depends on the number of contact points and hence, at constant particle size, directly on the porosity. The first paper consequently shows that the gas–solid interaction is crucial for the description of heat transfer in superinsulations. The factor regarding energy transfer at the wall impact of a gas molecule is called the thermal accommodation coefficient α (TAC). It describes the incompleteness of energy transfer at wall impact at a gas–solid boundary. In macroscopic systems, it can be neglected. However, in micro or nanoporous material systems, this factor becomes relevant because there are many material boundaries. Nev-

ertheless, in the literature, an accommodation coefficient of unity and thus complete energy transfer between a gas and solid surface is often assumed for air. Currently, measuring techniques are only available to determine the TAC of exterior surfaces. Here, the effects of surface roughness, which are difficult to quantify, are also measured. However, the TAC in the pores of a heterogeneous gas–solid mixture with micro- and nanopores is not accessible by measurement. Thus, in the second paper, a method is presented to compare the thermal accommodation of different gases on the pore walls of precipitated silica and fumed silica. A simple model from impact theory states that when a sphere with velocity $v \neq 0$ collides with a stationary sphere of equal weight, complete energy transfer occurs (Cf. billiard balls). This would correspond to an accommodation coefficient of unity. The more the masses of the balls differ from each other, the more incomplete the energy transfer is. Transferring this model to a gas particle in a wall impact, a TAC of 1 for $M_g = M_s$ can be obtained, where M_g is the molar mass of the gas particle, and M_s is the molar mass of the solid surface (here, of SiO_2). This assumption is consistent with the kinetic theory of gases; however, notably, some important effects are neglected here (e.g., polarity, rotational energy, adsorption effects). Since the molar masses of SiO_2 and SO_2 are almost identical, $\alpha = 1$ is assumed for this combination. Then, apparent TACs are determined for 6 other gases from thermal conductivity measurements relative to SO_2. The determined values follow the correlations of impact theory and can therefore be considered plausible. For the air/SiO_2 combination, $\alpha = 0.41$ and $\alpha = 0.33$ are obtained for precipitated and fumed silica, respectively. Although these values cannot be considered physically valid in general and are only valid in the context of the presented models, the assumption $\alpha = 1$ for air could be clearly refuted, and the significance of the TAC could be highlighted.

Since the validity of the models used for the gas thermal conductivity and the effective thermal conductivity is crucial for the evaluation of the results obtained so far, a literature review of such models is presented first in the next publication. It is shown that a large number of different calculation models exist for both the effective and gas thermal conductivity as well as parameters contained therein. Furthermore, it is usually unclear what measured values for particle and pore size should be used to properly apply the models to different porous materials. From the literature review, the most commonly used models are extracted. Together with the different methods of applying the measured values for pore and particle size, there are 2,800 possible combinations to calculate the gas pressure-dependent thermal conductivity of the investigated materials. All model combinations are applied to the 15 commercially available silica-based materials using a computer program. The materials consist of 6 precipitated silicas, 3 fumed silicas, 3 silica gels, and 3 types of glass beads. All materials are measured for their gas pressure-dependent thermal conductivity in combination with 6 different pore gases. The results are compared with those of the calculations to determine the most suitable model

combinations for the different materials. As a result, material-specific recommendations are made for the calculation. The average variance (coefficient of variation), without the use of adjustable parameters, is 10 %. To compare the models for gas thermal conductivity and coupling contribution in a meaningful way, the fractions for solid thermal conductivity and radiation are extracted from measurements at low gas pressures.

In the fourth publication, to apply the results to the real development of superinsulations, the favored model combinations are supplemented by models for solid and radiative conductivity. Thus, parameter studies on particle size and porosity can be performed for the different materials. To consider the influence of pore size distribution without having to perform a mercury porosimetry measurement for each material and porosity studied, a model is developed to calculate the distributions from only one measurement and the corresponding porosity. To properly include the radiation component, Fourier transform infrared spectrometry measurements are performed to determine the mass-specific extinction coefficient of the materials. The results of the parameter studies can be used in the future to select superinsulations' core materials. A particular focus of the work is also on the specific design of the insulation cores for different applications. The presented approach can be applied to material mixtures with additives, in particular infrared opacifiers, to optimize specific material mixtures for different conditions.

Thus, this work provides an important contribution to a targeted use of superinsulations. By using alternative core materials, high-performance insulation materials can contribute significantly to the energy turnaround in the future by making them attractive to additional sectors of the economy. In this context, the author considers the use of precipitated silica in particular to have great potential. Therefore, the outlook section addresses the targeted production of core materials based on precipitated silica. The proposed novel production process offers an improvement in the longevity of the panels by optimized aggregate structures. Furthermore, a time-consuming and cost-intensive process step in vacuum insulation panel production – namely the mixing of dry substances – would be eliminated, since all the necessary components would already be added in the liquid phase of the precipitation reactor. This would also lead to a more homogeneous distribution and better adhesion of the additives in or to the silica compared to the dry mixing process. This is expected to reduce the need for opacifiers and significantly increase the stability of the core materials. These developments could be a decisive factor for a successful energy turnaround.

Zusammenfassung

Diese Arbeit befasst sich mit der Wärmeübertragung in Silica-basierten Superisolatoren. In systematischer Abfolge werden vier Publikationen zu diesem Thema vorgestellt. Der Fokus liegt auf analytischen Berechnungsmethoden für die verschiedenen Wärmeübertragungsmechanismen. Diese werden mit einer Vielzahl von Messungen der gasdruckabhängigen Wärmeleitfähigkeit verglichen und entsprechend bewertet. Zur Durchführung der Wärmeleitfähigkeitsmessungen wurde ein spezieller Guarded-Hot-Plate-Apparatus entwickelt und aufgebaut. Dieser ermöglicht es, auch fragile Pulverpresslinge hinsichtlich ihrer gasdruckabhängigen Wärmeleitfähigkeit in einem Druckbereich von < 0.01 mbar bis Atmosphärendruck zu vermessen. Es wurden verschiedene Fällungskieselsäuren, pyrogene Kieselsäuren, Silicagele und Glasperlen untersucht. Die bekannten Wärmeübertragungsmechanismen in diesen Materialien können nicht vollkommen getrennt voneinander untersucht werden, da sie zur Kopplung neigen. Insbesondere ist eine Wechselwirkung zwischen der Wärmeleitung des Feststoffgerippes mit der Wärmeleitung der Gasphase zu beobachten. Dieser sogenannte Kopplungseffekt ist je nach Material unterschiedlich stark ausgeprägt. Als wesentliches Element dieser Arbeit wurde der Kopplungseffekt in verschiedenen Materialien quantifiziert und zu dessen Beschreibung wurden heuristische Modelle gefunden.

Die erste Veröffentlichung handelt von der Gas-Feststoff-Kopplung in Fällungskieselsäuren. In dieser wird den Fragen nachgegangen, ob sich verschiedene kommerziell erhältliche Fällungskieselsäuren hinsichtlich ihrer Neigung zur Kopplung unterscheiden und welche Materialeigenschaften für die Kopplung verantwortlich sind. Zur Bewertung wird der Kopplungseffektfaktor f eingeführt. Es hat sich gezeigt, dass zwischen den Produkten keine signifikanten Unterschiede zu erfassen sind. Stattdessen ist ein deutlicher, nahezu linearer Zusammenhang zwischen der Porosität und dem Kopplungseffektfaktor festgestellt worden. Daraus kann gefolgert werden, dass die untersuchten Fällungskieselsäuren auf der keine für den Wärmefluss entscheidenden strukturellen Unterschiede aufweisen. Die Gas-Feststoff-Kopplung wird vor allem den Bereichen um die Berührungspunkte der Partikel zugeschrieben. Der Kopplungseffektfaktor ist demnach von deren Anzahl und, bei konstanter Partikelgröße, direkt von der Porosität abhängig.

Es hat sich folglich gezeigt, dass die Gas-Feststoff-Wechselwirkung für die Beschreibung der Wärmeübertragung in Superisolationen von entscheidender Be-

deutung ist. Der Faktor der Energieübertragung beim Wandstoß eines Gasmoleküls heißt thermischer Akkommodationskoeffizient α (TAC). Er beschreibt den Temperatursprung, der sich an einer Gas-Feststoff-Grenze einstellt. In makroskopischen Systemen kann er vernachlässigt werden. In mikro-/nanoporösen gibt es jedoch viele stoffliche Grenzen, so dass dieser Faktor relevant wird. In der Literatur wird für Luft dennoch häufig ein Akkommodationskoeffizient von eins, und somit eine vollständige Energieübertragung zwischen Gas und Feststoffoberfläche, angenommen. Aktuell gibt es ausschließlich Methoden, um den TAC von makroskopischen Materialoberflächen zu bestimmen. Dabei werden auch schwer quantifizierbare Effekte der Oberflächenrauhigkeit mitgemessen. Der TAC in den Mikro- und Nanoporen eines heterogenen Gas-Feststoff-Gemisches ist jedoch messtechnisch nicht zugänglich. In der zweiten Veröffentlichung wird eine Methode vorgestellt, um die TACs verschiedener Gase an den Porenwänden von Fällungskieselsäure und pyrogener Kieselsäure miteinander zu vergleichen. Ein einfaches Modell aus der Stoßtheorie besagt, dass es beim Stoß einer Kugel mit einer Geschwindigkeit $v \neq 0$ auf eine gleich schwere, ruhende Kugel zur vollständigen Energieübertragung kommt (vgl. Billardkugeln). Das würde einem Akkommodationskoeffizienten von eins entsprechen. Je stärker die Massen der Kugeln voneinander abweichen, desto unvollständiger erfolgt der Energieübertrag. Wendet man dieses Modell auf ein Gasteilchen beim Wandstoß an, erhält man einen TAC von eins für $M_G = M_S$. Die Molmasse des Gasteilchens wird mit M_G, die der Feststoffoberfläche (hier von SiO_2) mit M_S abgekürzt. Diese Annahme entspricht der kinetischen Gastheorie, es muss jedoch bedacht werden, dass hier einige wichtige Effekte vernachlässigt werden (z.B. Polarität, Rotationsenergie, Adsorptionseffekte). Da die Molmassen von SiO_2 und SO_2 nahezu identisch sind wird für diese Kombination $\alpha = 1$ angenommen. Anschließend werden aus Wärmeleitfähigkeitsmessungen für sechs weitere Gase relativ zu SO_2 sogenannte scheinbare TACs bestimmt. Die ermittelten Werte folgen den Zusammenhängen der Stoßtheorie und können daher nachvollzogen werden. Für die Kombination Luft/SiO_2 ergibt sich $\alpha = 0.41$ und $\alpha = 0.33$ für Fällungs- bzw. pyrogene Kieselsäure. Obwohl diese Werte nicht als allgemein physikalisch gültig angesehen werden können und nur im Zusammenhang mit den vorgestellten Modellen gültig sind, kann die Annahme $\alpha = 1$ für Luft widerlegt und die Signifikanz des thermischen Akkommodationskoeffizienten bewiesen werden.

Die Gültigkeit der verwendeten Modelle für die Gaswärmeleitfähigkeit und die effektive Wärmeleitfähigkeit ist für die Bewertung der bisherigen Ergebnisse entscheidend. Deshalb wird in der nächsten Veröffentlichung zunächst eine Literaturrecherche solcher Modelle präsentiert. Dabei zeigt sich, dass sowohl für die effektive als auch für die Gaswärmeleitfähigkeit sowie für die darin enthaltenen Parameter eine Vielzahl unterschiedlicher Berechnungsmodelle existiert. Des Weiteren wird in der Regel keine Angabe dazu gemacht, welche Messwerte für die Partikel- und die Porengröße verwendet werden sollen, um die Modelle ordnungsgemäß auf verschiedene poröse Materialien anwenden zu können. Aus

der Recherche werden die in der Literatur am häufigsten verwendeten Modelle extrahiert. Zusammen mit den unterschiedlichen Verwendungsmöglichkeiten der Messwerte für Poren- und Partikelgröße ergeben sich 2800 Kombinationsmöglichkeiten, um die gasdruckabhängige Wärmeleitfähigkeit der untersuchten Materialien zu berechnen. Alle Modellkombinationen werden mithilfe eines Computerprogrammes auf die 15 kommerziell erhältlichen, Silica-basierten Materialien angewendet. Diese setzen sich aus sechs Fällungskieselsäuren, drei pyrogenen Kieselsäuren, drei Silicagelen und drei Glasperlensorten zusammen. Alle Materialien wurden hinsichtlich ihrer gasduckabhängigen Wärmeleitfähigkeit in Kombination mit sechs verschiedenen Porengasen vermessen. Die Ergebnisse wurden mit denen der Berechnungen verglichen, um die für die jeweiligen Materialien am besten geeigneten Modellkombinationen zu ermitteln. Als Ergebnis werden materialspezifische Empfehlungen zur Berechnung ausgesprochen. Die mittlere Abweichung liegt, ohne die Verwendung von anpassbaren Parametern, bei 10 %. Um die Modelle für die Gaswärmeleitfähigkeit und den Kopplungsbeitrag sinnvoll vergleichen zu können, wurden die Anteile der Feststoffwärmeleitfähigkeit und der Strahlung aus den Messungen bei sehr kleinen Gasdrücken extrahiert.

Die Ergebnisse sollen auf die reale Entwicklung von Superisolationen anwendbar sein. Deshalb wurden die favorisierten Modellkombinationen in der vierten Veröffentlichung mit Modellen für die Feststoff- und Strahlungsleitfähigkeit komplementiert. Somit können Parameterstudien über die Partikelgröße und die Porosität der verschiedenen Materialien durchgeführt werden. Damit der Einfluss der Porengrößenverteilung berücksichtigt werden kann, ohne für jedes Material und jede untersuchte Porosität eine Quecksilberporosimetrie-Messung durchführen zu müssen, wurde ein Modell entwickelt, um die Verteilungen aus nur einer Messung und der entsprechenden Porosität berechnen zu können. Um den Strahlungsanteil ordnungsgemäß miteinzubeziehen, wurden Fourier-Transform-Infrarotspektrometrie-Messungen durchgeführt. Auf diese Weise konnte der massenspezifische Extinktionskoeffizient der Materialien bestimmt werden. Die Ergebnisse der Parameterstudien können zukünftig bei der Auswahl der Kernmaterialien von Superisolationen eingesetzt werden. Ein Fokus der Arbeit liegt auf der gezielten Auslegung der Isolationskerne für verschiedene Anwendungen. Die präsentierte Vorgehensweise kann auch auf Materialmischungen mit Additiven, insbesondere mit Infrarottrübungsmitteln, übertragen werden, um Materialmischungen zweckgerichtet für verschiedene Gegebenheiten optimieren zu können.

Somit liefert diese Arbeit einen zentralen Beitrag für den systematischeren Einsatz von Superisolationen. Durch die Verwendung von alternativen Kernmaterialien können Hochleistungsdämmstoffe noch mehr zur Energiewende beitragen, indem sie für weitere Wirtschaftssektoren attraktiv werden. Der Autor sieht in diesem Zusammenhang vor allem in der Verwendung von Fällungskieselsäuren ein großes Potenzial. Daher beschäftigt sich die Arbeit im Ausblick mit der gezielten Produktion von Kernmaterialien auf Basis von Fällungskie-

selsäure. Das neuartige Produktionsverfahren verspricht eine Verbesserung der Langlebigkeit der Paneele durch optimierte Aggregatstrukturen. Des Weiteren würde ein zeit- und kostenintensiver Prozessschritt in der VIP-Herstellung - das Vermischen der Trockensubstanzen - entfallen, da alle benötigten Komponenten bereits in der Flüssigphase dem Fällreaktor zugegeben werden würden. Dies würde zudem zu einer homogeneren Verteilung und besseren Haftung der Additive in bzw. an der Kieselsäure führen. Dadurch wird eine Verringerung des Trübungsmittelbedarfs und eine deutlich erhöhte Stabilität der Kernmaterialien erwartet. Diese Entwicklungen könnten entscheidend zu einer erfolgreichen Energiewende beitragen.

Contents

Nomenclature

α_E, α — Energy/thermal accommodation coefficient

α_I — Momentum accommodation coefficient

$\bar{c}$ — Average thermal velocity

$\bar{g}$ — Average relative velocity

β — Dimensionless coefficient in Knudsen equation for λ_g

$\dot{Q}$ — Heat flux

η — Dynamic viscosity

$\hat{\eta}$ — Poisson's ratio

$\hat{E}$ — Rosseland average of the extinction coefficient

$\hat{n}$ — Particle Density

κ — Isentropic exponent

Λ — Wavelengths

λ — Thermal conductivity

λ_0 — Thermal conductivity at ambient conditions

ν — Kinematic viscosity

Φ — Scattering angle

ϕ — Porosity

ρ — Density

σ — Stefan-Boltzmann constant

τ — Mean free time

τ	Optical thickness
A	Area
b	Isobaric coefficient of expansion
c_p	Heat capacity at constant pressure
c_v	Heat capacity at constant volume
D	Particle size
d	Diameter, Pore size
d	Pore size
E	Extinction coefficient
F	Pressure load
f	Coupling effect factor
f^*	Degrees of freedom
F_R	Frictional force
g	Gravity
g^*	Temperature jump coefficient
j_N	Surface collision rate
k	Bolzmann constant
Kn	Knudsen number
L	Mean free path of gas molecules
M	Molar mass
N	Number of particles
N_g	Number density of gas particles
p	Pressure
Pr	Prandtl number
q	Heat flux density
R	Thermal resistance
Ra	Rayleigh number

T	Temperature
t	Time
T_W	Wall Temperature
v	Velocity
v_s	Speed of sound
X	Specimen thickness
x	Characteristic Length
Y	Elastic modulus
(T)AC	(Thermal) accommodation coefficient
CFD	Computational fluid dynamics
DLS	Dynamic light scattering
FS	Fumed silica
GS	Glass spheres
MAC	Momentum accommodation coefficient
MIP	Mercury intrusion porosimetry
PCS	Photon correlation spectroscopy
PS	Precipitated silica
SAXS	Small-angle x-ray scattering
SG	Silica gel
UV/VIS	Ultraviolet/visible
VIP	Vacuum insulation panel
ZBS	Zehner, Bauer, Schlünder

Chemical symbols

Ar	Argon
CO_2	Carbon dioxide
H_2SO_4	Sulfuric acid
HCl	Hydrogen chloride

He	Helium
Kr	Krypton
Na_2O	Sodium silicate
Na_2SO_4	Sodium sulfate
SF_6	Sulfur hexafluoride
$SiCl_4$	Silicon tetrachloride
SiO_2	Silicon dioxide
SO_2	Sulfur dioxide

Subscripts

∞	Infinity
eff	Effective
atm	Atmospheric
c	Coupling
cr	Critical
g	Gas
m	Mass specific
p	At constant pressure
p	Particle
ph	Phonons
r	Radiation
s	Solid
v	At constant volume
W	Wall

Chapter 1

Introduction

The energy transition is a global challenge, with the primary goal being to reduce greenhouse gas emissions. To achieve this, energy supply must be transformed, but energy consumption must also be drastically reduced. Thermal energy accounts for more than $50\,\%$ of Germany's total energy consumption and is used in a variety of applications, such as in space heating or air conditioning, for hot water and process heat, or for refrigeration [1]. To save energy in this sector, processes must become more efficient than in the past, and heat losses must be minimized as far as possible. Thermal insulation materials play a decisive role in the latter. To reduce heat losses, insulation materials must be used wherever technically generated temperature gradients are to be maintained. The thickness of the insulating material and its thermal conductivity λ determine how much heat is lost. Thermal conductivity is a material property and differs from one insulation material to another. To avoid exceeding a specific heat loss rate, a certain layer thickness of a given insulation material must be maintained. However, in doing so, one faces the limits of the available volume or must sacrifice the precious volume of the application, since thermal insulation reduces the usable volume, whether in the thermal storage unit, the home, or the thermally insulated transport box. Reducing thermal conductivity can therefore help not only to reduce heat loss but also to increase the usable volume. Materials with the lowest thermal conductivity are called thermal superinsulations. By definition, they have a lower thermal conductivity than still air and function according to the principle of the Knudsen or Smolochowski effect, which states that the thermal conductivity of a gas decreases with the gas pressure when the wall distance of the surrounding boundaries is in the same order of magnitude as the mean free path of the gas molecules. Conventional insulation materials are based on the principle of convection suppression. For this purpose, the critical Rayleigh number must not be exceeded, as described in Section 2.2.1. This is achieved by dividing the volume in which the heat transfer is to be suppressed into many small subspaces. In these small subspaces, or pores, the heat is no longer transferred by convection but only by thermal conduction of the enclosed gas and radia-

tion. In the case of air, $\lambda = 0.026\,\frac{W}{mK}$ under normal conditions. The goal is therefore to manage the subdivision into convection-free subspaces with as little solid matter as possible, such that the effective thermal conductivity of the total volume is, as far as possible, only slightly above the value of stationary air. In practice, thermal conductivities of conventional insulation materials in the range of $0.032\,\frac{W}{mK} - 0.050\,\frac{W}{mK}$ are achieved in this way. By making use of the Knudsen effect, it is possible to further reduce the effective thermal conductivity. In practice, this effect is used, for example, in the well-known double-walled Dewar vessels. Here, the absolute pressure must be in the range of approximately $10^{-7}\,bar$ in order to bring the mean free path of air molecules into the range of several centimeters, since the distance between the walls in the vessels is usually also in the centimeter range. Vacuum insulation panels (VIPs) have also been used for many years. These usually consist of a core material mixture of silica, an infrared opacifier, and a small amount of fiber. The compressed core material is vacuum-sealed in aluminum-vaporized plastic bags and then used in the construction industry, in medical transport containers, on thermal storage units, and in many other applications. A much more moderate vacuum is sufficient here because, in this case, the pores of the core material are to be understood as a wall gap. Thus, the mean free path must only be in that order of magnitude as well. The mean free path is in the micrometer range at air pressures around $10^{-3}\,bar$, which can be achieved with significantly lower technical effort than for the Dewar vessel.
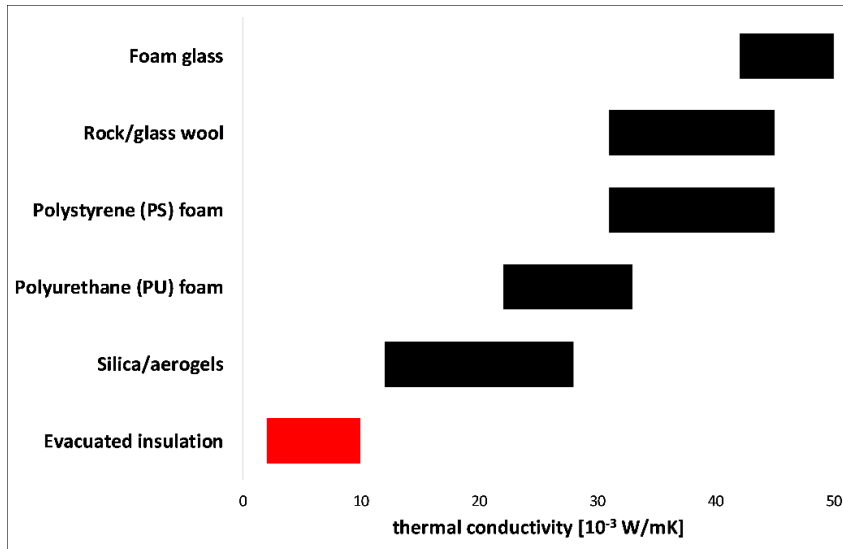
Figure 1.1: Comparison of the thermal conductivity of different insulation materials [2]

This effect can also be seen in Figure 1.1, because silicas or aerogels, for example, have nanopores of the same order of magnitude as the mean free path of air molecules at atmospheric pressure. This can lead to effective thermal conductivities smaller than the thermal conductivity of air. In the "Evacuated

Insulations" category, the mean free path is artificially increased by applying a vacuum so that the gas thermal conductivity λ_g in all pores becomes negligibly small. This results in a low effective thermal conductivity λ_{eff}, which is composed only of solid thermal conductivity λ_s and radiation λ_r. To design such super insulations, it is important to understand the thermal processes at the different size scales of these materials. Numerical calculation methods are useful in this regard [3, 4, 5, 6]. The Lattice Bolzmann method is particularly well suited for the size scale $10^{-9} - 10^{-6}\,m$ [7], on which the decisive mechanisms in superinsulations take place. These methods can provide highly accurate results, depending on how precisely the geometry of the corresponding materials can be mapped. Thus, simulations are key for the basic understanding of thermal processes. However, for the end user (e.g. a VIP producer), such methods are usually too time-consuming and difficult to integrate into daily business; analytical methods to make a quick estimation of the suitability of a potential core material are more convenient. Numerous analytical calculation methods are available in the literature for this purpose. They have been developed either empirically or on the basis of simplified theoretical approaches. Some of these models have been specifically tailored to certain materials, while others promise general validity.

Silica aerogel is an active field of research in this context because it is lightweight and offers highly efficient thermal insulation, which is why it is attracting increasing attention, not only in the rapidly growing aerospace industry [8] but also for buildings [9]. He and Xie [10], for example, conducted a comprehensive review of the existing aerogel-related heat transfer models. They discuss different approaches for the individual heat transfer mechanisms and conclude that some issues still require investigation to better reveal the heat transfer mechanism of silica aerogel insulations. Zeng et al. [11] considered various simplified geometries to calculate the thermal conductivity of aerogels. They compared a cubic array of intersecting square rods, a cubic array of intersecting cylindrical rods, and spherical structures to obtain results for the thermal conductivity of aerogel. Fu et al. [12] present a literature review on thermal conductivity modeling in aerogels. Their criticism is that the authors of the peer-reviewed papers did not consider the problem at the level of effective thermal conductivity and that realistic pore size distributions are not used to calculate gas thermal conductivity. Both issues are considered in the present work, although not for aerogels.

Another research area covers the modeling of packed beds in general. The focus here is not always on thermal insulators but on heat transfer models for various applications, such as fluidized beds, catalytic reactors, or rectification columns. In this context, models for effective thermal conductivity are discussed. However, such models are not limited to thermal conductivity but are also applied to other effective properties of heterogeneous materials, including the coefficient of thermal expansion, electric conductivity, di-electric constant (permittivity), and mechanical modulus [13]. The Knudsen effect is not al-

ways considered, because the size scale of the addressed applications does not always require it. Tsotsas and Martin [14] conducted a comprehensive review of numerous experimental and theoretical works on the thermal conductivity of packed beds. They classified the models into three types: Laplace equation models, parallel and series connection models, and unit cell models. In the present work, models of these types are also compared with one another, and their specific suitability for predicting the thermal conductivity of the studied material systems is evaluated. Zehner, Bauer, and Schlünder [15, 16] developed perhaps the best-known model for particle beds of different shapes: a unit cell model that is also known as the ZBS-model. The geometry of the unit cell does not necessarily correspond to the geometry of the particles in order to consider the influence of lateral heat flows occurring in reality, but still to be able to calculate under the assumption of parallel heat flow lines. Parzinger [17] provides an extensive literature review in his thesis, evaluating the best-suited calculation model to predict the thermal conductivity of sands at lunar ambient conditions. He also developed a unit cell model for the characterization of solid–gas coupling.

The technical literature contains many suggestions for calculating the thermal conductivity of various idealized structures. However, the relation to reality is often missing, such that one obtains no or only little information on the application of these models to actual materials. The question of which models provide the most realistic results, especially for fumed and precipitated silica, silica gel, and glass spheres, remains unanswered. Therefore, the present work addresses this open question by investigating the heat transfer processes in these materials at different size scales.

Chapter 2

Physical principals

2.1 Thermal conductivity

The thermal conductivity λ is the proportionality factor in Fourier's law. It describes the transport of heat through a body due to a temperature gradient, and it has the unit $\left[\frac{W}{mK}\right]$. Fourier's law is shown in Equation 2.1:

$$q = -\lambda \nabla T, \tag{2.1}$$

where q is the heat flux density. The thermal conductivity of pure substances is a material property and can be taken from various tables (e.g. [18]). In heterogeneous mixtures, the individual components have defined thermal conductivities, but this alone cannot describe the macroscopic heat flow. The proportionality factor for describing the macroscopic heat flow through a porous material is called the effective thermal conductivity λ_{eff}. It depends not only on the thermal conductivities of the individual components and the porosity ϕ but also on the structure and the size scales of the materials. It is one of the key objectives of this thesis to analytically describe the effective thermal conductivity of different porous materials.

2.2 Heat transfer in porous solids

In general, heat can be transferred through three mechanisms: thermal conduction, radiation, and convection. As will be shown in Section 2.2.1, convection can be neglected in most porous materials. The overall heat transfer in heterogeneous material systems, which consist of a solid and a gas phase, can therefore be described with conduction and radiation only. The conduction part, however, can be subdivided into solid conduction and gaseous conduction. In addition, a non-negligible and often even dominating coupling between the individual heat transfer mechanisms can be observed in many materials, which is also referred to as the coupling effect.

$$\lambda_{eff} = \lambda_s + \lambda_g + \lambda_r + \lambda_c. \tag{2.2}$$

The individual mechanisms are often represented as a superposition, as shown in Equation 2.2. The ratio of the individual contributions strongly depends on the material and can be influenced by specific intervention. More specifically, λ_s can be influenced by the pressing pressure applied in the production of the insulations, λ_g is a function of the pore size and the gas pressure, λ_r can be influenced by the admixture of additives, and λ_c depends primarily on the structure of the porous solid. In the development of superinsulations, the goal is to find an optimum to minimize the sum λ_{eff} as far as possible.

2.2.1   Convection

Convection is always coupled on macroscopic movement and hence a mass transfer of a fluid. This mass transfer can be caused by density differences (natural convection) or by an external source (forced convection). Forced convection does not usually occur in thermal insulation materials, and following the Rayleigh-Bernard convection theory, natural convection only occurs when the critical Rayleigh number is exceeded. Otherwise, the fluid is unstably stratified but hydrodynamically stable. This means that there is no flow separation and thus no convection. The critical Rayleigh number Ra_{cr} is 1707 for an upright cylinder with isothermal bottom and top plates and adiabatic side walls [19]. The Rayleigh number can be calculated using Equation 2.3:

$$Ra = \frac{gx^3}{\nu^2} b(T_W - T_\infty)Pr, \tag{2.3}$$

where g is the gravity; x is the length of the cylinder; ν is the kinematic viscosity; T_∞ and T_W are the temperatures of the gas in the cylinder and the bottom of the cylinder, respectively; and b is the isobaric coefficient of expansion, which is defined as $b = -\frac{1}{\rho}\frac{\partial \rho}{\partial T}$. For ideal gases $b = \frac{1}{T_\infty}$ can be assumed [20]. In technically relevant porous media (e.g. for thermal insulation materials), $Ra << Ra_{cr}$ holds in most cases. This can be shown in a calculation example with the following assumptions:

x	$1\,mm$
ν	$13.3\,\frac{mm^2}{s}\,(air)$
T_W	$293\,K$
T_∞	$273\,K$
Pr	$0.7368\,(air)$

Inserting this values in Equation 2.3 leads to a Rayleigh number of approximately 3. Since the pores of the materials investigated in this work are all significantly smaller than $1\,mm$, and no local temperature differences between wall and gas of $20\,K$ are reached, it can be assumed that the corresponding

Rayleigh numbers are even smaller. Thus, a contribution to the total heat transfer caused by convection is highly unlikely in the cases considered and can thus be neglected.

2.2.2 Radiation

If radiation transport in porous media is to be modeled, a distinction must first be made between two fundamentally different cases. If the structures of the material are large compared with the wavelength, the transport can be described mainly by the exchange between the surfaces. However, if the wavelength is of the same order of magnitude or even larger than that of the solid structures, the penetration of the radiation into the particles must also be considered. The porous material can then be considered as a continuum. Since this is the case for all materials in this work, only the continuum calculation procedure is shown in this section.

If there is no medium between them, the distance between the exchange surfaces is not a factor in radiative transfer. Thus, it is not meaningful to determine a proportionality factor λ_r for radiation processes in general. An exception is the "continuum" case when a non-transparent, porous medium is placed between the radiating surfaces. Here, the primary photon beam is absorbed or scattered many times, and the inner surfaces of the porous structure are emitting radiation to each other. In this case, the radiation transport can be considered as a diffusion process. Thus, it must first be clarified whether the porous solid is a transparent or non-transparent medium in the wavelength range relevant to a thermal radiation source. The transparency is determined by means of the optical thickness τ, which is given in Equation 2.4. A substance is considered to be non-transparent if its optical thickness is significantly greater than 1 over the entire wavelength range considered. Reiss [21] states that modeling the thermal radiation as a diffusive process is possible if the optical thickness is at least 15 for all wavelengths of interest.

The mean free path of the photons before they are absorbed or scattered is $\frac{1}{E}$. Thus, τ is the average frequency at which a photon of a given wavelength is absorbed and re-emitted or scattered before it passes through the material. Thus, the transmittance, which is $exp(-\tau)$ according to Lambert Beer's law, should be $< 10^{-6}$ for non-transparent media following Reiss.

$$\tau = E(\Lambda)X > 15.\tag{2.4}$$

If the condition in Equation 2.4, where X is the specimen thickness, is fulfilled and, thus, the consideration of radiative transport as a diffusive process is allowed, the radiation thermal conductivity λ_r can be calculated following the Rosseland diffusion approximation [22] according to Equation 2.5:

$$\lambda_r = \frac{16\sigma n^2}{3\hat{E}}T_r^3,\tag{2.5}$$

where σ is the Stefan-Boltzmann constant, and n is the refractive index (which can be assumed to be 1 for the materials considered in this work [21]). Furthermore, $\hat{E}$ is the Rosseland average of the extinction coefficient. It is an averaged extinction coefficient weighted by the blackbody spectrum $E_{bb}(\Lambda, T)$ of the temperature of interest. It can be obtained from the infrared spectrum via Equation 2.6:

$$\frac{1}{\hat{E}(T)} = \frac{\int_{\Delta\Lambda} \frac{1}{E(\Lambda)} \frac{\partial E_{bb}(\Lambda)}{\partial E_{bb}} d\Lambda}{\int_{\Delta\Lambda} \frac{\partial E_{bb}(\Lambda)}{\partial E_{bb}} d\Lambda}. \tag{2.6}$$

The temperature-dependent blackbody radiation spectrum $E_{bb}(\Lambda)$ is defined in Equation 2.7 after Plank's law of radiation:

$$E_{bb}(\Lambda, T) = \frac{C_1}{\Lambda^5 \left[exp\left(\frac{C_2}{\Lambda T}\right) - 1 \right]}, \tag{2.7}$$

with $C_1 = 3.741 * 10^8 \frac{W\mu m^4}{m^2}$, and $C_2 = 1.439 * 10^4 \, \mu m K$.

Integration of Equation 2.6 over the considered wavelength results in Equation 2.8, which can be used to calculate the Rosseland average extinction coefficient numerically from measured spectral data [23]:

$$\frac{1}{\hat{E}(T)} = \sum_{\Delta\Lambda} \frac{\frac{1}{E(\Lambda)} f_\Lambda(T) \Delta\Lambda}{\sum_{\Delta\Lambda} f_\Lambda(T) \Delta\Lambda}, \tag{2.8}$$

with

$$f_\Lambda(T) = \frac{\pi C_3 C_4}{2\Lambda^6} * \frac{1}{\sigma T^5} * \frac{exp\left(\frac{C_4}{\Lambda T}\right)}{\left[exp\left(\frac{C_4}{\Lambda T}\right) - 1 \right]^2}, \tag{2.9}$$

where $C_3 = 5.9544 * 10^-17 \frac{W}{m^2}$, and $C_4 = 1.4388 * 10^-2 \, mK$.

In the production of vacuum insulation panels (VIPs), opacifiers are mixed into the core materials to increase the emission coefficient of the insulation materials. Materials such as titanium dioxide, magnetite, silicon carbide, or carbon black can be used for this purpose. Depending on the material and the intended application, concentrations in the range of $10 - 40$ wt.% are used here. Thus, in practice, the radiation contribution is usually reduced to approximately a quarter of the original value. Chapter 7 details the effect of opacifiers.

2.2.3   Conduction over solid backbone

The thermal conduction of a solid material strongly depends on the crystalline or non-crystalline atomic structure of the material. In electrical conductors

with a defined lattice structure, the electrons can transport heat and therefore make the largest contribution to heat conduction. Since the electrical conductivity is also related to electrons, the ratio of both quantities to each other is constant and proportional to the absolute temperature T. This relationship is known as the Wiedemann–Franz law.

In amorphous, non-electrical conductors, such as silica, heat transport affected by phonons dominates. Phonons are quantized lattice vibration modes and are responsible for heat conduction in most non-metallic solids [24]. They belong to the quasiparticles. Thermal conductivity depends on how far phonons travel between scattering events. The average traveling distance is called the phonon mean free path L_{ph}. Kinetic theory defines the thermal conductivity as

$$\lambda_p = \frac{c_v v_s L_{ph}}{3}, \tag{2.10}$$

where c_v is the volumetric heat capacity, and v_s is the speed of sound (equivalent to the kinetic theory of gases in Section 2.3) [25]. When the geometric structures of the materials are in the order of magnitude of L_{ph} or smaller, phonon travel distances are no longer only limited by L_{ph} but also by the material surfaces. In this case, λ_p decrease with particle size when the particle size approaches the mean free path of phonons in the solid. The particle thermal conductivity can then be described via Equation 2.11, which identifies the thermal conductivity due to phonons having mean free paths less than L_{ph}^* [26]:

$$\lambda_p = \int_0^{L_{ph}^*} \frac{c_v(L_{ph}) v_s(L_{ph}) L_{ph}}{3} \, dL_{ph}. \tag{2.11}$$

Since there is no consensus on which models for phonon scattering should be chosen to form expressions for $c_v(L_p)$ and $v_s(L_p)$ [27, 28], and given that the geometric factor is difficult to capture for irregularly formed particles, the particle thermal conductivity λ_p is assumed to be $1 \frac{W}{mK}$ [29] for silica and $1.38 \frac{W}{mK}$ [30] for glass spheres in this thesis.

The solid thermal conductivity of a bed of perfect spheres with infinitesimal small point contacts would theoretically be 0. However, since the particles in a porous material are not perfect spheres and deform elastically on the contact points, a measurable solid thermal conductivity λ_s appears. The solid thermal conductivity can be described with the Hertz contact theory [31] and calculated via Equation 2.12 [32, 33, 34]:

$$\lambda_s = 3.44(1 - \phi)^{\frac{4}{3}} \left(\frac{1 - \hat{\eta}^2}{Y} \right)^{\frac{1}{3}} \lambda_P F^{\frac{1}{3}}, \tag{2.12}$$

where $\hat{\eta}$ is the Poisson ratio, Y is the elastic modulus, and F is the pressure load. The pressure load is caused either by gravity and the particles' own weight or by an external force. In the case of VIPs, the difference between

the internal pressure of the VIP and the atmospheric pressure p_{atm} must be considered.

2.2.4   Conduction over gas phase

The heat transfer mechanism, which is crucial to the functionality of vacuum insulation, is the conduction of heat through the gas phase λ_g. This mechanism strongly depends on the prevailing gas flow regime, which can be influenced by changing the cell or pore size or the gas pressure. Due to comparatively large pores, a fully developed continuum flow exists in the most conventional insulation materials. The mean free path L of air molecules at atmospheric pressure is 65 nm [35], while the pore sizes of conventional insulation materials are usually in the millimeter range. The mean free path increases with decreasing pressure. However, under continuum conditions, the thermal conductivity is only weakly dependent on the gas pressure. To understand this, it is important to remember that the thermal conductivity λ describes the property of a substance to transfer energy via particle collisions. On the one hand, the more particles are available for energy transport, the larger the thermal conductivity becomes. On the other hand, if there are many particles, the mean free path becomes smaller, so the energy cannot be transported as far in the individual steps, which leads to a reduction in the thermal conductivity. Both effects almost cancel each other out [36]. If the pressure, the pore size, or both are reduced such that the mean free path of the gas molecules is in the order of magnitude of the pore size, the distance over which the energy is transported in one individual step is no longer limited by the other particles, but by the pore wall. Thus, the heat flux becomes proportional only to the number of particles and no longer to the distance to the other particles. Thus, in a single gap of gap width x, the gas thermal conductivity λ_g has a strong pressure dependence, which follows a function in the form of Equation 2.13. This effect is utilized in thermal superinsulations by reducing both the pore size of the core materials and the gas pressure as much as possible.

$$\lambda_g(p,x) = \frac{\lambda_0}{1 + Kn}. \tag{2.13}$$

Here, Kn is the Knudsen number, which describes the ratio between the mean free path of the gas molecules and the pore size $\frac{L}{x}$, and λ_0 is the gas thermal conductivity at ambient conditions. The resulting gas thermal conductivity λ_g is a function of the gas pressure p because the mean free path L is a function of p. A detailed derivation can be taken from Section 2.3.

2.2.5   Coupling effect

The coupling thermal conductivity λ_c or coupling effect is the interaction between the different heat transfer mechanisms. This thesis focuses on the interaction between solid thermal conductivity and gas thermal conductivity be-

cause it is dominant for the investigated material classes. The coupling effect can also be described as the tendency of a given geometrical structure to form thermal series connections between the phases. For completely parallel gas and solid paths, no coupling occurs if they are adiabatic to each other. However, if one considers two parallel paths with direct contact, a small amount of coupling can already be detected. This is illustrated in Figure 2.1 (left), where a coupling heat flow occurs from the material with the higher thermal conductivity to the material with the lower thermal conductivity. This flow is caused by different temperature profiles and thus lateral temperature differences.
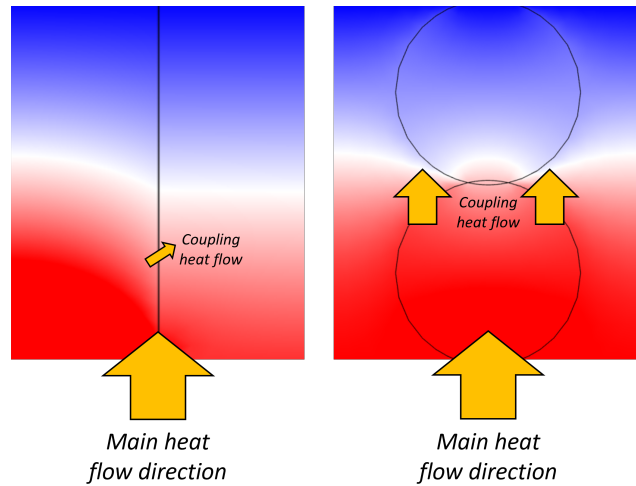
Figure 2.1: Schematic illustration of the coupling effect in different geometries. Left: parallel connection with direct contact; right: two touching spheres

The coupling effect is even greater if solid structures (e.g. in a porous material) are perpendicular to the heat flow. A geometry with a comparatively high coupling effect is shown on the right side of Figure 2.1. Following Heinemann [37], the "two touching spheres" or a bed of glass spheres would have a coupling effect factor $f = 7$. This means the ratio between the measured gas contribution λ_g to the theoretical value would be 7.

$$\lambda_c = f \cdot \lambda_g. \tag{2.14}$$

Metaphorically speaking, the air serves as a bridge for the heat between the particles. Zhao et al. [38] even describe an enhancement of the coupling effect by quasi-lattice vibrations of solid-like vibrating gas molecules trapped between nanoscale solid structures. They lead to a further increase in the coupling at the contact points of particles.

Extreme cases are the adiabatic parallel connection, where no coupling appears, and the series connection, where only coupling thermal conductivity can be detected. In reality, anything in between is possible. On the one hand, the coupling effect λ_c is negligible for foams with non-broken structure [39]. On the other hand, it can be the dominating effect for powders consisting of
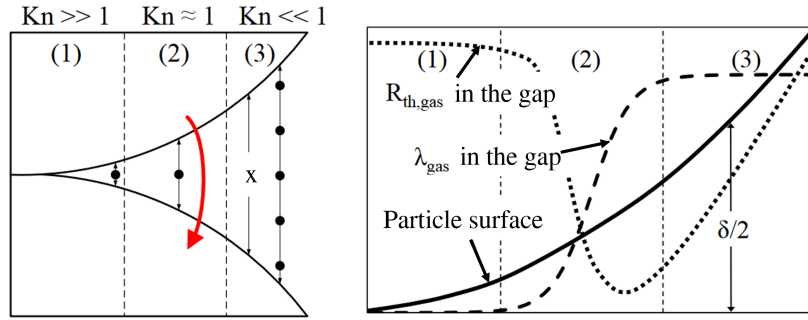
Figure 2.2: Influence of the Knudsen effect on thermal coupling in a gap between two touching particles (revised from [17])

hard grains. The coupling effect depends primarily on the structure of the material as well as on the size of the structures, since the Knudsen effect can have a local influence on the coupling. Parzinger [17] mentions that especially in gaps, interactions between the coupling effect and the Knudsen effect can occur. Since the gap distance decreases toward the contact point, the Knudsen number increases. As illustrated in Figure 2.2, this leads to an increase in thermal resistance R and a decrease in thermal conductivity λ_g. However, if one moves further away from the point of contact, the gap increases; the Knudsen number decreases; and at some point, when the Knudsen number becomes significantly smaller than 1, the Knudsen effect no longer has any influence. Then, λ_g approaches λ_0, and the thermal resistance increases with the gap width.

2.3 The kinetic theory of gases

The kinetic theory of gases is based on the idea that a gas consists of many small particles that move thermally. These particles collide with one another as well as with the walls. Energy conservation is valid because the collisions are assumed to be elastic. The laws relating to collisions of classical mechanics apply. From this model, all macroscopic state variables of gases can be derived from the mass M_g, the velocity v_g, and the number density N_g of the gas particles. The velocity distribution of gas particles in a void space must be determined in general as a solution to the Boltzmann equation. For a gas at rest and in thermodynamic equilibrium, this yields the Maxwell distribution [40], from which the average thermal velocity of a molecule $\bar{c}$ can be calculated via

$$\bar{c} = \sqrt{\frac{8kT}{m_g\pi}}, \tag{2.15}$$

and the average relative velocity $\bar{g}$ via

$$\bar{g} = \sqrt{2}\bar{c}, \tag{2.16}$$

where k is the Boltzmann constant, and T is the absolute temperature. Having a gas particle with a diameter d_g flying with an average relative velocity $\bar{g}$ through a volume with particle density $\hat{n}$, one can calculate the number of collisions per time unit (i.e. a collision frequency):

$$\nu = \hat{n}\pi d_g^2 \bar{g}. \tag{2.17}$$

Its inverse $\tau = \frac{1}{\nu}$ is called the mean free time. Figure 2.3 depicts such a particle's collision cylinder with diameter $2d_g$.
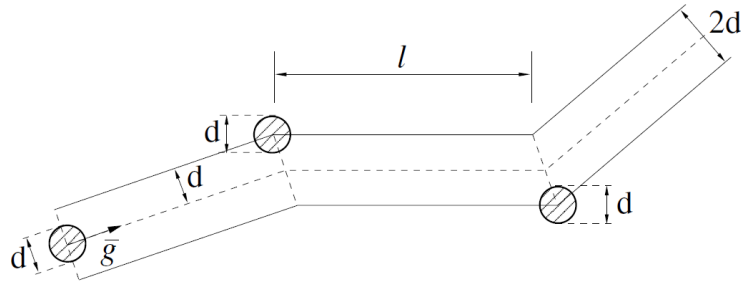
Figure 2.3: Collision cylinder of a molecule with diameter d [40]

Multiplying the mean free time by the mean thermal velocity yields the mean free path of the gas particles L, which is fundamental for this work. From the thermal equation of state of ideal gases, it can be derived that $\hat{n} = \frac{p}{kT}$, where p is the absolute pressure. Thus, for the mean free path of gas molecules, one obtains

$$L = \frac{k\,T}{\sqrt{2}\,\pi\,d_g^2\,p}. \tag{2.18}$$

Considering the behavior of the particles on a wall, one gets a surface collision rate j_N:

$$j_N = \frac{N}{A \cdot t} = \frac{\hat{n} \cdot \bar{c}}{4} = \frac{p \cdot \bar{c}}{4 \cdot k \cdot T}. \tag{2.19}$$

From these basic considerations, the macroscopic transport quantities viscosity, thermal conductivity, and diffusion can now be derived with the aid of the rigid sphere model. Sections 2.3.1 and 2.3.2 discuss viscosity and thermal conductivity, respectively. The transport properties are decisively influenced by the Knudsen number, which is the ratio of the mean free path L to a characteristic geometry x of the void space surrounding the gas particles. In the simplest model, this is the distance between two plane infinite plates:

$$Kn = \frac{L}{x}. \tag{2.20}$$

With the help of the Knudsen number, the gas can be divided into the following flow types [41].

Kn > 10	Free molecular flow
10 > Kn > 0.1	Transition regime
0.1 > Kn > 0.01	Slip flow
0.01 > Kn	Continuum flow / viscous range

Gases with a Knudsen number near or greater than 1 are called rarefied gases. In the free molecular flow regime, interactions between gas particles can be neglected. Thus, the particles collide only with the walls and not with one another. As a result, viscosity and thermal conductivity become directly proportional to the number of particles and hence to the pressure. In the viscous range, the opposite is true: the collisions with the walls now account for only a small proportion of the total number of collisions and can therefore be neglected. In this state, the particles fly only a fraction of the wall distance until the collision occurs. Now many particles are involved in the momentum or energy transport, but only some of them pass on in a forward direction, while the remainder move in a backward direction. The collisions therefore hinder the transport process from one plate to the other. This effect works against the favoring of the transport properties by an increased number of particles. Both effects balance each other out, such that viscosity and thermal conductivity in the viscous range are independent of pressure [42].

2.3.1 Viscosity

Due to its strong analogy to heat conduction while being easier to illustrate, viscosity is first briefly discussed in this section.

Moving a flat plate parallel to a stationary plate results in a force against the direction of motion, caused by the internal friction of the fluid between the plates. Given that in the molecular range, only collisions with the walls have to be considered, this force results from the change in momentum of the colliding gas particles:

$$F_{\mathrm{R}} = j_N \, A \, \alpha_{\mathrm{I}} \, M_{\mathrm{g}} \, (v_2 - v_1), \tag{2.21}$$

where v_1 and v_2 are the velocity of the gas and the plate, respectively, and α_I is the tangential momentum accommodation coefficient (MAC).

$$\alpha_{\mathrm{It}} = \frac{\text{Average tangential velocity of reflected particle}}{\text{Velocity of the plate}}.$$

The MAC describes the incompleteness of the momentum transfer at wall impact. Since the momentum accommodation at both walls must be considered,

the total effective MAC is calculated from the respective MACs α_{I1} and α_{I2} of both walls:

$$\alpha_I = \frac{\alpha_{I1}\,\alpha_{I2}}{\alpha_{I1} + \alpha_{I2} - \alpha_{I1}\,\alpha_{I2}}. \qquad (2.22)$$

An equal α_{I1} and α_{I2} results in

$$\alpha_I = \frac{\alpha_{I1}}{2 - \alpha_{I1}}. \qquad (2.23)$$

In the viscous range, the MAC only influences a thin boundary layer near the wall. Its influence can therefore be neglected, or complete accommodation can be assumed. Considering the momentum transfer of the particles among one another, for the frictional force F_R of a plate with area A, velocity v, and distance to the rigid plate x, one obtains the following according to [43]:

$$F_R = \eta A \frac{v}{x}. \qquad (2.24)$$

The proportionality factor η is called viscosity or dynamic viscosity. It results from the particle–particle collisions and can be determined via

$$\eta = \frac{5\,\pi}{32}\rho\,L\,\bar{c} \approx 0.5\,\rho\,L\,\bar{c}. \qquad (2.25)$$

2.3.2 Thermal conductivity

If matter is located between two places with a temperature gradient between them, thermal energy is transferred by means of thermal conduction. On a microscopic level, heat conduction can be considered analogous to viscosity, with the difference being that the energy transfer, not the momentum, is considered. The thermal energy of a particle is contained in its orbital motion (translational energy), in molecules with internal motions (vibration and rotation). This is described by the degree of freedom f^* of the particle. Noble gases have 3 degrees of freedom because of the possibility of translatory motion in all three spatial directions. Diatomic molecules have 5 degrees of freedom because they can additionally store energy in the rotation (but not around the nuclear axis, because the mass is concentrated only in the comparatively small nucleus). Further degrees of freedom by vibrational motions are hardly to be found in small molecules and at low temperatures. With increasing bond number and temperature, however, they occur more frequently. Since the heat capacity depends significantly on the degrees of freedom, it also increases with increasing temperature [42]. The following relationships apply:

$$c_V = \frac{f^*}{2} \cdot \frac{k}{M_g}; \quad c_p = \frac{f^* + 2}{2} \cdot \frac{k}{M_g} \qquad (2.26)$$

and

$$\kappa = \frac{c_p}{c_v}, \qquad (2.27)$$

where c_v and c_p are the heat capacities at constant volume and constant pressure, respectively, and κ is the isentropic exponent. Here, κ is always greater than 1, since c_p is always greater than c_v because of the additional volume change work.

Analogous to the friction force in Equation 2.21, the heat flux $\dot{Q}$ transferred via thermal conduction can be calculated for the case of molecular flow via

$$\dot{Q}_{mol} = j_N \cdot A \cdot \alpha_E \cdot c_v \cdot M_g \cdot (T_2 - T_1) \, , \qquad (2.28)$$

where T_1 and T_2 are the temperatures of the plate and particles before the wall impact, respectively, and α_E is the energy or thermal accommodation coefficient:

$$\alpha_E = \frac{\text{Actual heat flux}}{\text{Theoretical heat flux with complete accommodation}}. \qquad (2.29)$$

According to Knudsen [44], it can also be defined as

$$\alpha_E = \frac{T_1 - T_2}{T_1 - T_2'} = \frac{E_1 - E_2}{E_1 - E_2'}, \qquad (2.30)$$

where T_1, E_1 and T_2, E_2 are the mean temperatures and energy of the particles before and after the collision with the wall, respectively, and T_2', E_2' are the wall temperature and energy, respectively. The global energy accommodation coefficient in the plate model is composed of those energy accommodation coefficients of the two individual walls, analogous to the MAC. Since only α_E occurs below, it is simply referred to as the energy or thermal accommodation coefficient (TAC) or α. Similar to viscosity, one can now calculate a thermal conductivity λ for the viscous region using the model of hard spheres and assuming complete accommodation at the walls as follows:

$$\lambda = \frac{25\,\pi}{64}\,\rho\,L\,\bar{c}\,c_v. \qquad (2.31)$$

Now it is possible to establish a connection between the viscosity and the thermal conductivity of gases in the viscous range from Equations 2.25 and 2.31. This computational relation from the kinetic theory of gases is correct for noble gases but fails for molecules. Therefore, the correlation was empirically extended in the form of the Eucken correlation as follows:

$$\lambda = \frac{9\kappa - 5}{4}\,\eta\,c_v. \qquad (2.32)$$

This correlation is still highly accurate for noble gases. For diatomic gases, there are deviations up to $10\,\%$, and for polyatomic gases, deviations of some $10\,\%$ occur [45]. Thus, the correlation yields sufficiently accurate results for many applications.
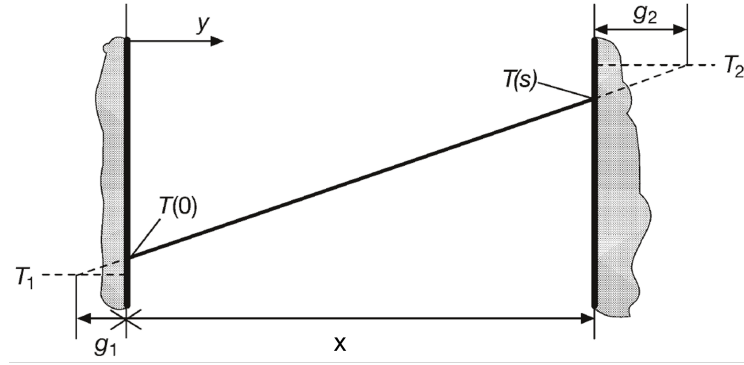
Figure 2.4: Schematic visualization of two parallel plates with temperature jump coefficients g_1 and g_2, adapted from [46]

2.3.3 The temperature jump

Caused by the gas dilution and the incomplete accommodation of energy at the wall impact, a temperature jump between the gas phase and the wall arises. The temperature of the gas directly at the wall can be described as follows:

$$T(y = 0) = T_W + g^* \left(\frac{\partial T}{\partial y} \right), \tag{2.33}$$

where y is the coordinate perpendicular to the wall, and T_W is the wall temperature. The coefficient of the temperature jump g^* is given by

$$g^* = \frac{2 - \alpha}{\alpha} \frac{15}{8} f^* L, \tag{2.34}$$

where

$$f^* = \frac{16}{15} \frac{1}{Pr} \frac{\kappa}{\kappa + 1}. \tag{2.35}$$

It can also be understood as an increase in the effective characteristic length x. This is shown schematically in Figure 2.4 for two parallel plates with temperature jump coefficients g_1^* and g_2^*. If the plates were moved away from each other by the distance $g_1^* + g_2^*$, the temperature profile would continue steadily. Under the assumption that both temperature jump coefficients are equal, this illustration leads to the following relation:

$$\frac{\lambda_g}{x} = \frac{\lambda_0}{2g^* + x}. \tag{2.36}$$

Converted to λ_g, this yields the basic equation for the gas thermal conductivity for Knudsen numbers smaller than 0.1 from the kinetic theory of gases:

$$\lambda_g = \frac{\lambda_0}{1 + 2\frac{g^*}{x}} = \frac{\lambda_0}{1 + \beta Kn}. \tag{2.37}$$

The dimensionless factor β results from this derivation:

$$\beta = 2\frac{2-\alpha}{\alpha}\frac{2\kappa}{\kappa+1}\frac{1}{Pr}.$$

(2.38)

 Equation 2.38 is often used exactly in this form to calculate the thermal conductivity of gases in porous media. However, other interpretations or simplifications also exist in the literature. A comparison of different calculation methods for the dimensionless factor β can be found in Paper 3 in Chapter 6.

Chapter 3

Materials and methods

3.1 Solid substances

The solid materials used in this study all consist of Silicon dioxide (SiO_2). Primarily various types of silica were used. All compounds of the general molecular formula $(SiO_2)_m \cdot nH_2O$ have the collective name silica. All synthetic silicas are originally produced from sand with further intermediates. The production processes can be categorized as either wet chemical processes or flame pyrolysis. Precipitated silica and silica gel (also called xerogel) are produced in wet chemical processes, while fumed silica is a product of pyrolysis. Figure 3.1 presents a summery of the different production routes.

All the different processes result in individual particle properties. They differ in size, shape, and bond strength. A basic comparison of the multiscalarity [48] of the materials used is shown in Figure 3.2. The size ranges of the particles listed here are only related to the materials investigated in this study and are therefore not valid for the material classes in general. The exact product specifications of all materials used can be found in Table 1 in Chapter 6. Silanol groups give the synthetic silicas a hydrophilic character. Precipitated silicas and silica gels generally have a higher silanol group surface density than fumed silicas. The silanol group density of fumed silica is approximately $2.5\,nm^{-2}$, and that of precipitated silica is $5-6\,nm^{-2}$ [49].

3.1.1 Precipitated silica

Precipitated silica has the most significant production volume. The precipitation is carried out from an aqueous alkali silicate solution (e.g. sodium silicate), with mineral acid such as sulfuric acid, according to the following equation [50]:

$$Na_2O \cdot 3.3\,SiO_2 + H_2SO_4 \longrightarrow 3.3\,SiO_2 + Na_2SO_4 + H_2O.$$
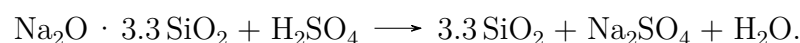
If the chemicals are continuously fed to the precipitation tank under constantly maintained alkalinity, precipitation of the silica occurs as colloidal pri-
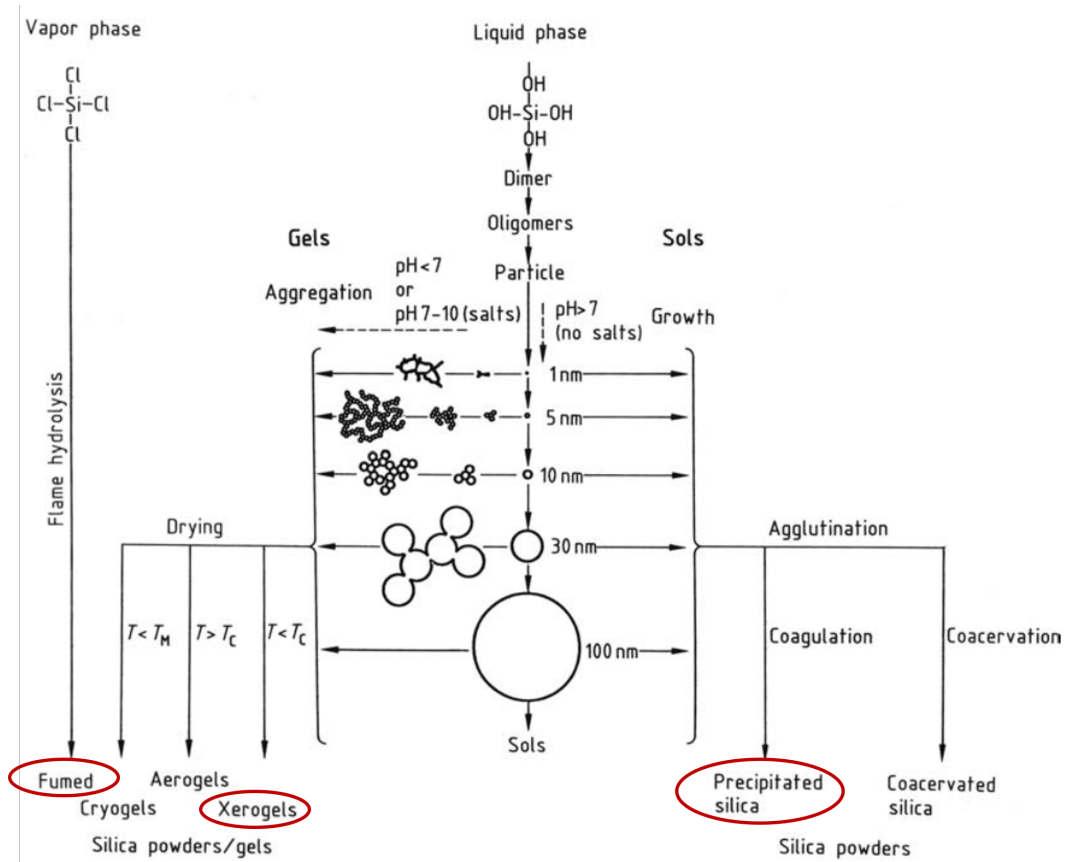
Figure 3.1: Different production routes of silica, revised from [47]; the material classes circled in red are investigated in the present study

Figure 3.2: The multiscalarity of the silica-based materials used with their respective size ranges

mary particles larger than $4 - 5\,nm$ and are coagulated into aggregates [51]. Temperature, the concentration of the solutions, and convection are important process parameters for reaction control. The end of the precipitation reaction is determined by a pH shift from alkaline to acidic, which stabilizes the precipitation product. Unwanted byproducts, such as sodium sulfate, are subsequently removed by filtration and washing processes. The resultant filter cake has a solid content between 15–25 %. The filter cake is dried using rotary kilns, flash dryers, or spray dryers. The drying process generally leads to the formation of agglomerates, whose size and distribution vary greatly depending on the drying process used. Therefore, regrinding must be carried out in most cases [52].

3.1.2 Silica gel

A gel can be defined as a solid structure that occupies the entire volume of liquid from which it was formed, while a precipitate is a solid formed in dense aggregates dispersed in a solution [53]. Silica gels are typically prepared similarly to precipitated silica but at a low pH by acidifying an aqueous solution of a soluble metal silicate, usually also sodium silicate. Acidification is usually done by treating the SiO_2 solution with a strong mineral acid, such as sulfuric acid or hydrochloric acid, until a pH is reached at which the SiO_2 solution transforms into a gel. The subsequently formed three-dimensional gel network thus includes the solvent used. The SiO_2 gel is then washed until no electrolytes are left. The pore structure is then adjusted by aging or post-treatment of the hydrogel [54]. It can be dried using traditional drying techniques known from precipitated silica to form a silica gel or xerogel. Thereafter, the dry product is milled to the desired aggregate size.
To completely preserve the particulate solid structure, the hydrogel would have to be dried in a supercritical state. The resulting products are called aerogels and have outstanding thermal properties. However, this process is highly complex, and aerogels are hence too expensive for most applications. Therefore, aerogels are not considered further in this thesis.

3.1.3 Fumed silica

The large-scale production of fumed silica by flame pyrolysis is also referred to as the "aerosil process." In this process, silicon tetrachloride is transferred to the gas phase before it reacts spontaneously with temporarily formed water to create highly dispersed silica within an oxyhydrogen flame at temperatures of approximately $1{,}000\,°C$. This process generates silica with a primary particle size from 7–$40\,nm$ and a Brunauer–Emmett–Teller (BET) surface area from 50–$600\,\frac{m^2}{g}$. The primary particles form aggregates by intergrowth and agglomerate through cohesion forces [51].

$$2\,H_2 + O_2 + SiCl_4 \xrightarrow{\hspace{0.5cm}1{,}000\ °C\hspace{0.5cm}} SiO_2 + 4\,HCl.$$
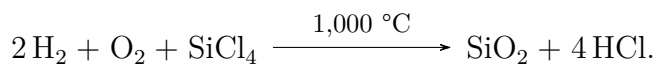
The change in flame temperature, concentration of reactants, and residence time of silica in the combustion chamber strongly influence the reaction. Thus, the particle size distribution, the specific surface area, and the particle morphology can be controlled by appropriate reaction control. The gaseous byproduct hydrogen chloride is separated from the silica. The resulting surface of fumed silica is almost pore-free [52].

3.1.4   Glass spheres

The conventional method for producing glass microspheres is the in-flame spheroidization method, where a continuous controlled flow of powdered glass is fed to a gas flame [55]. The irregularly shaped particles melt and form spheres due to surface tension. Glass microspheres are used industrially, for example in fixed-bed reactors [56] or as cryogenic insulation materials [57].

3.1.5   Pore size distribution via mercury intrusion porosimetry (MIP)

Pore size distribution is determined by a stepwise penetration of mercury into a porous structure under defined pressure [58]. The pressure required to fill a pore with the non-wetting liquid mercury is inversely proportional to the pore size. Mercury intrusion porosimetry (MIP) allows for the analysis of pore sizes over a wide range from approximately $3\,nm - 400\,\mu m$ [59]. Pore size distribution is calculated using the Washburn equation assuming fully wettable and cylindrical pores. The equation can be found, together with additional information about MIP, in Chapter 4. For the present thesis, two different devices were used, namely a Pascal 440 (*Co. Thermo Fisher*) and an AutoPore III (*Co. micromeritics*).

3.1.6   Primary particle size via small-angle x-ray scattering (SAXS)

The dominant interaction of an x-ray beam with solid matter is represented by elastic scattering (Thomson scattering) [60]. Equation 3.1 shows the fundamental relation describing the diffraction of X-rays by solid matter, where Λ is the wavelength, x is the size of the structure, and Φ is the scattering angle:

$$\Lambda = 2x\ sin(\Phi). \tag{3.1}$$

The equation shows that the angle of diffraction varies inversely with the structure size x. X-ray scattering is often used to study crystal lattices. Here, the lattice spacings represent the structure size. In ordinary crystals, particularly

those of inorganic matter, the majority of the observed lattice spacings are of the same order of magnitude as that of the x-ray wavelengths, which is in the Å range, such that the angles Φ are usually rather large. To examine particles, or rather heterogeneities in the matter, in the nanometer range, small scattering angles must be detected. The resulting beams would be close to the primary beam, thus requiring a large distance in the range of meters between sample and detector [61]. Small-angle x-ray scattering (SAXS) measurements can be used to determine the primary particle size and the fractal dimension of silica samples [62]. In the present thesis, a Xeuss 2.0 Camera (*Co. Xenocs, Grenoble, France*) was used for this purpose. More information can be found in [48].

3.1.7 Aggregate size via dynamic light scattering (DLS)

Dynamic light scattering (DLS) utilizes the property of monochromatic light to interact with particles via quasi-elastic scattering. In DLS or photon correlation spectroscopy, the particle size is determined by the diffusion coefficient. In this measurement method, a laser beam is directed into a dispersion of particles and then scattered by the particles. The scattered signal is detected, and the square of variation of the scattered light intensity, not the absolute scattered light intensity, is evaluated. Smaller particles diffuse faster; for example, due to Brownian molecular motion, large particles tend to have slow but pronounced intensity changes due to their inertia. These interactions result in a frequency shift of the scattering wave in the range between $10\,Hz$ and $10^6\,Hz$ [63]. The particle velocity can be determined accordingly. The diffusion constant is then calculated from the particle velocity, and the particle size is calculated via the Einstein equation. The measurement range for particle sizes is between $3\,nm$ and $3\,\mu m$ [64]. To determine the aggregate sizes of the FS, PS, and SG materials, suspensions were prepared with deionized water, followed by a 10-minute treatment with an ultrasonic tip to separate the aggregates. The measurements were performed with a Zetasizer (*Co. Malvern Panalytical Ltd*).

3.1.8 Agglomerate size via laser diffraction

In laser diffraction, particle size distributions are determined by measuring the angular dependence of the intensity of scattered light from a laser beam passing through a dispersed particle sample. Large particles scatter light at small angles relative to the laser beam, while small particles result in large scattering angles. The data of the angle-dependent scattered light intensity are analyzed and are the basis for calculating the size of the particles responsible for the diffraction pattern. For small particles ($< 50\,\mu m$), the Mie theory is used for this analysis [65]. For larger particles, one can use Fraunhofer diffraction theory, which states that the intensity of light scattered by a particle is

directly proportional to the particle size [66]. In the framework of this thesis, laser diffraction was used to determine the agglomerate size of the silica samples. Demineralized water was used as the dispersing liquid. Samples were stirred briefly in demineralized water using a propeller stirrer, and representative samples were analyzed after approximately 10 minutes of recirculation and stirring without ultrasonic dispersion. To avoid breaking up the agglomerates, no ultrasonic treatment was used. For the measurements, a Helos laser diffraction spectrometer (*Co. Sympatec*) with a "Quixel" wet disperser unit was employed.

3.1.9 Emission coefficient via Fourier-transformed infrared (FTIR) spectroscopy

To determine the Rosseland average extinction coefficient according to Equation 2.5, the infrared spectrum of the materials must be measured [67]. Fourier-transformed infrared (FTIR) spectroscopy monitors the interaction of functional groups in chemical molecules [68]. In the present thesis, the transmission spectrum of the investigated powders was measured. A light beam was directed onto a thin sample, and the light that passed through the sample (i.e. was not absorbed or scattered) was detected. The FTIR uses interferometry to record information about a material placed in the IR beam. This makes it possible to achieve a fast scan of the entire spectrum. The investigated spectra were recorded with an ALPHA-R (*Co. Bruker Optics GmbH, Ettlingen, Germany*) in the wavelength range from $10^{-6} - 10^{-5}\, m$. Polyethylene film was used as the specimen holder, and the powders were pressed onto the foil using a pressing tool specially developed for this application. Homogeneous layers in the order of $100\,\mu m$ were formed. The determined extinction coefficients are used in Chapter 7 to calculate the density-dependent radiation thermal conductivity.

3.2 Gases

For the thermal conductivity measurements, air was not the only gas used as the residual gas in the porous materials. Seven different gases were used instead: dry air, helium (He), argon (Ar), krypton (Kr), carbon dioxide (CO_2), sulfur dioxide (SO_2), and sulfur hexafluoride (SF_6). These gases were selected to represent a wide range of molar masses and gas thermal conductivities. The gases were all purchased from the Linde Gas Division (*Co. Linde GmbH, Germany*). Chapter 5 (Table 2) and Chapter 6 (Table 3) contain additional information about the individual gases.

3.3   Thermal conductivity measurements

Measurement methods for determining thermal conductivity can be divided into transient and steady-state methods. In transient methods, on the one hand, the step response of the temperature rise of a spontaneously generated temperature gradient on the opposite side of the sample is detected. Calculation methods of transient heat transport are used for the evaluation. This allows for a determination of the thermal diffusivity, but not the thermal conductivity. The specific heat capacity of the sample is therefore required for conversion to thermal conductivity. The decisive advantage of these methods is primarily the low time requirement. Examples are the transient hot wire, laser flash thermal diffusivity apparatus, and transient plane-source method (hot disk method).

Steady-state measurement methods, on the other hand, are independent of the storage term and are therefore suitable for the direct determination of thermal conductivity. The guarded hot plate (GHP) method is the most commonly used steady-state method for measuring the thermal conductivity of insulation materials. It is considered to be a reference method, and it is standardized by many countries [69]. Therefore, this method was chosen for the present work. The method takes its name from the guard heater surrounding the actual heater. It is brought to the same temperature as the actual heater to completely avoid lateral temperature gradients. The heat flow to be measured therefore follows parallel heat flow lines in the direction of the heat sinks (cooling plates). The cooling plates are located both above and below the heating plate and are separated by two identical samples.

A GHP apparatus specially adapted to the present requirements was set up as part of this thesis. Chapter 4 contains a schematic representation of the construction, a photograph, and an uncertainty analysis (Figure 1, Figure 2, and Table 1, respectively). For the measurement of the powders investigated, the sample mold can be removed completely from the vacuum chamber. This has the advantage that the sample preparation, which includes a mechanical compression step using a hydraulic press, can be carried out directly in the mold. Since many powders are still highly sensitive after this step, unnecessary stressing of the samples should be avoided. Furthermore, it is possible to reduce gaps between the plates to a minimum. Since gaps running horizontally can have a considerable influence on the measurement results in low pressure ranges, this procedure is important.

For sample preparation, a certain amount of powder is weighed into the mold. The powder should then be slightly pre-compacted with a press plunger. Thereafter, the heating plate (including the guard heater), which can also be completely removed from the vacuum chamber, is applied to the powder layer. The same amount of powder is then placed on top of the heating plate and slightly compacted again. Thereafter, the entire structure is compacted with the aid of the press plunger and a hydraulic press either to the desired pressure or to the

desired density. Afterwards, the chosen state (position or pressure) must be maintained for approximately one minute. When working with a defined pressure, the powder must be continuously pressed during this time, as it relaxes once the stamp comes to rest. The pressure must be released slowly to avoid relaxation cracks. The pressure plunger can then be removed carefully, and any surplus powder is removed by vacuuming. Now the mold is placed into the vacuum chamber on top of the lower cooling plate, and the upper cooling plate is placed on top of the upper sample. To hold everything together and to avoid gaps, an additional weight of approximately 10 kg is placed on top of the upper cooling plate. To measure under controlled atmospheres, the lid must be closed at this point. The heating plates (the actual plate and the guard) are then heated to 95 °C for at least three hours. At the same time, the vacuum pump is started to completely evacuate the chamber overnight. The next day, the vacuum chamber is flooded with the gas of interest several times before the actual measurement starts. In the associated LabVIEW (*Co. National Instruments*) program, 13 freely selectable pressure levels can be set that are automatically processed from top to bottom. Furthermore, the program allows one to set the duration for which the pressure levels are to be held. It has shown that a holding time of 20 minutes is suitable for most materials. The first half of this time is needed to adjust the pressure and power consumption; then, the measurement data can be recorded. For the pressure control loop, two individual capacitive pressure sensors with different measuring ranges are used: one for pressures $p > 14\,mbar$ and the other one for $p < 14\,mbar$. If necessary, a turbomolecular pump can also be added. In this case, a cold cathode gauge is used for pressure monitoring. Once the measurement of all pressure levels is completed, the recorded average power consumption of the heating plate is evaluated. For this purpose, Equation 3.2 is used to convert the results into a pressure-dependent thermal conductivity curve:

$$\lambda(p) = \frac{\dot{Q}\, X}{A\, \Delta T}, \tag{3.2}$$

where, $\dot{Q}$ is the recorded power consumption of the heating plate, which is equivalent to the heat flux through both samples; X is the sample thickness, A is the area of the heating plate and ΔT is the temperature difference between the heating and cooling plates.

Chapter 4

Paper 1: *Correlation of pore size distribution with thermal conductivity of precipitated silica and experimental determination of the coupling effect*

One crucial factor in modeling the effective thermal conductivity of porous media is the coupling effect. It can vary greatly depending on the type and structure of the investigated material. In some cases, its contribution is negligible, while in others, it exceeds the actual gas thermal conductivity many times over. In the literature, few data regarding the coupling effect factors of specific materials are available. As already mentioned, Reichenauer et al. [70] indicate a coupling effect factor of $f = 7$ for a bead of glass spheres, while Hemberger et al. [71] mention a coupling that is of the same order of magnitude as the pure gas-phase transport for carbon aerogels, which means $f \approx 1$. No literature data are available for fumed silica or precipitated silica. However, the author is pursuing the further development of precipitated silica as a promising core material for vacuum insulation. Therefore, in this chapter (Paper 1), the coupling effect factors of different precipitated silicas are investigated. In addition, the influence of different degrees of compression of the powders is studied. Conclusions can consequently be drawn about the influence of the specific microstructures of the different precipitated silicas as well as the pure influence of porosity.

Swimm's resistor model [72] describes the thermal coupling behavior of a dispersed solid–gas system using a simple series connection of thermal resistances. The derivations lead to the conclusion that if $\lambda_g \cdot x_s << \lambda_s \cdot x_g$, then the gas pressure dependence of thermal coupling between the gas and solid phases is,

formally, a vertical stretching of the s-curve for pure gaseous thermal conduction with a constant scaling factor f. Since porous media with high porosities are used for VIPs in general, $x_s < x_g$ can be assumed. Furthermore, the ratio between the bulk thermal conductivity of silica λ_p and the gas thermal conductivity λ_g (even at low Knudsen numbers) is at least $\frac{\lambda_p}{\lambda_g} = \frac{1\frac{W}{mK}}{0.026\frac{W}{mK}}$, which allows for the assumption that $\lambda_g < \lambda_p$ for all cases.
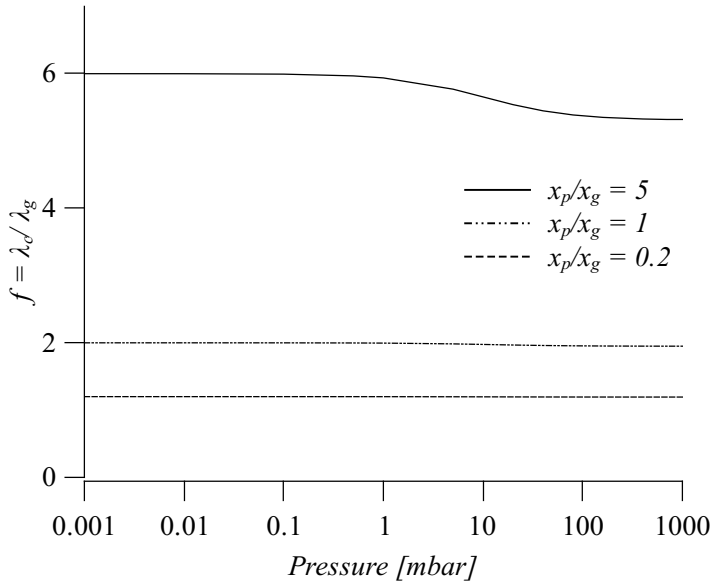
Figure 4.1: Coupling effect factor f over gas pressure calculated with the simple series connection model. For the calculation, a silica–air system with an air gap size of $20\,\mu m$ was considered.

Figure 4.1 shows the dependence of f calculated according to Swimm's simplified series model for different gas–solid fractions of air and silica. A pressure dependence, or a dependence of the ratio $\frac{\lambda_g}{\lambda_p}$, becomes significant only at high solid fractions. The smallest porosity investigated in this chapter (Paper 1) is 0.756, which would correspond to a maximum ratio of $\frac{x_p}{x_g} = 0.32$ in the simplified model. Thus, a linear scaling of the λ_g curve can be assumed in a good approximation. Coupling effect factors for different microgeometries were also determined by Swimm et al. using CFD simulations [73]. Values between $f = 3.4$ and $f = 6.3$ were obtained for different geometries but constant porosity.

In Chapter 4, it is shown that the microstructures of different precipitated silicas are similar with respect to their tendency to form a coupling thermal conductivity. Therefore, in the investigated porosity range from $0.76 - 0.92$, which is relevant for the VIP application, a linear course of the coupling effect

factor to the porosity can be assumed in a good approximation, as illustrated in Figure 7 of the paper.
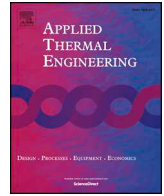
Research Paper

Correlation of pore size distribution with thermal conductivity of precipitated silica and experimental determination of the coupling effect

S. Sonnick[a,b,*], M. Meier[b], J. Ross-Jones[a,b], L. Erlbeck[a], I. Medina[a], H. Nirschl[b], M. Rädle[a]

[a] *Institute for Process Control and Innovative Energy Conversion, University of Applied Sciences Mannheim, Paul-Wittsack-Straße 10, 68163 Mannheim, Germany*
[b] *Institute for Mechanical Process Engineering and Mechanics, Karlsruhe Institute of Technology, Strasse am Forum 8, 76131 Karlsruhe, Germany*

HIGHLIGHTS

- Precipitated silica was tested for suitibility as core material for vacuum insulation.
- A guarded hot plate apparatus, measuring under vacuum conditions, was developed.
- Mercury intrusion porosimetry data were used to calculate gas-thermal conductivity.
- Model to predict thermal conductivity is presented (focus on coupling effect).

ARTICLE INFO

ABSTRACT

Vacuum insulation panels are high-performance insulating materials with considerably better thermal properties than conventional thermal insulation. Unfortunately, their use is limited to applications where their high price does not matter. To extend the application range of vacuum insulation, the authors try to replace the high-priced core material fumed silica with the cheaper precipitated silica. For this purpose, five commercially available precipitated silica samples were tested for their suitability as core material for vacuum insulations. They were pre-pressed with 5 bar and 30 bar each. To compare their thermal performances, a guarded hot plate apparatus for measuring thermal conductivities under vacuum was developed. The pore size distributions of the samples were measured by mercury intrusion porosimetry and used to calculate the gas thermal conductivity as a function of the residual pressure. For this purpose, a correction factor for the measured pore size distribution is introduced. Additionally, the coupling effect between gaseous and solid thermal conductivity could be determined through comparison with measured data. A model is presented to predict the thermal conductivity curve, even of unknown silica samples, solely using mercury intrusion porosimetry data.

1. Introduction

Thermal insulation materials are essential for sustainable energy management of processes and devices. Nowadays, most insulations consist of foam or fiber materials made of organic or inorganic base materials [1]. These conventional insulation materials all operate according to the same principle. They are composed of a wide network of solid material with air inclusions (pores) which are small enough to suppress convection within. The solid materials always have higher thermal conductivities than the included air. Thus the goal of manufacturers of conventional thermal insulation materials is to reduce the solid fraction as long as the conductivity of the insulation material approaches the value of air, which is $25.87 \frac{\text{mW}}{\text{mK}}$ at $20\,°C$ [2]. Most conventional materials on the market reach thermal conductivities

around 30–40 $\frac{mW}{mK}$.

Super-insulations operate on a principle based on the Knudsen effect, whereby the pore size of the material is of the same order of magnitude as or less than that of the mean free path of gas molecules. This leads to a phenomenon where the gaseous thermal conductivity inside the pores decreases. If the pore size is substantially smaller than the mean free path, thermal conductivity of the gas can be neglected. One possibility to achieve the Knudsen effect is to reduce the pore size. At atmospheric pressure, the pore size should be smaller than 65 nm at 20 °C so that it is smaller than the mean free path [3]. Alternatively, it is also possible to reduce the gaseous pressure inside the pores, which is the operating principle of vacuum insulation panels (VIP). Thus, super-insulations can reach lower overall thermal conductivity values as compared to free air. This special property makes such insulation

---

Nomenclature

Symbols

$\dot{Q}$	heat flux [W]
$\bar{x}$	average pore size [m]
D	fractal dimension [–]
d	diameter [m]
E	transport extinction coefficient [m^{-1}]
F	pressure load [bar]
f	coupling effect factor [–]
k_B	Boltzmann constant [J/K]
Kn	Knudsen number [–]
L	mean free path of molecules [m]
n	reflection index [–]
P	pressure of mercury intrusion porosimetry [Pa]
p	pressure [mbar]
T	temperature [K]
V	volume [m^3]
x	pore size [m]
Y	elastic modulus [Pa]
α	accommodation coefficient [–]
β	dimensionless coefficient for gaseous conductivity calculation [–]

γ	surface tension of mercury [Nm]
η	Poisson's ratio [–]
Θ	contact angle between mercury and silica [°]
κ	adiabatic coefficient [–]
λ	thermal conductivity [W/mK]
λ'	thermal conductivity of a single pore [W/mK]
$λ_0$	free gas thermal conductivity [W/mK]
σ	Stefan-Boltzmann constant [W/m^2K^4]
ϕ	porosity [m^3/m^3]

Subscripts and abbreviations

2d	two dimensional
3d	three dimensional
AM	air molecule
atm	atmospheric
c	coupling
g	gaseous
max	maximum/end of intrusion
r	radiative
s	solid
SM	solid material
sr	solid and radiative

materials very interesting for many applications where a good thermal dissociation is essential but space is limited, such as in cryogenic devices [4], heat storage tanks, in the building sector for restauration of historic monuments or if space inside the walls is required for thermal storage systems like phase change materials [5]. Most of the commercially available VIPs consist of core material mixtures made of fumed silica, because its nanoporous, hierarchical structure ensures low gaseous and solid conductivity values; some kind of opacifier to reduce radiation and fibers add mechanical stability to the material. The material is pressed, cut to the desired dimensions and sealed under vacuum in aluminized foils. These panels have thermal conductivities around 4–8 mW/mK right after production. Due to unavoidable minor leakages, the internal pressure increases constantly. The typical lifetime of a panel is estimated around 25 years [6], at which point the thermal conductivity doubles its initial value. For core materials made of fumed silica, this happens when the internal pressure reaches approximately 100 mbar. However, precipitated silica cores reach this point at around 10 mbar [6,7], while their initial value is basically the same. A great advantage of precipitated silica is its significantly lower price compared to fumed silica. Thus, precipitated silica can be attractive for some applications, such as thermal transport boxes, where long lifetimes are unnecessary. For this reason, the purpose of this work is to uncover correlations between thermal and structural properties, to understand the behavior of different precipitated silica samples for use in insulation materials, to ultimately define the perfect silica for the authors' application.

2. Measurements and analysis

To characterize and compare properties of different precipitated silica samples, five different types have been examined. The manufacturer of all samples is Grace Germany GmbH and the product names are Perkasil GT 3000 PD (GT), Syloid MX109 (MX), CP 513 – 11202 (CP), Perkasil KS 408 PD (KS) and Sylowhite SM 405 (SM). In the subsequent sections, the following shortcuts are used: GT, MX, CP, KS, SM. These are commercially available products and have been delivered in 15 kg or 25 kg bags. These samples were selected to get a good

overview of the company's product portfolio. All samples were prepared with external pressure loads of 5 bar and 30 bar with a hydraulic press. Furthermore, pore size distributions of all ten samples have been measured with mercury intrusion porosimetry and thermal conductivity over gas pressure, with a guarded hot plate apparatus.

2.1. Mercury intrusion porosimetry (MIP)

Mercury porosimetry analysis is the progressive intrusion of mercury into a porous structure under strictly controlled pressure [8]. Since the necessary pressure to intrude the non-wetting liquid mercury into a pore is inversely proportional to the pore size, it is possible to measure pore size distribution with this method. The main advantage is that it allows pore size analysis to be undertaken over a wide range of mesopore–macropore widths (routinely, from ca. 0.003 to ca. 400 μm) [9].

$$x(p) = -\frac{4\gamma cos(\Theta)}{P} \qquad (1)$$

MIP pore size distribution analysis is based on the Washburn equation (Eq. (1)) and on the assumption that pores are cylindrical and entirely and equally accessible to mercury. To calculate the minimum pore size x as a function of the particular mercury pressure level P, the surface tension of mercury γ and the contact angle between mercury and silica Θ are required. For the present work, Θ = 130°, $\gamma = 0,485$ N/m and a "*AutoPore III (co. micromeritics, USA)*" were used.

Besides pore size distribution, MIP-data can be used to determine the surface fractal dimension D of the pores. In this case, the fractal dimension of a solid is a parameter characterizing the degree of roughness of its surface [8].

$$log\left(\frac{dV}{dp}\right) = log(C) + (D - 4)log(P) \qquad (2)$$

By double-logarithmic application of Eq. (2), where P is the mercury pressure, V is the volume of mercury intruded into the pores and C is a constant, the fractal dimension D of the pores can be determined from the slope.

2.2. Test apparatus for thermal conductivity at various pressure levels

To measure thermal conductivity of silica samples at various pressure levels, a test bench, which is able to operate under vacuum, has been developed. It operates according to the principle of a guarded hot plate apparatus [10], where the measuring area in the center of the apparatus is surrounded by guard heaters which avoid heat losses from the measuring area to the surroundings. The measuring principle is shown in Fig. 1.

The whole structure is placed in a vacuum chamber composed of a stainless steel tank. A view into the opened tank is shown on Fig. 2. With the rotary vane vacuum pump P1, the valve V1 and two pressure sensors P1.1 and P1.2 for different pressure levels, it is possible to regulate the internal pressure from approximately 0.05 mbar up to atmospheric pressure. Two samples of equivalent thickness, between 5 and 15 mm, are placed between the heating plate and the two cooling plates. When testing loose samples, the powder samples can be pressed directly into the mold within the chamber. Pressing directly into the mold avoids air gaps between the samples and the plates, which is one of the main advantages of this self-constructed apparatus compared to commercial devices. The mold, as well as the heating and cooling plates have a quadratic base area of $0.0256\,\mathrm{m}^2$. The primary heater H1, in the center of the heating plate, has a base area of $6.4 * 10^{-3}\,\mathrm{m}^2$ and can be regulated to the requested heating plate temperature by electrical power. The guard ring H2 is regulated to the same temperature as H1 to ensure that all the heat from H1 flows towards the cooling plates and not into the surroundings. The cooling plates are made of aluminum and fit seamlessly into the mold. The plates contain spiraling channels with flowing cooling water to ensure an even temperature distribution. The temperature of the cooling water can be controlled by an external cryostat. In this way, the average temperature and range of interest can be chosen. Additionally, the outside temperature of the mold can be adjusted with heater H3 to isolate the chamber from the surrounding temperature. For all control loops, 12 PT100 temperature sensors T1.1 to T4.2 are positioned at several locations around the test stand.
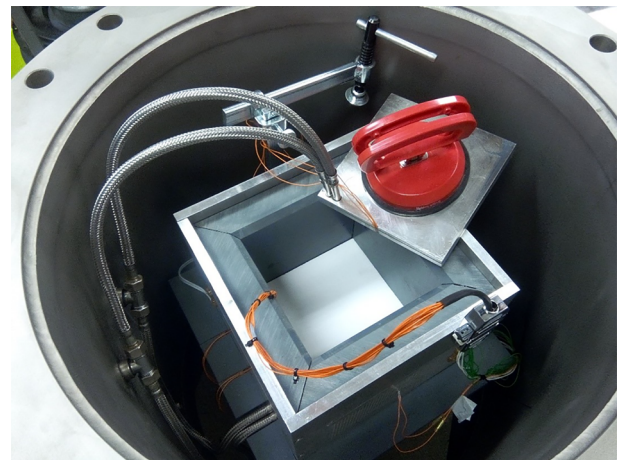
Fig. 2. View into the opened vacuum chamber. Cooling plate 1 can be seen outside the sample mold. Both samples, the heating plate and the cooling plate 2 are already in position.

Table 1
Measurement uncertainty for components of the guarded hot plate apparatus.

Temperature measurements		
		Error
Thermocouple	PT100 (1/3 DIN)	± 0.18 K
Transducer	MU-PT100-I420	0.100%
NIDAQ	USB.6008	0.153%
	Total	**0.183%**
Power measurement		
		Error
Measure power	Shunt resistor	1.000%
NIDAQ	USB.6008	0.147%
	Total	**1.011%**
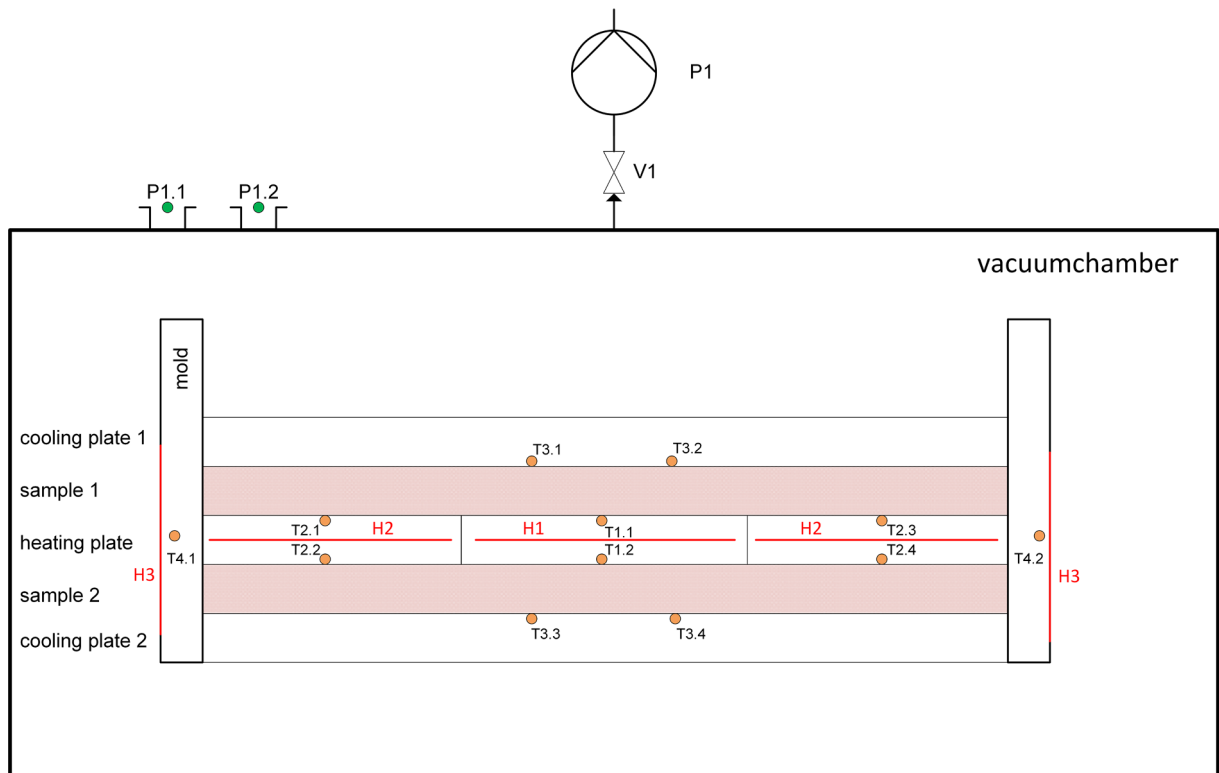
Fig. 1. Illustration of the test stand for measuring thermal conductivity at various pressure levels.

To characterize a sample, the chamber is evacuated to a pressure of approximately 0.05 mbar. After adjusting heating and cooling plate temperatures, it is necessary to wait until the temperature field is stable, which means the power input into H1 is constant. Power consumption of H1 as well as all temperature and pressure data are recorded every five seconds.

2.2.1. Uncertainty analysis of thermal conductivity measurement

Calculating the propagation of uncertainty using Table 1, together with the uncertainty for the thickness and area of the VIP, 1.5% and 1% respectively a total uncertainty of 2.07% for the thermal conductivity measurement is obtained.

To validate the device, a reference measurement needs to be performed. For this purpose a standard polystyrene board from NIST (National Institute of Standards and Technology) is used. At the present conditions (T = 30 °C and $\rho = 39.03 \frac{kg}{m^3}$) the test material is supposed to have a thermal conductivity of $0.0343 \frac{W}{mK} \mp 1.5\%$ [11]. The measured value of the newly developed guarded hot plate device is $0.0341 \frac{W}{mK}$. Thus, it matches perfectly within the uncertainty range of the test material.

Two capacitive pressure sensors are used, a "*MKS Baratron Type 122A*" and a "*Siemens SITRANS P200*" sensor to measure at low and high pressures respectively. Both sensors have a maximum uncertainty of 0.5%, whereas the "*MKS Baratron*" sensor is used between 0.01 and 14 mbar and the "*Siemens*" sensor between 14 mbar and atmospheric pressure.

3. Thermal transport theory and analytical model

Heat transfer in insulation materials is composed of three main mechanisms: solid thermal conductivity λ_s, radiative thermal conductivity λ_r (both mechanisms are only a function of temperature, which means for isothermal problems they can be assumed to be constant) and gaseous thermal conductivity λ_g which is a function of gas pressure p and the mean free path, for example the pore size x. A fourth mechanism which depends on the microscopic shape of the material and also on gas pressure is the coupling effect between solid and gaseous thermal conductivity λ_c [12]. λ_c is negligible for most foams [13] but plays a decisive role for silica based core materials, which are investigated in this work. Consequently, the thermal conductivity of an insulation material can be described as a sum of these four mechanisms as shown in Eq. (3) [13,14]. All heat transfer mechanisms are temperature dependent, however, in this work constant and steady state temperature are assumed.

$$\lambda(p) = \lambda_s + \lambda_r + \lambda_g(p) + \lambda_c(\lambda_g) \tag{3}$$

3.1. Solid thermal conductivity

Heat flow over the solid phase of a bulk powder λ_s depends on various material properties. Of course, the thermal conductivity λ_{SM} of the solid material itself plays an important role, but also the porosity ϕ and the thermal contact resistance between the particles are influential. The contact resistance is not easy to capture and depends on the Poisson's ratio η, the elastic modulus Y, the radius of the particles and the effecting pressure load F. These influences are summarized in Eq. (4), which is used by many authors to calculate solid thermal conductivity [4,15].

$$\lambda_s = 3,44(1-\phi)^{\frac{4}{3}}\left(\frac{1-\eta^2}{Y}\right)^{\frac{1}{3}}\lambda_{SM}F^{\frac{1}{3}} \tag{4}$$

3.2. Radiative thermal conductivity

In most macroscopic cases, radiation can be described with the Rossland approximation for optically thick materials. Thus, it is possible to calculate an equivalent conductivity λ_r using Eq. (5) [6].

$$\lambda_r = \frac{16\sigma n^2 T^3}{3E(T)} \tag{5}$$

In this case T is the radiative temperature and can be calculated with the surface temperatures of the sample T_1 and T_2 using Eq. (6), where $E(T)$ is the transport extinction coefficient, σ is the Stefan-Boltzmann constant and n the reflection index, $n \approx 1$ for opacified silica.

$$T = \sqrt[3]{\frac{(T_1^2 + T_2^2)(T_1 + T_2)}{4}} \tag{6}$$

To reduce radiative heat transfer, opacifiers such as carbon black, TiO_2 or silicon carbide are used. Caps and Fricke [16] found $E = 3600$ m^{-1} for pure precipitated silica and values up to $E = 26000$ m^{-1} for opacified precipitated silica.

3.3. Gaseous thermal conductivity

Considering the Knudsen effect, thermal conductivity of gases surrounded by a solid material is a function of geometric size and gas pressure or rather the mean free path of gas molecules. The Knudsen Number Kn is used to quantify the relation between the mean free path of molecules L and the geometric size of the confined space, for example the pore size x.

$$\lambda_g = \frac{\phi * \lambda_0(T)}{1 + 2 * \beta * Kn} \tag{7}$$

In Eq. (7) [4] λ_0 is the thermal conductivity of the gas at atmospheric pressure, ϕ is the porosity of the insulation material and β is a dimensionless coefficient depending on an accommodation coefficient α and the adiabatic coefficient of the gas κ. It can be calculated via Eq. (8) [4]. The accommodation coefficient is a measure for the quality of energy exchange between the gas molecules and the solid surface. The adiabatic coefficient is the relation between heat capacity at constant pressure c_p and heat capacity at constant volume c_v.

$$\beta = \frac{5\pi}{32} * \frac{9\kappa - 5}{\kappa + 1} * \frac{2 - \alpha}{\alpha} \tag{8}$$

The value for β for the relationship between air and nanoporous silica is taken from the following references and is assumed to be 1.5 for this paper: $\beta = 1.5$ [17], $\beta = 1.6$ [18], $\beta = 1.5$ [19]

3.4. Coupling effect

Using Eq. (3) it is assumed, that all thermal resistances are arranged in a simple parallel configuration. Basically this assumption is correct, but as already mentioned for most materials a coupling of the different heat transfer mechanisms occurs; for example a coupling between solid thermal conductivity and radiation [20] or, and this is the focus of the present study, a coupling between solid and gaseous thermal conductivity. If, at the microscopic scale, the heat resistance between two solid phases is lower by passing a gas phase than the solid path, the resulting thermal conductivity exceeds the expected sum of gaseous and solid thermal conductivity. The effect is mainly caused by intervening gas molecules in the contact area of two particles. Some models to describe the coupling between these two mechanisms have been proposed, in most of the cases for silica aerogels [21–23]. In the simplest case, the phenomenon can be described as a series connection of

thermal resistances. Swimm [24] describes, that for common insulation materials, where λ_s is significantly higher than λ_g the simple linear relation shown in Eq. (9) is valid.

$$\lambda_c = \lambda_g * f \tag{9}$$

In this model, all influencing parameters like the particle surface geometry near the area of particle to particle contact or the thermal conductivity of the solid are combined in one factor f. Heinemann [17] mentioned, that in a bed of glass spheres, comparing the total thermal conductivity of the evacuated and the non-evacuated specimen, the contribution from the gas is seven times as large as expected just from the thermal conductivity of still air. This would mean for a bed of glass spheres f would be 7.

3.5. Calculation of thermal conductivity of various silica samples via pore size distribution

To predict the thermal conductivity of the investigated precipitated silica samples, pore size distribution measured with MIP of the compacted powder have been used.

Calculation starts with the mean free path of the air molecules L as a function of gas pressure p [25].

$$L(p) = \frac{k_B * T}{\sqrt{2} * \pi * d_{AM}^2 * p} \tag{10}$$

With $k_B = 1.38 * 10^{-23}\frac{J}{K}$ as the Boltzmann constant, T for the absolute Temperature and $d_{AM} = 3.65 * 10^{-10}$ m as the mean diameter of air molecules.

Following, for every pore size x and gas pressure p the Knudsen number Kn can be calculated [4].

$$Kn(p, x) = \frac{L}{x} \tag{11}$$

This results in a matrix of Knudsen numbers, which can be used to determine the gaseous thermal conductivity for every pressure and pore size

$$\lambda'_g(p, x) = \frac{\lambda_0}{1 + 2 * \beta * Kn} \tag{12}$$

with λ_0 as the thermal conductivity of air at atmospheric pressure and β as a factor depending on interaction between the gas and the surface of the solid described in the section "gaseous thermal conductivity".

The overall gaseous thermal conductivity can now be calculated

$$\lambda_g(p) = \phi \int \lambda'_g \frac{dV}{V_{max}} dx \tag{13}$$

with V as the intrusion volume and V_{max} as the total intrusion volume measured with MIP.

As previously mentioned, the solid thermal conductivity λ_s and the radiative thermal conductivity λ_r can be assumed to be constant. Thus $\lambda_{sr} = \lambda_s + \lambda_r$ is an offset value, which can be determined by measuring thermal conductivity at a very low pressure level, where λ_g and λ_c are negligible.

4. Results and discussion

4.1. Results of thermal conductivity measurements

Each silica sample was measured twice with applied pressure loads of 5 bar and twice with 30 bar, over a range of 14 pressure levels between 0.05 mbar and atmospheric pressure. The results for all the samples are shown in Fig. 4 (dash and dash-dot lines). As expected, thermal conductivity approaches a constant value at very low internal pressures and increases between 1 mbar and 10 mbar. A characteristic behavior for nanoporous silica samples is a slope $\frac{d\lambda}{dp} > 0$ for $p_{atm} = 10^3$ mbar, which is evidence for the presence of pores smaller
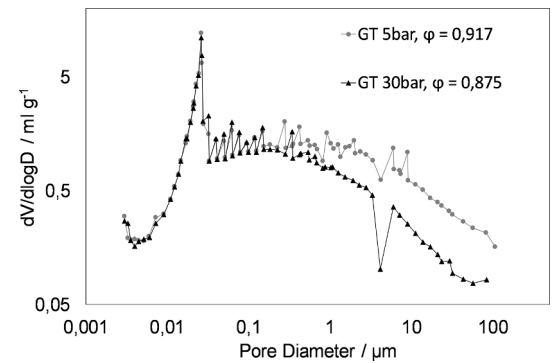

Fig. 3. Pore size distribution of "GT" prepared with two different pressure loads (5 bar and 30 bar), measured with mercury intrusion porosimetry, ϕ is the porosity of the sample.

than the mean free path of air molecules at atmospheric pressure (68 nm), following the Knudsen-theory.

4.2. Mercury intrusion porosimetry

To measure the pore size distribution of the investigated silica samples, each sample was prepared with different pressure loads (5 bar and 30 bar), heated at 350 °C and 50 mbar for 16 h and subsequently analyzed with mercury intrusion porosimetry. Fig. 3 shows the pore size distribution of the sample "GT" pressed with 5 bar and 30 bar respectively. It could be shown for all samples, that mechanical treating of the powder had negligible influence on pores smaller than about 200 nm. The measured pore size distribution can be used to calculate gaseous thermal conductivity, as it is necessary to know the volumetric percentage of every pore size.

4.3. Calculation of thermal conductivity without coupling effect

Thermal conductivity curve progressions calculated with $\lambda(p) = \lambda_{sr} + \lambda_g(p)$ and Eq. (10) are shown in Fig. 4 (solid and dotted lines), purposely leaving out the coupling effect. Therefore, λ_{sr} was taken from the measured value at the lowest gas pressure where no gaseous thermal conductivity is present. As expected, measured thermal conductivity rises faster than the calculated thermal conductivity due to the missing coupling effect. In all cases, the strongly compressed samples (30 bar) have a higher solid thermal conductivity than the less strongly compressed ones (5 bar) which leads to a higher offset in thermal conductivity. It can also be seen that the thermal conductivity of the 30 bar samples increases less strongly with an increase of the internal pressure than that of the 5 bar samples. This can be explained by the fact that the average pore size has decreased due to pressing. The average pore sizes of all samples (5 bar and 30 bar), related to the volumetric frequency are listed in Table 2.

The smaller pores lead to lower overall gaseous thermal conductivities at high gas pressure levels. In some cases (GT, KS and CP), this effect even causes an intersection of the 30 bar and 5 bar curves, although the solid conductivity and thus the starting point of the 30 bar curves are much higher.

On the other hand, taking a closer view at low pressure levels it is noticeable that the calculated curves rise faster than the experimental ones, although no coupling effect is considered, which leads to an intersection of both curves. In Fig. 4, this effect is only visible for GT - 5 bar (where the solid and the dashed lines intersect) but present for all samples. This may indicate that the measured pore sizes are too large. Most common uncertainties in terms of the mercury intrusion measurement, such as the bottle neck effect and compression of the sample, lead to an underestimation of the pore size [9,26,27]. Therefore, erroneous data of pore size distribution can be precluded as a reason for
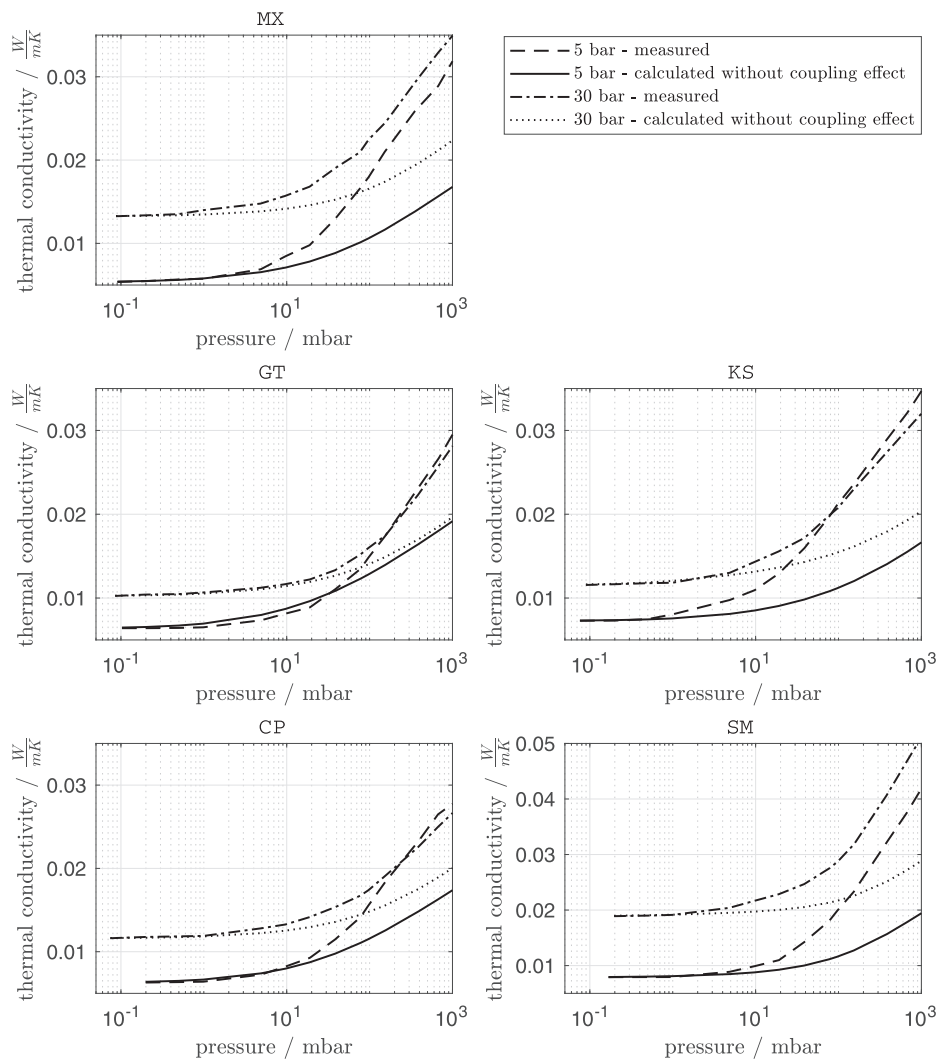
Fig. 4. Results of the thermal conductivity measurements of five samples of precipitated silica, pre-pressed with 5 and 30 bar compared to the corresponding calculated curves without consideration of the coupling effect.

Table 2
Average pore sizes of silica samples in μm.

Sample	MX	GT	KS	CP	SM
5 bar	6,0	6,7	3,7	4,4	2,8
30 bar	2,8	4,0	2,4	3,0	4,4

the present phenomenon. Just like most pore measuring methods, MIP in combination with the Washburn equation classifies pores by their internal pore width defined as the diameter of a cylindrical pore [28]. By using this pore size value for calculating the Knudsen number with Eq. (11) it is assumed, that the gas molecules inside the pores always "see" the largest possible distance between the pore walls. This assumption however is incorrect since gas molecules are evenly distributed throughout the whole system.

This means, the probability for a gas molecule to "see" in the direction of heat flow $\dot{Q}$, a smaller distance than the measured pore size is very high. The behavior is illustrated in Fig. 5. The average distance for a circular, two-dimensional pore can be calculated with the integral of the circular function of the unit circle.
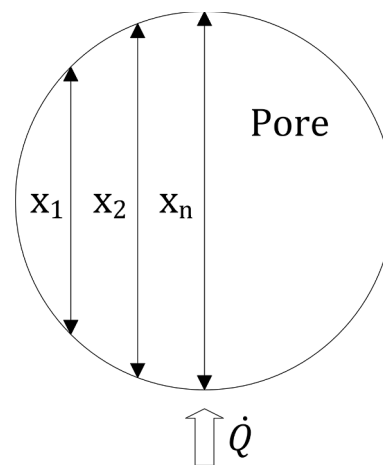
Fig. 5. Illustration of the available distances for a gas molecule inside a spherical pore.

$$\bar{x}_{2d} = \frac{1}{1-0} \int_0^1 \sqrt{1-x^2}\, dx = \frac{\arcsin(1)}{2} = \frac{\pi}{4} \tag{14}$$

Geometrically speaking, the result $\bar{x} = \frac{\pi}{4}$ is a quarter of the area of the unit circle. Extending this method to 3 dimensions, for a spherical pore, the mean distance equals one eighth of the unit sphere volume, which is $\frac{\pi}{6}$. Therefore, the following correction of the pore size distribution for spherical pores is assumed.

$$\bar{x} = \frac{\pi}{6} x \tag{15}$$

The correction leads to a curve with a smaller intersection-tendency and a better agreement with the measured values, especially in the low pressure range. Also for the following procedure of fitting the coupling effect factor, the correction of the pore size distribution data is helpful to obtain small deviations between the measured and calculated curves.

4.4. Determination of the coupling effect

The previous results visualize the important role of the coupling effect. For the present investigation the linear model from Swimm et al. [24] is used. It is determined that for most of the tested samples the model fits very well. Thus, the coupling effect factor f is determined by fitting the calculated curves to the experimental data using the method

Table 3
Coupling effect factor f, porosity ϕ measured with MIP and fractal dimension D for the five samples prepared with 5 bar and 30 bar external pressure load.

Sample		MX	GT	KS	CP	SM
5 bar pressure load	f	1.90	0.96	2.96	1.36	3.04
	ϕ	0.859	0.917	0.866	0.876	0.816
	D	3.15	3.04	3.18	3.11	3.12
30 bar pressure load	f	2.29	1.29	1.96	1.38	3.65
	ϕ	0.854	0.875	0.852	0.883	0.756
	D	3.19	3.17	3.04	3.25	2.89

of least squares. Therefore, in Eq. (9) only the parameter f is variable. The resulting curves, compared to the experimental results are shown in Fig. 6.

The obtained coupling effect factors f are listed in Table 3. Values from 0.96 for GT – 5 bar to 3.65 for SM – 30 bar are included. Also listed in Table 3 are the porosity ϕ and the surface fractal dimension D of the pore-surface, both determined by MIP.

The coupling effect basically depends on the relationship between gaseous and solid thermal conductivity, which is influenced by the geometry of the solid material. The basic structure of the five silica materials should be rather similar because they are all precipitated
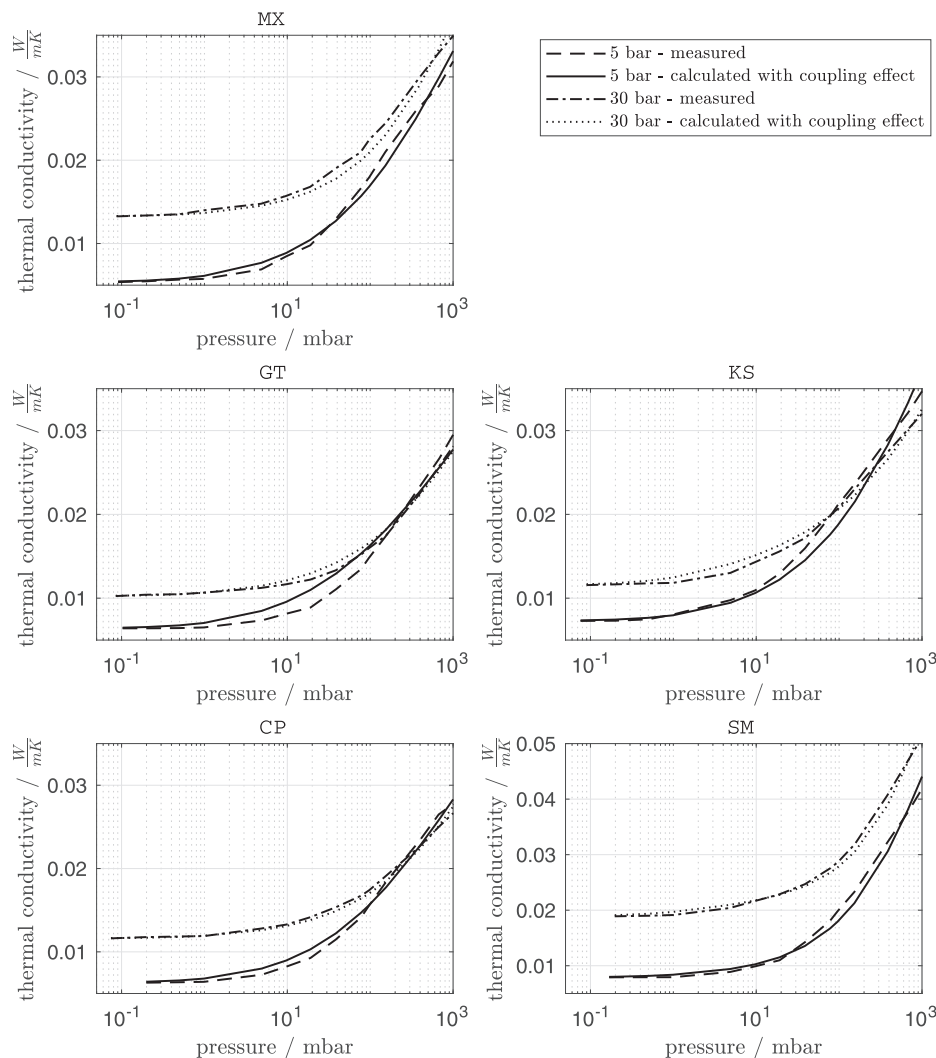

Fig. 6. Results of the thermal conductivity measurements of five samples of precipitated silica, pre-pressed with 5 and 30 bar compared to the corresponding calculated curves with adapted linear fitting parameter f.

silica, which means they consist of the same base material and are produced in similar processes. The similarity of the pore structure can be seen very clearly at the low fluctuations of the fractal dimension D in Table 3. According to the theory of fractal geometry, the fractal dimension of a surface must be in the range $2 < D < 3$. Nevertheless, it is not uncommon that fractal dimensions determined with MIP larger than 3 are obtained [29]. Therefore, the results can be used to compare the surface structures of the materials. In this regard, the values in Table 3 can all be classified as "very rough surfaces".

Moreover, with an increase in the bulk density of the pressed powder not only does the solid thermal conductivity increase, but also the number of spots where coupling between solid and gaseous conductivity can occur. Therefore, a linear relationship between the porosity ϕ and the coupling effect factor f was determined. For the investigated range of porosities $\phi = 0.76$ to $\phi = 0.92$ the corresponding linear function

$$f(\phi) = -18.68\phi + 17.94 \tag{16}$$

is found. The coefficient of determination R^2 is 0.94, if one outlier (KS – 5 bar) is excluded, which is marked gray in Fig. 7. The function allows a good estimation of the coupling effect factor f, using data generated by mercury intrusion porosimetry only. Furthermore, gaseous thermal conductivity can be calculated using a measured pore size distribution in Eq. (13) and the coupling effect factor can be used to complete an adequate estimation of thermal conductivity as a function of gas pressure for any precipitated silica material.

5. Conclusion

The developed guarded hot plate apparatus delivers reliable results. The measured thermal conductivities of precipitated silica were as expected, but it also became clear that the simplified representations of precipitated silica as a core material for VIPs often presented in the literature were not applicable. In some cases, large differences between the products and the sample preparation had a considerable influence on the thermal properties. In the end, it was possible to develop a model to predict thermal conductivity as a function of gas pressure from available mercury intrusion porosimetry data. In particular, for the five investigated samples of precipitated silica, it is now possible to accurately predict the thermal conductivity as a function of gas pressure. Furthermore, extrapolations to predict the effect of alternative pore gases or the further thermal conductivity in higher pressure ranges are conceivable. Moreover, estimations for any unknown silica products or similar structures can be made with the new model. The estimation of the coupling effect as a function of porosity (Fig. 7) can help to make a preselection of new materials with regard to their suitability as thermal insulation, as manufacturers of precipitated silica often have the opportunity to measure pore size distributions by MIP. However, since precipitated silica is not very common for the application of thermal insulation yet, there is no information on thermal properties from the
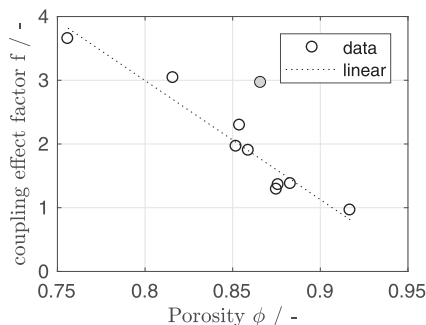
manufacturers. This gap can now be closed with the newly gained knowledge.

The comparison of the tested materials shows that the pore size distribution is a decisive influencing factor on the thermal properties of a silica product, nevertheless the coupling effect must not be neglected. Within the tested samples, the coupling effect is responsible for at least a doubling of the gaseous thermal conductivity for the material GT (5 bar) with f = 0.96 and can even cause a tremendous increase of λ_g with f = 3.65 (30 bar) for the material SM. The determined dependence of the coupling effect on the porosity ϕ leads to the realization that the optimization with regard to a low density of the silica based core material has a double relevance. A low density and thus high porosity leads, on the one hand, to a low solid thermal conductivity (Eq. (4)) and on the other hand to the mentioned low coupling effect. Thus, obviously pre-pressing the powders with high pressures does not lead to a decrease in the overall thermal conductivity of precipitated silica based core materials for vacuum insulation panels. In future work, attempts could be made to reduce the overall thermal conductivity by reducing the solid thermal conductivity. This should be possible by reducing the basic particle size and therefore increase the number of particle-particle resistances. Furthermore, investigating the effect of alternative pore gases could be helpful in order to validate the presented model and also as another strategy to decrease the overall thermal conductivity.

Acknowledgments

References

[1] A.M. Papadopoulos, State of the art in thermal insulation materials and aims for future developments, Energy Build. 37 (1) (2005) 77–86.
[2] V. e V, Ed., D2 Stoffwerte von bedeutenden reinen Fluiden, in: VDI-Wärmeatlas, Springer Berlin Heidelberg, 2013, pp. 175–356.
[3] S.G. Jennings, The mean free path in air, J. Aerosol Sci. 19 (2) (Apr. 1988) 159–166.
[4] M.G. Kaganer, Thermal insulation in cryogenic engineering, CERN Document Server, 1969. [Online]. Available: < http://cds.cern.ch/record/103864 > . (accessed: 08-Feb-2018).
[5] S. Sonnick, et al., Temperature stabilization using salt hydrate storage system to achieve thermal comfort in prefabricated wooden houses, Energy Build. 164 (2018) 48–60.
[6] M. Bouquerel, T. Duforestel, D. Baillis, G. Rusaouen, Heat transfer modeling in vacuum insulation panels containing nanoporous silicas—a review, Energy Build. 54 (2012) 320–336.
[7] J. Ross-Jones, M. Gaedtke, S. Sonnick, M. Rädle, H. Nirschl, M.J. Krause, Conjugate heat transfer through nano scale porous media to optimize vacuum insulation panels with lattice Boltzmann methods, Comput. Math. Appl., (2018).
[8] S. Lowell, J.E. Shields, M.A. Thomas, M. Thommes, Characterization of Porous Solids and Powders: Surface Area, Pore Size and Density, Springer, Netherlands, 2004.
[9] J. Rouquerol, et al., Liquid intrusion and alternative methods for the characterization of macroporous materials (IUPAC Technical Report), Pure Appl. Chem. 84 (1) (2011) 107–136.
[10] C16 Committee, Test Method for Steady-State Heat Flux Measurements and Thermal Transmission Properties by Means of the Guarded-Hot-Plate Apparatus, ASTM International.
[11] R.R. Zarr, A.L. Pintar, Standard reference materials: SRM 1453, Expanded Polystyrene Board, for Thermal Conductivity from 281 K to 313 K, Spec. Publ. NIST SP – 260-175, Dec. 2012.
[12] X. Lu, R. Caps, J. Fricke, C.T. Alviso, R.W. Pekala, Correlation between structure and thermal conductivity of organic aerogels, J. Non-Cryst. Solids 188 (3) (1995) 226–234.
[13] G. Reichenauer, U. Heinemann, H.-P. Ebert, Relationship between pore size and the gas pressure dependence of the gaseous thermal conductivity, Colloids Surf. Physicochem. Eng. Asp. 300 (1) (2007) 204–210.
[14] J. Fricke, U. Heinemann, H.P. Ebert, Vacuum insulation panels—From research to market, Vacuum 82 (7) (2008) 680–690.
[15] H. Reiss, K6 Superisolierungen, in: VDI-Wärmeatlas, V. e V, (Ed). Springer Berlin Heidelberg, 2013, pp. 1153–1220.
[16] R. Caps, J. Fricke, Thermal conductivity of opacified powder filler materials for vacuum insulations, Int. J. Thermophys. 21 (2) (2000) 445–452.
[17] U. Heinemann, Influence of water on the total heat transfer in 'evacuated' insulations, Int. J. Thermophys. 29 (2) (2008) 735–749.
[18] J. Fricke, H. Schwab, U. Heinemann, Vacuum insulation panels – exciting thermal properties and most challenging applications, Int. J. Thermophys. 27 (4) (2006) 1123–1139.
[19] R. Coquard, D. Quenard, Modeling of Heat Transfer in Nanoporous Silica - Influence of Moisture (2007), 13.
[20] R. Viskanta, R.J. Grosh, Heat transfer by simultaneous conduction and radiation in an

Fig. 7. Linear relationship of the porosity measured with MIP and the coupling effect factor f.

absorbing medium, J. Heat Transf. 84 (1) (1962) 63–72.

[21] C. Bi, G.H. Tang, Z.J. Hu, H.L. Yang, J.N. Li, Coupling model for heat transfer between solid and gas phases in aerogel and experimental investigation, Int. J. Heat Mass Transf. 79 (2014) 126–136.

[22] Z.-Y. Li, C.-Y. Zhu, X.-P. Zhao, A theoretical and numerical study on the gas-contributed thermal conductivity in aerogel, Int. J. Heat Mass Transf. 108 (2017) 1982–1990.

[23] J.-J. Zhao, Y.-Y. Duan, X.-D. Wang, B.-X. Wang, Effects of solid–gas coupling and pore and particle microstructures on the effective gaseous thermal conductivity in aerogels, J. Nanoparticle Res. 14 (8) (2012) 1024.

[24] K. Swimm, S. Vidi, G. Reichenauer, H.-P. Ebert, Coupling of gaseous and solid thermal conduction in porous solids, J. Non-Cryst. Solids 456 (2017) 114–124.

[25] S.Q. Zeng, A. Hunt, R. Greif, Mean free path and apparent thermal conductivity of a gas in a porous medium, J. Heat Transf. 117 (3) (1995) 758–761.

[26] J. Zhou, G. Ye, K. van Breugel, Characterization of pore structure in cement-based materials using pressurization–depressurization cycling mercury intrusion porosimetry (PDC-MIP), Cem. Concr. Res. 40 (7) (2010) 1120–1128.

[27] S. Diamond, Mercury porosimetry: an inappropriate method for the measurement of pore size distributions in cement-based materials, Cem. Concr. Res. 30 (10) (2000) 1517–1525.

[28] R.L. Carr, Evaluating flow properties of solids, 1965.

[29] B. Zhang, S. Li, Determination of the surface fractal dimension for porous media by mercury porosimetry, Ind. Eng. Chem. Res. 34 (4) (1995) 1383–1386.

Chapter 5

Paper 2: *Thermal accommodation in nanoporous silica for vacuum insulation panels*

The thermal accommodation coefficient (TAC) α is a measure of the imperfection of the energy exchange of a gas molecule at wall impact. Loosely speaking, the TAC is for heat transport via molecular collisions what the emission coefficient is for radiative transport. In macroscopic systems, its influence is negligible and is therefore usually not considered. In micro- or nanoporous materials, however, the gas–wall collisions account for a significant fraction of the total collision number and must therefore be considered. In the gas thermal conductivity equation (Equation 2.37)), the TAC is part of the dimensionless parameter β. In Paper 1 (Chapter 4), the TAC was, like in many other publications [70, 74, 12], assumed to be the unity for the collisions of the air molecules at the silica surfaces. That is, complete energy exchange between gas and wall molecules is assumed. This assumption is examined in detail in this chapter (Paper 2) by evaluating the pressure-dependent thermal conductivity measurement data of fumed and precipitated silica in combination with different pore gases. Essentially, the TAC depends on the following influencing variables: molar mass of the gas molecules M_g, degrees of freedom of the gas molecules, molar mass of the molecules of the solid surface M_s, surface condition (roughness, adsorbed molecules, impurities), and temperature T. However, the temperature influence can be neglected in a temperature range of approximately $200\,\mathrm{K}$ to $400\,\mathrm{K}$ [75]. Moreover, the accommodation coefficient can be assumed to be independent of the Knudsen number [76]. Comparatively few data can be found in the literature for α, some with significant deviations. However, there is general agreement on the accommodation coefficient's tendency to decrease with increasing temperature and decreasing molar mass of the gas, as long as the molar mass of the gas is smaller than

that of the solid surface. Direct measuring techniques are only available to determine the TAC of exterior surfaces [77].

A simple calculation method to determine the TAC as a function of the molar masses of the gas and wall molecules can be derived from the kinetic theory of gases or the elastic impact theory. If one assumes that the energy of the wall molecule involved in the collision is $E_s = 0$ before the collision, then from Equation 2.30, the following Equation 5.1 can be derived:

$$\alpha = \frac{E'_s}{E_g} = \frac{\frac{1}{2} M_s v'^2_s}{\frac{1}{2} M_g v^2_g},\tag{5.1}$$

where E'_s is the energy of the wall molecule after the collision, and E_g is the energy of the gas particle before the collision, which is equal to the total energy of the system at this state. From elastic collision theory, it is also known that

$$v'_s = \frac{2(M_g v_g + \cancel{M_s v_s})}{M_s + M_g} - \cancel{v_s}.\tag{5.2}$$

The function can be shortened as shown, since $E_s = 0$ is assumed. After substituting Equation 5.2 into Equation 5.1, the calculation formula for the TAC α proposed, for example, by Kaganer [32] results in

$$\alpha = \frac{4 M_s M_g}{(M_s + M_g)^2} = 1 - \left(\frac{M_s - M_g}{M_s + M_g}\right)^2.\tag{5.3}$$

The literature contains further attempts to find analytical approximations for the TAC, mostly also depending on the molar mass of the gas and that of the interacting molecules of the solid surface. Some of them are discussed in Chapter 7. Furthermore, some numerical solutions which are largely based on molecular dynamics simulations exist [78, 79]. For both approaches, it is difficult to consider all influencing parameters. Especially in the pores of a porous solid, sometimes at the nanometer level, it is impossible to measure all the necessary influencing parameters or even to measure the thermal accommodation coefficient directly. The literature consequently contains no data for the TAC for such problems, and many application-oriented authors hence use $\alpha = 1$ for "heavy" gases such as air and $\alpha = 0.2$ for "light" gases such as helium.

In this chapter (Paper 2), a reverse approach is presented. The previous assumption, which is supported by Swimm's investigations, that the coupling effect factor f can be assumed to be constant over wide ranges of $\frac{\lambda_p}{\lambda_g}$ leads to the conclusion that it is only dependent on the geometry of the solid and its porosity. It therefore does not depend on the type of residual gas in the pores if the solid system remains constant. Thus, on the one hand, if the coupling effect factor can be determined, the only unknown in the system of equations is the accommodation coefficient. However, on the other hand, to determine f according to the previously presented method, knowledge of the accommodation coefficient is required. Thus, the TAC for one gas–solid pairing would

have to be known to calculate those of the other pairings. According to Equation 5.3, $\alpha = 1$ for $M_s = M_g$. Since the molar masses of SO_2 and SiO_2 are almost identical, $\alpha_{SO_2} = 1$ is assumed for the TAC of sulfur dioxide in silica pores in this chapter (Paper 2). Based on this assumption, the coupling effect factor and, from this, the TACs for the other gases can be determined. Therefore, it should be mentioned that the values for α determined in Paper 2 do not correspond to the true physical TAC. Instead, a relative value to SO_2 or an apparent accommodation coefficient to be used only for the calculation of thermal conductivities is presented.

Thermal accommodation in nanoporous silica for vacuum insulation panels

S. Sonnick[a,b,*], M. Meier[b], G. Ünsal-Peter[a], L. Erlbeck[a], H. Nirschl[b], M. Rädle[a]

[a] CeMOS − Center for Mass Spectrometry and Optical Spectroscopy, Mannheim University of Applied Sciences, Paul-Wittsack-Straße 10, 68163 Mannheim, Germany
[b] Institute for Mechanical Process Engineering and Mechanics, Karlsruhe Institute of Technology, Straße am Forum 8, 76131 Karlsruhe, Germany

ABSTRACT

The thermal accommodation coefficient is a measure for the quality of thermal energy exchange between gas molecules and a solid surface. It is an important parameter to describe heat flow in rarefied gases, for example, in aerospace or vacuum technology. As special application, it plays a decisive role for the thermal transport theory in silica filled vacuum insulation panels. So far, no values have been available for the material pairings of silica and various gases. For that reason, this paper presents thermal conductivity measurements under different gas-pressure conditions for precipitated and fumed silica in combination with the following gases: helium, air, argon, carbon dioxide (CO_2), sulfur dioxide (SO_2), krypton, and sulfur hexafluoride (SF_6). Additionally, a calculation method for determining thermal accommodation coefficients from the thermal conductivity curves in combination with the pore size distribution of silica determined by mercury intrusion porosimetry is introduced. The results are compared with existing models.

© 2020 The Author(s). Published by Elsevier Ltd. This is an open access article under the CC BY-NC-ND license. (http://creativecommons.org/licenses/by-nc-nd/4.0/)

1. Introduction

Vacuum insulation panels are high-performance thermal insulations, which offer an extremely high thermal resistance with a very small space requirement. Their function is based on the so-called Knudsen effect, which presupposes that the mean free path length of the gas molecules is in the same order of magnitude as the pore size of the solid structure. By using nanoporous materials such as silica and/or applying a vacuum this can be achieved. In this way it is possible to reduce the amount of heat transferred through the gas phase to a negligible amount. It is well known that the Knudsen model [1] can be used when the gas thermal conductivity in evacuated porous materials is considered [2−4]. This is important when the gas flow is in the transition region, where the pore size x is in the same order of magnitude as the mean free path of the molecules L. There are, however, two difficulties with the calculation of gas thermal conductivity in vacuum insulation panels. The first one is that especially for silica-based materials with spherical particles a strong coupling between the solid and the gaseous thermal conductivity needs to be taken into account. This coupling differs significantly for different silica

materials but can be estimated as a function of the porosity, at least for precipitated silica. That was shown in the previously published paper [5]. The second problem, which is examined in more detail in the present publication is, that the Knudsen model requires the thermal accommodation coefficient (TAC) α. The TAC is a measure for the quality of energy exchange between the gas molecules and the solid surface. In a manner of speaking, it describes the boundary condition for the flow of gas molecules in the slip and transition flow regimes [6]. It was Maxwell [7] who first introduced the idea that a fraction α of gas molecules is remaining in thermal equilibrium with the surface while the remaining part α -1 is scattered. Later, Smoluchowski [8] verified the suggestion experimentally when he found a temperature jump at the solid-gas interface. The term "thermal accommodation coefficient", however, was first used by Knudsen [1]. He defined it as the relationship between two temperature differences

$$\alpha = \frac{T_1 - T_2}{T_1 - T_2'} \tag{1}$$

where T_1 is the mean temperature of the molecules before colliding with the solid surface and T_2 and T_2' are the temperatures of the molecules scattered and fully accommodated to the surface respectively. Especially for rarefied gases where individual collisions of single gas molecules with the surface are more important than at continuum conditions, the AC is not negligible [9]. Due to the fact that α is a function of many parameters, like the kind of gas, the

* Corresponding author at: CeMOS − Center for Mass Spectrometry and Optical Spectroscopy, Mannheim University of Applied Sciences, Paul-Wittsack-Straße 10, 68163 Mannheim, Germany.
E-mail address: s.sonnick@hs-mannheim.de (S. Sonnick).

Nomenclature

Symbols

d_{kin}	kinetic diameter of molecules, m
f	coupling effect factor, -
k_B	Boltzmann constant, J/K
Kn	Dimensionless Knudsen number, -
L	mean free path of molecules, m
M	molar mass, g/mol
p	pressure, mbar
R	gas constant, J/Kmol
T	temperature, K
V	volume, m^3
x	pore size, m
α	accommodation coefficient, -
β	dimensionless coefficient for gaseous conductivity calculation, -
κ	adiabatic coefficient, -
λ	thermal conductivity, W/mK
λ'	thermal conductivity of a single pore, W/mK
λ_0	free gas thermal conductivity, W/mK
ϕ	porosity, -

Subscripts and abbreviations

c	coupling
g	gaseous
max	maximum / end of intrusion
r	radiative
s	solid
sr	solid and radiative

surface materials, temperature, adsorption effects and surface roughness, it is nearly impossible to find data for every occurring problem. It is well known that thermal accommodation increases with increasing surface roughness, because gas molecules do more than one collision, on the average, before leaving the surface [10]. In addition, an increasing molar mass of the gas molecules leads to an increasing α, because of the lower velocity and therefore longer residence time of the molecules at the surface [11], but the accommodation coefficient is generally independent of the gas pressure [12]. Thus, TACs are reasonably constant for a given gas and surface combination [13]. Some models exist to describe the TAC based on classical mechanics [14−16] or quantum mechanics [17−19], but they either require very detailed information about the solid surface condition [20], which is difficult to access in nanoporous materials, or are only valid for extreme clean surfaces which do not occur in practice. For that reason many authors assume α = 1 when calculating gas thermal conductivity in porous silica materials which are filled with air or rarefied air, for example in vacuum insulation panels [21−23]. The resulting error is not to be neglected. It was shown that in the transition region in particular the gas thermal conductivity increases by approximately 70% if a value of 0.8 instead of 0.1 is used for α [24]. Thus, the goal of this work is to analytically determine TACs especially for different silica materials in combination with different gases like helium, air, argon, carbon dioxide (CO_2), sulfur dioxide (SO_2), krypton, and sulfur hexafluoride (SF_6).

One can find values for individual material pairings in the literature. Some of them are listed in Table 1. Furthermore, Saxena and Joshi [25] collected an extensive compilation of measured TAC values for different material pairings by different authors. The fluctuation of the available values can be due to the different measuring methods but also to minimal differences in the surface quality of the materials or of contaminations on the surfaces. Unfortunately, it is almost impossible to obtain values for different silica materials and especially their inner pore surfaces as they can be found in vacuum insulation panels (VIPs).

2. Thermal transport theory in porous media

Thermal transport in porous media is composed of three main mechanisms: thermal conductivity over the solid backbone of the material λ_s, radiation λ_r and gaseous thermal conductivity λ_g. In a macroscopic surrounding λ_g is almost independent from the gas pressure p because of two mutually cancelling effects. As the pressure decreases, the number of gas molecules involved in heat transfer decreases as well, which would normally reduce thermal conductivity. The second effect is, that at the same time the mean free path increases, causing the individual distances at which the gas particles transport the energy to become larger, which in turn would lead to an improvement of the heat transfer [29]. Both effects happen at the same time when changing the gas pressure in a macroscopic surrounding. The situation changes if the mean free path gets in the same order of magnitude as the representative size scale, which bounds the surrounding room. In this case, the distance at which the energy can be transported in one step is not limited by the mean free path but by the size of the surrounding volume, which for porous materials is the pore size. Hence, the thermal conductivity becomes a function of the gas pressure.

A fourth mechanism which basically depends on the microscopic shape of the material and gas pressure is the coupling effect between solid and gaseous thermal conductivity λ_c [30]. This coupling is negligible for most foams [31] but plays a decisive role for silica based core materials.

This becomes clear when looking at Fig. 1 which shows the different heat transfer mechanisms using the example of two touching spherical particles. Consequently, the thermal conductivity of a silica material can be described as a sum of these four mechanisms as

Table 1
Examples of thermal accommodation coefficients for different solid-gas pairings from the literature.

| Solid	Gas	Thermal accommodation coefficient	Measuring method	Temperature [K]	Source
Tungsten (extremely clean surface)	Argon	0.2357	thin filament thermal conductivity cell	308.15	[12]
Silica, fumed	CO_2	0.45	absorption of the radiation of a Q−switched laser	300	[26]
	NO	0.33			
Nickel	Helium	0.385	thin filament thermal conductivity cell	298.15	[10]
	Krypton	0.965			
Platinum	Helium	0.368			
	Krypton	0.959			
Platinum	Helium	0.28	concentric spherical shells heat flux measurement	314.5	[27]
	Argon	0.85			
304 stainless steel	Nitrogen	0.8	parallel plates temperature drop measurement	308.15	[28]
	Argon	0.87			
	Helium	0.36 (machine finish), 0.4 (polished finish)			
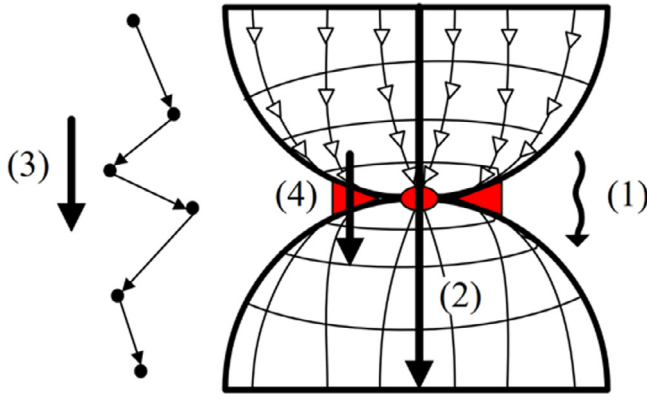
Fig. 1. Heat transfer mechanisms in porous media: radiation λ_r (1), solid thermal conductivity λ_s (2), gas thermal conductivity λ_g (3) and coupling effect λ_c (4), modified from [32].

shown in Eq. (2) [3,31]. All heat transfer mechanisms are temperature dependent, however, in this work constant and steady state temperature is assumed.

$$\lambda(p) = \lambda_s + \lambda_r + \lambda_g(p) + \lambda_c(\lambda_g) \tag{2}$$

In the present case, particular attention must be paid to the gas thermal conductivity, since it is decisive for the determination of the TACs. It can be described with Eq. (7).

$$\lambda_g{}' = \frac{\lambda_0(T)}{1 + 2 * \beta * Kn} \tag{3}$$

In Eq. (3) [33] λ_0 is the thermal conductivity of the gas at atmospheric pressure and β is a dimensionless coefficient depending on the thermal accommodation coefficient α and the adiabatic coefficient of the gas κ. It can be calculated via Eq. (4) [33]. The adiabatic coefficient is the relationship between specific heat capacity at constant pressure c_p and constant volume c_v.

$$\beta = \frac{5\pi}{32} * \frac{9\kappa - 5}{\kappa + 1} * \frac{2 - \alpha}{\alpha} \tag{4}$$

The dimensionless Knudsen number Kn is the decisive dimensionless parameter for the description of gas thermal conductivities in rarefied gases. It describes the ratio between the mean free path of the gas molecules L and a representative physical length scale. Because the Knudsen model was developed for the case of parallel plates, the physical length scale would be the distance between the plates. In a porous material with almost spherical pores, a correction factor needs to be considered as was mentioned in the previously published paper [5]. The modified equation for the dimensionless Knudsen number is shown in Eq. (5).

$$Kn(p, x) = \frac{6L}{\pi x} \tag{5}$$

Now it is obvious how sensitive the TAC is in terms of gas thermal conductivity. A dependency of gas thermal conductivity plotted over Kn-number on different TACs can be found in [24]. The mean free path L is a function of the gas pressure and the kinetic diameter of the gas molecule. It can be determined according to the kinetic gas theory using Eq. (6)

$$L(p) = \frac{k_B * T}{\sqrt{2} * \pi * d_{kin}{}^2 * p} \tag{6}$$

with $k_B = 1.38 * 10^{-23} \frac{J}{K}$ as the Boltzmann constant, T as the absolute temperature and d_{kin} as the kinetic diameter of the gas molecules. A molecule can have more than one size characterizing dimension if it is not spherical. The kinetic diameter d_{kin} is the size of the sphere of influence that can lead to a scattering event [34]. It can be calculated

with the kinetic gas theory out of the dynamic viscosity or the thermal conductivity of the gas.

Another model to predict the gas-thermal conductivity, which is considered very similar to the Knudsen model, was proposed by Bourret [35] and is shown in Eq. (7).

$$\lambda_g = \frac{\lambda_g^0}{1 + \frac{\lambda_g^0}{xp} \sqrt{\frac{\pi MT}{2R}}} \tag{7}$$

The decisive difference between this and Knudsen's model is that neither the thermal accommodation coefficient nor the isentropic exponent are taken into account. The type of gas is only considered by the molar mass. It is to be examined whether this is permissible.

Following, if taking into account the pore size distribution of the silica material, which can be measured with mercury intrusion porosimetry, for every pore size x and gas pressure p the dimensionless Knudsen number Kn can be calculated. This results in a matrix of dimensionless Knudsen numbers, which can then be used to determine the gaseous thermal conductivity for every pressure and pore size using Eq. (3).

The overall gaseous thermal conductivity can now be calculated via Eq. (8)

$$\lambda_g(p) = \phi \int \lambda_g' \frac{dV}{V_{max}} dx \tag{8}$$

with dV as the pore volume which refers to the pore size x, V_{max} as the total pore volume of the material and φ as the porosity of the silica material.

As previously mentioned, the solid thermal conductivity λ_s and the radiative thermal conductivity λ_r can be assumed to be constant. Thus $\lambda_{sr} = \lambda_s + \lambda_r$ is an offset value, which can be determined by measuring thermal conductivity at a very low pressure level, where λ_g and λ_c are negligible.

The coupling effect was found to be in a linear relationship to the gas thermal conductivity [30,36], so it is possible to introduce a coupling effect factor f, as it is shown in Eq. (9).

$$\lambda_c = \lambda_g * f \tag{9}$$

In order to fit the calculated gas thermal conductivity with the measured ones, e.g. using the least square method, like it was performed in [5], a thermal accommodation coefficient must be assumed. For that reason, the TAC was assumed to have the value "1" for the gas whose molar mass is closest to that of the solid material. Because according to the theory

$$\alpha = \frac{4M_s M_g}{(M_s + M_g)^2} = 1 - \left(\frac{M_s - M_g}{M_s + M_g}\right)^2 \tag{10}$$

the TAC is unity if the molar masses of the colliding gas and solid molecules are equal [33]. In Eq. (10) M_s and M_g are the molar masses of the solid and the gas respectively.

3. Materials and method

For the present investigation, one type of precipitated silica (PS, *co. Grace Germany GmbH*) and one type of fumed silica (FS, *co. Wacker Chemie AG*) are used. Prior to the measurements, the samples have been compressed with 5 bar and dried completely. The samples were heated for about 3 hours at 100°C and an absolute pressure of < 0.1 mbar. They were then stored for longer than 12 h at < 0.1 mbar

For determination of the pore size distribution of the silica materials an "AutoPore III (*co. micromeritics, USA*)" is used.

To measure the thermal conductivity over the gas pressure, a self-constructed guarded hot plate apparatus is used. The sample size is $160 \times 160 \times \approx 6$ mm. The measurement is conducted with a heating plate temperature of 45°C and a cooling plate temperature of 15°C.

Table 2
Important physical properties of all gases used in the experiments.

Gas name	λ_0 [W/mK] [37]	d_{kin} [nm]	K [-]	M [g/mol]
Helium (He)	0.1536	0.26 [38]	1.67	4.00
Air	0.02625	0.36	1.40	28.96
Argon (Ar)	0.0177	0.34 [39]	1.67	39.95
Carbon dioxide (CO_2)	0.01705	0.33 [40]	1.29	44.01
Sulfur dioxide (SO_2)	0.0095	0.36 [39]	1.35	64.06
Krypton (Kr)	0.00949	0.36 [39]	1.67	83.80
Sulfur hexafluoride (SF_6)	0.0135	0.55 [39]	1.10	146.05

The kinetic diameter of air molecules was calculated as average value from the corresponding individual gases.

Thus, the average temperature is 30°C. More detailed information about the measurement apparatus and the uncertainty analysis for the thermal conductivity measurement as well as a more detailed description of the pore size measurement can be found in [5].

For the measurements under a certain gas atmosphere, first the test bench has to be flooded with the corresponding gas to prevent any influences. Then the vacuum chamber is evacuated in order to record the measuring points from the lowest pressure upwards. The used gases and their physical properties are listed in Table 2.

To determine the coupling effect factor f and the accommodation coefficient α, calculated thermal conductivities need to be fitted to the measurement results with f and α as variables. Because the molar masses of the solid surface SiO_2 and the gas SO_2 are very close to each other, regarding to Eq. (10) it can be assumed that α is maximum for this material pairing. Based on this assumption, alpha was set to unity ($\alpha = 1$) for that special case, knowing that a complete energy transfer is unrealistic. Consequently, the coupling effect factor can be determined by fitting calculated to measured data of SiO_2. The coupling effect is a geometric phenomenon [30] and therefore independent from the kind of gas. Thus, the coupling effect factor determined with SO_2 remains constant for all gases and the TAC can be fitted accordingly. The whole procedure performed to determine the thermal accommodation coefficient of the listed gases and the inner pore walls of silica is presented schematically in Fig. 2.
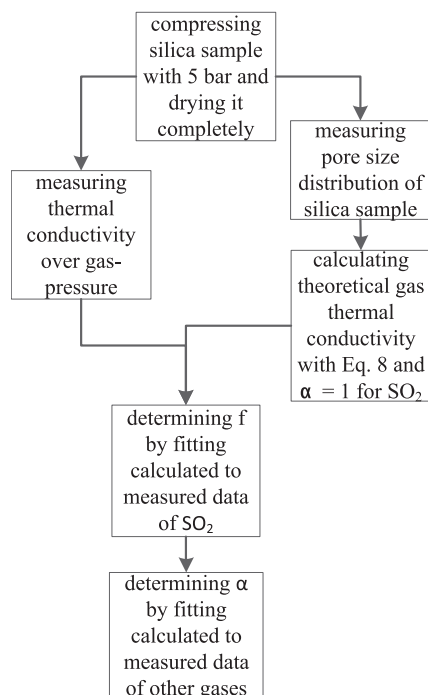

Fig. 2. Flow chart of the performed procedure to determine TACs for different gases.

4. Results and discussion

The porosities ϕ of the silica samples measured with mercury intrusion porosimetry are 0.876 and 0.967 for precipitated and fumed silica respectively. The pore size distributions of both samples are plotted in Fig. 3. As expected, fumed silica shows a higher porosity which is caused by its pearly, open and hierarchic structure compared to precipitated silica which tends to have a bulky and aggregated structure [41]. Their nanopores differ a little. PS and FS show peaks at around 9.4 nm and 12.5 nm respectively.

The sum of the solid thermal conductivity and the radiation λ_{sr} can be measured at very low pressure conditions and has been found to be 0.0051 W/mK for PS and 0.0062 W/mK for FS, both with a standard deviation of 0.0003 W/mK.

Gas thermal conductivity λ_g over gas pressure p curves for all gases are shown in Fig. 4, for PS in the upper graph and FS in the lower graph. In general, it can be stated that gases with a higher thermal conductivity λ_0 show a faster increase in the resulting gas thermal conductivity λ_g with increasing gas pressure and thus normally also higher values at atmospheric pressure. However, it also becomes clear that not only the thermal conductivity but also the molecule diameter and weight play a decisive role. If SF_6 is taken for example, which with 146.05 g/mol is by far the heaviest and with 5.5 Å the largest of all tested gas molecules, it can be seen that the increase is fast in low pressure regions due to the small resulting mean free path of gas molecules. This means that the dimensionless Knudsen number is already very small at relatively low pressures, which leads to the assumption that the gas thermal conductivity is fully developed at lower pressures. Thus, at higher pressure conditions the curve flattens which results in a comparatively low thermal conductivity at atmospheric pressure.

The coupling effect factor f for the tested precipitated and fumed silica material is equal to 3.91 and 0.53 respectively. The resulting thermal accommodation coefficients are listed in Table 3 as well as in Figs. 5 and 1. The factors f and α were determined using the method already described and shown schematically in Fig. 2.

TACs increase with increasing molar mass as long as the gas molecules are of smaller mass than the solid ones and start to decrease again if this point has been exceeded. This totally fits to Kaganer's theory, which is shown in Eq. (10). Because the molar masses of silica (60.08 g/mol) and SO_2 (64.07 g/mol) are very close to each other, this is where the maximum position of the function is located. However, the theory shows higher values than the measurements for all gases. This can have many reasons, but most likely it is because Kaganer's simple formula is more of an estimate since neither a temperature influence nor the surface conditions like roughness or adsorption effects are included. As mentioned, the results are not close to Kagener's model, but compared to the measurement results listed in Table 1 they seem explainable. If, for example, the result of CO_2 is compared with [26] where the TAC of CO_2 in combination with FS was also measured, the present result (0.48) is fairly close to the literature value (0.45) considering that these are different silica products and measuring methods. It should be noted in the margin that the adsorption of sulfur dioxide on the silica surfaces might cause modifications in the surface behavior. It is well known that surfaces coated with adsorbed gases tend to have higher thermal accommodation coefficients [20,42,43]. Thus, this effect would underline the assumption of a maximum value for the thermal accommodation coefficient of SiO_2 - SO_2. In addition, the measurements for all gases show slightly higher values for precipitated than for fumed silica. This behavior may be related to the hydroxyl groups on the surface of silica particles. Due to their production process in general precipitated silicas have more hydroxyl groups than pyrolytically produced silicas [44]. Surface groups that are not integrated into the amorphous solid structure and are thus more weakly bound tend to increase the accommodation coefficient [45]. This could be the explanation for the
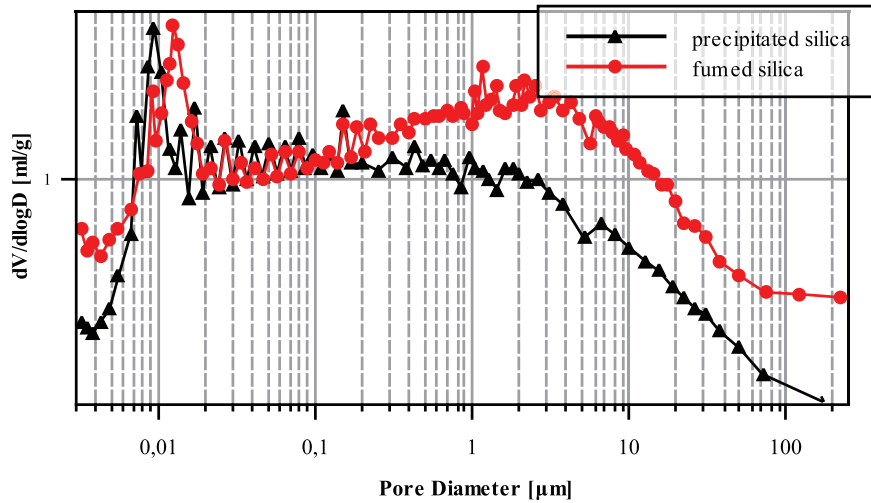
Fig. 3. Pore size distribution of precipitated and fumed silica samples measured with mercury intrusion porosimetry.

higher TACs of precipitated silica. I addition, pyrogenic silica has a higher purity than precipitated silica [46]. Impurities consist mainly of various salts from the wet-chemical precipitation process. If the impurities are regarded as surface contamination, which tends to lead to an increase in the accommodation coefficient [47], this could also be a reason for the higher values.

Another interesting finding from the measurements is the clearly different coupling effect factor *f* of precipitated and fumed silica. FS has a coupling effect factor of only 0.53 while the PS investigated has a
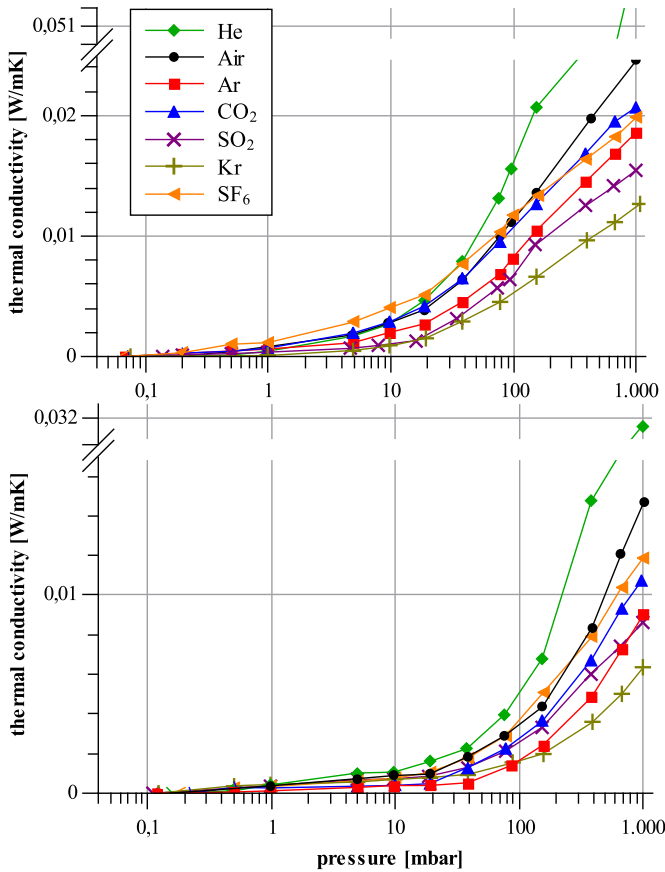
coupling effect factor of 3.91. That is a result of their different structure in the two to three-digit nanometer range and thus an indication that the coupling effect mainly takes place in this order of magnitude. Both silica types have primary particles around 10 nm. Despite this, as mentioned, their aggregate structure is very different. The two touching spheres pictured in Fig. 1 could be understood to mean that the coupling effect takes place between the primary particles, but this is not correct. The gussets between the primary particles are so small that even at atmospheric pressure there is no gas thermal conductivity and thus no coupling effect between solid and gas thermal conductivity. If one imagines the spherical structure depicted as a spherical aggregate of precipitated silica, however, one understands why the coupling effect factor is greater here than in the case of fumed silica.

Fig. 6 shows a comparison of the present results including thermal accommodation coefficient and coupling effect to the measured data of PS and krypton as an example. Additionally, thermal conductivity calculated with the measured pore size distribution of PS and the model of Bourret [35] are plotted in the graph. One can see that it is not possible to represent the heat transfer in silica samples with this model. It is not expedient to neglect the thermal accommodation coefficient as it depends very much on the substance pairing and does not only correlate with the molar mass of the gas. Supplementing the coupling effect in Bourret's model does not lead to consistent values, although the coupling effect only depends on the geometry of the solid structure. Thus, it should be independent of the type of gas.

Note: Raw data of thermal conductivity measurement as well as pore size distributions are available via "Mendeley Data".

5. Conclusion

In the presented work thermal conductivity of two silica samples one precipitated and one fumed has been measured under rarefied gas conditions in combination with the gases helium, air, argon, carbon

Fig. 4. Gas thermal conductivity of different gases in precipitated silica (upper graph) and fumed silica (lower graph) as a function of the residual gas pressure, y-axis is split between 0.025 and 0.05 W/mK at the upper and between 0.017 and 0.03 W/mk at the lower plot for better legibility.

Table 3

Thermal accommodation coefficients for different silica materials in combination with different gases.

	Precipitated silica	Fumed silica
He	0.12	0.09
Air	0.41	0.33
Ar	0.58	0.32
CO_2	0.72	0.48
Kr	0.75	0.52
SF_6	0.43	0.43
SO_2	1.00	1.00
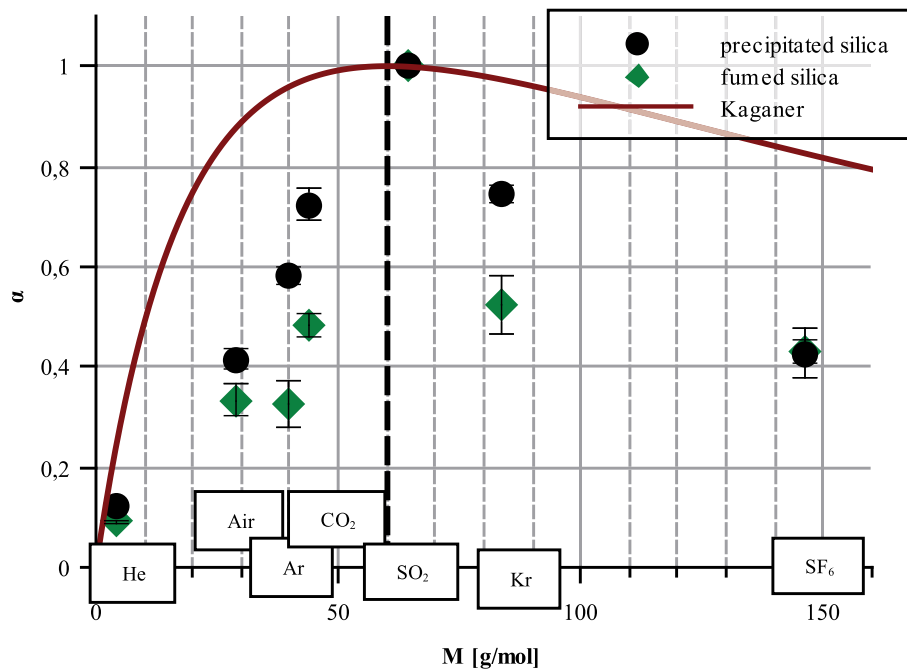
**Fig. 5.** Thermal accommodation coefficients of different gases with different molar masses compared with the results based on the theory of Kaganer; the dotted vertical line shows the molar mass of the solid material SiO$_2$.
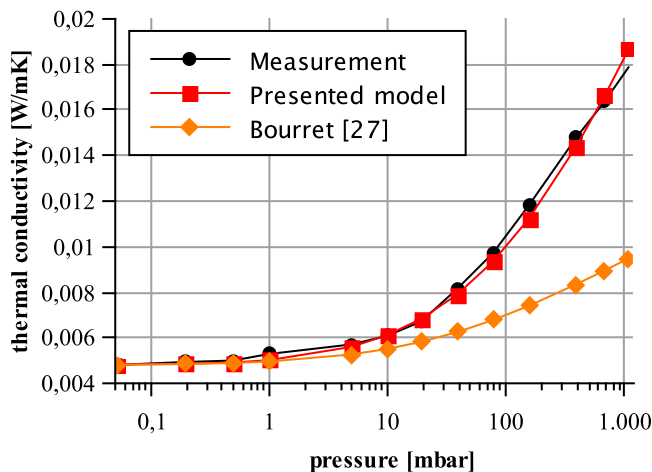

Fig. 6. Comparison of Bourret's [26] model with the presented method of calculation and measured data for precipitated silica and krypton as an example.

dioxide (CO$_2$), sulfur dioxide (SO$_2$), krypton, and sulfur hexafluoride (SF$_6$). The pore size distribution of both samples has been measured with mercury intrusion porosimetry. A calculation procedure is presented to predict gas thermal conductivity as a function of the pore size and gas pressure. In this regard, the coupling between solid and gas thermal conductivity is also taken into account. Furthermore, thermal accommodation coefficients for the inner pore wall-gas boundary layer of silica could be determined experimentally for the first time. The TACs are very important for the complete understanding of the thermal processes in silica materials used for vacuum insulation panels. Until now it was common practice to assume a value of $\alpha = 1$ for air. If one considers the determined result of $\alpha = 0.42$ and $\alpha = 0.32$ for air and precipitated and fumed silica, respectively, it becomes clear that this assumption should be reconsidered. The authors make no claim of total accuracy for the values determined because the values are not measured directly but calculated through measurements of the overall heat flux of the samples. In addition, $\alpha = 1$ was assumed for SO$_2$ which is certainly not correct in a mathematical sense. On the one hand, the molecular masses of

SO$_2$ and SiO$_2$ are not exactly identical and on the other hand, a loss-free energy transfer is rather unlikely even with the same molecular masses of gas and solid surface. Nevertheless, the results have a considerable benefit compared to previous practices in the application of the Knudsen model especially in the field of vacuum insulations. The measurement results for the TACs show an almost linear curve when plotted above the molar mass. They rise with increasing molar mass of the gas up to $M_g = M_s$ and then decrease again linearly with a smaller slope. The basic course is therefore identical to that proposed by Kaganer. In addition, the method presented is compared with a model in which the thermal accommodation coefficient does not occur. It could be shown that the thermal accommodation coefficient cannot be neglected in any case. Furthermore, it was established that the assumption of too high thermal accommodation coefficients leads to an underestimation of the coupling effect. That newly generated findings should be taken into account in future investigations in this field.

Declaration of competing interest

The authors declare that they have no known competing financial interests or personal relationships that could have appeared to influence the work reported in this paper.

Acknowledgments

References

[1] M. Knudsen, Die molekulare Wärmeleitung der Gase und der Akkommodationskoeffizient, Ann. Phys. 339 (1911) 593–656, doi: 10.1002/andp.19113390402.

[2] M. Bouquerel, T. Duforestel, D. Baillis, G. Rusaouen, Heat transfer modeling in vacuum insulation panels containing nanoporous silicas—a review, Energy Build. 54 (2012) 320–336, doi: 10.1016/j.enbuild.2012.07.034.

[3] J. Fricke, U. Heinemann, H.P. Ebert, Vacuum insulation panels—from research to market, Vacuum 82 (2008) 680–690, doi: 10.1016/j.vacuum.2007.10.014.

[4] J. Ross-Jones, M. Gaedtke, S. Sonnick, M. Rädle, H. Nirschl, M.J. Krause, Conjugate heat transfer through nano scale porous media to optimize vacuum insulation panels with lattice Boltzmann methods, Comput. Math. Appl (2018), doi: 10.1016/j.camwa.2018.09.023.

[5] S. Sonnick, M. Meier, J. Ross-Jones, L. Erlbeck, I. Medina, H. Nirschl, et al., Correlation of pore size distribution with thermal conductivity of precipitated silica and experimental determination of the coupling effect, Appl. Therm. Eng (2019), doi: 10.1016/j.applthermaleng.2019.01.074.

[6] A. Agrawal, S.V. Prabhu, Survey on measurement of tangential momentum accommodation coefficient, J. Vac. Sci. Technol. A. 26 (2008) 634–645, doi: 10.1116/1.2943641.

[7] J.C. Maxwell, The Scientific Papers of James Clerk Maxwell, Dover Publications Inc N. Y., 1890, p. 829.

[8] M.S. von Smolan, Ueber Wärmeleitung in verdünnten Gasen, Ann. Phys. 300 (1898) 101–130, doi: 10.1002/andp.18983000110.

[9] F.O. Goodman, Thermal accommodation, Prog. Surf. Sci. 5 (1974) 261–375, doi: 10.1016/0079-6816(74)90005-7.

[10] I. Amdur, L.A. Guildner, Thermal Accommodation Coefficients on Gas-covered Tungsten, Nickel and Platinum[1], J. Am. Chem. Soc. 79 (1957) 311–315, doi: 10.1021/ja01559a018.

[11] K.J. Daun, G.J. Smallwood, F. Liu, Investigation of thermal accommodation coefficients in time-resolved laser-induced incandescence, J. Heat Transf. (2008) 130, doi: 10.1115/1.2977549.

[12] L.B. Thomas, C.L. Krueger, S.K. Loyalka, Heat transfer in rarefied gases: critical assessments of thermal conductance and accommodation of argon in the transition regime, Phys. Fluids. 31 (1988) 2854, doi: 10.1063/1.866994.

[13] S.A. Schaaf, Mechanics of rarefied gases, Handb. Phys. 3 (1963) 591–624, doi: 10.1007/978-3-662-10109-4_5.

[14] F.O. Goodman, H.Y. Wachman, Formula for thermal accommodation coefficients, J. Chem. Phys. 46 (1967) 12.

[15] R.M. Logan, Calculation of the energy accommodation coefficient using the soft-cube model, Surf. Sci. 15 (1969) 387–402, doi: 10.1016/0039-6028(69)90131-9.

[16] B. Baule, Theoretische Behandlung der Erscheinungen in verdünnten Gasen, Ann. Phys. 349 (1914) 145–176, doi: 10.1002/andp.19143490908.

[17] J.M. Jackson, N.F. Mott, R.H. Fowler, Energy exchange between inert gas atoms and a solid surface, Proc. R. Soc. Lond. Ser. Contain. Pap. Math. Phys. Character 137 (1932) 703–717, doi: 10.1098/rspa.1932.0166.

[18] J.R. Manson, Simple model for the energy accommodation coefficient, J. Chem. Phys. 56 (1972) 3451–3455, doi: 10.1063/1.1677719.

[19] F.O. Goodman, J.D. Gillerlain, Rejection of the devonshire theory of accommodation coefficients in gas−surface interactions (Including a correction for bound state transitions), J. Chem. Phys. 57 (1972) 3645–3648, doi: 10.1063/1.1678821.

[20] S. Song, M.M. Yovanovich, Correlation of thermal accommodation coefficient for "engineering" surfaces, ASME HTD 69 (1987) 107–116.

[21] J. Fricke, H. Schwab, U. Heinemann, Vacuum insulation panels − exciting thermal properties and most challenging applications, Int. J. Thermophys. 27 (2006) 1123–1139, doi: 10.1007/s10765-006-0106-6.

[22] U. Heinemann, Influence of water on the total heat transfer in 'evacuated' insulations, Int. J. Thermophys. 29 (2008) 735–749, doi: 10.1007/s10765-007-0361-1.

[23] R. Coquard, D. Quenard, Modeling of heat transfer in nanoporous silica - influence of moisture, in: 8th Int. Vac. Insul. Symp., Würzburg, Germany, 2007, p. 13.

[24] D. Bayer, A new facility for the experimental investigation on nano heat transfer between gas molecules and ceramic surfaces, in: 32nd Int. Therm. Conduct. Conf., Indiana USA, 2014, p. 8.

[25] S.C. Saxena, R.K. Joshi, Thermal Accommodation and Adsorption Coefficients of Gases, Hemisphere Pub. Corp., New York, 1989.

[26] L. Doyennette, M. Margottin−Maclou, H. Gueguen, A. Carion, L. Henry, Temperature dependence of the diffusion and accommodation coefficients in nitrous oxide and carbon dioxide excited into the (00°1) vibrational level, J. Chem. Phys. 60 (1974) 697–702, doi: 10.1063/1.1681095.

[27] H. Yamaguchi, M.T. Ho, Y. Matsuda, T. Niimi, I. Graur, Conductive heat transfer in a gas confined between two concentric spheres: From free-molecular to continuum flow regime, Int. J. Heat Mass Transf. 108 (2017) 1527–1534, doi: 10.1016/j.ijheatmasstransfer.2016.12.100.

[28] D.J. Rader, J.N. Castaneda, J.R. Torczynski, T.W. Grasser, W.M. Trott, Measurements of Thermal Accommodation Coefficients, Sandia National Laboratories, 2005, doi: 10.2172/876357.

[29] P.W. Atkins, J. de Paula, Wärmeleitung, Phys. Chem., John Wiley & Sons, 2006, pp. 672–673.

[30] K. Swimm, S. Vidi, G. Reichenauer, H.-P. Ebert, Coupling of gaseous and solid thermal conduction in porous solids, J. Non-Cryst. Solids. 456 (2017) 114–124, doi: 10.1016/j.jnoncrysol.2016.11.012.

[31] G. Reichenauer, U. Heinemann, H.-P. Ebert, Relationship between pore size and the gas pressure dependence of the gaseous thermal conductivity, Colloids Surf. Physicochem. Eng. Asp 300 (2007) 204–210, doi: 10.1016/j.colsurfa.2007.01.020.

[32] S. Parzinger, Analytische Modellierung der temperatur- und gasdruckabhängigen effektiven Wärmeleitfähigkeit von Pulvern, Technische Universität München, 2014.

[33] M.G. Kaganer, Thermal insulation in cryogenic engineering, Israel Program for Scientific Translations (1969).

[34] G. Joos, I.M. Freeman, Theoretical Physics, Courier Corporation, 1986.

[35] F. Bourret, Mesure de la diffusivité thermique de mousses de carbone par la méthode flash et modélisation de la conductivité thermique radiative, Université de Dijon (1995).

[36] K. Swimm, G. Reichenauer, S. Vidi, H.-P. Ebert, Impact of thermal coupling effects on the effective thermal conductivity of aerogels, J. Sol Gel Sci. Technol. 84 (2017) 466–474, doi: 10.1007/s10971-017-4437-5.

[37] D2 Stoffwerte von bedeutenden reinen Fluiden, in: V. e V (Ed.), VDI-Wärmeatlas, Springer, Berlin Heidelberg, 2013, pp. 175–356. http://link.springer.com/referenceworkentry/10.1007/978-3-642-19981-3_12. (accessed March 20, 2017).

[38] S. Matteucci, Y. Yampolskii, B.D. Freeman, I. Pinnau, Transport of gases and vapors in glassy and rubbery polymers, Mater. Sci. Membr. Gas Vap. Sep., John Wiley & Sons, Ltd, 2006, pp. 1–47, doi: 10.1002/047002903X.ch1.

[39] D.W. Breck, Zeolite Molecular Sieves: Structure, Chemistry and Use, John Wiley & Sons Inc, 1974 https://www.abebooks.de/9780471099857/Zeolite-Molecular-Sieves-Structure-Chemistry-0471099856/plp. (accessed September 10, 2019).

[40] A.F. Ismail, K. Khulbe, T. Matsuura, Gas Separation Membranes: Polymeric and Inorganic, Springer International Publishing, 2015, https://www.springer.com/de/book/9783319010946. (accessed September 10, 2019).

[41] M. Meier, S. Sonnick, E. Asylbekov, M. Rädle, H. Nirschl, Multi-scale characterization of precipitated silica, Powder Technol. 354 (2019) 45–51, doi: 10.1016/j.powtec.2019.05.072.

[42] J.K. Roberts, The adsorption of hydrogen on tungsten, Math. Proc. Camb. Philos. Soc. 30 (1934) 74–79, doi: 10.1017/S030500410001241X.

[43] Isao Yasumoto, Accommodation coefficients of helium, neon, argon, hydrogen, and deuterium on graphitized carbon, J. Phys. Chem. 91 (1987) 4298–4301, doi: 10.1021/j100300a019.

[44] E. Guesnet, B. Bénane, D. Jauffrès, C.L. Martin, G.P. Baeza, G. Foray, et al., Why fumed and precipitated silica have different mechanical behavior: contribution of discrete element simulations, J. Non-Cryst. Solids. 524 (2019) 119646, doi: 10.1016/j.jnoncrysol.2019.119646.

[45] J.W. Lu, W.A. Alexander, J.R. Morris, Gas−surface energy exchange and thermal accommodation of CO_2 and Ar in collisions with methyl, hydroxyl, and perfluorinated self-assembled monolayers, Phys. Chem. Chem. Phys. 12 (2010) 12533–12543, doi: 10.1039/B921893A.

[46] Fumed silica and Precipitated silica-Anten Chemical Co., Ltd., (n.d.). http://www.antenchem.com/en/News/Silicas-Technology/FumedsilicaandPrecipitatedsilica.html. (accessed December 10, 2019).

[47] W.M. Trott, D.J. Rader, J.N. Castañeda, J.R. Torczynski, M.A. Gallis, L.A. Gochberg, Experimental determination of thermal accommodation coefficients for microscale gas-phase heat transfer, in: Am. Vac. Soc. 54th Int. Symp., Seattle, WA, 2007.

Chapter 6

Paper 3: *Methodical selection of thermal conductivity models for porous silica-based media with variation of gas type and pressure*

In Chapter 5 (Paper 2), the thermal accommodation coefficient was identified as an important parameter in describing the thermal conductivity of porous silica, and an apparent TAC was determined for different gas–solid pairings. For this purpose, a reverse approach was employed by using common calculation models for thermal conductivity in which the TAC is required as an input parameter. The TAC was then used as the only unknown fit variable to align the calculations with measurement results. The work demonstrates that the influence of this parameter on the calculation of effective thermal conductivities is significant. However, the presented results are only valid for the investigated materials and have no general validity. The variation in the determined apparent accommodation coefficients of fumed and precipitated silica (see Chapter 5, Figure 5) not only show an actual difference in the surface properties of the particles but also are the result of other factors not considered in the calculation, such as particle or pore geometry on various size scales. Such structural differences can be seen in Figure 6.1, which presents transmission electron microscope images of the agglomerates of precipitated and fumed silica.
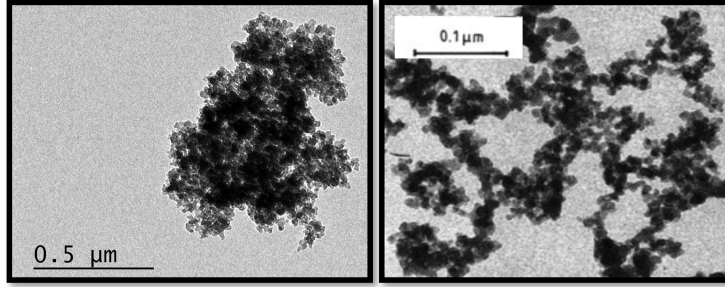
Figure 6.1: Transmission electron microscope images of a precipitated silica agglomerate (left) and a fumed silica agglomerate (right, [50])

These shape-related material properties can hardly be quantified, and almost no analytical calculation models in the literature include such factors. One possible approach to find a quantitative measure of the particle shape is to determine the fractal dimension of the particles. This concept was investigated in the framework of this thesis, but no correlations between the fractal dimension and thermal conductivity could be established. Nevertheless, countless calculation models in the literature utilize different approaches that promise to determine the thermal conductivity of porous media. However, not all of these models fit all porous materials equally well. Reasons for this are, for example, the already mentioned differences in the microstructures of the materials. Some models have been specifically designed with certain materials in mind, while others randomly fit with one material or another. These relationships are investigated in a large-scale study in the following paper, with the goal to find the best-suited calculation methods for the material classes of fumed and precipitated silica, silica gel, and glass sphere fillings. To focus on user-friendly solutions, only models that can be used with generally accessible input parameters are compared. The required material values, as shown in Equation 6.1, are limited to the pore size (distribution) d, the particle size D, and the porosity ϕ:

$$\lambda_{eff} = f(d, D, \phi). \tag{6.1}$$

Different calculation models for the effective thermal conductivity as well as for the individual parameters of the gas thermal conductivity are combined, and the results are compared with measurements of different materials and material–gas pairings. Furthermore, the models are supplied with different measured values of the materials' particle and pore sizes, and the models are also compared and evaluated. This results in 2,800 different calculation methods from which favorable model combinations for the different porous solids could be extracted.

Methodical selection of thermal conductivity models for porous silica-based media with variation of gas type and pressure

Sebastian Sonnick [a,b,*], Lars Erlbeck [a], Manuel Meier [b], Hermann Nirschl [b], Matthias Rädle [a]

[a] *Mannheim University of Applied Sciences, Paul-Wittsack-Straße 10, Mannheim, 68163, Germany*
[b] *Karlsruhe Institute of Technology, Straße am Forum 8, Karlsruhe, 76131, Germany*

ABSTRACT

If the effective thermal conductivity of a silica powder in any gas atmosphere is to be calculated analytically, one is faced with a whole series of decisions. There are a lot of different models for the gas thermal conductivity in the pores, the thermal accommodation coefficient or the effective thermal conductivity itself in the literature. Furthermore, it has to be decided which input parameters should be used. This paper gives an overview and recommendations as to which calculation methods are best suited for the material classes of precipitated silica, fumed silica, silica gel and glass spheres. All combinations of the described methods result in a total of 2800 calculation models which are compared with pressure-dependent thermal conductivity measurements of 15 powdery materials with 7 different gases using Matlab computations. The results show that with a model based on a spherical unit cell, which considers local Knudsen numbers, the measuring points of all powder-gas combinations can be determined best with an average variance of about 18.5%. If the material class is known beforehand, the result can be predicted with an average accuracy of about 10% with the correspondingly determined methods.

1. Introduction

The calculation of the effective thermal conductivity of porous media has concerned scientists for more than a century. Understanding the influence of the different heat transfer mechanisms is fundamental in many fields like super insulation materials [1,2], astronomy [3,4], reactor technology, fluidized beds and many more. There is an almost infinite number of numerical [5–7] and analytical [8–10] prediction models. Despite this, or perhaps because of it, the user is often faced with the question of which calculation method is the right one for the own specific case. Tsotsas et al. [11] show an illustrative review of early models of different complexity. Parzinger [12] also provides a very comprehensive listing of 59 different models for the prediction of the effective thermal conductivity of porous media in his thesis. Aichelmayer [13] gives a broad review of different models which he classifies according to their suitability for different solid-fluid conductivity ratios. Bjurström et al. [14] compare several models to calculate the thermal conductivity of silica gel. They obtain the best results with Luikov's model [15] which is also investigated in the present

work. Jayachandran [16] compared measurements of glass-air and ceramic-air packed beds with different models and found good agreement of their 2-D square cylinder unit cell model with measured data. Bouquerel et al. [17] list and compare different models for all heat transfer mechanisms in vacuum insulation panels filled with different silica based core materials. They also show measured values from the literature and make general statements concluding that accurate modeling of gas thermal conductivity is a major challenge.

In the literature empirical fitting parameters are often used to adapt the model results to available measurement results of certain materials [18]. In some cases this approach can make sense, since the investigated porous media can be of very different nature and therefore deviate strongly from the model conceptions. However, in the present work adjustable parameters to give good fits to experimental data will be deliberately avoided in order to demonstrate and compare the raw, unaltered form of the models as they are presented to the end user. Models are often validated with measured values from different authors due to a lack of measurement data. The measurements are often carried out in different laboratories by different people using different methods. In this work, however, all thermal conductivity values originate from the same apparatus and were recorded at the same temperature. Like-

---

* Corresponding author.
 E-mail address: s.sonnick@hs-mannheim.de (S. Sonnick).

Nomenclature

ETC	Effective thermal conductivity
GTC	Gas thermal conductivity
λ	Thermal conductivity
FS	Fumed silica
PS	Precipitated silica
SG	Silicagel
GS	Glass spheres
d_{peak}	Peak value of pore size measurements
d_{dist}	Pore size distribution
CO_2	Carbon dioxide
SF_6	Sulfur hexafluoride
SO_2	Sulfur dioxide
β	Dimensionless coefficient
Kn	Knudsen number
α	Thermal accommodation coefficient
M_G	Molar mass of gas molecules
M_S	Molar mass of solid surface molecules
T	Temperature
L	Mean free path of gas molecules
k	Boltzmann constant
d_{kin}	Kinetic molecular diameter
p	Pressure
x	Pore size
V	Volume
D_{gr}	Particle size, grain size
d_{pore}	Measured pore size
KC	Kozeny's Correction
ϕ	Porosity
Λ	$1 - \phi$
ϕ_{uc}	Porosity of a unit cell
ϕ_{corr}	Corrected porosity which accounts for λ_g
Nu_r	Empirical parameter for radiation in ZBS model
S	Mean-variance between progressions of measured and calculatet thermal conductivity over pressure curve
N	Number of materials investigated
J	Number of gases investigated
D_{aggl}	Agglomerate size
D_{aggr}	Aggregate size
D_{prim}	Primary particle size
Indices	
base	Related to $\lambda_s + \lambda_r$ (measured at very low pressures)
c	Related to the coupling between λ_s and λ_g
eff,SV	Effective, calculated with Schumann and Voss model
g	Gas inside pores
g'	Gas in specific pore size
m	Measured
0	At ambient conditions
p	Particle
r	Radiation
s	Solid backbone of a porous media

wise, the secondary parameters such as pore or particle size distribution were determined using the same and thus comparable methods and were performed with the exact same samples like the thermal conductivity measurements.

In this paper, an overview of a variety of analytical calculation models for the determination of the effective thermal conductivity of porous media is provided. They are classified in terms of their complexity and input parameters. The results of the calculations are compared with thermal conductivity measurements of silica-

based porous materials at different residual gas pressures, using different types of gases (air, helium, argon, CO_2, SO_2, SF_6, and krypton). Six precipitated silicas, three fumed silicas, three silica gels and three glass packed beads were analyzed. Thus, from a chemical point of view, the solid material is the same for all samples studied, although the surface properties may differ. The focus of the investigation is on the heat conduction through the disperse gas phase at varying gas pressures below atmospheric conditions and its coupling with the solid phase. In Chapter 4.1 and 4.2 effective thermal conductivity models which only use the so-called primary parameters are presented. These are the thermal conductivities of the fluid and solid phase as well as the porosity of the materials. The so-called secondary parameters needed for the models in Chapter 4.3 are limited to the particle or pore size or their distributions respectively. Evaluating other models often requires knowledge of additional input parameters like packing arrangement or number of contact points which in general, are not available. Consequently, required data in this work do not go beyond pore- and particle sizes. The mentioned primary and secondary parameters can either be measured directly or taken from the literature. An exception is the gas thermal conductivity inside the pores, since it is a function of the gas pressure and the pore size. In the literature, one can find many options for calculating gaseous thermal conductivity in the pores of porous media with consideration of the Smoluchowski effect. An overview of the most common ones is presented in Chapter 3. The presented effective thermal conductivity (ETC) models are combined with the different gas thermal conductivity (GTC) models and then compared with the measured values. Due to the enormous amount of models and calculation methods in this field, it was impossible to examine all those found in the literature. The aim was to provide an overview of the best-known and most diverse models.

GTC models and ETC models with secondary parameters require pore and/or particle size information. The selection and post-processing of such measurement data represents a decision as difficult and much debated as that of the correct computational model. Therefore, this paper also discusses several options on this issue. Thus, the user ultimately has to reach three basic decisions: which ETC model, which GTC model and which geometric size input parameter should be taken for the particular case. This work will help the user in decision-making, as all the options presented for the three questions are combined and compared with the underlying measurement data using a numerical computing platform. The impacts of the different options are examined and recommendations are made for the four material groups investigated.

2. Materials and methods

2.1. Porous media

In this paper, a total of 15 powdery substances were investigated, all of which consist of amorphous silicone-dioxide (SiO_2). These are six precipitated silicas (PS), three fumed silicas (FS), three silica gels (SG) and three types of glass beads (GS). Five PS samples are from *"W. R. Grace and Company"* (Gr), one is from *"Evonik Industries"* (Ev). The fumed silica samples are from *"Wacker"* (Wa) and *"Evonik Industries"* (Ev). Silica gel samples are all from *"W. R. Grace and Company"* (Gr). Two types of glass spheres are from *"Bassermann Minerals"* (Ba) and the other one is a no-name blasting agent (Bl). Table 1 lists all the solid materials investigated and the specifications available for each. X and ✓ stand for "data unavailable" and "data available", respectively. For materials with a multiscale structure, two or three values are listed for primary particle size D_{prim}, aggregate size D_{aggr} and agglomerate size D_{aggl} in case of fumed or precipitated silica, or D_{prim} and D_{aggl} in case of silica gel. PS and FS have a three-scale struc-

Table 1

List of all investigated porous materials with according available properties. The material names are composed of material type_company_number.

Material	Porosity ϕ [-]	Mean particle size D_{prim} / D_{aggr} / D_{aggl} [μm]	Peak pore size d_{peak} [μm]	Pore size distribution d_{dist}
PS_Gr_01	0.88	0.0208 / 0.1174 / 12.5	0.023	✓
PS_Gr_02	0.91	0.0058 / 0.1738 / 8.9	0.382	✓
PS_Gr_03	0.89	0.0119 / 0.1176 / 8.8	0.008	✓
PS_Gr_04	0.87	0.0198 / 0.1041 / 12.5	0.023	✓
PS_Gr_05	0.81	X / 0.2211 / 7	0.269	✓
PS_Ev[a]	0.88	0.0272 / 0.2119 / 6.5	0.020	✓
FS_Wa	0.94	0.0223 / 0.0944 / 43.1	0.012	✓
FS_Ev	0.93	0.0267 / 0.0564 / 38.9	0.014	✓
FS_VIP[b]	0.90	0.0244 / 0.1390 / 66.9	0.023	✓
SG_Gr_01	0.90	0.0134 / 3.2 / -	0.008	✓
SG_Gr_02	0.90	0.0125 / 11.2 / -	0.008	✓
SG_Gr_03	0.67	0.0038 / 8 / -	1.548	✓
GS_Bl	0.35	56.9 / - / -	17.913	✓
GS_Ba_01	0.56	3.5 / - / -	1.091	✓
GS_Ba_02	0.31	22.2 / - / -	6.273	✓

[a] Hydrophobic PS

[b] Ready mixed core material for vacuum insulation panels, which consists of fumed silica, cellulose fibers and silicon carbide as an opacifier.

Table 2

Material values of the powdery materials used for the calculations.

Thermal conductivity of silica (samples 1 - 12)	1 W/mK	[21]
Density of silica (samples 1 - 12)	2200 kg/m^3	[21]
Thermal conductivity of glass spheres (samples 13 -15)	1.38 W/mK	[22]
Density of glass spheres (samples 13 -15)	2560 kg/m^3	[23]

ture. The primary particles sinter together during the production to form aggregates with sizes in the three-digit nanometer range. These aggregates tend to connect to form the so-called agglomerates due to Van der Waals forces. In the case of silica gels, a large network of primary particles was crushed to form the particles. Here, no further agglomeration is assumed. Therefore, only two size scales are given in the table, the primary particles and the aggregates. Primary particle sizes were measured with a Xenocs Xeuss 2.0 SAXS (small-angle x-ray scattering) camera for all multiscale samples. Agglomerate sizes have been measured by laser diffraction (*Co. Malvern and Co. Sympatec*) using a wet dispersion process. Aggregate sizes have been measured by dynamic light scattering in deionized water using a Zetasizer (*Co. Malvern Panalytical Ltd, UK*) with a 10-minute upstream dispersion step with an ultrasonic tip. The glass sphere sizes were determined by a digital light microscope (*Co. Keyence*). For the pore size distributions mercury intrusion porosimetry measurements using an AutoPore III (*Co. micromeritics, USA*) and a Pascal Series Mercury Intrusion Porosimeter (*Co. Thermo Fisher*) have been carried out. Pore size distributions of all materials are shown in the appendix in Fig. A.1. Some of the presented data have already been published in Meier et al. [19,20]. All solid material values for the different samples are shown in Table 2.

2.2. Gases

The gas pressure-dependent thermal conductivity has been measured for all materials listed in Table 1. For this purpose, all of the gases listed in Table 3 have been used for an individual measurement (except for krypton which was only used for some of the materials due to supply difficulties).

2.3. Thermal conductivity measurements

The gas pressure-dependent thermal conductivity was measured with a self-constructed guarded hot plate apparatus. It is located in a vacuum chamber so that the residual gas atmosphere can be adjusted between approximately 0.05 *mbar* and atmospheric pressure. The special feature of the apparatus is that the entire measuring chamber as well as the hot plate can be removed from the apparatus in order to carry out sample preparation, i.e. compaction of the powdery materials with a hydraulic press directly on site. This avoids cracks and gaps between the plates and the samples as far as possible. A more precise description of the setup and an error consideration can be taken from our earlier work [24]. For sample preparation, the powdered materials are baked and dried directly in the apparatus for at least 3 hours at 95 °C and < 1 *mbar*. The vacuum chamber is purged twice with the regarding gas. Finally, $N = 13$ thermal conductivity values are recorded at gas pressures between 0.05 *mbar* and atmospheric pressure starting at atmospheric pressure.

3. Calculation of the gas thermal conductivity

When calculating the gas thermal conductivity, the dilution of the gas or the type of gas flow is decisive. A measure for this is the Knudsen number (Kn). It is explained in more detail in Chapter 3.2. Kn is often used to categorize into different flow regions. A common classification into molecular flow ($Kn > 10$), transition region ($10 > Kn > 0.1$), slip flow ($0.1 > Kn > 0.01$) and continuum flow ($0.01 > Kn$) was proposed by Chambre [25]. In the continuum region and free molecular flow, the thermal conductivity can easily be derived using the kinetic theory of gases [26]. In the continuum region, the thermal conductivity is almost independent of the pressure because of two mutual canceling effects. For one thing, the more particles are available to transport energy, the higher the thermal conductivity is. Secondly, if there are many particles, the mean free path becomes smaller, thus the energy is not transported as far between the individual collisions, which leads to a reduction of the thermal conductivity. Both effects almost cancel each other out [27]. With increasing Knudsen number, however, the mean free path is increasingly influenced by the particle-wall collisions, and thus by the pore size, rather than by the particle-particle collisions. This behavior results in a pressure dependence and is called Soluchowski or Knudsen effect. An exact derivation of the thermal conductivity of gases in the transition region would be very difficult due to the complexity of the Boltzmann equation. Therefore, it is common to interpolate between the continuum solution and the free molecular flow solution. This results in an equation developed by Prasolov [28] (Eq. 1).

$$\lambda_{gas} = \frac{\lambda_0}{1 + \beta Kn} \tag{1}$$

Table 3

List of gases used for the thermal conductivity measurements and their properties of interest.

|	Thermal conductivity $\lambda_0 [\frac{W}{mK}]$	Molar mass $M[\frac{g}{mol}]$	Kinetic molecular diameter $d_{kin}[10^{-10}m]$	Isentropic Exponent ($\kappa(\frac{c_p}{c_v})[-]$)
Air	0.0262	28.96	3.69	1.4
Helium	0.1536	4.00	2.19	1.68
Argon	0.0177	39.95	3.64	1.68
CO_2	0.0171	44.01	4.55	1.29
Krypton	0.0095	83.8	4.13	1.68
SF_6	0.0135	146.05	6.17	1.29
SO_2	0.0095	64.07	5.42	1.29
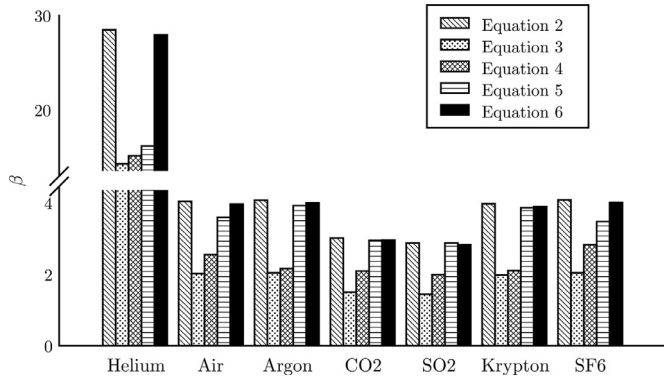
Fig. 1. Dimensionless parameter β for all gas types investigated in this paper calculated with equations from Table 4.

Table 4

Different equations from the literature to calculate the dimensionless parameter β.

Equation	References
$\beta = 2 * \frac{2-\alpha}{\alpha} \frac{2\kappa}{\kappa+1} \frac{1}{Pr}$ (2)	[15,29,30]
$\beta = \frac{2-\alpha}{\alpha} \frac{2\kappa}{\kappa+1} \frac{1}{Pr}$ (3)	[31]
$\beta = 2\frac{2-\alpha}{\alpha}$ (4)	[32–34]
$\beta = \frac{1}{\alpha} \frac{9\kappa-5}{\kappa+1}$ (5)	[35]
$\beta = \frac{5\pi}{16} \frac{9\kappa-5}{\kappa+1} \frac{2-\alpha}{\alpha}$ (6)	[24,36,37]

From the structure of this equation it is clear that $\lim_{Kn\to\infty} \lambda_g(Kn) = 0$ and $\lim_{Kn\to0} \lambda_g(Kn) = \lambda_0$. It is well known that gas molecules do not tend to perform a complete energy exchange with the wall during the collision. This leads to a temperature jump at the interface. Mathematically, this phenomenon can also be understood as an increase of the wall distance. In Eq. (1) this effect is represented by the dimensionless parameter β. There are several definitions for β in the literature, which are listed in Table 4. It is a function of at least one of the following parameters: isentropic exponent κ (which is the relation between specific heat at constant pressure and specific heat at constant volume $\frac{c_p}{c_v}$), the thermal accommodation coefficient α (which will be discussed in Chapter 3.1 in detail) and the Prandtl Number Pr. The resulting β values for the investigated gases in combination with a silica surface differ greatly from the gases and also from the equations as can be seen in Fig. 1.

3.1. Accommodation coefficient

The thermal accommodation coefficient (TAC) α is a measure for the imperfection of the energy exchange of a gas molecule at wall impact. The TAC is for heat transport via molecular collisions like the emission coefficient for radiative transfer. Essentially, it depends on the following influencing variables: Molar mass of
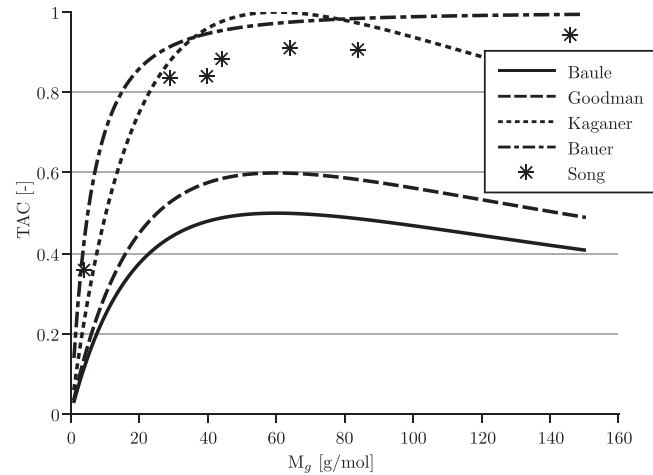
Fig. 2. Accommodation coefficients calculated with different models plotted over the molar mass of the gas molecule. Song's model also depends on degree of freedom of the respective molecule so it was only calculated for the types of gas investigated in this paper.

gas molecules M_G, degrees of freedom of gas molecules, molar mass of the solid surface material M_S, surface properties (roughness, adsorbed molecules, impurities) and temperature. In the literature only a few data are available with partly significant deviations. General agreement exists, however, on the tendency that the accommodation coefficient decreases with increasing temperature and decreasing molar mass of the gas. Some well-known formulas for calculating the accommodation coefficient are given below.

The resulting TACs are plotted against the molar mass of the gas particles in Fig. 2. From the solid sphere theory and the law of conservation of momentum, an approximation of the TAC can be derived from the masses of the gas molecules and the molecules of the solid surface. According to Baule [38], if only translational energy is transferred and each gas particle hits the surface only once, Eq. (7) can be derived.

$$\alpha = \frac{2M_G M_S}{(M_G + M_S)^2} \qquad (7)$$

This equation was extended by Goodman [39], who used it to obtain good agreement with measured values in the temperature range 0 - 500 K. He postulated Eq. (8).

$$\alpha = 2.4 \frac{\frac{M_G}{M_S}}{\left(1 + \frac{M_G}{M_S}\right)^2} \qquad (8)$$

Another approximation mentioned by Kaganer [29] is shown in Eq. (9).

$$\alpha = 1 - \left(\frac{M_S - M_G}{M_S + M_G}\right)^2 \qquad (9)$$

Song [40] not only takes the masses of the molecules but also the degrees of freedome of the gas molecules into account. He de-

rives Eq. (10),

$$\alpha = exp\left[C_0\left(\frac{T-T_0}{T_0}\right)\right]\left(\frac{M_G^*}{C_1 + M_G^*}\right)$$
$$+ \left\{1 - exp\left[C_0\left(\frac{T-T_0}{T_0}\right)\right]\right\}\frac{2.4\frac{M_G}{M_S}}{(1 + \frac{M_G}{M_S})^2} \qquad (10)$$

where $M_G^* = M_G$ for monatomic gases and $M_G^* = 1.4 * M_G$ for diatomic or polyatomic gases and

$C_0 =$	-0.57	dimensionless
$C_1 =$	6.8	units of M_G
$T_0 =$	273	K.

Bauer, on the other hand, describes a negligible influence of the surface properties and recommends for estimation a correlation of the molar mass of the gas and the TAC at room temperature, which is shown only graphically in his paper [41]. The relationship is best described by a function of the form $y = \frac{a}{(x+x_0)^2}$. For this particular case, Eq. (11) could be derived from the figure.

$$\alpha = 1 - \frac{144.6}{(M_G + 12)^2} \qquad (11)$$

3.2. The knudsen number and the characteristic length

The Knudsen number is a measure of the dilution of the gas and describes the ratio between the mean free path of the gas molecules L to a characteristic length x ($Kn = L/x$). The higher the Knudsen number, the greater is the dilution of the gas. The mean free path of the gas molecules is the average distance a gas molecule can travel before it collides with another one. It can be calculated according to the kinetic theory of gases via Eq. (12) [42].

$$L = \frac{k\,T}{\sqrt{2}\,\pi\,d_{kin}^2\,p} \qquad (12)$$

There are various interpretations in the literature for the characteristic length in a porous material. The original definition by Kaganer [29] refers to two opposing parallel plates. In this case, the distance between the plates is the characteristic length. The situation is different in the void spaces of a porous material. The pore shapes are usually very chaotic and deviate strongly from two opposite plates. Therefore, the aim of an analytical solution is to find the best approximation to reality for different porous media. There are different approaches to this purpose, which will be discussed in the following. Many authors simply use the mean pore size as characteristic length. This assumption deviates relatively strongly from the real conditions, but represents a simple and fast estimation method. Another common method is to use a correction factor for the pore size or, if no pore size measurement data are available, to calculate the pore size from the particle size. Details on this are elucidated in Chapter 3.3. If available, it is possible to use the pore size distribution d_{dist} instead of the mean or peak pore size d_{peak} for the calculation. In this case, a corresponding Knudsen number must be calculated for each occurring pore size, and from this a gas thermal conductivity. It can then be weighted according to the volume fraction associated with the different pore sizes, as it is shown in Eq. (13).

$$\lambda_g = \int \lambda_g' \frac{dV}{V_{max}} dx \qquad (13)$$

With λ_g' as gas thermal conductivity in pores with pore size x, dV as pore volume of the pores with size dx and V_{max} as total pore volume.

Table 5
Summary of different methods to calculate gas thermal conductivity in pores.

Dimensionless parameter β	TAC α	Characteristic length x
Eq. (2)	Baule (Eq. 7)	d_{peak}
Eq. (3)	Goodman (Eq. 8)	d_{dist}
Eq. (4)	Kaganer (Eq. 9)	$d_{peak} * \frac{\pi}{6}$
Eq. (5)	Song (Eq. 10)	$d_{dist} * \frac{\pi}{6}$
Eq. (6)	Bauer (Eq. 11)	D_{aggl} & KC
		D_{aggr} & KC
		D_{prim} & KC

3.3. Corrections of the geometric parameters

In addition to the mentioned calculation methods, some suggestions for the correction of the measured quantities exist in order to either convert them into the required parameters or to adapt them to the models. If, for example, no direct measured values for the pore size are available, the Kozeny's correction (KC) for calculating the average gap distance x for equal-sized spherical particles from the particle sizes D_{prim}, D_{aggr} or D_{aggl} and the porosity ϕ can be used [29,43,44]. It results from the ratio of pore volume and particle surface area and is shown in Eq. (14).

$$x = \frac{2}{3}\frac{\phi}{1-\phi}D_{gr} \qquad (14)$$

Even if measured values for the pore size or the pore size distribution are available, correction methods can be useful due to the fact that measured pore sizes do not necessarily represent the average gap distance in pores. In our previous works [24,45], the average gap distance in spherical pores was calculated from the pore size with Eq. (15).

$$x = \frac{\pi}{6}d_{pore} \qquad (15)$$

3.4. Summary of possible calculation methods for the gas thermal conductivity

The calculation options for the TAC α, the dimensionless parameter β and the characteristic length x described in the previous chapters are summarized in Table 5. The variations result in 175 possible combinations to calculate the gas thermal conductivity with Eq. (1).

4. Calculation of the effective thermal conductivity

The effective thermal conductivity λ_{eff} is the macroscopically observed, apparent thermal conductivity of a material composite or a porous medium. It is composed of the thermal conductivities of the individual components, their proportion and the structural distribution. In the following, various models for predicting the effective thermal conductivity of porous media are presented. Basically, it is assumed that the total thermal conductivity is composed of the four components: solid thermal conductivity λ_s, thermal conductivity by radiation λ_r, gas thermal conductivity λ_g and the coupling term λ_c as it is shown in Eq. (16). Convection can be neglected since the gases are not moving in such small pores [46,47].

$$\lambda_{eff} = \lambda_s + \lambda_r + \lambda_g + \lambda_c \qquad (16)$$

The two components λ_s and λ_r are assumed to be independent of gas pressure. Their sum can be determined by thermal conductivity measurements at very low pressures, since it can then be assumed that the thermal conductivity of the gas is completely suppressed. These two mechanisms are represented by the baseline on the bottom of Fig. 3 and are summarized below as λ_{base}. The
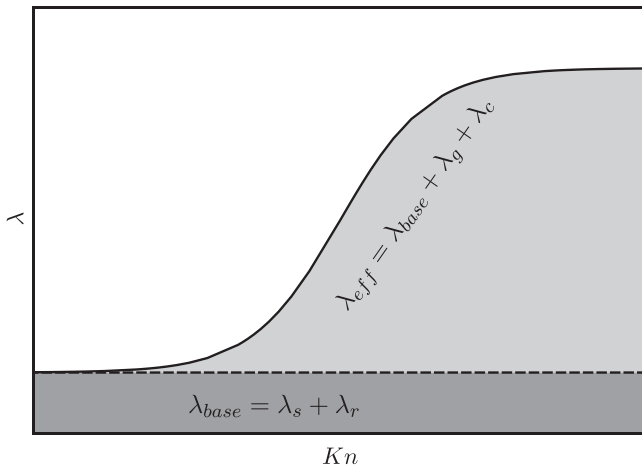
Fig. 3. Schematic diagram of typical thermal conductivity versus Knudsen number curve; x-axis is logarithmic and inverted.

gas thermal conductivity is a function of the Knudsen number Kn, which in turn is a function of pressure as well as of the geometric size of the void space. It can be determined as described in Chapter 3. The coupling term λ_c can be understood as the interaction between the other heat transfer mechanisms, primarily between λ_s and λ_g. For example, having a unit cell of two ideal spheres in contact with infinitesimally small contact area, the solid heat conduction in the direction of the line connecting the two centers of the spheres is also infinitesimally small if the gas heat conduction is completely suppressed. If the gas between the spheres now obtains a non-zero thermal conductivity, the effective thermal conductivity of the entire unit cell exceeds the pure gas thermal conductivity (provided that λ_p is greater than λ_g). Fig. 3 shows not an actual measurement or calculation. It is only a schematic representation to visualize different heat transfer mechanisms.

Different types of prediction models for the effective thermal conductivity of porous media are presented below. According to their approach and complexity, they are divided into the categories "Geometry independent models", "Unit Cell Models" and "Models with consideration of local Knudsen numbers".

4.1. Geometry independent models

For this type of prediction model, one needs minimal knowledge about the investigated materials. It is sufficient to know the thermal conductivities of the two phases and the porosity. These data are called primary parameters in some references. According to [13], these models work best for small solid/fluid thermal conductivity ratios. Accordingly, they should be applicable in the present investigation especially for pressure ranges close to atmospheric pressure and gases with rather high thermal conductivity.

4.1.1. Series and parallel connection model

The simplest model for describing the thermal conductivity of porous media is a serial or parallel connection of the thermal resistances of the individual phases. The weighting of the individual phases is usually done according to their porosity. The pure serial or parallel connection represents the lower and upper limit case. Combinations of the two limiting cases are usually used. The serial part can be understood as the contribution of the coupling effect. A well-known model of this kind was already developed by Russel [48] in 1935. He presented two versions of his formula which differ in which of the two phases is disperse. In the case of powdery substances, the fluid can always be regarded as the disperse phase. The corresponding version is shown in Eq. (17). Since Rus-

sel's model does not provide for a continuous solid path, the effective thermal conductivity approaches zero when the gas thermal conductivity disappears. In order to prevent this and to make the model comparable with the others, the measured value λ_{base} is added to the original equation.

$$\lambda_{eff} = \lambda_{base} + \lambda_g \left(\frac{\Lambda^{2/3} + \frac{\lambda_g}{\lambda_p}\left(1 - \Lambda^{2/3}\right)}{\Lambda^{2/3} - \Lambda + \frac{\lambda_g}{\lambda_p}\left(1 - \Lambda^{2/3} + \Lambda\right)} \right) \tag{17}$$

Λ is $1 - \phi$ and ϕ is the porosity, which is defined as the volumetric ratio of void spaces in a porous media.

4.1.2. Maxwell

Maxwell formulated two limiting cases for very large and very small porosities in his composite medium problem as early as 1873 [49]. The first case mentioned assumes a fluid with suspended sherical solid particles and the second a solid with widely spaced sherical fluid-filled voids. In both cases, the spheres show no interactions with each other. Therefore, λ_{base} is added to the result again. In the present work only the first version is used which is shown in Eq. (18).

$$\lambda_{eff} = \lambda_{base} + \lambda_g \left(\frac{2\phi + \frac{\lambda_p}{\lambda_g}(3 - 2\phi)}{3 - \phi + \frac{\lambda_p}{\lambda_g}\phi} \right) \tag{18}$$

4.1.3. Scaling model

Swimm et al. [36] propose a scaling model that is developed on the basis of simple interconnections of thermal resistances. It provides for a linear dependence of the coupling effect on the gas thermal conductivity for a wide range of solid to fluid thermal conductivity ratios. The corresponding function is shown in Eq. (19).

$$\lambda_{eff} = \lambda_{base} + \lambda_g(1 + F\phi) \tag{19}$$

According to this, in one of our previous works [24], the relationship shown in Eq. (20) was determined for precipitated silica with air as the pore gas and a porosity range between 0.76 and 0.92. For this purpose, the results were fitted to thermal conductivity measurements with F as the only fit parameter. Five different precipitated silicas were used, each of which was compressed to different degrees in order to include as large a porosity range as possible.

$$\lambda_{eff} = \lambda_{base} + \lambda_g(-18.68\phi + 18.94) \tag{20}$$

4.2. Unit cell models

The models discussed in this chapter, consider particle geometry in some way. These are all unit cell models. A unit cell is a substitute geometry for the smallest structures that repeat over and over again in a porous medium. The unit cell geometry is derived from the porosity and/or the particle size.

4.2.1. Sphere model

Kaganer proposes a model for spherical backed beds based on a cylindrical unit cell with two spheres in contact in his 1969 paper [29]. A sketch of this unit cell is shown in Fig. 4. The heat flux at each distance to the contact point is calculated as a series connection from the thermal resistances $\frac{2x'_p}{\lambda p}$ and $\frac{x'_g}{\lambda_g}$, and weighted as a parallel connection according to their circular area fractions perpendicular to the heat flux direction. The resulting thermal conductivity is then assigned to a certain area fraction of the total heat transfer area via porosity. In addition, the average number of contact points of the spheres is also calculated from the porosity. The effective thermal conductivity after integration over the radius of the cylindrical unit cell finally results in Eq. (21). Again, λ_{base} is added, since the contact points of the spheres are infinitesimally
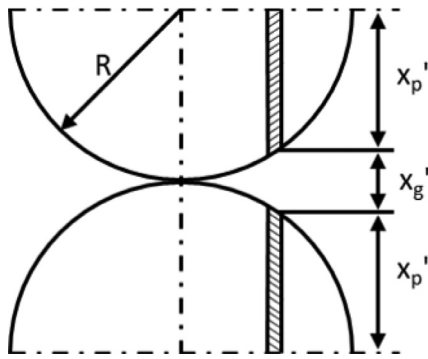
Fig. 4. Cylindrical unit cell of the sphere model.

small and thus the effective thermal conductivity together with the gas thermal conductivity would otherwise approximate zero.

$$\lambda_{eff} = \lambda_{base} + \lambda_g \left[\frac{5.8(1-\phi)^2}{k} \left(\frac{1}{k} \ln \frac{\lambda_p}{\lambda_g} - 1 - \frac{k}{2} \right) + 1 \right] \quad (21)$$

Here $k = 1 - \frac{\lambda_g}{\lambda_p}$.

Cunnington and Brodt [50,51] also use Eq. (21). In this model, the gas thermal conductivity is independent of the location and is either assumed as $\lambda_g = \lambda_0$ for the case of continuum flow or determined by taking into account the Soulochowski effect via a relationship listed in Chapter 3. Particle size is not considered in this type of computational model. Numerous authors [52,53] present similar unit cell models. They are the attempt to take into account the coupling effect between solid and gas thermal conductivity by the simplified consideration of a geometry as close to reality as possible. It is common to weight the coupling contribution and the pure gas thermal conductivity with corrected porosities for example by comparing the porosity of the unit cell with the real porosity. Some different approaches to this are listed in [54].

4.2.2. Schumann and Voss

The model of Schumann and Voss [55] is based on a planar unit cell with a particle geometry in the form of a hyperbola. The exact function of the hyperbola is determined by a shape factor which is denoted as P in the following. P is related to the porosity of the unit cell ϕ_{uc} as described in Eq. (22).

$$\phi_{uc} = P(P+1) \ln \left(\frac{1+P}{P} \right) - P \quad (22)$$

Since this equation has a limit value of 0.5, the maximum possible unit cell porosity in this model is $\phi_{uc} = 0.5$. Most of the materials investigated here have a higher porosity than this. For this cases P was assumed to be 200 which leads to a unit cell porosity very close to $\phi_{uc} = 0.5$. Consequently, a corrected porosity ϕ_{corr} is introduced in Eq 23. For the particular case of $\phi_{uc} = 0.5$ the term $\frac{\phi_{uc}}{1-\phi_{uc}}$ becomes one and the corrected porosity can be written as $\phi_{corr} = \phi - (1 - \phi)$. For $\phi < 0.5$, $\phi_{corr} = 0$.

$$\phi_{corr} = \phi - (1 - \phi) \frac{\phi_{uc}}{1 - \phi_{uc}} \quad (23)$$

The original Schumann and Voss equation for the effective thermal conductivity is shown in Eq. (24).

$$\lambda_{eff,SV}$$
$$= \lambda_g \left(\phi^3 + \frac{\frac{\lambda_s}{\lambda_g}(1-\phi^3)}{1+P\left(1-\frac{\lambda_s}{\lambda_g}\right)} \left[1 + \frac{P(1+P)\left(1-\frac{\lambda_s}{\lambda_g}\right)}{1+P\left(1-\frac{\lambda_s}{\lambda_g}\right)} \right] \ln \left(\frac{1+P}{P\frac{\lambda_s}{\lambda_g}} \right) \right) \quad (24)$$
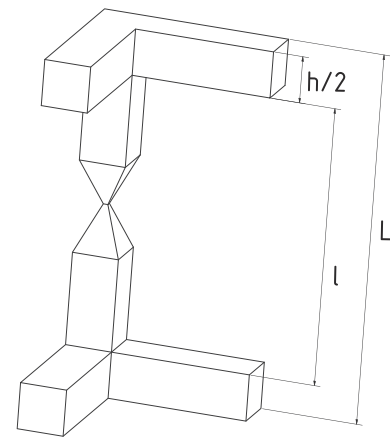
Fig. 5. Unit cell of Luikovs model reconstructed after [15].

To include the corrected porosity and once again to account for λ_{base} at very low pressure levels, the formula was extended as can be seen in Eq. (25).

$$\lambda_{eff} = \lambda_{base} + (1 - \phi_{corr}) * \lambda_{eff,SV} + \phi_{corr} * \lambda_g \quad (25)$$

4.2.3. Luikov

The unit cell presented by Luikov et al. [15] consists of a skeleton of thermal resistors, as can be seen in Fig. 5. The spot in the middle accounts for the contact resistance between particles. The geometric sizes of the unit cell L and l can be calculated from the particle size and the porosity of the bulk material.

In the original literature the relation $\frac{h}{l}$ is given in tabular form only. In the present work the polynomic equation shown in Eq. (26) with a coefficient of determination of 0.9995 was used instead.

$$\frac{h}{l} = 209.03\phi^6 - 744.65\phi^5 + 1054.40\phi^4 - 762.77\phi^3$$
$$+ 304.07\phi^2 - 68.73\phi + 8.70 \quad (26)$$

Luikov's method for the calculation of the effective thermal conductivity is shown in Eq. (27).

$$\lambda_{eff} = \frac{1}{\frac{1}{\left(\frac{h}{L}\right)^2} + A} + v_g * \left(1 - \frac{h}{L} \right)^2 + \frac{2}{1 + \frac{h}{l} + \frac{1}{v_g \frac{h}{L}}} \quad (27)$$

Where

$$A = \frac{1}{\frac{\lambda_c}{\lambda_p} + \frac{v_g}{4 k_k k_m} \left(\frac{h}{L}\right)^2 * 10^3}$$

$$\frac{h}{L} = \frac{\frac{h}{l}}{1 + \frac{h}{l}}$$

and

$$v_g = \frac{\lambda_g}{\lambda_p}$$

The factors k_m and k_k are an empirical coefficient and the coefficient of particle adhesion, respectively. They are assumed to be $k_m = 1$ and $k_k = 1.5$ according to an example calculation in the original paper. For λ_c the following term is used to ensure that the thermal conductivity at very low pressures corresponds to the measured one. This is again due to comparability to the other models.

$$\lambda_c = \frac{\lambda_p}{\frac{\lambda_p}{\lambda_{base}} - \frac{1}{\left(\frac{h}{L}\right)^2}}$$

4.2.4. Zehner, Bauer, Schlünder

In their 1970 paper [56], Zehner, Bauer, and Schlünder developed what is probably the best-known model for bulk particles of different geometries. They introduced the shape factor C which determines the geometry of the model particle in a unit cell. The formula for determining the particle geometry is shown in Eq. (28).

$$r^2 + \frac{z^2}{(B - (B-1)x)^2} = 1 \tag{28}$$

Where

$$B = C\left(\frac{1-\phi}{\phi}\right)^{\frac{10}{9}}$$

For spherical fillings, $C = 1.25$ as suggested by the authors. Since no recommendation was made for multi-scale geometries and hierarchical structures, $C = 1.25$ is used in this work for all materials. The resulting model particle geometry, however, does not correspond to a sphere. This is explained by the fact that one tries to compensate errors which are made by the assumption of parallel heat flow lines in the following procedure. The final function for the effective thermal conductivity, obtained by integration over the radius of the unit cell is given in Eq. (29).

$$\lambda_{eff} = \lambda_{base} + \lambda_g * \left\{ \left(1 - \sqrt{1-\phi}\right) + \sqrt{1-\phi}\frac{2}{1 - \frac{\lambda_g}{\lambda_p}B} \right.$$
$$\left. \left[\frac{\left(1 - \frac{\lambda_g}{\lambda_p}\right)B}{\left(1 - \frac{\lambda_g}{\lambda_p}B\right)^2} \ln \frac{\lambda_p}{B\lambda_g} - \frac{B+1}{2} - \frac{B-1}{1 - \frac{\lambda_g}{\lambda_p}B} \right] \right\} \tag{29}$$

In Eq. (29) the pure gas thermal conductivity is weighted with the corrected porosity $\left(1 - \sqrt{1-\phi}\right)$ and the coupling part determined with the unit cell with $\sqrt{1-\phi}$ respectively. This relationship was derived using the analogy of heat conduction and diffusion and was determined by measuring diffusion coefficients of porous media.

The Zehner, Bauer, Schlünder model is often called ZBS-model and is used and sometimes modified by many researchers. Sih and Barlow [57] for example postulated a modified form and compared it with 424 measured data. The comparison shows the predictions to be accurate within a range of ± 30% relative error.

4.3. Unit cell models with consideration of local Knudsen numbers

In the models shown in 4.1 and 4.2, a homogeneous thermal conductivity over the entire gas space is assumed. However, this leads to an inaccurate representation of reality in the Knudsen range, since the thermal conductivity depends on the distance to the wall at each point. If one assumes locally different Knudsen numbers in the void space, correspondingly varying gas thermal conductivities result over the radius of the unit cell. Near the contact point of the particles, small gap widths x'_g (Fig. 4) with high Knudsen numbers occur. As one moves further away from the point of contact in the x-direction, the gap width increases and Kn decreases. This results in a variation of the total thermal conductivity of the unit cell that depends on the particle size. As in the unit cell models without consideration of the local Knudsen number, the coupling term determined over the unit cell and the pure gas thermal conductivity is weighted according to corrected porosities. In this particular case, decisions must therefore be made regarding the characteristic geometry both when determining the gas thermal conductivity and when designing the unit cell. Therefore, the models following now are calculated for all materials with multi scale geometry with corresponding multiple input parameters for the particle size if available, i.e. for PS and FS for the primary particle, aggregate and agglomerate size and for SG for primary particle and aggregate size.
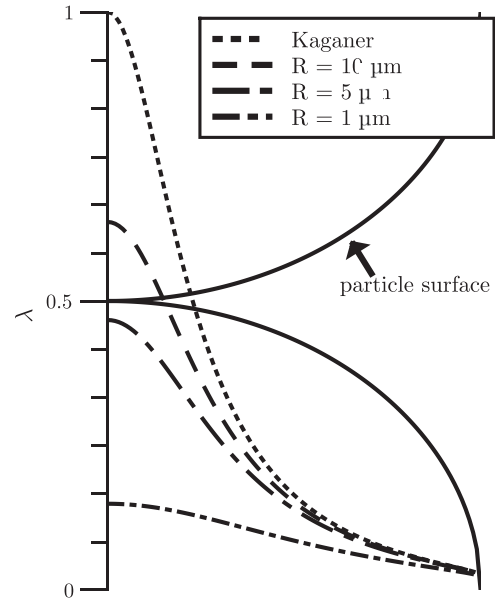
Fig. 6. Thermal conductivity progressions in a unit cell over the radius calculated with local Knudsen numbers for different particle sizes. $\lambda_p = 1 \frac{W}{mK}$, λ_g calculated with Eq. (1) using the material values of air at atmospheric pressure and $\beta = 4.3$.

4.3.1. Sphere model

Swimm et al. [58] propose to calculate the thermal conductivity in a cylindrical unit cell with locally different Knudsen numbers. The unit cell is divided into a finite number of cylindrical shells and their thermal resistances are calculated as parallel connections. Since the void distance in each cylindrical shell is different, different Knudsen numbers and thus different gas thermal conductivities result. The void distance over the radius for a division into N cylinder shells for the i-th shell results in Eq. (30). Accordingly, D and R are the diameter and the radius of the primary particles, aggregates or agglomerates.

$$x(i) = D - 2\sqrt{R^2 - \left(\frac{i}{N}R\right)^2} \tag{30}$$

The area perpendicular to the heat flow of the regarding cylinder shell is $A_i = \pi(2i - 1)\left(\frac{R}{N}\right)^2$. The coupling conductivity of the entire unit cell can consequently be calculated via Eq. (31), in which λ'_g is calculated as a function of $x(i)$ for every i with the respective formula from Chapter 3.

$$\lambda_c = \frac{2}{R\pi} \sum_{i=1}^{N} A_i \left(\frac{D - x(i)}{\lambda'_g} + \frac{x(i)}{\lambda_p}\right)^{-1} \tag{31}$$

To calculate the effective thermal conductivity of the bulk material, the thermal conductivity of the pure gas phase λ_g and that of the unit cell λ_c are weighted according to a corrected porosity ϕ_{corr} as shown in Eq. (32).

$$\lambda_{eff} = \lambda_{base} + \phi_{corr}\lambda_g + (1 - \phi_{corr})\lambda_c \tag{32}$$

For the spherical unit cell Eq. (23) results in Eq. (33) as it was used by the original authors.

$$\phi_{corr} = \frac{3\phi - 1}{2} \tag{33}$$

To illustrate the influence of the local Knudsen numbers, the thermal conductivity curves in a unit cell with spherical particles of different radii are shown in Fig. 6. For comparison, the curve progression with homogeneous gas thermal conductivity in the entire unit cell, as used by Kaganer, for example, is also shown.

Swimm's model was improved by Guo and Tang [37] especially for aerogels by considering an overlapping of the spheres and taking into account a coupling not only in the gap between the particles but also between particle chains and air gaps. As this is aerogel specific, it was not further investigated in this paper.

4.3.2. Zehner, Schlünder

Zehner and Schlünder [34] further developed their well-known model from [56] by also considering the Smoluchowski effect locally in the interparticle voids. For this purpose, a local Knudsen number is calculated at each location by correcting the global Knudsen number Kn to $Kn^* = \frac{Kn}{(1-x(r))}$. After integration over the radius of the unit cell λ_c can be written as shown in Eq. (34).

$$\lambda_c = \lambda_0 \frac{2}{N-M} \left\{ \frac{\left[N - (1 + Kn) \frac{\lambda_0}{\lambda_p} \right] B}{(N-M)^2} \ln \frac{N}{M} \right.$$
$$\left. - \frac{B-1}{N-M}(1 + Kn) - \frac{B+1}{2B} \frac{\lambda_p}{\lambda_0} [1 - (N - M) - (B - 1)Kn] \right\} \quad (34)$$

with

$$M = B \left[\frac{\lambda_0}{\lambda_p} + Kn(1 + Nu_r^*) \right]$$

and

$$N = (1 + Nu_r^*)(1 + Kn)$$

The Knudsen number occurring here can be distinguished from the Knudsen number used to calculate pure gas thermal conductivity. The particle size must be used to calculate the Knudsen number in order to adequately describe the size of the gap in which the coupling thermal conductivity occurs. For materials with a multiscale structure, the decision between primary particle size, aggregate size and agglomerate size is again of crucial importance. Nu_r is an empirical parameter to account for the radiation. The calculation can be taken from the original literature. With the corrected porosity $1 - \sqrt{1 - \phi}$ one gets Eq. (35) for the effective thermal conductivity.

$$\lambda_{eff} = (1 - \sqrt{1 - \phi})(\lambda_g + \phi \lambda_0 Nu_r) + \sqrt{1 - \phi} \lambda_c \quad (35)$$

4.4. Slavin

In this unit cell model from Slavin [59] the roughness of the particles is taken into account. The model treats the spheroids as being perfect spheres, separated at their contact points by a short cylinder of area d and length 2hr representing the surface roughness. In the present investigation for multi scale structures the radii of the next smaller structure was chosen as hr. For the primary particles a complete smooth surface and for the glass spheres a constant roughness of 0.1 μm was assumed. As in other models, the unit cell is divided into different regions which are then considered as parallel or in series. The gas thermal conductivity in the space between the particles is divided into an inner and an outer region. Where the regions begin and end depends on the particle size and the mean free path. In the inner region, the Smoluchowski effect is considered with a global Knudsen number. The individual calculation steps can be taken from the original literature. Eq. (36) shows the calculation of the effective thermal conductivity of the unit cell as a parallel and series connection of the individual heat resistances G_x of different parts of the unit cell.

$$\lambda_{eff} = \left\{ G_{rv} + G_{gv} \left[G_r + N_c \left(\frac{G_s(G_i + G_o + G_c)}{G_s + G_i + G_o + G_c} \right) \right] \right\} \frac{L_s}{A_{cp} + A_v} \quad (36)$$

N_c is the average effective number of contact points of a particle which is 1.5 according to Slavin et al., the height of the unit cell $L_s = \sqrt{\frac{8}{3}} R$ and A_{cp} and A_v are the area of the particle and the

void space respectively. To "fix" the low pressure conductivity and for comparability with the other models the contact resistance was set to $G_c = \lambda_{base} \frac{A_{cp} + A_v}{N_c L}$. Slavin's model does not include a classical term λ_g like the other models. Therefore, the results here do not distinguish between the calculation methods for β and the geometric size x.

5. Evaluation procedure

In order to evaluate the results obtained with the different models and calculation methods, they need to be compared with the measured ETCs. The mean-variance S of the calculated to the measured thermal conductivity values for gas pressure levels $j = 1 : N$ as shown in Eq. (37) is used for this purpose.

$$S = \frac{\sum_{j=1}^{N} \left| \frac{\lambda_m(j) - \lambda_{eff}(j)}{\lambda_m(j)} \right|}{N} \quad (37)$$

This approach results in one S value for every solid gas combination. Thus, an average of the mean-variances S for all materials and gases $\bar{S}_{all}$ can be calculated for every combination of calculation methods. For example the average variance for the sphere model in combination with Eq. (3) for β, Baules model for α and the pore size distribution + sphere correction for x. In this way a total number of 175 $\bar{S}_{all}$ values are generated for every ETC model and stored in a matrix called R_{all}. The $\bar{S}_{all}$ values provide information to assess the suitability of the models for calculating the thermal conductivity curves of any unknown silica-based porous material. In order to be able to make a statement about the suitability of the models for the calculation of individual material groups, average values of the corresponding variances $\bar{S}_{PS}$, $\bar{S}_{FS}$, $\bar{S}_{SG}$ and $\bar{S}_{GS}$ are also calculated and stored in tables R_{PS}, R_{FS}, R_{SG} and R_{GS}, respectively. A summary of the calculation steps that were performed for the evaluation using a MATLAB (*Co. The MathWorks Ink.*) calculation program is shown below. The entire code for one exemplary ETC model is provided as supplementary material.

```
for D_part = [D_aggl; D_aggr; D_prim]
  for α = [Eq. (7) : Eq. (11)]
    for β = [Eq. (2) : Eq. (6)]
      for λ_g = f(x) - Six options for x (see Table 5)
        for m = 1 : N (N = 15 materials)
          for i = 1 : J (J = 7 gases)
            λ_eff = [Eq. (17), (18), (20), (21), (25), (27), (29),
                     (32), (34), (36)]
            S = [Eq. 37]
          end
          S̄ = (Σ S(m,i)) / (N*J)
        end
      end
    end
  end
end
```

$$R_{all}, R_{PS}, R_{FS}, R_{SG}, R_{GS} = \begin{bmatrix} \bar{S}_{1,1} & \cdots & \cdots \\ \vdots & \ddots & \vdots \\ \cdots & \cdots & \bar{S}_{7,25} \end{bmatrix}$$

For each effective thermal conductivity model a total of five matrices R are calculated, each with 175 $\bar{S}$ values, one with mean values for all tested materials and four more for each material class (PS, FS, SG, GS). Each matrix consists of 7 x 25 mean-variances $\bar{S}$ which were determined using the described combination of calculation methods. The lowest mean-variance in each case indicates the best-suited combination for the corresponding material class.

6. Results and discussion

After calculating the thermal conductivity progressions for all porous medium-gas combinations with all mentioned combinations of equations for α, β and x, the variances $\bar{S}$ (or matrices R) were summarized in tables, which are accordingly available as supplementary material. The smaller the $\bar{S}$ value, the better the respective combination of calculation models works for the corresponding class of materials (PS, FS, SG, GS) or, in the case of $\overline{S_{all}}$, for the totality of all materials. The best three combinations for each ETC model were extracted and are called "favorites" in the following. The lists of favorites for all material classes are shown in the appendix in Tables B.1–B.5. To get an additional overview of which GTC models lead to the most promising results in general, mean values of all variances which have been calculated with the different models for α, β and x are shown in Table 6. There is one row for the totality of all materials and one for every material class. Since all model combinations which include the respective GTC models have been taken into account for the calculation of the mean variances the absulut values are very high. But even if influences of the "good" as well as of the "worse" ETC-models can be found here, it serves as an adequate measure to compare the influences of the calculation methods for α, β and x. The difference between them, on the other hand, allows a statement to be made about which GTC model provides good results for which material class with the highest probability. On the other hand, the spread of the data can be used to make a qualitative statement about the sensitivity of the results to the different GTC models. The greater the spread, the more important it is to choose the right model in the corresponding category.

The compilation in Table 6 shows that in general it seems reasonable to use one of the older models, e.g. Baule's or Goodman's for the calculation of the TAC. These models predict significantly smaller TACs than the newer ones (Fig. 2). This finding does not allow any statement about the actual thermal accommodation coefficients between a silica surface and the different gases. Only a recommendation for the calculation of the gas thermal conductivity can be given here. The hypothesis that either recent literature classifies TACs fundamentally too high (which is not suspected by the authors) or that an adjustment is necessary in some common models for the calculation of the gas thermal conductivity, is supported by the findings of our previous work [45], which indicates

lower TACs as well. Taking into account that recent measurements or simulations from the literature regarding the TAC [60,61] are more in line with the newer models of e.g. Bauer or Song it can be assumed that they are more physically correct than the older ones even though they seem to have more accordance in the current investigation.

The best equations to calculate the dimensionless parameter β are Eq. (2) and Eq. (6). They differ only slightly and lead to the highest β-values as is shown in Fig. 1. In contrast, there is exactly a factor of 0.5 between Eq. (2) and Eq. (3). Interestingly, Eq. (3) occurs particularly often in the favorites in combination with the newer models for α. This reinforces the tendency to even lower β-values and therefore higher gas thermal conductivities. This combination occurs strikingly often for PS. A possible explanation for this is a higher concentration of silanol groups on the surface of PS compared to FS for example and potentially the clear different particle shape. Silanol groups affect the molar mass of the surface layer, by which the gas molecules collide, and thus the energy accommodation between them. Different pore shapes or roughness can have many effects on the thermal conductivity like multiple molecule collisions, changes of the mean free distance of gas molecules, or of the coupling effect.

As expected, it is advisable to calculate the gas thermal conductivity with the help of the pore size distribution and Eq. (13), if corresponding data are available. Additionally, it can be recommended for most materials to use the correction from Eq. (15). If no measured data of the pore size distribution are available, the Kozeny correction can be applied as described. It is essential to ensure that in this case the aggregate size is used for PS and the primary particle size for FS or SG. For precipitated as well as fumed silica this procedure seems to be even more promising than the use of the pore size distribution. However, the results shown in Table 6 only indicate a rough trend and must not be overestimated. The results may be overlaid by other influencing parameters and do not necessarily coincide with the actual model combinations to be favored for the different material classes as described below. In the following subsections Fig. 7 shows the measured data for all materials investigated in comparison to the calculated results of the model combination, which fitted best on the over all average. Figs. 8 to 11 show the same measured values in comparison to the favorite model combination for the different individual material classes.

6.1. All materials

The best results for all porous materials on average were achieved with the Sphere ETC model with consideration of the local Knudsen number (Section 4.3.1) in combination with Bauer's model for α, Eq. (6) for β and the pore size distribution without correction as the geometric size. Thus, if the material of interest is from unknown nature or if a material is involved that was not examined in this study, this model combination leads to the most promising results. In this case the aggregate size should be used as the geometric size parameter of the unit cell of the sphere model. The calculated values have a mean-variance of 18.5% to the measurements and are shown in Fig. 7 together with the measured values.

6.2. Precipitated silica

The measurement results of precipitated silica were also best obtained by the sphere model with consideration of local Knudsen numbers as it was presented by Swimm et al. (Section 4.3.1). The local Knudsen number in the sphere model is best calculated using the agglomerate size in case of PS. However, for the determination of the gas thermal conductivity, the simple calculation via the peak

Table 6

Average variances which were obtained with the calculation methods for α, β and the geometric size in percent.

	all	PS	FS	SG	GS
α					
Baule	46.8	38.6	51.6	40.3	64.7
Goodman	48.4	39.0	53.5	41.4	69.2
Kaganer	55.4	40.5	60.8	45.7	89.1
Song	56.6	41.2	63.0	46.9	90.6
Bauer	59.0	41.9	65.5	48.6	96.7
β					
Eq. (2)	50.5	39.5	55.6	42.7	75.0
Eq. (3)	57.0	41.1	62.8	46.9	92.8
Eq. (4)	55.1	40.8	61.1	45.8	86.8
Eq. (5)	52.9	40.3	59.1	44.5	80.3
Eq. (6)	50.7	39.5	55.7	42.8	75.4
x					
d_{peak}	46.0	36.2	34.2	40.1	82.8
d_{dist}	42.2	29.0	37.9	31.2	83.4
$d_{peak} * \frac{\pi}{6}$	43.9	37.5	34.9	40.4	69.0
$d_{dist} * \frac{\pi}{6}$	38.2	29.8	31.1	30.8	69.4
D_{aggl} + KC	107.5	84.2	214.6		
D_{aggr} + KC	48.9	29.2	31.7	64.1	
D_{prim} + KC	46.1	35.7	27.6	41.1	89.9

Fig. 7. Results of the best model combination to forecast thermal conductivity over pressure progressions (solid lines) and according to measurement results (asterisks) for an arbitrary silica material.
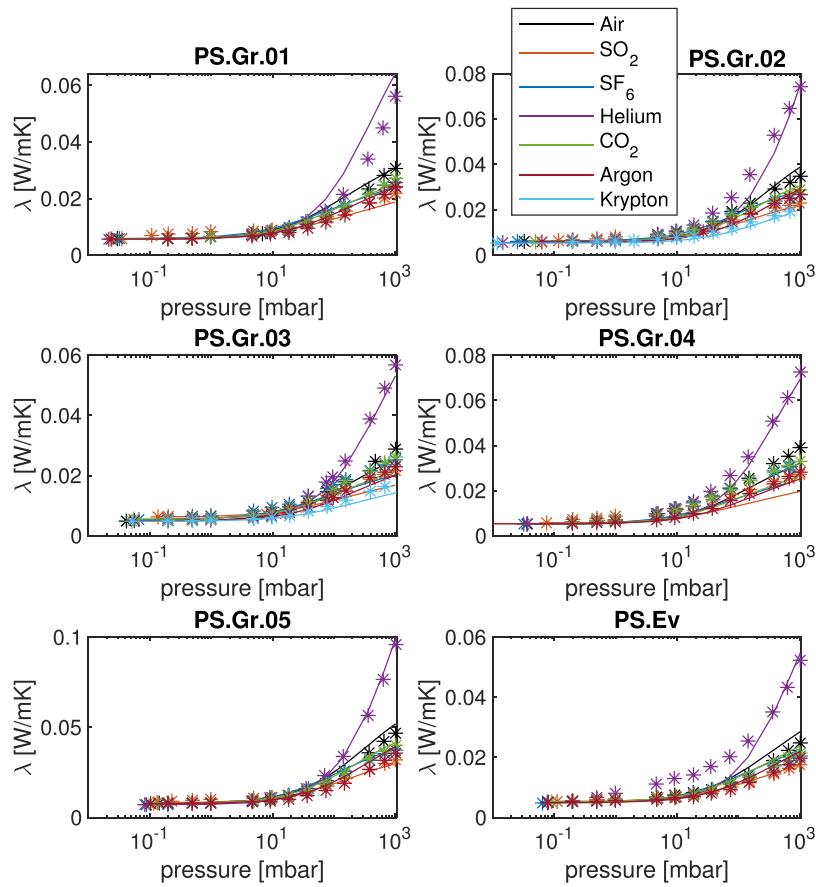
Fig. 8. Results of the best model combination to forecast precipitated silica thermal conductivity over pressure progressions (solid lines) and according to measurement results (asterisks).

of the mercury intrusion porosimetry measurements together with the formula from Bauer for α and Eq. (4) for β is suitable. This is one of the very few examples where the use of the peak size was convincing. If the pore size distribution with correction is used instead, the mean-variance is only 0.07% worse. Since the assumption suggests that the good performance of the peak size could be incidental, the use of the pore size distribution can also be recommended instead. Thus, a mean accuracy of 10.6% can be obtained for forecasting the thermal conductivity progression of precipitated silica as it is shown in Fig. 8.
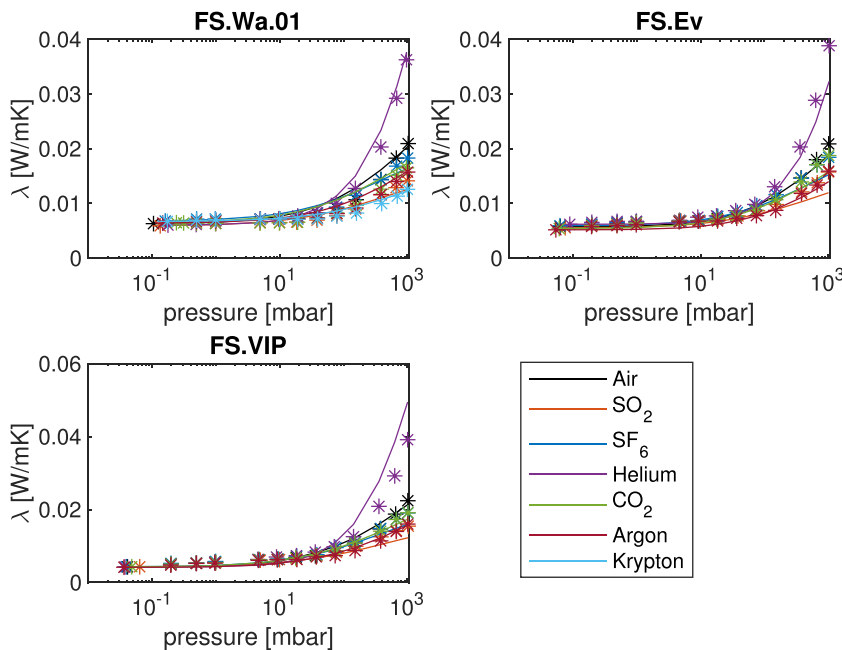
Fig. 9. Results of the best model combination to forecast fumed silica thermal conductivity over pressure progressions (solid lines) and according measurement results (asterisks).
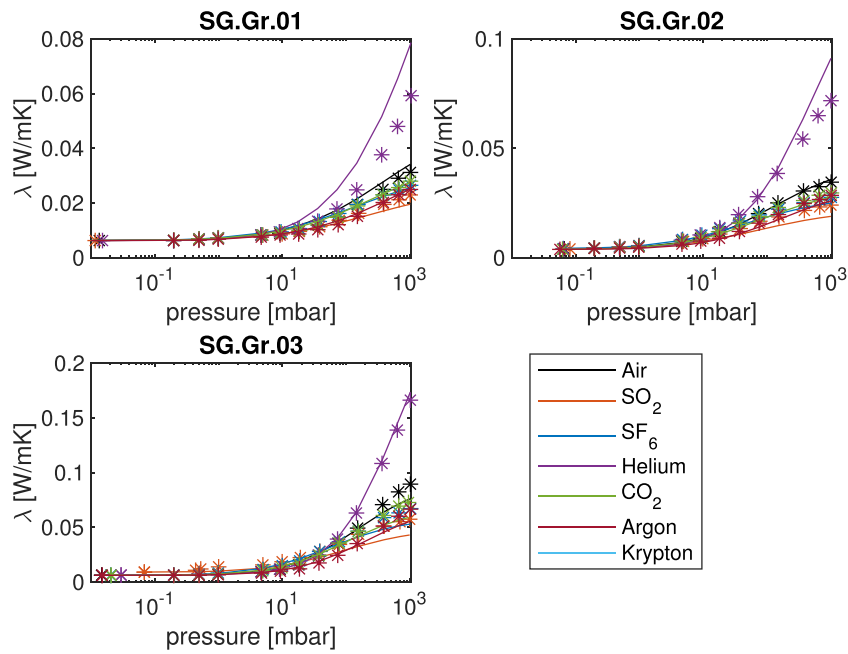
Fig. 10. Results of the best model combination to forecast silica gel thermal conductivity over pressure progressions (solid lines) and according to measurement results (asterisks).

6.3. Fumed silica

The thermal conductivity progressions of fumed silica can be predicted by many models with a very good accuracy. In the favorites, the $\overline{S_{FS}}$ value is mostly around 10%. There is a very clear tendency to Baule's and Goodman's models for α, Eq. (2) and Eq. (6) for β as well as the pore size distribution with correction for x. However, the very best result was achieved with the Kaganer's model for α, Eq. (2) for β and the pore size distribution for x in combination with the new model from Zehner and Schlünder (Section 4.3.2) and the aggregate size for the calculation of the local Knudsen number in the unit cell. This combination leads to

the mean-variance of 9.2%. The respective progressions are plotted in Fig. 9.

6.4. Silica gel

An even more accurate prediction than with fumed silica could only be achieved with silica gel. Although most of the $\overline{S_{SG}}$ values in the favorites are closer to 15%, the smallest value was just 8.7%. That is the most precise combination of prediction methodes of the whole investigation. It was obtained, like for PS, by the sphere model with consideration of the local Knudsen number (Section 4.3.1). However, this time it was the aggregate size that
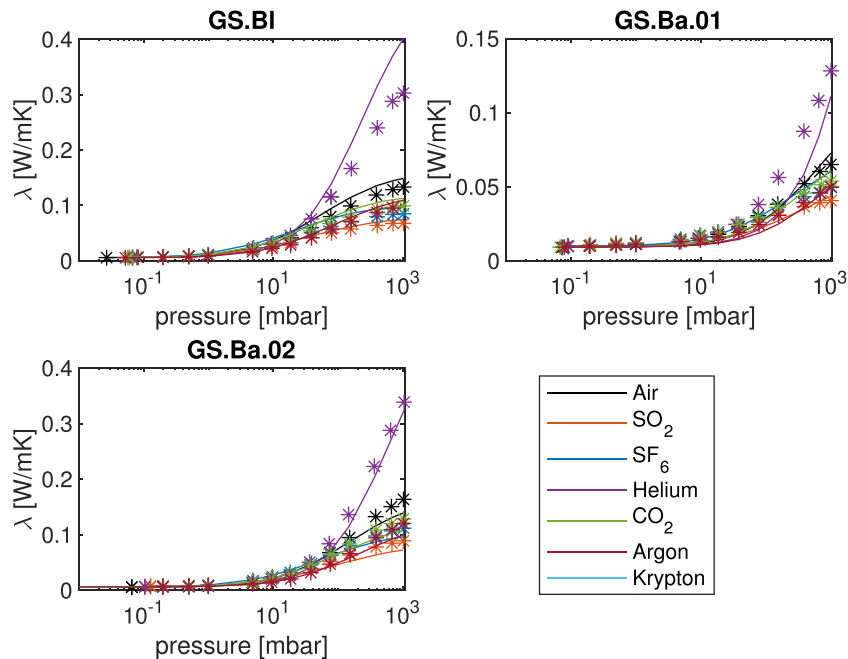

Fig. 11. Results of the best model combination to forecast glass spheres thermal conductivity over pressure progressions (solid lines) and according to measurement results (asterisks).
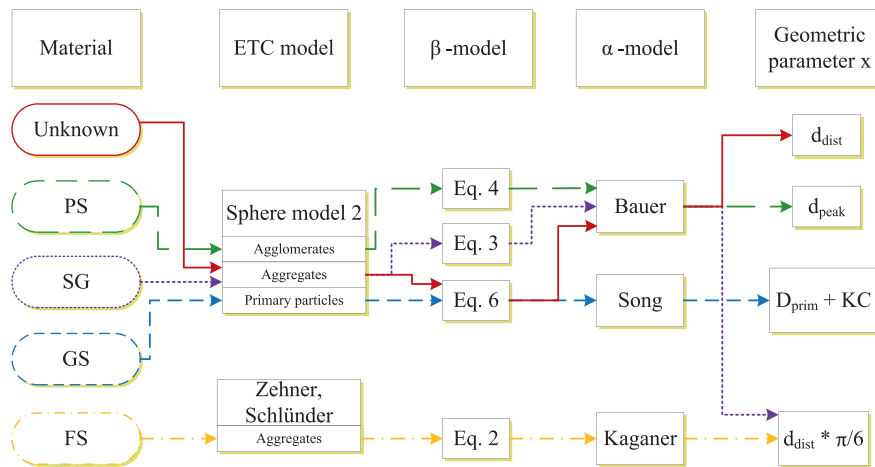
Fig. 12. Flowchart for the selection of models to calculate effective thermal conductivity of different silica based porous materials.

was most suitable for the calculation of the local Knudsen number, not the agglomerate size. However, this is due to the fact that this size scale does not exist for silica gels. Therefore, it is also the "largest particles" that should be used for the calculation with the sphere model.

6.5. Glass spheres

Surprisingly, glass spheres have turned out to be the most unpredictable material class in terms of ETC, although the porous media offer the seemingly most straightforward structure. Best results could be obtained again with the sphere model from Section 4.3.1. This is not surprising, because the spherical shape of the unit cell fits very well to the original shape of the particles. The sphere model delivers the best results in combination with Eq. (6) for β, Song's model for α and the particle size with Kozeny's correction for the calculation of the GTC. Results are shown in Fig. 11 accordingly.

7. Conclusion

In the present study, 15 porous media which are all based on silicon dioxide have been characterized in terms of pressure-dependent thermal conductivity in combination with 7 different gases each. Furthermore, the structural properties of the materials have been investigated. Pore size distributions were measured with mercury intrusion porosimetry and particle sizes with small angle x-ray scattering, dynamic light scattering, laser diffraction and digital light microscopy. Ten popular analytical models from the literature to calculate the effective thermal conductivity of porous media are presented and categorized as follows: Geometry independent models, unit cell models and unit cell models with consideration of local Knudsen numbers. Additionally, several models to calculate the gas thermal conductivity in the pores of the materials have been presented. Altogether the study results in 2800 possible combinations which have been examined using a Matlab code and compared with the measurements. The crucial finding of the paper is probably that basically all models promise better accuracy than is achieved in practice with the real measurement data presented. This is not surprising, because most of the models have been created for special material groups or with regard to some other measured data. The effective thermal conductivity of an unknown porous silica material with an arbitrary Knudsen gas inside of the pores can be forecasted with an average accuracy of about 18.5%, using the sphere model with consideration of the local Knudsen number. In conclusion, this rather compli-

cated model, which requires the use of a computer performs best on the overall average. But, also the simple models presented by Russel or Maxwell still deliver an acceptable overall variance of about 20%. However, it turns out that it is helpful to know about the material class, because by selecting a suitable GTC and ETC model combination, a significantly smaller average error of about 10% can be achieved. More precisely, for the material classes PS, FS, SG and GS minimum average errors of 10.5%, 9.2%, 8.7% and 11.9% could be obtained, respectively. In all cases it was a unit cell ETC model with consideration of the local Knudsen number which performed best. The size scale of the unit cell should be taken from the largest particle size scale for PS, SG and GS. That means agglomerate size for PS, aggregate size for SG and the simple (primary) particle size for GS. One exception is FS, which is best calculated using the aggregate size, even though FS tends to form large agglomerates. The size scale that is decisive for the heat transport does not seem to be that of the agglomerates but that of the aggregates. This behavior can be explained by the unusual structure of FS and makes clear why fumed silica is usually preferred in the production of vacuum insulation panels instead of the cheaper precipitated silica, despite similar porosity and particle size. In most of the cases it can be recommended to use the pore size distribution to calculate the gas thermal conductivity if it is available. Additionally, it can be helpful to use the pore size correction which is shown in Eq. (15) in some cases. If the pore size distribution is not available, the particle size with Kozeny's correction (Eq. 14) can be used instead. If so, it is advisable to use the aggregate size for PS and the primary particle size for FS and SG.

The study has shown that different models for calculating thermal conductivities have their justification because different models fit best for different materials. Fig. 12 shows a scheme for one potential selection of models for different silica based materials recommended by the authors of the study. If one follows the advice given in this paper, gas pressure-dependent thermal conductivities of silica-based porous materials can be predicted with fairly good accuracy in most cases. The knowledge can be used in the development of new thermal insulation or in all other areas where the thermal conductivity of porous media in combination with a Knudsen gas is of interest.

Declaration of Competing Interest

The authors declare that they have no known competing financial interests or personal relationships that could have appeared to influence the work reported in this paper.

Acknowledgments

Appendix A. Pore size distributions

Taking a closer look at the pore size distributions which are shown in Fig. A.1 one can see the different pore structures of the materials. It is evident that different materials, even from the same material group, can show a significant difference in the position of the pore peak even if porosity and thermal conductivity only differ slightly. In the case of PS two samples (PS.Gr.02 and PS.Gr.05) show a peak in the size scale of the aggregates and the other four in the primary particle size scale. Nevertheless, they do not have much in common in terms of porosity or thermal conductivity. This shows that it can lead to inaccuracies to use the peak size only for the calculation of the GTC. Instead, the whole distribution should be taken into account if possible. Furthermore, the narrow distribution of the glass beads is striking. From this, it can be seen that the pile structure is fundamentally different from the other materials.
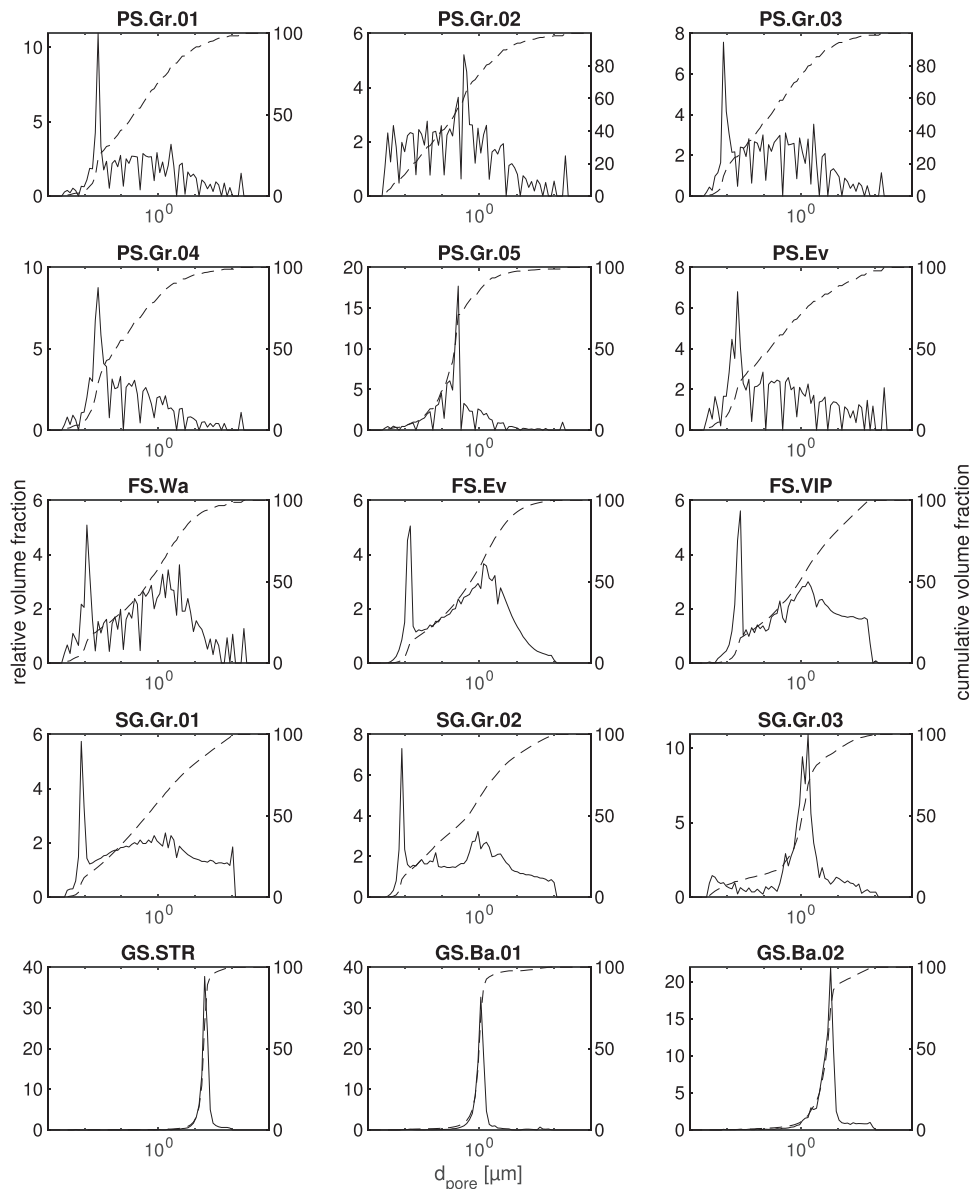

Fig. A1. Pore size distributions of all materials investigated, measured with mercury intrusion porosimetry. The primary and secondary axes represent the relative and the cumulative volume fraction and are plotted in solid and dashed lines respectively. The x-axis shows the pore sizes in μm.

Appendix B. Favorites of model combinations

Table B1
Over all favorites - three GTC model combinations with the lowest $\overline{S_{all}}$ values for every ETC model.

		α	β	x	$\overline{S_{all}}$
Russel	1	Goodman	Eq. (5)	$d_{dist} * \frac{\pi}{6}$	0.2003
	2	Goodman	Eq. (4)	$d_{dist} * \frac{\pi}{6}$	0.2012
	3	Baule	Eq. (2)	d_{dist}	0.2014
Maxwell	1	Song	Eq. (2)	$d_{dist} * \frac{\pi}{6}$	0.2092
	2	Song	Eq. (6)	$d_{dist} * \frac{\pi}{6}$	0.2092
	3	Baule	Eq. (5)	d_{dist}	0.2095
Scaling Model	1	Baule	Eq. (6)	$d_{dist} * \frac{\pi}{6}$	0.2206
	2	Baule	Eq. (2)	$d_{dist} * \frac{\pi}{6}$	0.2207
	3	Goodman	Eq. (2)	$d_{dist} * \frac{\pi}{6}$	0.2223
Sphere model 1	1	Baule	Eq. (5)	$d_{dist} * \frac{\pi}{6}$	0.2476
	2	Baule	Eq. (4)	$d_{dist} * \frac{\pi}{6}$	0.2480
	3	Goodman	Eq. (5)	$d_{dist} * \frac{\pi}{6}$	0.2488
Schumann and Voss	1	Baule	Eq. (5)	$d_{dist} * \frac{\pi}{6}$	0.2132
	2	Baule	Eq. (4)	$d_{dist} * \frac{\pi}{6}$	0.2139
	3	Goodman	Eq. (5)	$d_{dist} * \frac{\pi}{6}$	0.2166
Luikov	1	Baule	Eq. (2)	$d_{dist} * \frac{\pi}{6}$	0.4382
	2	Baule	Eq. (6)	$d_{dist} * \frac{\pi}{6}$	0.4427
	3	Goodman	Eq. (2)	$d_{dist} * \frac{\pi}{6}$	0.5018
Zehner, Bauer, Schlünder	1	Baule	Eq. (6)	$d_{dist} * \frac{\pi}{6}$	0.2667
	2	Baule	Eq. (2)	$d_{dist} * \frac{\pi}{6}$	0.2669
	3	Goodman	Eq. (2)	$d_{dist} * \frac{\pi}{6}$	0.2670
Sphere model 2 **primary particles**	1	Kaganer	Eq. (5)	d_{dist}	0.2285
	2	Bauer	Eq. (2)	d_{dist}	0.2287
	3	Bauer	Eq. (6)	d_{dist}	0.2287
Sphere model 2 **aggregates**	1	Bauer	Eq. (6)	d_{dist}	0.1849
	2	Kaganer	Eq. (5)	d_{dist}	0.1850
	3	Bauer	Eq. (2)	d_{dist}	0.1851
Sphere model 2 **agglomerate**	1	Bauer	Eq. (6)	d_{peak}	0.1860
	2	Bauer	Eq. (2)	d_{peak}	0.1863
	3	Kaganer	Eq. (5)	d_{peak}	0.1870
Zehner, Schlünder **primary particles**	1	Kaganer	Eq. (3)	d_{dist}	0.3608
	2	Bauer	Eq. (3)	d_{dist}	0.3629
	3	Song	Eq. (3)	d_{dist}	0.3630
Zehner, Schlünder **aggregates**	1	Kaganer	Eq. (2)	d_{dist}	0.3272
	2	Kaganer	Eq. (6)	d_{dist}	0.3273
	3	Kaganer	Eq. (3)	$d_{dist} * \frac{\pi}{6}$	0.3274
Zehner, Schlünder **agglomerate**	1	Kaganer	Eq. (2)	d_{peak}	0.4790
	2	Kaganer	Eq. (6)	d_{peak}	0.4790
	3	Kaganer	Eq. (3)	$d_{peak} * \frac{\pi}{6}$	0.4790
Slavin **primary particles**	1	Baule		d_{peak}	0.6675
	2	Baule		d_{dist}	0.6675
	3	Baule		$d_{peak} * \frac{\pi}{6}$	0.6675
Slavin **aggregates**	1	Baule		d_{peak}	0.4759
	2	Baule		d_{dist}	0.4759
	3	Baule		$d_{peak} * \frac{\pi}{6}$	0.4759
Slavin **agglomerate**	1	Baule		d_{peak}	0.5151
	2	Baule		d_{dist}	0.5151
	3	Baule		$d_{peak} * \frac{\pi}{6}$	0.5151

Table B2

Precipitated silica favorites - three GTC model combinations with the lowest $\overline{S_{PS}}$ values for every ETC model.

		α	β	x	$\overline{S_{PS}}$
Russel	1	Kaganer	Eq. (4)	d_{dist}	0.1567
	2	Bauer	Eq. (5)	D_{aggr} + KC	0.1581
	3	Kaganer	Eq. (3)	d_{dist}	0.1583
Maxwell	1	Bauer	Eq. (3)	D_{aggr} + KC	0.1432
	2	Song	Eq. (3)	D_{aggr} + KC	0.1507
	3	Bauer	Eq. (4)	D_{aggr} + KC	0.1511
Scaling Model	1	Goodman	Eq. (3)	d_{dist}	0.1551
	2	Kaganer	Eq. (4)	$d_{dist} * \frac{\pi}{6}$	0.1558
	3	Goodman	Eq. (4)	d_{dist}	0.1561
Sphere model 1	1	Bauer	Eq. (3)	D_{aggr} + KC	0.1415
	2	Bauer	Eq. (4)	D_{aggr} + KC	0.1524
	3	Song	Eq. (3)	D_{aggr} + KC	0.1528
Schumann and Voss	1	Bauer	Eq. (5)	D_{aggr} + KC	0.1403
	2	Song	Eq. (4)	D_{aggr} + KC	0.1423
	3	Song	Eq. (5)	D_{aggr} + KC	0.1467
Luikov	1	Baule	Eq. (2)	$d_{dist} * \frac{\pi}{6}$	0.1927
	2	Baule	Eq. (6)	$d_{dist} * \frac{\pi}{6}$	0.1941
	3	Goodman	Eq. (2)	$d_{dist} * \frac{\pi}{6}$	0.2130
Zehner, Bauer, Schlünder	1	Bauer	Eq. (4)	D_{aggr} + KC	0.1382
	2	Bauer	Eq. (3)	D_{aggr} + KC	0.1407
	3	Song	Eq. (3)	D_{aggr} + KC	0.1416
Sphere model 2	1	Bauer	Eq. (3)	D_{aggr} + KC	0.2140
primary particles	2	Song	Eq. (3)	D_{aggr} + KC	0.2283
	3	Bauer	Eq. (4)	D_{aggr} + KC	0.2290
Sphere model 2	1	Bauer	Eq. (3)	D_{aggr} + KC	0.1954
aggregates	2	Bauer	Eq. (3)	d_{dist}	0.2062
	3	Song	Eq. (3)	D_{aggr} + KC	0.2101
Sphere model 2	1	Bauer	Eq. (4)	d_{peak}	0.1051
agglomerate	2	Bauer	Eq. (3)	$d_{peak} * \frac{\pi}{6}$	0.1058
	3	Bauer	Eq. (3)	d_{peak}	0.1064
Zehner, Schlünder	1	Baule	Eq. (2)	D_{aggl} + KC	0.2073
primary particles	2	Baule	Eq. (6)	D_{aggl} + KC	0.2089
	3	Goodman	Eq. (2)	D_{aggl} + KC	0.2280
Zehner, Schlünder	1	Bauer	Eq. (3)	D_{aggr} + KC	0.1908
aggregates	2	Bauer	Eq. (3)	d_{dist}	0.1952
	3	Song	Eq. (3)	D_{aggr} + KC	0.1998
Zehner, Schlünder	1	Kaganer	Eq. (3)	d_{peak}	0.2904
agglomerate	2	Kaganer	Eq. (4)	d_{peak}	0.2914
	3	Song	Eq. (3)	d_{peak}	0.2916
Slavin	1	Bauer		d_{peak}	0.4384
primary particles	2	Bauer		d_{dist}	0.4384
	3	Bauer		$d_{peak} * \frac{\pi}{6}$	0.4384
Slavin	1	Bauer		d_{peak}	0.4294
aggregates	2	Bauer		d_{dist}	0.4294
	3	Bauer		$d_{peak} * \frac{\pi}{6}$	0.4294
Slavin	1	Baule		d_{peak}	0.4805
agglomerate	2	Baule		d_{dist}	0.4805
	3	Baule		$d_{peak} * \frac{\pi}{6}$	0.4805

Table B3
Fumed silica favorites - three GTC model combinations with the lowest $\overline{S_{FS}}$ values for every ETC model.

		α	β	x	$\overline{S_{FS}}$
Russel	1	Baule	Eq. (2)	$d_{dist} * \frac{\pi}{6}$	0.1020
	2	Baule	Eq. (6)	$d_{dist} * \frac{\pi}{6}$	0.1032
	3	Goodman	Eq. (2)	$d_{dist} * \frac{\pi}{6}$	0.1221
Maxwell	1	Baule	Eq. (5)	$d_{dist} * \frac{\pi}{6}$	0.0944
	2	Goodman	Eq. (6)	$d_{dist} * \frac{\pi}{6}$	0.0945
	3	Goodman	Eq. (2)	$d_{dist} * \frac{\pi}{6}$	0.0949
Scaling Model	1	Baule	Eq. (2)	$d_{dist} * \frac{\pi}{6}$	0.1119
	2	Baule	Eq. (6)	$d_{dist} * \frac{\pi}{6}$	0.1130
	3	Bauer	Eq. (5)	D_{prim} + KC	0.1228
Sphere model 1	1	Baule	Eq. (5)	$d_{dist} * \frac{\pi}{6}$	0.0951
	2	Baule	Eq. (2)	d_{dist}	0.0957
	3	Goodman	Eq. (5)	$d_{dist} * \frac{\pi}{6}$	0.0959
Schumann and Voss	1	Baule	Eq. (2)	$d_{dist} * \frac{\pi}{6}$	0.0951
	2	Baule	Eq. (6)	$d_{dist} * \frac{\pi}{6}$	0.0958
	3	Goodman	Eq. (2)	$d_{dist} * \frac{\pi}{6}$	0.1090
Luikov	1	Baule	Eq. (5)	D_{prim} + KC	0.1363
	2	Baule	Eq. (4)	D_{prim} + KC	0.1369
	3	Goodman	Eq. (6)	D_{prim} + KC	0.1396
Zehner, Bauer, Schlünder	1	Goodman	Eq. (6)	$d_{dist} * \frac{\pi}{6}$	0.0931
	2	Goodman	Eq. (2)	$d_{dist} * \frac{\pi}{6}$	0.0932
	3	Baule	Eq. (5)	$d_{dist} * \frac{\pi}{6}$	0.0960
Sphere model 2	1	Goodman	Eq. (3)	$d_{dist} * \frac{\pi}{6}$	0.1038
primary particles	2	Song	Eq. (2)	$d_{dist} * \frac{\pi}{6}$	0.1041
	3	Kaganer	Eq. (6)	$d_{dist} * \frac{\pi}{6}$	0.1041
Sphere model 2	1	Kaganer	Eq. (6)	$d_{dist} * \frac{\pi}{6}$	0.0988
aggregates	2	Goodman	Eq. (3)	$d_{dist} * \frac{\pi}{6}$	0.0989
	3	Kaganer	Eq. (2)	$d_{dist} * \frac{\pi}{6}$	0.0992
Sphere model 2	1	Baule	Eq. (2)	d_{peak}	0.1187
agglomerate	2	Baule	Eq. (2)	$d_{peak} * \frac{\pi}{6}$	0.1188
	3	Baule	Eq. (6)	d_{peak}	0.1198
Zehner, Schlünder	1	Baule	Eq. (3)	d_{dist}	0.0986
primary particles	2	Kaganer	Eq. (4)	$d_{dist} * \frac{\pi}{6}$	0.1003
	3	Kaganer	Eq. (5)	$d_{dist} * \frac{\pi}{6}$	0.1004
Zehner, Schlünder	1	Kaganer	Eq. (2)	$d_{dist} * \frac{\pi}{6}$	0.0919
aggregates	2	Kaganer	Eq. (6)	$d_{dist} * \frac{\pi}{6}$	0.0920
	3	Goodman	Eq. (3)	$d_{dist} * \frac{\pi}{6}$	0.0928
Zehner, Schlünder	1	Song	Eq. (3)	d_{peak}	0.7584
agglomerate	2	Kaganer	Eq. (3)	d_{peak}	0.7585
	3	Bauer	Eq. (3)	d_{peak}	0.7588
Slavin	1	Bauer		d_{peak}	0.3411
primary particles	2	Bauer		d_{dist}	0.3411
	3	Bauer		$d_{peak} * \frac{\pi}{6}$	0.3411
Slavin	1	Bauer		d_{peak}	0.3345
aggregates	2	Bauer		d_{dist}	0.3345
	3	Bauer		$d_{peak} * \frac{\pi}{6}$	0.3345
Slavin	1	Baule		d_{peak}	0.5514
agglomerate	2	Baule		d_{dist}	0.5514
	3	Baule		$d_{peak} * \frac{\pi}{6}$	0.5514

Table B4
Silica gel favorites - three GTC model combinations with the lowest $\overline{S_{SG}}$ values for every ETC model.

		α	β	x	$\overline{S_{SG}}$
Russel	1	Kaganer	Eq. (5)	d_{dist}	0.1567
	2	Song	Eq. (3)	$d_{dist} * \frac{\pi}{6}$	0.1573
	3	Song	Eq. (6)	d_{dist}	0.1580
Maxwell	1	Kaganer	Eq. (3)	d_{dist}	0.1779
	2	Song	Eq. (3)	d_{dist}	0.1798
	3	Kaganer	Eq. (4)	d_{dist}	0.1834
Scaling Model	1	Goodman	Eq. (2)	d_{dist}	0.1317
	2	Goodman	Eq. (6)	d_{dist}	0.1319
	3	Goodman	Eq. (3)	$d_{dist} * \frac{\pi}{6}$	0.1322
Sphere model 1	1	Kaganer	Eq. (5)	d_{dist}	0.1919
	2	Kaganer	Eq. (4)	d_{dist}	0.1922
	3	Song	Eq. (3)	$d_{dist} * \frac{\pi}{6}$	0.1931
Schumann and Voss	1	Kaganer	Eq. (3)	$d_{dist} * \frac{\pi}{6}$	0.1654
	2	Kaganer	Eq. (6)	d_{dist}	0.1656
	3	Kaganer	Eq. (2)	d_{dist}	0.1659
Luikov	1	Baule	Eq. (2)	$d_{dist} * \frac{\pi}{6}$	0.1565
	2	Baule	Eq. (6)	$d_{dist} * \frac{\pi}{6}$	0.1584
	3	Goodman	Eq. (2)	$d_{dist} * \frac{\pi}{6}$	0.1910
Zehner, Bauer, Schlünder	1	Kaganer	Eq. (3)	$d_{dist} * \frac{\pi}{6}$	0.1762
	2	Kaganer	Eq. (6)	d_{dist}	0.1767
	3	Goodman	Eq. (3)	d_{dist}	0.1768
Sphere model 2 primary particles	1	Baule	Eq. (2)	D_{aggl} + KC	0.2528
	2	Baule	Eq. (2)	D_{aggr} + KC	0.2528
	3	Baule	Eq. (6)	D_{aggl} + KC	0.2542
Sphere model 2 aggregates	1	Bauer	Eq. (3)	$d_{dist} * \frac{\pi}{6}$	0.0867
	2	Song	Eq. (3)	$d_{dist} * \frac{\pi}{6}$	0.0901
	3	Song	Eq. (3)	d_{dist}	0.0906
Sphere model 2 agglomerate					
Zehner, Schlünder primary particles	1	Baule	Eq. (2)	D_{aggl} + KC	0.2419
	2	Baule	Eq. (2)	D_{aggr} + KC	0.2419
	3	Baule	Eq. (6)	D_{aggr} + KC	0.2424
Zehner, Schlünder aggregates	1	Kaganer	Eq. (3)	D_{prim} + KC	0.2315
	2	Bauer	Eq. (3)	D_{prim} + KC	0.2315
	3	Song	Eq. (3)	D_{prim} + KC	0.2334
Zehner, Schlünder agglomerate					
Slavin primary particles	1	Bauer		d_{peak}	0.4889
	2	Bauer		d_{dist}	0.4889
	3	Bauer		$d_{peak} * \frac{\pi}{6}$	0.4889
Slavin aggregates	1	Baule		d_{peak}	0.5983
	2	Baule		d_{dist}	0.5983
	3	Baule		$d_{peak} * \frac{\pi}{6}$	0.5983
Slavin agglomerate					

Table B5
Glass spheres favorites - three GTC model combinations with the lowest $\overline{S_{GS}}$ values for every ETC model.

		α	β	x	$\overline{S_{GS}}$
Russel	1	Baule	Eq. (5)	$d_{dist} * \frac{\pi}{6}$	0.1450
	2	Baule	Eq. (4)	$d_{dist} * \frac{\pi}{6}$	0.1482
	3	Goodman	Eq. (5)	$d_{dist} * \frac{\pi}{6}$	0.1511
Maxwell	1	Baule	Eq. (2)	D_{aggl} + KC	0.1274
	2	Baule	Eq. (2)	D_{aggr} + KC	0.1274
	3	Baule	Eq. (2)	D_{prim} + KC	0.1274
Scaling Model	1	Baule	Eq. (2)	$d_{dist} * \frac{\pi}{6}$	0.3123
	2	Baule	Eq. (6)	$d_{dist} * \frac{\pi}{6}$	0.3158
	3	Baule	Eq. (2)	$d_{peak} * \frac{\pi}{6}$	0.3387
Sphere model 1	1	Baule	Eq. (2)	$d_{dist} * \frac{\pi}{6}$	0.2121
	2	Baule	Eq. (6)	$d_{dist} * \frac{\pi}{6}$	0.2144
	3	Baule	Eq. (2)	$d_{peak} * \frac{\pi}{6}$	0.2212
Schumann and Voss	1	Baule	Eq. (2)	$d_{dist} * \frac{\pi}{6}$	0.1954
	2	Baule	Eq. (6)	$d_{dist} * \frac{\pi}{6}$	0.1973
	3	Baule	Eq. (2)	$d_{peak} * \frac{\pi}{6}$	0.2017
Luikov	1	Baule	Eq. (2)	$d_{peak} * \frac{\pi}{6}$	1.3121
	2	Baule	Eq. (6)	$d_{peak} * \frac{\pi}{6}$	1.3258
	3	Baule	Eq. (2)	$d_{dist} * \frac{\pi}{6}$	1.3577
Zehner, Bauer, Schlünder	1	Baule	Eq. (2)	$d_{dist} * \frac{\pi}{6}$	0.3360
	2	Baule	Eq. (6)	$d_{dist} * \frac{\pi}{6}$	0.3398
	3	Baule	Eq. (2)	$d_{peak} * \frac{\pi}{6}$	0.3432
Sphere model 2	1	Song	Eq. (6)	D_{prim} + KC	0.1185
primary particles	2	Song	Eq. (2)	D_{prim} + KC	0.1186
	3	Bauer	Eq. (2)	D_{prim} + KC	0.1204
Sphere model 2 aggregates					
Sphere model 2 agglomerate					
Zehner, Schlünder	1	Baule	Eq. (2)	$d_{peak} * \frac{\pi}{6}$	0.7804
primary particles	2	Baule	Eq. (6)	$d_{peak} * \frac{\pi}{6}$	0.7805
	3	Baule	Eq. (2)	$d_{dist} * \frac{\pi}{6}$	0.7807
Zehner, Schlünder aggregates					
Zehner, Schlünder agglomerate					
Slavin	1	Baule		d_{peak}	1.5975
primary particles	2	Baule		d_{dist}	1.5975
	3	Baule		$d_{peak} * \frac{\pi}{6}$	1.5975
Slavin aggregates					
Slavin agglomerate					

Supplementary material

Supplementary material associated with this article can be found, in the online version, at doi:10.1016/j.ijheatmasstransfer.2022.122519

References

[1] M. Alam, H. Singh, M.C. Limbachiya, Vacuum insulation panels (VIPs) for building construction industry – a review of the contemporary developments and future directions, Appl Energy 88 (11) (2011) 3592–3602, doi:10.1016/j.apenergy.2011.04.040.

[2] J. Fricke, U. Heinemann, H.P. Ebert, Vacuum insulation panels - from research to market, Vacuum 82 (7) (2008) 680–690, doi:10.1016/j.vacuum.2007.10.014.

[3] S.E. Wood, A mechanistic model for the thermal conductivity of planetary regolith: 1. the effects of particle shape, composition, cohesion, and compression at depth, Icarus 352 (2020) 113964, doi:10.1016/j.icarus.2020.113964.

[4] E.S. Huetter, N.I. Koemle, G. Kargl, E. Kaufmann, Determination of the effective thermal conductivity of granular materials under varying pressure conditions, Journal of Geophysical Research: Planets 113 (E12) (2008), doi:10.1029/2008JE003085.

[5] J. Ross-Jones, M. Gaedtke, S. Sonnick, M. Rädle, H. Nirschl, M.J. Krause, Conjugate heat transfer through nano scale porous media to optimize vacuum insulation panels with lattice boltzmann methods, Computers & Mathematics with Applications (2018), doi:10.1016/j.camwa.2018.09.023.

[6] J. Ross-Jones, M. Gaedtke, S. Sonnick, M. Meier, M. Rädle, H. Nirschl, M.J. Krause, Pore-scale conjugate heat transfer simulations using lattice boltz-

mann methods for industrial applications, Appl Therm Eng 182 (2021) 116073, doi:10.1016/j.applthermaleng.2020.116073.

[7] M. Wang, J. Wang, N. Pan, S. Chen, Mesoscopic predictions of the effective thermal conductivity for microscale random porous media, Physical Review E 75 (3) (2007) 036702, doi:10.1103/PhysRevE.75.036702. Publisher: American Physical Society

[8] S.-L. Wang, Z. Jin, J.-N. Li, B.-X. Zhang, Y.-B. Wang, Y.-R. Yang, X.-D. Wang, D.-J. Lee, Theoretical modeling of thermal conductivity of alumina aerogel composites based on real microstructures, J. Taiwan Inst. Chem. Eng. 120 (2021) 150–160, doi:10.1016/j.jtice.2021.03.003.

[9] B. Yu, P. Cheng, Fractal models for the effective thermal conductivity of bidispersed porous media, J. Thermophys Heat Transfer 16 (1) (2002) 22–29, doi:10.2514/2.6669. Publisher: American Institute of Aeronautics and Astronautics

[10] A.P. Senthil Kumar, V. Prabhu Raja, P. Karthikeyan, Comparison of geometry dependent resistance models with conventional models for estimation of effective thermal conductivity of two-phase materials, Heat Mass Transfer 46 (11) (2010) 1379–1394, doi:10.1007/s00231-010-0660-0.

[11] E. Tsotsas, H. Martin, Thermal conductivity of packed beds: a review, Chem. Eng. Process. 22 (1) (1987) 19–37, doi:10.1016/0255-2701(87)80025-9.

[12] S. Parzinger, Analytische Modellierung der temperatur- und gasdruckabhängigen effektiven Wärmeleitfähigkeit von Pulvern, Technical University Munich, 2014 Ph.D. thesis.

[13] H.T. Aichlmayr, F.A. Kulacki, The Effective Thermal Conductivity of Saturated Porous Media, in: G.A. Greene, J.P. Hartnett†, A. Bar-Cohen, Y.I. Cho (Eds.), Advances in Heat Transfer, volume 39, Elsevier, 2006, pp. 377–460, doi:10.1016/S0065-2717(06)39004-1.

[14] H. Bjurström, E. Karawacki, B. Carlsson, Thermal conductivity of a microporous particulate medium: moist silica gel, Int J Heat Mass Transf 27 (11) (1984) 2025–2036, doi:10.1016/0017-9310(84)90189-3.

[15] A.V. Luikov, A.G. Shashkov, L.L. Vasiliev, Y.E. Fraiman, Thermal conductivity of porous systems, Int J Heat Mass Transf 11 (2) (1968) 117–140, doi:10.1016/0017-9310(68)90144-0.

[16] S. Jayachandran, K.S. Reddy, Estimation of effective thermal conductivity of packed beds incorporating effects of primary and secondary parameters, Thermal Science and Engineering Progress 11 (2019) 392–408, doi:10.1016/j.tsep.2018.12.011.

[17] M. Bouquerel, T. Duforestel, D. Baillis, G. Rusaouen, Heat transfer modeling in vacuum insulation panels containing nanoporous silicas - a review, Energy Build 54 (2012) 320–336, doi:10.1016/j.enbuild.2012.07.034.

[18] C. Huang, G. Wei, L. Cui, Z. Zhou, X. Du, Gaseous thermal conductivity studies on mesoporous silica particles based on a bimodal-pore distribution model, Int. J. Therm. Sci. 160 (2021) 106668, doi:10.1016/j.ijthermalsci.2020.106668.

[19] M. Meier, S. Sonnick, E. Asylbekov, M. Rädle, H. Nirschl, Multi-scale characterization of precipitated silica, Powder Technol 354 (2019) 45–51, doi:10.1016/j.powtec.2019.05.072.

[20] M. Meier, Über den Entstehungsprozess poröser Strukturen am Beispiel der Partikelbildung von kolloidalem Silika und der Haufwerksbildung von gefällter Kieselsäure, Karlsruhe Institute of Technology, 2021 Ph.D. thesis.

[21] S. Pramanik, A. Manna, A. Tripathy, K.K. Kar, Current Advancements in Ceramic Matrix Composites, in: K.K. Kar (Ed.), Composite Materials, Springer Berlin Heidelberg, Berlin, Heidelberg, 2017, pp. 457–496, doi:10.1007/978-3-662-49514-8_14.

[22] E.H. Ratcliffe, Thermal conductivities of fused and crystalline quartz, Br. J. Appl. Phys. 10 (1) (1959) 22–25, doi:10.1088/0508-3443/10/1/306.

[23] Sovitec, Sovitec_msds_en_omicron_p0, 2016, https://www.sovitec.com/sites/default/files/2016-05/Sovitec_MSDS_En_Omicron_P0.pdf.

[24] S. Sonnick, M. Meier, J. Ross-Jones, L. Erlbeck, I. Medina, H. Nirschl, M. Rädle, Correlation of pore size distribution with thermal conductivity of precipitated silica and experimental determination of the coupling effect, Appl Therm Eng (2019), doi:10.1016/j.applthermaleng.2019.01.074.

[25] P.A. Chambre, S.A. Schaaf, Flow of rarefied gases, Princeton University Press, 2017.

[26] E.H. Kennard, Kinetic theory of gases, volume 483, McGraw-hill New York, 1938.

[27] P.W. Atkins, J.d. Paula, Wärmeleitung, in: Physikalische Chemie, John Wiley & Sons, 2006, pp. 672–673.

[28] R.S. Prasolov, Generalization of the equation of the thermal conductivity of gases, Izv. VUZ'ov, Priborostr. (1961).

[29] M.G. Kaganer, Thermal insulation in cryogenic engineering, Israel Program for Scientific Translations, 1969. http://cds.cern.ch/record/103864

[30] S.Q. Zeng, A. Hunt, R. Greif, Mean free path and apparent thermal conductivity of a gas in a porous medium, J Heat Transfer 117 (3) (1995) 758–761, doi:10.1115/1.2822642.

[31] J. Fricke, X. Lu, P. Wang, D. Büttner, U. Heinemann, Optimization of monolithic silica aerogel insulants, Int J Heat Mass Transf 35 (9) (1992) 2305–2309, doi:10.1016/0017-9310(92)90073-2.

[32] O. Krischer, Die Grundlagen der Wärmeübertragung, in: O. Krischer, W. Kast (Eds.), Trocknungstechnik: Die wissenschaftlichen Grundlagen der Trocknungstechnik, Springer, Berlin, Heidelberg, 1978, pp. 68–168, doi:10.1007/978-3-642-61879-6_5.

[33] N. Wakao, S. Kagei, Heat and mass transfer in packed beds, Taylor & Francis, 1982.

[34] P. Zehner, E.U. Schlünder, Einfluß der wärmestrahlung und des druckes auf den wärmetransport in nicht durchströmten schüttungen, Chem. Ing. Tech. 44 (23) (1972) 1303–1308, doi:10.1002/cite.330442305.

[35] K. Denpoh, Modeling of rarefied gas heat conduction between wafer and susceptor, IEEE Trans. Semicond. Manuf. 11 (1) (1998) 25–29, doi:10.1109/66.661281.

[36] K. Swimm, S. Vidi, G. Reichenauer, H.P. Ebert, Coupling of gaseous and solid thermal conduction in porous solids, J Non Cryst Solids 456 (2017) 114–124, doi:10.1016/j.jnoncrysol.2016.11.012.

[37] J.F. Guo, G.H. Tang, A theoretical model for gas-contributed thermal conductivity in nanoporous aerogels, Int J Heat Mass Transf 137 (2019) 64–73, doi:10.1016/j.ijheatmasstransfer.2019.03.106.

[38] B. Baule, Theoretische behandlung der erscheinungen in verdünnten gasen, Ann Phys 349 (9) (1914) 145–176, doi:10.1002/andp.19143490908.

[39] F.O. Goodman, H.Y. Wachman, Formula for thermal accommodation coefficients, J. Chem. Phys. 46 (1967) 12.

[40] S. Song, M.M. Yovanovich, Correlation of thermal accommodation coefficient for 'engineering' surfaces, ASME HTD 69 (1987) 107–116. http://www.mhtl.uwaterloo.ca/old/paperlib/papers/contact/gap_cond/engineer.pdf

[41] R. Bauer, Effektive radiale wärmeleitfähigkeit gasdurchströmter schüttungen mit partikeln unterschiedlicher form und größenverteilung: Mit 7 tafeln, VDI-Verl., Düsseldorf, 1977.

[42] G.M. Kremer, Basic Principles of the Kinetic Theory, in: G.M. Kremer (Ed.), An Introduction to the Boltzmann Equation and Transport Processes in Gases, Springer, Berlin, Heidelberg, 2010, pp. 1–35, doi:10.1007/978-3-642-11696-4_1.

[43] C.W. Kosten, The mean free path in room acoustics, Acta Acustica united with Acustica 10 (4) (1960) 245–250.

[44] S.V. Belov, O.G. Kartuesov, V.M. Polyaev, Mean pore size of porous metals, Soviet Powder Metallurgy and Metal Ceramics 11 (1972) 733–734, doi:10.1007/BF00801273.

[45] S. Sonnick, M. Meier, G. Ünsal Peter, L. Erlbeck, H. Nirschl, M. Rädle, Thermal accommodation in nanoporous silica for vacuum insulation panels, International Journal of Thermofluids 1–2 (2020) 100012, doi:10.1016/j.ijft.2019.100012.

[46] X. Lu, R. Caps, J. Fricke, C.T. Alviso, R.W. Pekala, Correlation between structure and thermal conductivity of organic aerogels, J Non Cryst Solids 188 (3) (1995) 226–234, doi:10.1016/0022-3093(95)00191-3.

[47] Z. Kovács, S. Szanyi, I. Budai, K. Lakatos, Laboratory Tests of High-Performance Thermal Insulations, in: J. Littlewood, R.J. Howlett, A. Capozzoli, L.C. Jain (Eds.), Sustainability in Energy and Buildings, Springer Singapore, Singapore, 2020, pp. 73–82.

[48] H.W. Russell, Principles of heat flow in porous insulators, J. Am. Ceram. Soc. 18 (1) (1935) 1–5, doi:10.1111/j.1151-2916.1935.tb19340.x.

[49] J.C. Maxwell, A treatise on electricity and magnetism, volume 1, Oxford: Clarendon Press, 1873.

[50] G.R. Cunnington, C.L. Tien, Heat Transfer in Microsphere Insulation in the Presence of a Gas, in: V.V. Mirkovich (Ed.), Thermal Conductivity 15, Springer US, Boston, MA, 1978, pp. 325–333, doi:10.1007/978-1-4615-9083-5_39.

[51] K.H. Brodt, Thermal insulations Cfc - alternatives and vacuum insulation, Technische Universiteit Delft, 1995 Ph.D. thesis. https://repository.tudelft.nl/islandora/object/uuid%3Abc13442-c6c0-4ded-8948-3e65518ab305

[52] R.G. Deissler, C.S. Eian, Investigation of effective thermal conductivities of powders, National Advisory Committee for Aeronautics (1952).

[53] D. Kunii, J.M. Smith, Heat transfer characteristics of porous rocks: II. thermal conductivities of unconsolidated particles with flowing fluids, AlChE J. 7 (1) (1961) 29–34, doi:10.1002/aic.690070109.

[54] M. Matsushita, M. Monde, Y. Mitsutake, Predictive calculation of the effective thermal conductivity in a metal hydride packed bed, Int J Hydrogen Energy 39 (18) (2014) 9718–9725, doi:10.1016/j.ijhydene.2014.04.072.

[55] T. Schumann, V. Voss, Heat flow through granulated material, Fuel 13 (8) (1934) 249–256.

[56] P. Zehner, E.U. Schlünder, Wärmeleitfähigkeit von schüttungen bei mäßigen temperaturen, Chem. Ing. Tech. 42 (14) (1970) 933–941, doi:10.1002/cite.330421408.

[57] S.S. Sih, J.W. Barow, The prediction of the emissivity and thermal conductivity of powder beds, Part. Sci. Technol. 22 (4) (2004) 427–440, doi:10.1080/02726350490501682. Publisher: Taylor & Francis

[58] K. Swimm, G. Reichenauer, S. Vidi, H.-P. Ebert, Gas pressure dependence of the heat transport in porous solids with pores smaller than 10 microns, Int J Thermophys 30 (4) (2009) 1329–1342, doi:10.1007/s10765-009-0617-z.

[59] A.J. Slavin, V. Arcas, C.A. Greenhalgh, E.R. Irvine, D.B. Marshall, Theoretical model for the thermal conductivity of a packed bed of solid spheroids in the presence of a static gas, with no adjustable parameters except at low pressure and temperature, Int J Heat Mass Transf 45 (20) (2002) 4151–4161, doi:10.1016/S0017-9310(02)00117-5.

[60] T. Feng, A. Rai, D. Hun, S.S. Shrestha, Molecular dynamics simulations of energy accommodation between gases and polymers for ultra-low thermal conductivity insulation, Int J Heat Mass Transf 164 (2021) 120459, doi:10.1016/j.ijheatmasstransfer.2020.120459.

[61] A.T. Rosenberger, E.B. Dale, D. Ganta, J.P. Rezac, Investigating properties of surfaces and thin films using microsphere whispering-gallery modes, in: Laser Resonators and Beam Control X, volume 6872, International Society for Optics and Photonics, 2008, p. 68720U, doi:10.1117/12.772655.

Chapter 7

Paper 4: *Silica-based core materials for thermal superinsulations in various applications*

In Chapter 6 (Paper 3), for the first time, specific recommendations could be made regarding which analytical models are most useful for the prediction of the gas pressure-dependent thermal conductivity of precipitated silicas, fumed silicas, silica gels, and micro glass spheres. This newly generated knowledge can be used in the development of superinsulations for various applications. With the computational models and input parameters appropriate for the different powders, the gas pressure-dependent thermal conductivity of the core materials can be predicted with an average accuracy of 10 %. This prediction requires only industry standard measured values and no complicated and time-consuming computer simulations. Furthermore, no adjustable fitting parameters are required. However, in the previous study, only the pressure-dependent gas thermal conductivity, including the coupling effect, was investigated. Solid thermal conductivity λ_s and radiation λ_r were combined in the value λ_{base} and taken from thermal conductivity measurements at low pressure levels.

For the design of new thermal superinsulations, all heat transfer mechanisms must be considered (i.e. also solid thermal conductivity and radiation). In the following paper, which explores the determination of the optimum product specifications of the investigated materials for superinsulations in various applications, they are calculated accordingly. For their determination, common and literature-known models were first tested for their applicability and finally combined with the λ_g models to perform parameter studies. Since the specific extinction coefficient E_m is required to calculate the radiation conductivity, spectroscopic investigations were carried out on the materials used. This resulted in mean specific extinction coefficients of 12.9 and 50.6 for pure silica powders and opacified silica, respectively. The E_m values are Rosseland

averages and were determined using Equation 2.6. For comparison, Hrubesh and Pekala [80] found a specific extinction coefficient of 22.7 for silica aerogel and 84.2 for opacified silica aerogel.

To calculate the solid thermal conductivity λ_s, a widely used model of Kaganer which is shown in Equation 2.12, based on the Hertz contact theory, was used. This requires not only the thermal conductivity of the particles and their mechanical properties but also the load applied to the powder. In VIPs, the difference between the internal pressure and the atmospheric pressure is applied to the core material. This corresponds to approximately 1 bar. For thermal conductivity measurements in the guarded hot plate (GHP) apparatus, the entire measurement chamber was vacuumed so that the load of the atmosphere was absorbed by the surrounding stainless-steel tank and did not apply to the samples. Thus, only the cold plate's own weight and an additional weight of a few kilograms to prevent gaps loaded the samples during the measurements. For the silica samples with high porosity, the measurements could nevertheless be reproduced well by the results calculated with 1 bar of external pressure load (i.e. $10 \frac{t}{m^2}$). By contrast, the solid thermal conductivities of the samples with lower porosities, especially the glass spheres, were greatly overestimated by the calculations due to the sample preparation. To produce a smooth surface, a homogeneous density, and optimal contact with the heating and cooling plates, the samples were pressed into shape before measurement. The materials were compressed under a pressure of approximately 5 bar. While this only resulted in a smooth surface for materials with smaller porosities, the materials with larger porosities were plastically deformed by this process. The reasons are explained in detail in this chapter (Paper 4). This leads to the fact that the compacts had an increased solid thermal conductivity even without a continuously acting load. Nevertheless, this behavior is desirable in the production of VIPs, since this cohesion enables the formation of stable sheets from the core material mixtures.

To consider the influence of the pore size distribution of the investigated materials without having to perform a mercury intrusion porosimetry (MIP) measurement for each calculation, a model was developed within the scope of the paper to estimate the pore size distribution of silica powders as a function of their porosity. The model takes into account that larger pores disappear first during mechanical compression of the powders, and it considers a threshold value under which the pores are not affected by the compression at all. The result of a single pore size distribution measurement is required as the input parameter for every material investigated. The measurement can be performed at any porosity (preferably in the middle of the study's range). Parameter studies to calculate the gas pressure-dependent effective thermal conductivity versus porosity and particle size for the materials could hence be conducted. While the pore size distribution of silica depends not only on the particle size

but also on many other factors (e.g. aggregate structure, van der Waals forces, electrostatic forces), the sizes of the voids in glass spheres are directly related to the particle size. This is evident in Paper 3, where the particle size converted with Kozeny's correction is recommended to calculate the gas thermal conductivity. It is even preferable to directly measure pore size by MIP for glass sphere beads. Accordingly, the pore size of the glass spheres was calculated using Kozeny's correction rather than the newly developed model.

A high number of models exist in the literature for λ_{eff} and λ_g and for the influencing parameters. In the this chapter (Paper 4), however, it was possible to use the favorable model combinations for the respective materials from the preliminary study [81]. To classify the results of the parameter studies, criteria for different applications of superinsulations were established and discussed accordingly. As a result, specific material recommendations are presented in Paper 4 for the construction sector, (medical) transport boxes, superinsulation at atmospheric pressure, and switchable VIPs.

RESEARCH ARTICLE

Silica-based core materials for thermal superinsulations in various applications

Sebastian Sonnick[1] 🄳 | Hermann Nirschl[2] | Matthias Rädle[1]

[1]Center for Mass Spectrometry and Optical Spectroscopy, Mannheim University of Applied Sciences, Mannheim, Germany

[2]Institute of Mechanical Process Engineering and Mechanics, Karlsruhe Institute of Technology, Karlsruhe, Germany

Correspondence
Sebastian Sonnick, Center for Mass Spectrometry and Optical Spectroscopy, Mannheim University of Applied Sciences, Paul-Wittsack-Straße 10, Mannheim 68163, Germany.
Email: s.sonnick@hs-mannheim.de

Summary

Vacuum insulation panels (VIP) are usually manufactured using standardized manufacturing processes based on empirical values and in most cases with any fumed silica as the main component of the core material. However, not all applications have the same requirements in terms of thermal conductivity and service life. Therefore, it is useful to adapt the kind of core materials and their product specifications, such as particle size and porosity, to the different applications. Furthermore, in some applications cheaper core materials, like precipitated silica, would be a reasonable alternative. To replace the time-consuming series of measurements for this purpose, this work offers comprehensive parameter studies to determine the optimum product properties of precipitated silica, fumed silica, silica gel, and glass spheres for use in the building sector, in transport boxes, as a superinsulation at atmospheric pressure, and as a switchable VIP. As a result, not only the preferred materials but also their porosities and particle sizes are presented. For atmospheric pressure and construction applications, fumed silica has to be preferred. For the transport sector and switchable VIPs as well as certain special applications, precipitated silica and silica gel may well be reasonable alternatives.

KEYWORDS

effective thermal conductivity, silica-based core materials, superinsulations, vacuum insulation panel

1 | INTRODUCTION

In times of climate change, efficient thermal insulation that is precisely tailored to the various applications is essential. The aim is not only to reduce the heat flux as much as possible but also to save space. With the goal to generate more usable volume in homes, transport boxes, heat storage units, or any other conceivable application, so-called superinsulations are becoming increasingly popular.[1] They are characterized by the fact that their

thermal conductivities are lower than that of resting air,[2] that is, less than $0.026 \frac{W}{mK}$. The most common superinsulations are vacuum insulation panels (VIP) and aerogels. The most widely used core material for VIPs is fumed silica.[3] However, since this material is very expensive and thus increases the overall price of the insulation, scientists are searching for viable alternatives.[4] For this purpose, inexpensive filler materials[5] or even waste materials[6] are added to the fumed silica to lower the price. However, alternative materials such as foams[7] or

fibers[8] are also being investigated and used in some cases.[9] Silica aerogel is the most promising material for atmospheric pressure superinsulation and is therefore intensively studied.[10] However, it is very high price makes it uneconomical for many applications. Therefore, this work also investigates alternative silica-based materials that may represent a cost advantage over traditionally used materials for both vacuum and atmospheric pressure applications. Glass fiber-based VIP cores are also a low-cost silica-based alternative.

They are primarily used for short-term applications. However, since the calculation models used in this work refer to particulate systems only, glass-fiber-based VIPs are not discussed. In addition to the physical and technical requirements, there is growing interest in sustainable[11] or oil-free alternative materials.[12] Insulation materials based on amorphous silica, such as fumed or precipitated silica, silica gel (silica xerogel), or sometimes even glass spheres can optimally meet these requirements. On the other hand, it is known from Resalati et al[13] that especially fumed silica has a very high environmental impact due to its energy-intensive production. Therefore, this work examines also alternative silica-based materials in more detail and, for the first time, recommendations are given for their product properties to be targeted for the various applications of superinsulations.

By definition, a superinsulator can only exist due to the so-called Knudsen effect. It states that the thermal conductivity of a gas, for example, in the pore of an insulating material, decreases significantly when the mean free path of the gas molecules becomes larger than the surrounding space, that is, the pore. The ratio of the mean free path length L to the size of the void space x is therefore called Knudsen number Kn. To achieve a significant reduction in thermal conductivity, either the gas pressure can be reduced or the pore size can be decreased. This effect is used, for example, in vacuum insulation panels. Here, porous, open-pore core material is formed into a panel shape and sealed under a vacuum using a barrier film. In some materials, such as some kinds of silica, the Knudsen effect is already achieved at atmospheric pressure, since at least some of the pores are of the same size as the mean free path of air molecules (approx. 68 nm). Although this fundamental relationship is clear since Knudsen,[14] the applicability of the corresponding analytical calculation models for real porous media is not yet fully understood.[15] Heat transfer in porous media is mainly composed of three mechanisms: gas thermal conductivity λ_g, solid thermal conductivity λ_s, and radiation λ_r. Moreover, a coupling λ_c between the above mechanisms must be considered which strongly depends on the microstructure of the materials. In particular, the ratio between gas thermal conductivity and the resulting coupling with the solid phase is difficult to capture for chaotic structures. It depends on the Knudsen number and can make the largest overall contribution to the total heat transfer. There are many different calculation models, especially for the gas and coupling contribution in the literature some of which give very different results.

Therefore, in their last publication,[16] the authors presented a selection guide for such models specifically for the material groups fumed silica (FS), precipitated silica (PS), silica gel (SG), and glass spheres (GS). From a total of 2800 possible combinations of analytical models for the calculation of the effective thermal conductivity and the gas thermal conductivity, the one with the best agreement with the measurement results was determined. Thus, it is possible to predict the gas pressure-dependent thermal conductivity for the mentioned substances with an average deviation of about 10% without any parameter adjustment or fitting. As input parameters, the thermal conductivities of the two phases (solid λ_p and gas λ_g), the porosity ϕ, the mean particle size D, and the pore size distribution d_{dist} are required. To be able to predict the thermal conductivity of potential insulation materials as reliably as possible using analytical methods, the correct models must be used. Combining these gas thermal conductivity models with common ones for solid conductivity and radiation, it is possible to determine the optimal product specifications of fictitious silica-based core materials for different requirements.

Contrary to a large number of calculation models for the different heat transfer mechanisms in general, there are not many attempts in the literature to predict the gas pressure-dependent thermal conductivity in a product-specific way. Verma et al[17] used numerical methods to predict the effective thermal conductivity of perlite with different product specifications. They were able to classify the result between the two ideal cases "hexagonal packing" and "simple cubic packing." Rottmann et al[18] also developed a model for perlite. They used several fitting parameters to get a good agreement with measurements between 293 and 1073 K. Bi et al[19] present a model specifically for aerogels which, taking into account porosity and particle size, provides good agreement with measured values. Generally, the research activity in the field of aerogels is very strong. Singh et al[20] describe the heat transfer mechanisms in different fumed silica. However, neither the density nor the particle size is taken into account when calculating the gas contribution. In this respect, the present paper shows clear advantages. Thus, for the first time, the various calculation models and input parameters can be optimally assigned to the materials mentioned to precisely investigate the influences of

the different product specifications. For this purpose, parameter studies are presented in which the gas pressure-dependent thermal conductivity is calculated for the mentioned materials as a function of particle size and porosity. The results are evaluated according to different criteria for the applications: VIPs for the building sector, VIPs for transport boxes, atmospheric pressure superinsulations, and switchable VIPs. Finally, recommendations are made for optimal product properties for the production of tailor-made VIPs or superinsulations.

2 | CALCULATION METHODS

First, the calculation methods for determining the individual heat transfer components and finally the models used for the effective thermal conductivity will be presented. The calculation procedure differs for all materials. This will be explained in more detail below. All calculations, as well as the measurements, are performed at a constant mean temperature of 30°C. Furthermore, dry gases with zero humidity are used.

2.1 | Gas thermal conductivity

For the calculation of the thermal conductivity of a Knudsen gas the common equation according to Prasolov is used.[21] It is shown in Equation (1) where λ_0 is the thermal conductivity of the gas at atmospheric conditions, β is a dimensionless factor, and Kn is the Knudsen number.

$$\lambda_g = \frac{\lambda_0}{1 + \beta Kn} \qquad (1)$$

The Knudsen number is the ratio between the mean free path of gas molecules L and a characteristic geometric quantity $x \left(Kn = \frac{L}{x} \right)$. The mean free path can be calculated using Equation (2).

$$L = \frac{k\,T}{\sqrt{2}\,\pi\,d_{kin}^2\,p} \qquad (2)$$

The selection of the geometric size x, on the other hand, raises some questions. Therefore, in the previous study[16] it was investigated which measured values should be used for the individual material classes to obtain the most realistic results. The pore size, pore size distribution, and different particle sizes are available for selection, each with and without various corrections. Another controversial topic is the calculation of the dimensionless factor β. Most promising calculation methods for
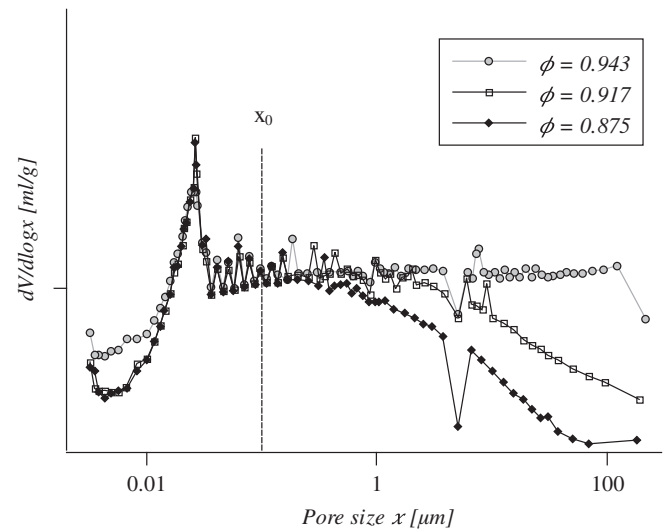

FIGURE 1 Pore size distributions measured with mercury intrusion porosimetry of the same precipitated silica sample which was treated with different amounts of pressure beforehand

different material classes could be determined as favorites in the preliminary study and can now be used accordingly.

2.1.1 | Pore size distribution

For many materials it has proven to make sense to consider the pore size distribution for the geometric parameter x in Equation (1). For this purpose, an individual thermal conductivity is calculated for each pore size that occurs and summed up over its volume fraction. In parameter studies, however, this is difficult to implement, since the pore size distribution is inseparably related to the porosity and the particle size. Nevertheless, to be able to work with distributions, a method is used to determine the pore size distribution of a certain sample with a certain particle size as a function of the porosity. For this purpose, only one measurement curve recorded with mercury intrusion porosimetry (MIP) at any porosity is required. Mechanical compaction of the powders does not affect all pore sizes equally. Logically, the largest pores disappear first. Investigations on samples compressed to different porosities have shown that the pores below a certain limit are not affected at all or only very slightly by the mechanical compaction. For clarification, the pore size distributions of the same precipitated silica which was compressed to different degrees are shown in Figure 1.

The threshold value up to which the pores are influenced by mechanical compression is related to the smallest particle unit connected by real material bridges. Therefore, the aggregate size is a good guide value for the
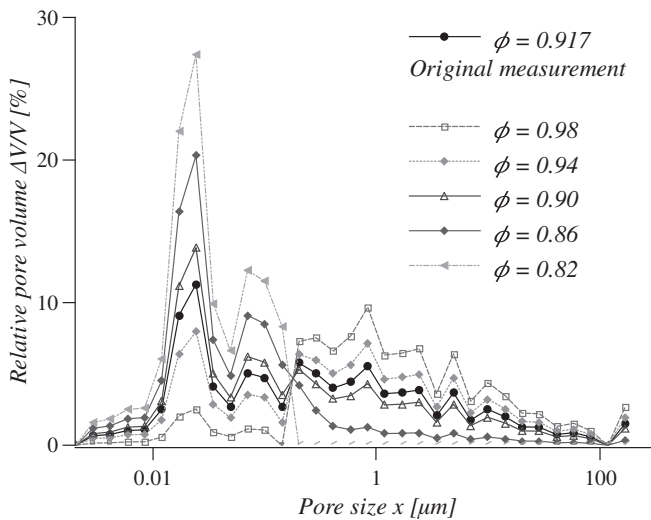
FIGURE 2   Relative pore size distributions of precipitated silica calculated with Equations (3) and (4)

materials investigated here. To calculate the pore size distribution as a function of porosity, the measured relative pore size distribution $\frac{\Delta V}{V}(\phi_1)$ at arbitrary porosity ϕ_1 is used as a basis. Then, a pore size x_0 is chosen below which no influence of compression on the pores is assumed. Initially, the aggregate size can be used here. To determine the relative pore size distribution $\frac{\delta V}{V}(\phi_2)$ Equation 3 is applied for all pore size fractions $\overline{x} < x_0$ while for all $\overline{x} > x_0$ Equation 4 can be used.

$$\frac{\Delta V}{V}(\overline{x} < x_0, \phi_2) = \frac{\Delta V}{V}(\phi_1) \times \frac{\phi_1}{\varphi^*} \qquad (3)$$

$$\frac{\Delta V}{V}(\overline{x} > x_0, \phi_2) = \frac{\Delta V}{V}(\phi_1) \times \phi_1 - F\phi^* \left(\frac{\Delta V}{V}(\phi_1) \times \phi_1 \right. \quad (4)$$

$$\left. - C_1 b^{10^6(x-x_0)} \right)$$

Here, $\frac{\Delta V}{V}$ is the relative volume fraction of a given pore size fraction $\overline{x}$, ϕ_1 is the original porosity of the measured sample, ϕ_2 is the porosity to be calculated, C_1 is the relative volume fraction of the pore size fraction x_0, and $b = 10^{-4}$. Factor F is fitted with the condition $\sum \frac{\Delta V}{V}(\phi_2) = \sum \frac{\Delta V}{V}(\phi_1)$. The ratio ϕ^* can be called apparent porosity and is calculated via Equation (5).

$$\phi^* = \frac{\phi_2(1 - \phi_1)}{(1 - \phi_2)} \qquad (5)$$

This method works only for $\sum \frac{\Delta V}{V}(\overline{x} < x_0, \phi_2) < \sum \frac{\Delta V}{V}(\phi_1)$. If this condition is only slightly missed, a smaller x_0 can

possibly be chosen. In the present work, the following values for x_0 were found to be useful: fumed silica ($x_0 = 70$ nm), precipitated silica ($x_0 = 100$ nm), and silica gel ($x_0 = 200$ nm). The pore size distributions of precipitated silica with porosities between 0.8 and 0.98 result from Equations (3) and (4) are shown as an example in Figure 2. For glass beads, the measurement of the pore size distribution by MIP proved to be inappropriate. Therefore, the calculation of the characteristic geometric size x from the particle size using Kozeny's correction[22] is used instead.

2.1.2 | Dimensionless coefficient β

The dimensionless parameter β depends primarily on the thermal accommodation coefficient α and thus on the temperature jump at the gas/solid boundaries in the porous material. It can be described with different analytical equations from the literature, which can sometimes lead to considerably different results. It has been shown that the equations are preferred depending on the material under investigation. The exact relationships are described in Sonnick et al.[16] In Table 1, the most promising equations for α and β for the individual materials are listed accordingly.

2.2 | Radiation

The radiative transfer portion of the total heat conduction can be calculated as a diffusion process if the optical thickness of the porous material is large over the entire wavelength range of interest and the mean free path of photons is small compared to the distance over which significant temperature changes occur.[28] This can be assumed for all technical relevant silica-based insulation materials. Thus, it is possible to specify a radiation-induced fraction of the total heat transfer in terms of a radiative thermal conductivity λ_r. It can be calculated by use of the Rosseland diffusion approximation[29] according to Equation 6.

$$\lambda_r = \frac{16\sigma n^2}{3\hat{E}(T, \phi)} T_{rad}^3 \qquad (6)$$

Here, σ is the Stefan-Boltzmann constant, n is the refractive index (which can be assumed to be one of the materials considered in this work[2]). $\hat{E}$ is the Rosseland average of the extinction coefficient. It is an average overall $E(\Lambda)$ which is weighted by the blackbody spectrum of the temperature of interest. It can be calculated according to Siegel and Hawell[30] via Equation (7).

TABLE 1 Recommended methods to calculate α and β for different porous media according to Sonnick et al[16]

Material	α	β
Precipitated silica	$\alpha = 1 - \frac{144.6}{(M_G+12)^2}$	$\beta = 2 \times \frac{2-\alpha}{\alpha} \frac{2\kappa}{\kappa+1} \frac{1}{Pr}$
Fumed silica	$\alpha = 1 - \left(\frac{M_S-M_G}{M_S+M_G}\right)^2$	$\beta = 2 \times \frac{2-\alpha}{\alpha} \frac{2\kappa}{\kappa+1} \frac{1}{Pr}$
Silica gel	$\alpha = 1 - \frac{144.6}{(M_G+12)^2}$	$\beta = \frac{2-\alpha}{\alpha} \frac{2\kappa}{\kappa+1} \frac{1}{Pr}$
Glass spheres	$\alpha = exp\left[C_0\left(\frac{T-T_0}{T_0}\right)\right]\left(\frac{M_G^*}{C_1+M_G}\right) + \left\{1 - exp\left[C_0\left(\frac{T-T_0}{T_0}\right)\right]\right\} \frac{2.4\frac{M_G}{M_S}}{\left(1+\frac{M_G}{M_S}\right)^2}$	$\beta = \frac{5\pi}{16} \frac{9\kappa-5}{\kappa+1} \frac{2-\alpha}{\alpha}$

Notes: Original references PS: α^{23}, β^{24}; FS: α^{24}, β^{24}; SG: α^{23}, β^{25}; GS: α^{26}, $\beta.^{27}$

$$\frac{1}{\hat{E}(T)} = \sum_{\Delta\Lambda} \frac{\frac{1}{E(\Lambda)} f_\Lambda(T)\Delta\Lambda}{\sum_{\Delta\Lambda} f_\Lambda(T)\Delta\Lambda} \qquad (7)$$

with

$$f_\Lambda(T) = \frac{\pi C_3 C_4}{2\Lambda^6} \times \frac{1}{\sigma T^5} \times \frac{\exp\left(\frac{C_4}{\Lambda T}\right)}{\left[\exp\left(\frac{C_4}{\Lambda T}\right) - 1\right]^2} \qquad (8)$$

where $C_3 = 5.9544 \times 10^{-17} \frac{W}{m^2}$ and $C_4 = 1.4388 \times 10^{-2}$ mK.

The average radiation temperature T_{rad} is defined by the two wall temperatures T_1 and T_2 using Equation (9). In this work, 45 and 15°C were used for T_1 and T_2, respectively, as the thermal conductivity measurements were carried out with these temperatures.

$$T_{rad}^3 = \frac{T_1^4 - T_2^4}{4(T_1 - T_2)} \qquad (9)$$

The spectral extinction coefficient $E(\Lambda)$ can be obtained by spectroscopic measurements determining the transmittance as a function of the sample length.[31] This procedure is shown in Section 3.2.

2.3 | Solid thermal conductivity

The heat transfer across the solid backbone of a particle bed is strongly influenced by the particle-particle contact areas. Assuming elastic deformation of the particles in the contact regions, the Hertz contact theory can be applied to calculate the solid thermal conductivity λ_s[24] using Equation (10).

$$\lambda_s = 3.44(1-\phi)^{\frac{4}{3}}\left(\frac{1-\eta^2}{Y}\right)^{\frac{1}{3}} \lambda_P F^{\frac{1}{3}} \qquad (10)$$

Here, η is the Poisson's ratio, Y the elastic modulus, and F the pressure load caused by at least the weight of the powder itself and sometimes, like in the case of vacuum insulation panels, by an additional external pressure load.

2.4 | Effective thermal conductivity

The macroscopic proportionality factor describing the heat flow through a dispersed medium at a certain temperature difference is called effective thermal conductivity λ_{eff}. It is not a "true" material value but is composed of the thermal conductivities of the individual components as well as many other influencing parameters. For porous media, there are numerous mathematical models for λ_{eff}. In the following, they will also be referred to as ETC models. On the one hand, they describe the interaction between the individual conductivities, in this case λ_s and λ_g, which is also referred to as the coupling effect or coupling conductivity λ_c. On the other hand, the ETC models are used to weight the individual components according to the porosity ϕ. In the preliminary study[16] mentioned above, the most common ETC models from the literature were investigated and classified with regard to the materials investigated. The most promising model for each material is used for the present parameter studies as well.

2.4.1 | Precipitated silica, silica gel, and glass spheres

For the material groups PS, SG, and GS, a model is used which is based on a cylindrical unit cell of two touching hemispheres with the simplifying assumption of parallel heat flow lines. It was developed by Swimm et al[32] and is based on a parallel connection of finitely small cylindrical shells of the mentioned unit cell. Each cylindrical shell is calculated as a series connection of the solid and

gas fractions applicable to the corresponding radius. In this process, a separate Knudsen number is calculated for each cylindrical shell according to the height of the gas fraction and thus an individual gas thermal conductivity is obtained.

$$x(i) = D - 2\sqrt{R^2 - \left(\frac{i}{N}R\right)^2} \qquad (11)$$

In 11 $D - x(i)$ is the void distance of the ith cylindrical shell, N is the total number of cylindrical shells, and D and R are diameter and radius. At this point, different measurement values should be used for D and R for the different materials. For PS, SG, and GS it has proven to be purposeful to use the largest conglomerates perceptible as individual particles accordingly. Glass beads are not multiscale. Therefore, the simple particle size or primary particle size is used here. Silica gel consists of aggregates which in turn are composed of small sintered primary particles. Here, the aggregate size has to be selected. Precipitated silica even has a three-stage structure. Here, the aggregates, driven by different adhesive forces, form the so-called agglomerates. Consequently, in the case of PS, the average agglomerate diameter for D in Equation (11) should be used.

$$\lambda_c = \frac{2}{R\pi} \sum_{i=1}^{N} A_i \left(\frac{D - x(i)}{\lambda_{g'}} + \frac{x(i)}{\lambda_p}\right)^{-1} \qquad (12)$$

The coupling thermal conductivity λ_c is the reciprocal sum of the individual shells, weighted by the respective area fraction A_i. $\lambda_g{}'$ is the gas thermal conductivity of the individual shells. To calculate the effective thermal conductivity of the porous material, the thermal conductivity of the pure gas phase λ_g and that of the unit cell λ_c are weighted according to a corrected porosity ϕ_{corr} as shown in Equation (13).

$$\lambda_{eff} = \lambda_{base} + \phi_{corr}\lambda_g + (1 - \phi_{corr})\lambda_c \qquad (13)$$

The corrected porosity ϕ_{corr} results from the porosity of the unit cell and the porosity of the investigated material ϕ.

$$\phi_{corr} = \frac{3\phi - 1}{2} \qquad (14)$$

2.4.2 | Fumed silica

For fumed silica, the ETC model of Zehner and Schlünder[33] gives the best results. Like the sphere model of

Swimm et al it is a unit cell model with consideration of local Knudsen numbers. The difference is that the surface of the model particles is not described by the sphere function, but by Equation (15).

$$r^2 + \frac{z^2}{(B - (B-1)x)^2} = 1 \qquad (15)$$

where

$$B = C\left(\frac{1 - \phi}{\phi}\right)^{\frac{10}{9}}$$

The local Knudsen number is given as a function of the radius with $Kn^* = \frac{Kn}{(1 - x(r))}$. Integration over r leads to Equation (16) which can be used to calculate the coupling conductivity.

$$\lambda_c = \lambda_0 \frac{2}{N - M} \left\{ \frac{\left[N - (1 + Kn)\frac{\lambda_0}{\lambda_p}\right]B}{(N - M)^2} \ln\frac{N}{M} \right.$$

$$\left. - \frac{B - 1}{N - M}(1 + Kn) - \frac{B + 1}{2B}\frac{\lambda_p}{\lambda_0}[1 - (N - M) - (B - 1)Kn] \right\} \qquad (16)$$

with

$$M = B\left[\frac{\lambda_0}{\lambda_p} + Kn\right]$$

and

$$N = 1 + Kn$$

Zehner and Schlünder proposed different correction factors C for differently shaped particles. For example, $C = 1.25$ is recommended for spheres. Since no recommendation is available for irregularly shaped fumed silica particles, $C = 1.25$ is assumed here. The aggregate size is used to calculate the Knudsen number to adequately describe the size of the gap in which the coupling thermal conductivity occurs. The consideration of thermal radiation in the original model was neglected here since it is calculated separately. Using the corrected porosity $(1 - \sqrt{1 - \phi})$ the effective thermal conductivity can be calculated with Equation (17).

$$\lambda_{eff} = \left(1 - \sqrt{1 - \phi}\right)\lambda_g + \sqrt{1 - \phi}\lambda_c \qquad (17)$$

3 | MEASUREMENTS

Although this work is mainly theoretical, some measurements are required for the determination of input parameters and validations. Fourier transform infrared (FTIR) spectroscopy was performed to determine the emission coefficient of the materials and ultimately to determine λ_r. Furthermore, measurements of thermal conductivity at very low pressures are performed to validate the results of the calculations of λ_s and λ_r. The gas thermal conductivity and the coupling effect have already been extensively validated in the mentioned preliminary study. For the measurements, 15 different powdery samples including fumed and precipitated silica, silica gel, and glass spheres were used. The specifications of the materials including primary particle size, aggregate size, agglomerate size, porosity, and pore size distribution have been measured with small angle X-ray scattering, dynamic light scattering, laser diffraction, and MIP, respectively and can be taken from.[16]

3.1 | Solid and radiation thermal conductivity

At very low pressures or large Knudsen numbers ($Kn \gg 1$), the gas thermal conductivity can be completely neglected. Thus, there is no coupling between the gas and solid phases and only the radiative thermal conductivity and the solid thermal conductivity remain. Consequently, the sum of these two components can be determined by thermal conductivity measurements at very low pressures. The following equation applies:

$$\lambda_{base} = \lambda(p_{min}) = \lambda_s + \lambda_r \tag{18}$$

The samples to be analyzed were measured in a vacuum guarded hot plate apparatus. For this purpose, the apparatus was vacuumed to the maximum possible level overnight (approx. 0.05 mbar) and the sample was dried completely so that no moisture was left. In this condition, the values for λ_{base} were recorded.

The cooling and heating plate temperatures were 15 and 45°C, respectively, resulting in a mean measurement temperature of 30°C. The central measuring area of the guarded hot plate is $(8 \text{ cm})^2$. The entire plate including the guard ring is $(16 \text{ cm})^2$. The samples are mechanically compacted directly in the measuring chamber using a hydraulic press to a sample thickness between 6 and 8 mm. A detailed description of the measurement apparatus and error analysis can be found in.[34]

3.2 | Extinction coefficient

The determination of the average extinction coefficient $\hat{E}$ is fundamental for the calculation of the radiation thermal conductivity λ_r. Thus, transmission spectroscopy measurements have been performed using an FTIR spectrometer (*Bruker ALPHA II*). The samples were pressed onto a thin polyethylene film using a self-developed pressing device. This resulted in small platelike bodies with a thickness in the order of 100 μm. The polyethylene film was used as a support material and thus also for the background measurement. The result of the measurements is a spectrum $E(\Lambda)$. Where Λ is the wavelength. The mass of the sample and the diameter of the pressing device can be used to determine the area density m_a. To obtain the mass-specific extinction coefficient E_m, the average extinction coefficient $\hat{E}$ from Equation (7), which can be calculated from the measured $E(\Lambda)$ spectra, must be divided by m_a. To get the radiation thermal conductivity λ_r as a function of the porosity one can extend Equations (6) to (19) as follows.

$$\lambda_r = \frac{16\sigma n^2}{3E_m\rho_s(1-\phi)}T_{rad}^3 \tag{19}$$

where ρ_s is the density of the non-porous solid skeleton. In the case of silica-based materials $\rho_s = 2200\frac{kg}{m^3}$.[35] The bulk density of the porous materials is given by $\rho = \rho_s(1-\phi)$.

4 | RESULTS AND DISCUSSION

We first discuss the results for λ_s and λ_r. Then, the parameter studies of the effective thermal conductivity of the different materials are evaluated. Finally, their relevance to the various applications of superinsulations is discussed.

4.1 | Solid and radiation thermal conductivity

The results for the radiation thermal conductivities obtained with Equation (19) using the spectroscopic measurement results are shown in Figure 3. The λ_r values are plotted against the porosity of the measured materials. Each circle represents a silica-based material. The density which was used for the calculations is the same as for the thermal conductivity measurements. Standard deviations are plotted as error bars which are only visible as lines in the data points. The dotted line in Figure 3 was fitted to
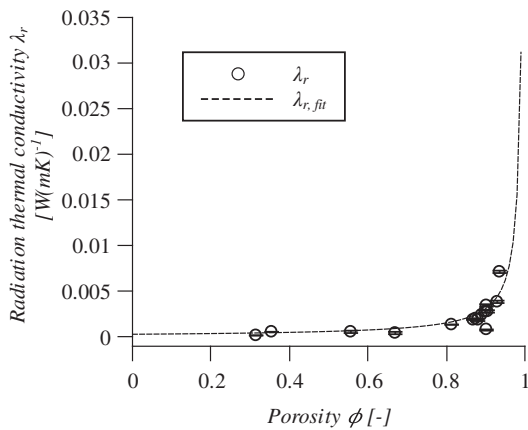
FIGURE 3 Calculated radiation thermal conductivity over porosity of silica-based materials. Circles: Calculated via Equation (19) using measured extinction coefficients; Dashed line: Calculation with fitted E_m
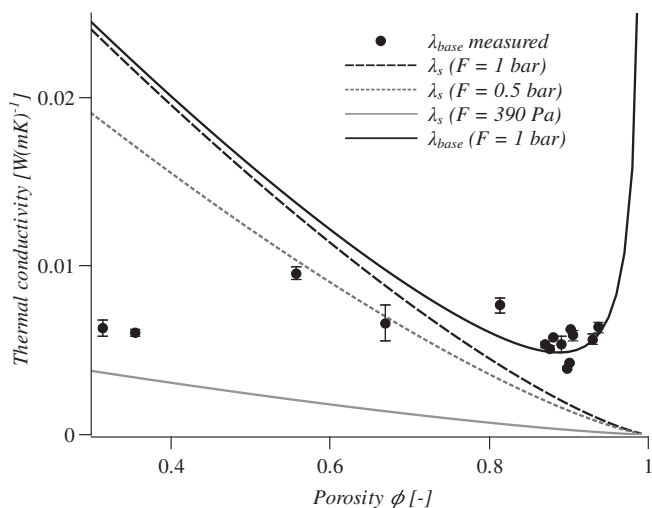

FIGURE 4 Calculated λ_s curves for different amounts of mechanical load F, calculated λ_{base} for $F = 1$ bar, and measured λ_{base} values for all samples investigated over porosity

the data points using the mass-specific extinction coefficient E_m as a fitting parameter. The procedure leads to Equation (20) for the porosity-dependent radiation thermal conductivity of silica-based powders at wall temperatures $T_1 = 45°C$ and $T_2 = 15°C$.

$$\lambda_r = \frac{3.118 * 10^{-4}}{(1 - \phi)} \qquad (20)$$

To calculate λ_{base}, the solid thermal conductivity λ_s has to be determined as well. It can be calculated as already mentioned via Equation (10). One decisive factor is the mechanical load F of the powder bulk. Three curves for the solid thermal conductivity calculated with

$F = 1$ bar, $F = 0.5$ bar, and $F = 390$ Pa are shown in Figure 4. A 390 Pa corresponds approximately to the load to which the samples were subjected during the thermal conductivity measurements. 1 bar, on the other hand, corresponds to the load on a VIP by atmospheric pressure. Furthermore, in Figure 4, the measured values for λ_{base} of all investigated materials are shown. Finally, a calculated curve for λ_{base} is shown, which is the sum of $\lambda_s(F = 1\ bar)$ and λ_r. It is found that the measured values of the materials with porosities greater than 0.8 agree relatively well with the calculated curve ($\lambda_{base}(F = 1$ bar)). However, the lower the porosity, the further the measured values move away from the calculated curve. The main reason for this is the assumed mechanical load because to achieve a smooth surface and the desired porosity, the samples were compacted before the thermal conductivity measurement. For this purpose, approx. 4 bar of compression pressure was applied. During this process, the pressed samples with higher porosities, such as from FS, PS, and some silica gels, deform plastically. The very small particles of these materials approach each other during the pressing process and are then held together for example by van der Waals forces, electrostatic interactions, or simple form closure. This attraction affects the solid thermal conductivity like a mechanical load from outside. Powders with higher porosities, such as glass beads, merely deform elastically during sample preparation. Their particles are too large to be significantly affected by the above-mentioned attractive forces and too spherical for form closure. During the measurement, only 390 Pa weight on the samples, which then have relatively low solid thermal conductivity if they have low porosity at the same time. Nevertheless, for the further calculations of all materials the curve $\lambda_{base}(F = 1$ bar) is used because in the scenario of a VIP, the atmospheric pressure weights equally on all materials.

4.2 | Effective thermal conductivity

In Sections 4.2.1 to 4.2.4, the results of the calculation of the effective thermal conductivity for the investigated materials are presented and discussed. Parameter studies were performed on the particle size relevant to the corresponding materials, as well as on the porosity. The chosen value domains are based on measurements, so that realistic ranges of the material data are studied in each case. The chosen domains can be found in Table 2. The different types of particle sizes (primary particles, aggregates, and agglomerates) are specified due to the different multiscalarities of the materials as well as the preferred calculation methods for each material according to.[16]

TABLE 2 Selected domains for the parameter study on porosity and the decisive particle size

|	PS	FS	SG	GS
Porosity	0.80 to 0.98	0.80 to 0.98	0.80 to 0.98	0.3 to 0.7
Particle size	Agglomerates	Aggregates	Aggregates	Primary particles
	5 to 40 μm	50 to 225 nm	5 to 40 μm	1 to 100 μm
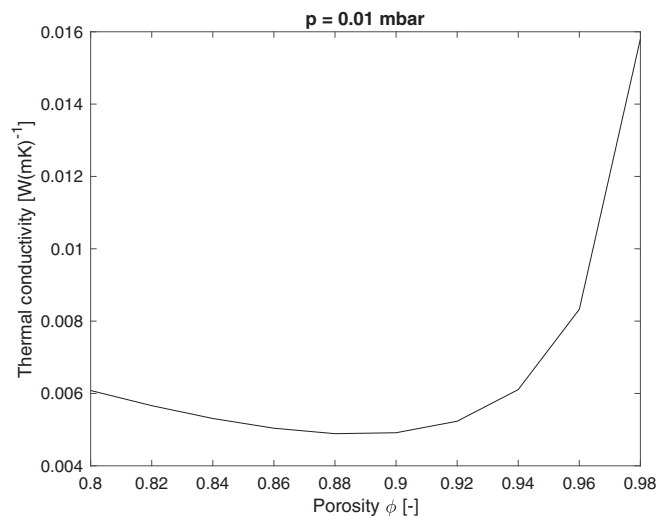
FIGURE 5 Calculated thermal conductivity values over porosity for $P = .01$ mbar. Under the assumptions made, this curve applies in principle to all materials and particle sizes investigated

Porosity is used in the calculation both to determine the pore size distribution (Section 2.1.1) and as an input parameter for the corresponding ETC model (Section 2.4). For all materials, it is equally true that the lowest thermal conductivity can be achieved at the lowest possible pressure and a porosity of 0.89. This applies to all materials, since λ_{base} does not depend on particle or pore size but only on porosity, at least under the assumptions made. It was calculated with $P = 0.01$ mbar, and is shown in Figure 5 as a function of the porosity. The results are valid for all materials investigated.

In the following subsections, the results of the parameter studies for the pressure levels $P = 100$ and $P = 1000$ mbar of the individual materials are shown in Figures 6–9, respectively. In Section 4.2.5, the advantages and disadvantages of the individual materials for different applications are discussed.

4.2.1 | Precipitated silica

The thermal conductivity of precipitated silica at high gas pressures and small porosities is characterized by a strong coupling effect λ_c. As shown in Figure 6, the curves from the direction of small porosities come from a very high level, then drop down to the minimum value and rise

again due to increased gas thermal conductivity and a rapidly increasing radiation fraction in the direction of $\phi = 1$. The optimum porosity, that is, the one with the lowest thermal conductivity, increases with increasing pressure. For the smallest investigated particle size of 5 μm, the minimum values are obtained at $\phi = 0.86$ for $P = 100$ mbar and $\phi = 0.92$ for $P = 1000$ mbar. We can also observe that the optimum porosity also increases with increasing agglomerate size. This is due to the fact that the coupling effect is more pronounced for larger particles than for small ones, and the coupling contribution for precipitated silica depends approximately linearly on the porosity.[34]

4.2.2 | Fumed silica

For fumed silica, a significantly reduced tendency for coupling between λ_s and λ_g is observed compared to the other materials investigated. Therefore, it has proven useful to use aggregate size instead of agglomerate size as the unit cell size of the ETC model, since smaller particles provide less coupling than larger ones in the pressure range investigated. Here, again, the tendency that the optimum porosity also increases with increasing particle size can be observed. However, since the particles studied are much smaller than for PS, the optimum porosities are also much smaller. For FS, the porosity has a comparatively small effect on the effective thermal conductivity, especially in the range of common aggregate sizes of about 150 nm. Here, in the porosity area from $\phi = 0.82$ to $\phi = 0.9$, the decreasing coupling effect and the increasing radiative and gaseous thermal conductivity fractions seem to cancel each other out to a large extent.

4.2.3 | Silica gel

Although here the usual aggregate sizes are in the same order of magnitude as the agglomerates of the precipitated silicas, one does not achieve as low thermal conductivities for silica gels as for PS, especially in the higher pressure ranges. At the model level, this is obviously related to the calculation method for β. The factor of 2 in the formula used for PS leads to significantly lower gas thermal conductivities. In reality, this effect is probably
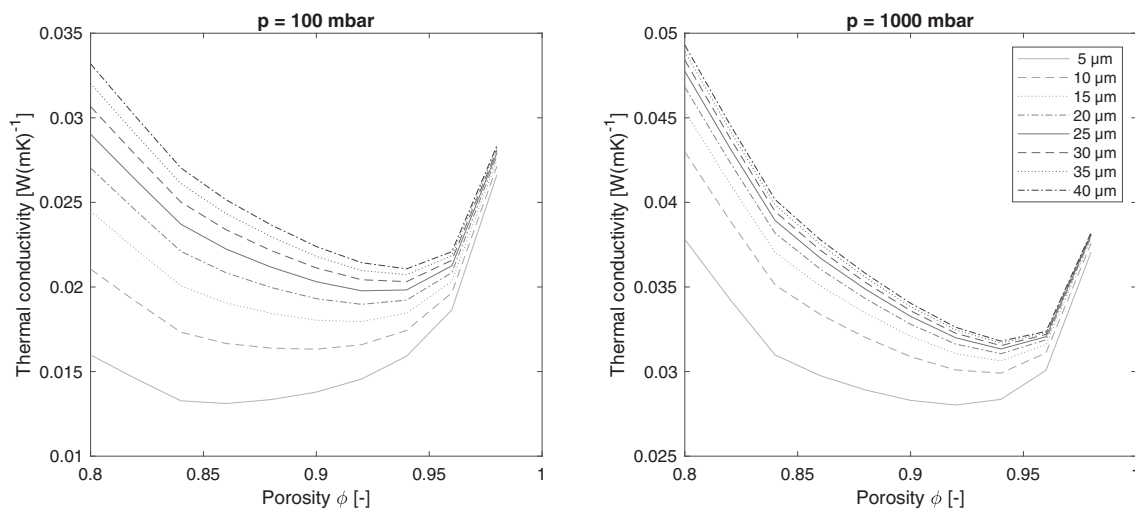
FIGURE 6 Calculated precipitated silica effective thermal conductivity values over porosity for different pressure stages and agglomerate sizes
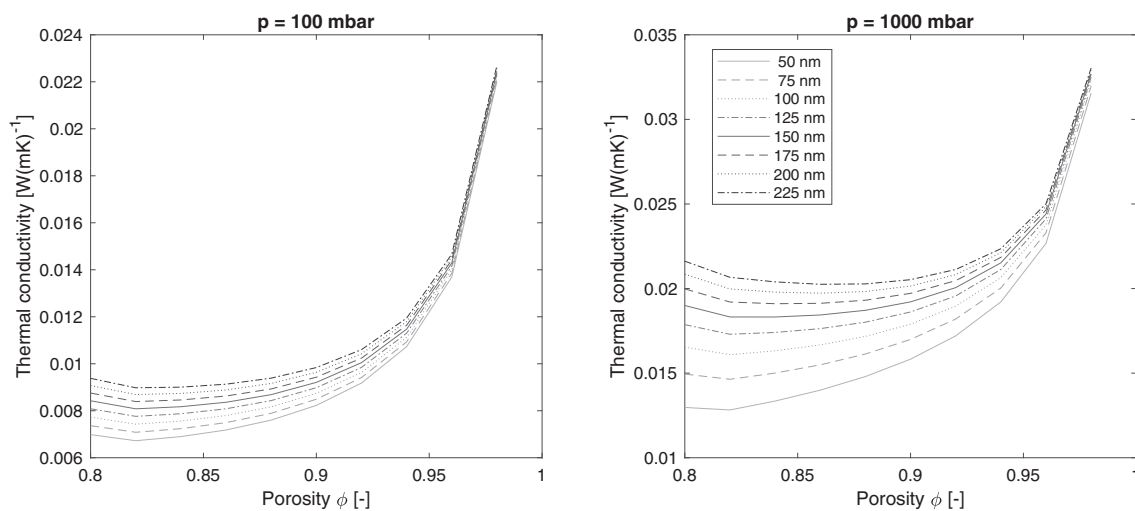

FIGURE 7 Calculated fumed silica effective thermal conductivity values over porosity for different pressure stages and aggregate sizes
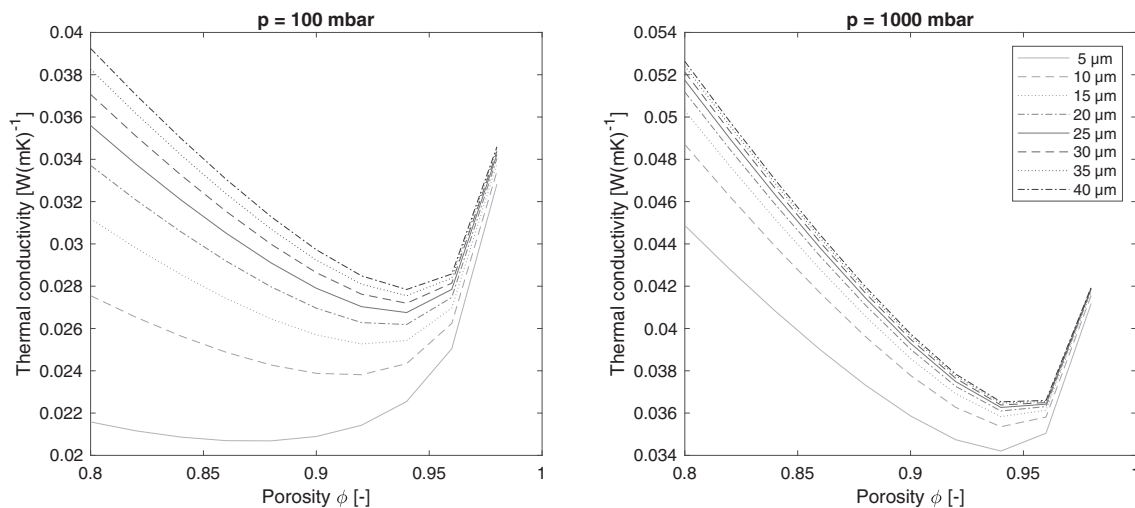

FIGURE 8 Calculated silica gel effective thermal conductivity values over porosity for different pressure stages and aggregate sizes
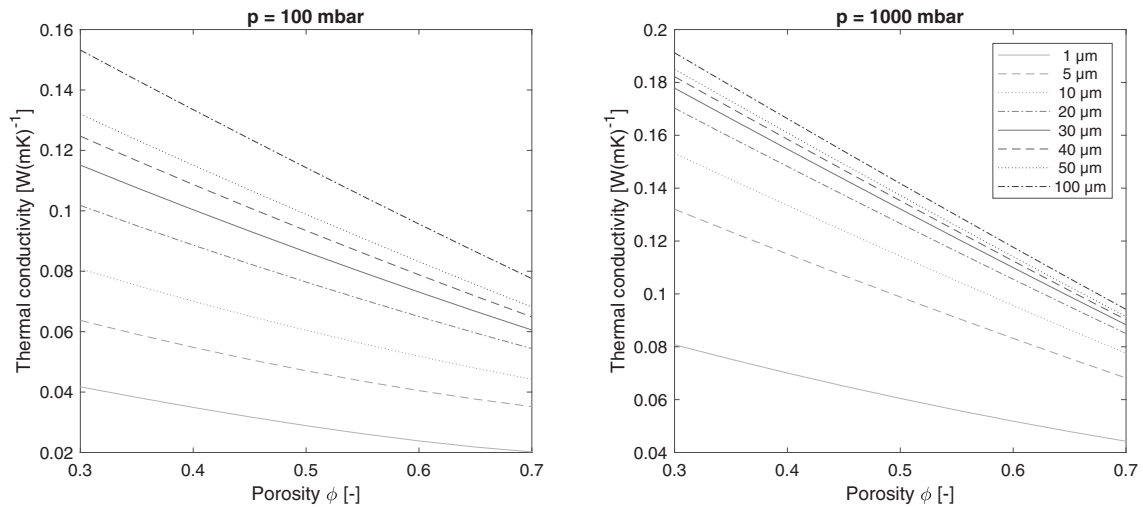
FIGURE 9 Calculated glass spheres' effective thermal conductivity values over porosity for different pressure stages and particle sizes

TABLE 3 Suitability of the different materials for the various applications according to previously defined criteria

Application	Value	PS	FS	SG	GS
Buildings	Particle size	min.	min.	min.	min.
($\lambda_{100\ \text{mbar}}$)	Porosity	0.86	0.82	0.88	max.
	Thermal conductivity $\left[\frac{W}{mK}\right]$	0.0131	0.0067	0.0207	0.0202
Transport boxes	Porosity	0.89	0.89	0.89	0.89
(λ_{base})	Thermal conductivity $\left[\frac{W}{mK}\right]$	0.0049	0.0049	0.0049	0.0049
Atmospheric pressure	Particle size	min.	min.	min.	min.
($\lambda_{1000\ \text{mbar}}$)	Porosity	0.92	0.82	0.94	max.
	Thermal conductivity $\left[\frac{W}{mK}\right]$	0.028	0.0128	0.0342	0.0442
Switchable VIPs	Particle size	max.	max.	max.	max.
$SW = \frac{\lambda(p=1000\ mbar)}{\lambda_{base}}$	Porosity	min.	0.90	0.84	min.
	SW	8.09	4.18	8.82	7.93

related to the denser nature of the SG aggregates, while the PS agglomerates do have a certain intrinsic porosity and small contact points between the aggregates. Due to the fact that the gas thermal conductivity increase strongly with higher porosity, the curves are particularly steep compared to PS for example. This leads to a very small range of optimum porosities. As a consequence, the optimum porosity range would have to be maintained very precisely when using silica gel as the core material.

4.2.4 | Glass spheres

The investigated porosity range is much smaller for glass beads than for the other materials because this material forms a much denser bulk in reality. Therefore, the thermal conductivity at low pressures is primarily characterized by solid thermal conductivity. Here, a reduction in porosity helps to reduce the overall thermal conductivity in a steady manner. In the higher pressure ranges, a very pronounced coupling effect is added which now dominates the total thermal conductivity and thus leads to considerable differences between minimum and maximum pressure.

4.2.5 | Core materials for different applications

To be able to select theoretically optimum core materials for the various applications, the most important properties in each case must be defined. The main criteria for selecting a suitable core material for the various applications were selected as follows:
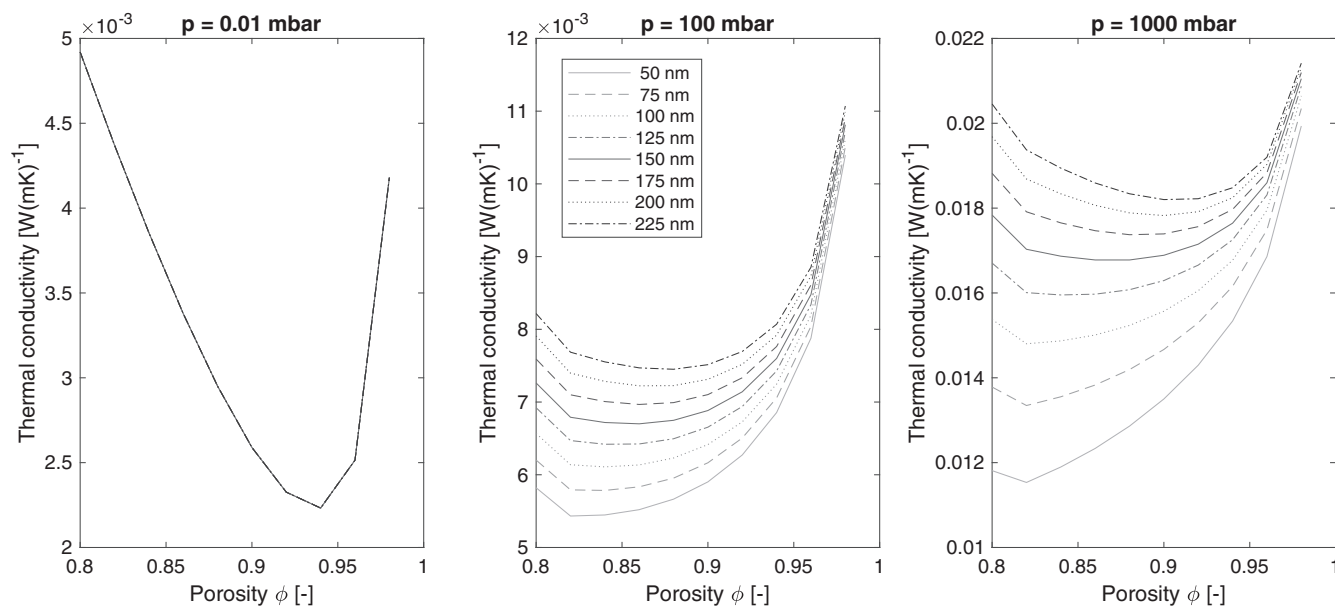
FIGURE 10   Calculated opacified fumed silica effective thermal conductivity values over porosity for different pressure stages and particle sizes

- Building sector:
  Even though researchers are working intensively on the development of new and increasingly better high-barrier films for VIPs,[36] a minimum degree of gas diffusion through the envelope can never be avoided. Therefore, in long-term applications, like the building sector, in addition to a low initial thermal conductivity, and the longevity of the VIP is primarily decisive. Since gas diffusion through the barrier film is independent of the VIP-core, the main consideration when selecting the core material is a moderate increase in thermal conductivity with increasing pressure. Therefore, the thermal conductivity at 100 mbar is considered a reference.
- Transport boxes: The packaging industry is the classical example of a VIP with a short life expectancy. Return systems for transport boxes already exist, but despite this, the boards, also due to damage, do not achieve by far the service lives of the VIPs used in the construction sector. Therefore, the decisive parameter here is the initial thermal conductivity, that is, the thermal conductivity at very low pressures λ_{base} immediately after production.
- Atmospheric pressure insulations: Silica-based materials are also suitable for use at atmospheric pressure. They are petroleum-free, non-flammable, pressure-stable, and have low conductivity values. Logically, the thermal conductivity at $P = 1000$ mbar is decisive here.

- Switchable VIPs: In some special applications it can be advantageous to be able to switch the insulation on and off by gas pressure differences. In this case, it is important to find a material with a maximum ratio $\frac{\lambda(p=1000\,mbar)}{\lambda_{base}}$. The desired absolute heat transfer can be adjusted via the material thickness and the pressure.

Of course, in addition to the gas pressure-dependent thermal conductivity, there are other important parameters that can be decisive in the selection of core materials. However, since such influences are difficult to quantify within this framework, they are taken into account only qualitatively when evaluating the results.

Such parameters are, for example, the price per volume or per thermal resistance. In addition, weight is very important in mobile applications like transport boxes. Furthermore, the ability to absorb water molecules and the corresponding effect on the thermal conductivity of the materials must be considered to calculate the service life of the VIP.[37] An equally important criterion for some materials can be processability. For the classic production method, it is necessary to be able to press the core materials into reasonably stable sheets to ensure further processing. This requirement can be even more important for atmospheric pressure applications, where the materials are not placed in a stabilizing vacuum package. Fumed silica is particularly well suited for this purpose, as the particles interlock well due to the hierarchical aggregate structure. This step is usually less successful for

materials with more spherical particles. In this case, alternative production techniques, such as the pouring technique, must be used. However, especially for transport boxes (or also on thermal storage units), this method can be advantageous in combination with free-flowing materials, as it allows the VIPs to remain bendable and thus minimizes edge effects. Moreover, dealing with switchable VIPs it must be possible to aerate and deaerate in as short a time as possible.[38] Furthermore, alternative gases with higher thermal conductivities can be considered for this application to further increase the *SW* factor.[39] However, all these "soft" criteria will be considered only marginally in this work.

The conductivity-related results of the respective categories can be found in Table 3. The first column lists the applications and again the corresponding criteria. The following columns show the relevant material properties and the respective results. The indication of absolute values for the calculated thermal conductivities must be considered with care because the achieved extreme values depend on the freely chosen limits of the parameter studies. Furthermore, the mentioned uncertainty of the calculation models needs to be considered. For example, the minimum thermal conductivity of fumed silica at atmospheric pressure of $0.0128 \frac{W}{mK}$ is, to the authors' current knowledge, a value that has never been met by measurement. It must be taken into account that in reality additional influencing factors not considered here may affect the ETC of the materials. For example, to compress fumed silica to porosity of the calculated 0.84, such high pressures would probably have to be used that the solid heat conduction would increase strongly. It should therefore be mentioned at this point that this is an idealized consideration. Nevertheless, the results give an indication of how the perfect core material would have to be structured for the applications shown.

For the **building sector**, fumed silica is clearly to be favored. The low coupling fraction caused by the small aggregates leads to the smallest increase in thermal conductivity with increasing pressure. The optimum porosity is $\phi = 0.82$, which is comparatively low. This effect can also be explained by the low λ_c. With decreasing porosity, the solid thermal conductivity and the coupling fraction increase, while the radiative conductivity and the gas thermal conductivity decrease. If the coupling conductivity is low due to the small aggregates, the optimum is rather in the direction of smaller porosities. For silica-based insulation materials at **atmospheric pressure**, fumed silica is also the favorite. The reason is the same as for the building sector.

For **transport boxes**, the most important factor is the low initial thermal conductivity of the VIPs. As already mentioned, λ_{base} is the same for all materials

under the assumptions made. The most important thing here is to meet the optimum porosity of $\phi = 0.89$ as good as possible. Precipitated silica is therefore proposed as the core material to be favored at this point since it is the comparatively cheapest material. The challenge here, however, is the production of the cores, since the mechanical stability of the compacts during production can only be guaranteed to a limited extent.[40] Possibly contrary to the intuitive assumption, a particularly large spread between minimum and maximum values is not obtained for **switchable VIPs** at high porosities, but rather at low ones. Although the switchable fraction, namely the gas phase, is volumetrically larger at higher porosities, the number of particles and thus the number of contact points is smaller. Especially for materials with spherical microstructures, the most decisive contribution of heat transfer is the coupling between solid and gas phases. This coupling takes place at the contact points. As already discussed in Sonnick et al[34] for precipitated silica, the coupling increases approximately linearly with porosity for constant particle size. This relationship only holds for the technically relevant porosity range shown. The highest ratio between the thermal conductivity at atmospheric pressure and the minimum conductivity is observed for silica gel with a porosity of $\phi = 0.84$, where the difference between PS and SG is not large. Here, therefore, the decision is rather influenced by economic or technical factors again.

4.2.6 | Opacified core materials

In practice, opacifiers are added to the core materials to suppress the heat transfer by radiation in most cases. The reduction of λ_r can possibly lead to a shift of the optimum of the previously investigated parameters. This must be taken into account in the design of core materials. In this study, the emission coefficient of a VIP core material consisting of fumed silica and magnetite as well as silicon carbide was also determined as an example. The mass-specific emission coefficient E_m increases from an average of $12.9 \frac{m^2}{kg}$ to $50.6 \frac{m^2}{kg}$ compared to the pure materials consisting of SiO_2 only. This results in a reduced radiation thermal conductivity and thus a different result of the parameter study which can be seen in Figure 10. The optimum porosity for the building application and the application at atmospheric pressure is still $\phi = 0.82$, while the porosity to be preferred for transport boxes increases significantly, namely to $\phi = 0.94$. However, the optimal porosity range must be observed much more precisely in this case, since λ_{base} increases steeply both just above and just below the optimal porosity. The dependencies on particle size remain unchanged.

5 | CONCLUSION

To calculate the gas pressure-dependent thermal conductivity of porous silica-based materials on the basis of their so-called primary product properties, all heat transfer mechanisms (λ_s, λ_r, λ_g, and λ_c) must be calculated individually and can then be combined with each other. The ideal equations and input parameters vary for different materials. In this paper, parameter studies were performed to determine the influences of porosity and particle size on the gas pressure-dependent thermal conductivity of precipitated silica, fumed silica, silica gel, and glass spheres. The Rosseland approximation was used to calculate the radiative thermal conductivity λ_r. The emission coefficient obtained was measured by infrared spectroscopic methods on the silica-based materials. To calculate the solid thermal conductivity λ_s, a common model based on the Hertz contact theory was used. The sum of the two fractions λ_s and λ_r corresponds to the thermal conductivity at very low gas pressures λ_{base}. It was measured using a vacuum guarded hot plate apparatus and agrees well with the calculated values. The most difficult part to predict is the combination of the thermal conductivity of the gas λ_g and the coupling term λ_c, which is responsible for the increase of the effective thermal conductivity with increasing pressure. It can be calculated from a combination of models for the effective and the gas thermal conductivity which can be taken from.[16] As a result, specific recommendations could be made regarding the type of material and the corresponding material properties in terms of particle size and porosity. Of course, particle size and porosity are inextricably linked in reality. Therefore, it is only possible to a limited extent to vary the two separately in material development. The combinations of material values shown in the parameter studies are therefore initially only fictitious. Crucial findings are shown in Table 3 and are summarized in the following paragraphs (important results are in bold).

5.1 | Building sector and atmospheric pressure application

The parameter studies show a clear advantage of **fumed silica** over the other investigated materials for the construction sector, where a long service life of the VIPs is in focus, as well as for the application at atmospheric pressure. In particular, long durability and low thermal conductivity under atmospheric pressure are achieved when **aggregate size** is chosen **as small as possible** and porosity is set to $\phi = \mathbf{0.82}$. Although the parameter study yields noticeably small absolute values for this

combination, the results for the optimum porosity and particle size are correct and should be considered for future development of appropriate core materials. The small absolute values for fumed silica result from the fact that, in contrast to the other materials, the aggregate size is used instead of the agglomerate size for calculating the effective thermal conductivity. While this approach has significant advantages over using agglomerate size, it generally leads to a slight underestimation of thermal conductivity. The truth probably lies somewhere between the aggregates and the agglomerates, since the coupling effects on both size scales overlap here. However, those on the order of magnitude of the aggregates, that is, roughly in the three-digit nanometer range, clearly predominate for fumed silica. Furthermore, the porosity optimum at 0.82 requires a plausibility check. In future work, it would be helpful to include the effect of the pressure required to achieve a certain porosity and its effect on the solid thermal conductivity to exclude misleading conclusions. Nevertheless, low porosities or high densities can make sense for the building sector. This will slightly increase the initial thermal conductivity, but the increase over time caused by gas thermal conductivity and coupling can be effectively reduced by decreasing the porosity (and thus the average pore size). In addition, the weight is of little importance in the construction sector.

5.2 | Transport boxes

Since λ_{base} in this study depends only on the porosity of the materials, the choice of material for VIPs in the transport sector seems to be irrelevant. Thus, the decision must be made primarily on the basis of economic factors, which is why a clear recommendation is made at this point to use **precipitated silica** for the transport sector. The optimum porosity, in this case, is $\phi = \mathbf{0.89}$. For the same reason, precipitated silica is also the right choice for special applications where the pressure increase due to leakage can be compensated by means of a monitoring system and a built-in vacuum pump.

5.3 | Switchable VIP

For switchable VIPs, the factor between fully vacuumed and fully vented materials is most important. This is about the same for precipitated silica, silica gel, and glass beads, which is why economic factors should also be included in the decision. However, there is a slight tendency for **silica gel** to exhibit the largest switching effect with a factor $SW = 8.82$ at a porosity of $\phi = \mathbf{0.84}$ and **maximum particle size**.

5.4 | Opacified material

Furthermore, it must be taken into account that the optima determined in this work are only valid for the corresponding pure substances. Since additives such as opacifiers are frequently used in practice, the considerations can be adjusted accordingly. The investigation of opacified fumed silica shows that the properties to be preferred may well differ from those of the pure substances. Furthermore, opacifier type and concentration can influence the results significantly. However, the procedure shown can also be applied in unchanged form to materials with modified optical properties. The extension of the parameter study with a focus on opacified materials would therefore be an interesting topic for follow-up research.

DATA AVAILABILITY STATEMENT

The data that support the findings of this study are available from the corresponding author upon reasonable request.

ORCID

Sebastian Sonnick https://orcid.org/0000-0003-1625-2782

REFERENCES

1. Wernery J, Mancebo F, Malfait WJ, O'Connor M, Jelle BP. The economics of thermal superinsulation in buildings. *Energy Buildings*. 2021;253:111506. doi:10.1016/j.enbuild.2021.111506
2. Reiss H. K6 superinsulations. *VDI heat atlas*. Berlin, Heidelberg: Springer; 2010:1013-1052.
3. Alotaibi SS, Riffat S. Vacuum insulated panels for sustainable buildings: a review of research and applications. *Int J Energy Res*. 2014;38(1):1-19. doi:10.1002/er.3101
4. Almeida FA, Corker J, Ferreira N, et al. Alternative low cost based core systems for vacuum insulation panels. *Cienc e Tecnol dos Mat*. 2017;29(1):e151-e156. doi:10.1016/j.ctmat.2016.10.002
5. Alam M, Singh H, Brunner S, Naziris C. Experimental characterisation and evaluation of the thermo-physical properties of expanded perlite––fumed silica composite for effective vacuum insulation panel (VIP) core. *Energy Buildings*. 2014;69:442-450. doi:10.1016/j.enbuild.2013.11.027
6. Li CD, Saeed MU, Pan N, Chen ZF, Xu TZ. Fabrication and characterization of low-cost and green vacuum insulation panels with fumed silica/rice husk ash hybrid core material. *Mater Design*. 2016;107:440-449. doi:10.1016/j.matdes.2016.06.071
7. Notario B, Pinto J, Solorzano E, Saja dJA, Dumon M, Rodríguez-Pérez MA. Experimental validation of the Knudsen effect in nanocellular polymeric foams. *Polymer*. 2015;56:57-67. doi:10.1016/j.polymer.2014.10.006
8. Di X, Gao Y, Bao C, Ma S. Thermal insulation property and service life of vacuum insulation panels with glass fiber chopped strand as core materials. *Energy Buildings*. 2014;73:176-183. doi:10.1016/j.enbuild.2014.01.010
9. Li CD, Chen ZF, Wu WP, et al. Core materials of vacuum insulation panels: a review and beyond. *Appl Mech Mater*. Vol 174–177; 2012:1437-1440. Advanced Building Materials and Sustainable Architecture ISBN: 9783037854235, Swizerland: Trans Tech Publications Ltd. doi:10.4028/www.scientific.net/AMM.174-177.1437
10. Zhao S, Siqueira G, Drdova S, et al. Additive manufacturing of silica aerogels. *Nature*. 2020;584(7821):387-392. Number: 7821. Nature Publishing Group. doi:10.1038/s41586-020-2594-0
11. Zach J, Hroudová J, Korjenic A. Environmentally efficient thermal and acoustic insulation based on natural and waste fibers. *J Chem Technol Biotechnol*. 2016;91(8):2156-2161. doi:10.1002/jctb.4940
12. Balo F, Sua LS. Techno-economic optimization model for "sustainable" insulation material developed for energy efficiency. *Int J Appl Ceramic Technol*. 2018;15(3):792-814. doi:10.1111/ijac.12855
13. Resalati S, Okoroafor T, Henshall P, Simões N, Gonçalves M, Alam M. Comparative life cycle assessment of different vacuum insulation panel core materials using a cradle to gate approach. *Build Environ*. 2021;188:107501. doi:10.1016/j.buildenv.2020.107501
14. Knudsen M. Die molekulare Wärmeleitung der Gase und der Akkommodationskoeffizient. *Ann Phys*. 1911;339(4):593-656. doi:10.1002/andp.19113390402
15. Yang M, Sheng Q, Guo L, Zhang H, Tang G. How gas-solid interaction matters in graphene-doped silica aerogels. *Langmuir*. 2022;38(7):2238-2247. American Chemical Society. doi:10.1021/acs.langmuir.1c02777
16. Sonnick S, Erlbeck L, Meier M, Nirschl H, Rädle M. Methodical selection of thermal conductivity models for porous silica-based media with variation of gas type and pressure. *Int J Heat and Mass Transf*. 2022;187:122519. doi:10.1016/j.ijheatmasstransfer.2022.122519
17. Verma S, Singh H. Predicting the conductive heat transfer through evacuated perlite based vacuum insulation panels. *Int J Thermal Sci*. 2022;171:107245. doi:10.1016/j.ijthermalsci.2021.107245
18. Rottmann M, Beikircher T. Pressure dependent effective thermal conductivity of pure and SiC-opacified expanded perlite between 293 K and 1073 K. *Int J Thermal Sci*. 2022;179:107652. doi:10.1016/j.ijthermalsci.2022.107652
19. Bi C, Tang GH, Hu ZJ, Yang HL, Li JN. Coupling model for heat transfer between solid and gas phases in aerogel and experimental investigation. *Int J Heat Mass Transf*. 2014;79:126-136. doi:10.1016/j.ijheatmasstransfer.2014.07.098
20. Singh H, Geisler M, Menzel F. Experimental investigations into thermal transport phenomena in vacuum insulation panels (VIPs) using fumed silica cores. *Energ Buildings*. 2015;107:76-83. doi:10.1016/j.enbuild.2015.08.004

21. Prasolov RS. *Generalization of the equation of the thermal conductivity of gases*. Priborostr: Izv. VUZ'ov; 1961.

22. Kosten CW. The mean free path in room acoustics. *Acta Acustica United with Acustica*. 1960;10(4):245-250.

23. Bauer R. *Effektive radiale Wärmeleitfähigkeit gasdurchströmter Schüttungen mit Partikeln unterschiedlicher Form und Größenverteilung: mit 7 Tafeln*. Düsseldorf: VDI-Verl; 1977.

24. Kaganer MG. Thermal insulation in cryogenic engineering. *Israel Program Sci Transl*. 1969;1:6-21.

25. Fricke J, Lu X, Wang P, Büttner D, Heinemann U. Optimization of monolithic silica aerogel insulants. *Int J Heat Mass Transf*. 1992;35(9):2305-2309. doi:10.1016/0017-9310(92)90073-2

26. Song S, Yovanovich MM. Correlation of thermal accommodation coefficient for 'engineering' surfaces. *ASME HTD*. 1987; 69:107-116.

27. Swimm K, Vidi S, Reichenauer G, Ebert HP. Coupling of gaseous and solid thermal conduction in porous solids. *J Non Cryst Solids*. 2017;456:114-124. doi:10.1016/j.jnoncrysol.2016.11.012

28. Reiss H. 3. Approximate solutions of the equation of transfer. In: Reiss H, ed. *Radiative Transfer in Nontransparent, Dispersed Media* (Springer Tracts in Modern Physics). Berlin, Heidelberg: Springer; 1988:96-138.

29. Rosseland S. *Astrophysik: Auf Atomtheoretischer Grundlage*. Vol. 11. Berlin Heidelberg: Springer-Verlag; 2013:254.

30. Siegel R, Howell J. *Thermal Radiation Heat Transfer*. New York, NY: Mc GRAW HILL Book Company; 1972.

31. Dietrich B, Fischedick T, Heissler S, Weidler PG, Wöll C, Kind M. Optical parameters for characterization of thermal radiation in ceramic sponges—experimental results and correlation. *Int J Heat Mass Transf*. 2014;79:655-665. doi:10.1016/j.ijheatmasstransfer.2014.08.023

32. Swimm K, Reichenauer G, Vidi S, Ebert HP. Gas pressure dependence of the heat transport in porous solids with pores smaller than 10 microns. *Int J Thermophys*. 2009;30(4):1329-1342. doi:10.1007/s10765-009-0617-z

33. Zehner P, Schlünder EU. Einfluß der Wärmestrahlung und des Druckes auf den Wärmetransport in nicht durchströmten Schüttungen. *Chemie Ingenieur Technik*. 1972;44(23):1303-1308. doi:10.1002/cite.330442305

34. Sonnick S, Meier M, Ross-Jones J, et al. Correlation of pore size distribution with thermal conductivity of precipitated silica and experimental determination of the coupling effect. *Appl Therm Eng*. 2019;150:1037-1045. doi:10.1016/j.applthermaleng.2019.01.074

35. Pramanik S, Manna A, Tripathy A, Kar KK. Current advancements in ceramic matrix composites. In: Kar KK, ed. *Composite Materials*. Berlin, Heidelberg: Springer Berlin Heidelberg; 2017: 457-496.

36. Miesbauer O, Kucukpinar E, Kiese S, Carmi Y, Noller K, Langowski HC. Studies on the barrier performance and adhesion strength of novel barrier films for vacuum insulation panels. *Energy Buildings*. 2014;85:597-603. doi:10.1016/j.enbuild.2014.06.054

37. Yrieix B, Morel B, Pons E. VIP service life assessment: interactions between barrier laminates and core material, and significance of silica core ageing. *Energy Buildings*. 2014;85:617-630. doi:10.1016/j.enbuild.2014.07.035

38. Erlbeck L, Sonnick S, Wössner D, Nirschl H, Rädle M. Impact of aeration and deaeration of switchable vacuum insulations on the overall heat conductivity using different core materials and filling gases. *Int J Energy Environ Eng*. 2020;11(4):395-404. doi:10.1007/s40095-020-00356-y

39. Sonnick S, Meier M, Ünsal G, Erlbeck L, Nirschl H, Rädle M. Thermal accommodation in nanoporous silica for vacuum insulation panels. *Int J Thermofluids*. 2020;1-2:100012. doi:10.1016/j.ijft.2019.100012

40. Guesnet E, Bénane B, Jauffrès D, et al. Why fumed and precipitated silica have different mechanical behavior: contribution of discrete element simulations. *J Non Cryst Solids*. 2019;524: 119646. doi:10.1016/j.jnoncrysol.2019.119646

Chapter 8

Conclusion

This publication-based thesis includes four peer-reviewed papers. The overall goal is to achieve as complete an understanding as possible of the heat transfer mechanisms in particulate, silica-based superinsulations. In particular, the main objective is to find applicable calculation methods for real materials and not "only" to set up theoretical models for idealized systems. The work begins with an introduction to the topic as well as a presentation of the theoretical background to this subject area. Special attention is paid to the kinetic theory of gases and the Knudsen effect, which are the decisive physical principles in superinsulations and vacuum insulation panels (VIPs). Although various silica-based materials are investigated throughout this thesis, a special focus is on precipitated silica, which the author considers to be an underestimated alternative to high-priced fumed silica in the field of VIPs.

The **first publication**, "*Correlation of pore size distribution with thermal conductivity of precipitated silica and experimental determination of the coupling effect,*" deals exclusively with precipitated silica. Five different commercially available products were examined. The focus of the investigation was on the characterization of the thermal coupling effect, which is particularly important for porous media composed of more or less spherical particles, such as precipitated silica. Pore size distributions from mercury intrusion porosimetry data were used to calculate the gas thermal conductivity in the pores, considering the Knudsen effect. Therefore, a correction factor was introduced to account for the spherical shape of the pores. The coupling effect is proportional to the gas thermal conductivity and can thus be represented by a linear factor – the coupling effect factor f. The question was whether this factor depends on the type of material or porosity. The investigations revealed a linear dependence of the coupling effect factor on the porosity. However, a measurable correlation between the different products and the coupling effect could not be established. It can consequently be concluded that the different manufacturing conditions of the precipitated silicas have no or only a minor influence on the coupling effect. In the further course of the thesis (in particular Paper 3

in Chapter 6), it becomes clear that the coupling effect depends not only on the porosity but also on the agglomerate size of the precipitated silica. However, this dependence could not be detected here, since the agglomerates of the precipitated silicas studied were in the narrow size range of $7\,\mu m$ to $12.5\,\mu m$. Assuming constant particle size for the different products, only the number of contact points and therefore the porosity ϕ influence the amount of coupling. A simplified representation is shown in Figure 8.1.
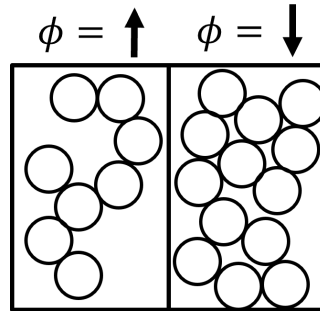

Figure 8.1: Simple graphical representation of low and high porosity, resulting in high and low numbers of contact points and thus high and low coupling effect factors, respectively

In the further progress of the research work, other silica-based materials were analyzed. Applying the method presented in the first paper to these materials also resulted in approximately linear curves with a negative slope for the coupling effect factor versus porosity (see Figure 8.2).
The strongly different tendencies for the coupling of the different materials is evident here. Within a material class, f increases with decreasing porosity and thus an increasing number of contact points. The slope is similar for silica gel and glass spheres and much smaller for fumed silica. The fumed silica samples were only investigated in a narrow porosity range. Fumed silica generally tends to have extremely low coupling thermal conductivity. This circumstance is primarily discussed in Paper 3 and is one of the main reasons that this material has been considered the favorite for the production of VIPs to date.

In the **second publication**, "*Thermal accommodation in nanoporous silica for vacuum insulation panels,*" the influence of the thermal accommodation coefficient (TAC) on the effective thermal conductivity of fumed and precipitated silica with different residual pore gases is examined. The frequently made assumption $\alpha = 1$ for air in silica pores is verified and disproved. Assuming that the coupling effect factor depends only on the solid framework and only negligibly on the thermal conductivity ratio between solid and gas, a reverse approach to determine an apparent TAC is presented. The results are TACs that increase with increasing molar mass of the gases as long as the molar mass of the gas is lower than that of the solid surface. For heavy gases with molar
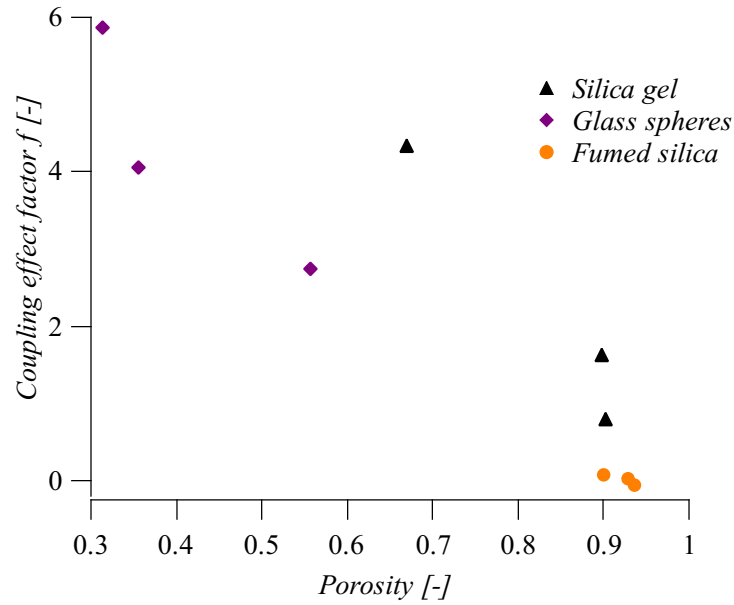
Figure 8.2: Coupling effect factors f of silica gel, fumed silica and glass spheres plotted over their porosity

masses greater than that of the surface, the TAC starts to decrease again. This basic relationship can be derived from impact theory and can also be found, for example, in the calculation of the thermal conductivity of gas mixtures. For two-substance mixtures different molar masses have a negative deviation from the linear dependence of the thermal conductivity on the composition of the gas mixtures [82]. As mentioned, the values obtained are not actual thermal accommodation coefficients but apparent values that are only valid in the context of the models used. Numerous material-specific influencing factors were not considered here to be able to present general, reliable physical values for the actual TAC. In subsequent investigations, it becomes clear that the theoretical models should be adapted precisely to the materials and that the calculation of the TAC should not be carried out with the same methods in all cases. In this work, the model conception from the impact theory could be confirmed using a reverse approach from thermal conductivity measurements and thus serves as a basis for the subsequent investigations in order to select adequate calculation methods for the follow-up studies.

In conclusion, the TAC and the resulting temperature jump at any gas–solid surface in porous insulation materials contribute significantly to these materials' performance. In the case of a complete energy transfer between air and, for example, the silica pore walls, the effective thermal conductivities of silica would be significantly higher. For clarification, the gas pressure-dependent thermal conductivity of the precipitated silica studied in Paper 2 was calculated once with the determined value of $\alpha = 0.41$ and once with the frequently
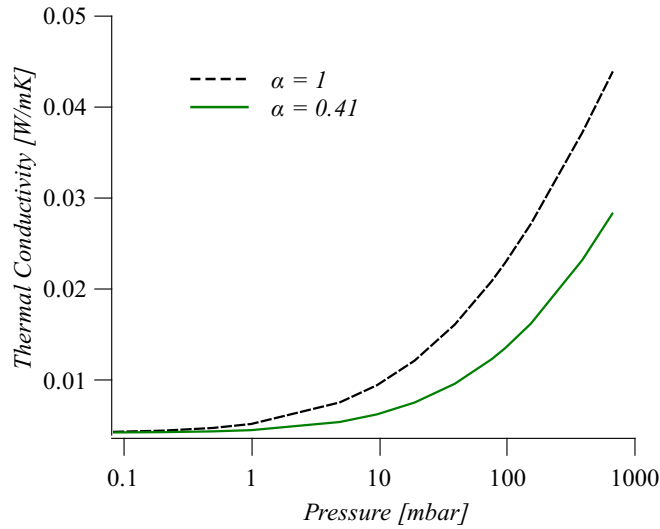
Figure 8.3: Gas pressure-dependent thermal conductivity of precipitated silica – calculated using different TACs

used assumption $\alpha = 1$. The results are depicted in Figure 8.3. The same models as those presented in the paper were used for the calculation. The difference is significant and again underlines the relevance of this parameter.

The determination of the TAC for use in thermal conductivity calculations is a controversial topic. However, the choice of the correct accommodation coefficient is not the only difficult decision a user must make when modeling the gas pressure-dependent thermal conductivity of porous media. For the subsequent determination of the dimensionless coefficient β, there are also numerous proposals in the literature. Furthermore, it is not self-explanatory which measured quantities should be used for the geometric factor x in real porous media. Therefore, in the **third publication**, "*Methodical selection of thermal conductivity models for porous silica-based media with variation of gas type and pressure*," a literature review is presented in which the calculation models in question for the determination of the gas thermal conductivity are examined. After the calculation of the gas thermal conductivity the respective results must then be further processed in a suitable model to determine the effective thermal conductivity. Numerous models can be used for this purpose; they are summarized and classified in the context of the paper. After the comparison of all possible model combinations with measured thermal conductivity data of 15 silica-based materials, model recommendations are made for the different materials. The average coefficient of variation is $10\,\%$. Some physically explicable findings emerge. For example, the measured quantities of the different, favorable particle sizes (primary particles, aggregates, agglomerates) for the calculations offer a useful indication of the size scale on which the decisive heat transfer processes take place in the various materials. It is clear,

for instance, that for fumed silica, primarily the aggregate size is important, while for precipitated silica, the agglomerate size is key. Other recommendations such as the different models for calculating α or β do not necessarily have a direct physical relation to the corresponding materials. These findings can be regarded as empirical. The point is that important factors influencing the effective thermal conductivity, such as the shape of the solid structures and the number of silanol groups, among many others, cannot be represented directly in analytical models. Therefore, these material-specific influencing factors are indirectly considered via the choice of different calculation models.

The **fourth and final publication**, "*Silica-based core materials for thermal superinsulations in various applications,*" is concerned with the application of the knowledge gained in the previous papers to the development of insulation materials. Since the requirements for thermal superinsulation differ greatly for different applications, tailor-made core materials can have prime advantages. Decisions regarding the core materials sometimes have significant economic or technical consequences. Therefore, it is important to adapt the core materials used to the corresponding application. To this end, parameter studies on the particle size and porosity of the different materials were carried out to make specific recommendations for the different applications. The model combinations determined in Paper 3 were applied to the material classes PS, FS, SG, and GS. The results regarding material selection were ultimately unsurprising. Fumed silica remains the first choice in the construction sector and for applications at atmospheric pressure. For transport boxes and special applications such as switchable or re-vacuumable VIPs, however, the recommendation is to utilize precipitated silica. Its lower (energy) input during production and the resulting lower price make this material highly attractive compared with fumed silica. For the first time, it was also possible to make recommendations regarding the optimum porosity for various applications. For each material, a certain porosity results from an individual pressing pressure. These dependencies should be considered in future developments. Where additives are used, in particular infrared opacifiers, it must be noted that changes with regard to the optimum porosity may occur. The modified optical properties may lead to a shift of the optimum in the direction of higher porosities. However, the presented method can easily be transferred to any material mixture based on the substances presented. For this purpose, only the mass-specific extinction coefficient and a mercury intrusion measurement are required. Apart from pure thermal conductivity, other criteria must be considered when selecting core materials. In addition to the abovementioned economic factors, not all materials are equally suitable for every superinsulation production process. Fumed silica is best suited to the production of classical VIPs due to its mechanical properties. Practical experience has shown that with precipitated silica, it is only possible to press stable sheets to a limited extent and with great effort. However, there are ideas on how to overcome this and other challenges regard-

ing precipitated silica VIPs. They are presented in Chapter 9 and have the potential not only to make superinsulations and especially VIPs economically accessible for a range of new applications but also to open up a new era in the field of thermal superinsulation materials.

Chapter 9

Outlook

Precipitated silica is, mainly due to the lower price, already a promising candidate for short-term applications such as medical transport boxes or food transport. The material is also quite attractive for systems in which re-vacuuming is intended. It is not easy to obtain exact numbers for the market prices of the different types of silica. For fumed silica, Almeida et al., for example, report a market price of approximately 4 €/kg in their 2017 paper [83], whereas the 2017 IHS Markit report states an average price per kilogram of $8.35 for fumed silica and $2.20 for precipitated silica on the Western European market [84]. However, it is clear that precipitated silica is much cheaper than fumed silica. This will always be the case, as the production costs for fumed silica are significantly higher in terms of both technical equipment and energy. Only a fraction of the energy is required to produce precipitated silica compared with fumed silica. Nevertheless, no product based on precipitated silica has yet been fully established. The main disadvantages of currently available products are, on the one hand, a less advantageous particle and pore structure, which leads to an earlier increase in thermal conductivity compared with fumed silica (coupling effect). Thus, the service life of such panels is reduced, since a minimal diffusion through the envelop cannot be avoided. On the other hand, classical precipitated silicas are more difficult to process into manageable panels than fumed silica due to their comparatively spherical aggregate structure [85]. At present, neither precipitated silica nor fumed silica are produced in an optimized way for use in vacuum insulation panels (VIPs). The market is currently still limited compared with the large silica-processing industries such as the tire, paint, or cosmetics industries. To further advance the energy turnaround by reducing greenhouse gas emissions, cost-effective yet high-performance insulation materials are becoming increasingly important. A rapidly growing market share of silica-based insulation materials is hence expected in the next few years. Especially in the wet chemical precipitation process, there are many opportunities for product improvements in terms of insulation properties. Thus, different approaches to create a new product class based on precipitated silica are briefly discussed in Sections 9.1 – 9.3.

9.1 Continuous precipitation in micro or flow reactor and continuous filtration

The first proposal concerns improvement to the particle structure of the precipitated silica. An optimization in this respect could improve the service life of the resulting VIP. Classical silica precipitation occurs in large batch-process stirred reactors. The process is inexpensive and delivers large product quantities with a quality sufficient for the applications to date. However, the process is comparatively slow and poorly controllable. Continuous precipitation in a flow reactor could provide some advantages. The flow reactor allows almost instantaneous changes in the most important process parameters, namely pH, temperature, and convection. In addition, the range of these parameters is significantly increased. This increased flexibility will make it possible to understand the reaction kinetics of silica precipitation more precisely and to influence it in a targeted manner. Selective adjustment of the primary particle size and observation of aggregate growth are valuable tools in the development of new silica products. Particle growth can be observed in-situ in the micro or flow-through reactor using, for example, UV/VIS backscatter measurement techniques. Targeted reaction termination and immediate further processing can be used to achieve smaller agglomerates.

Continuous precipitation (or even a classical batch process) in combination with continuous filtration can be used to produce specific aggregate or agglomerate sizes. If the aggregates formed are continuously removed from the process, newly formed primary particles cannot attach to the existing secondary particles, but must form new ones. Thus, continuous filtration could be a simple and effective tool to achieve previously impossible product specifications even in the stirred reactor.

9.2 Addition of fibers and opacifiers during precipitation

One time-consuming and inefficient process step in the production of VIPs is the mixing of the individual components. The components are dry and of different morphology and surface charge. The homogenization of liquids is known to be much less challenging. In the classical precipitation process, this task is performed by a regular stirrer. If the required additives (infrared opacifiers and fibers) are already added to the stirred reactor, the subsequent step in VIP production can be completely omitted. The components would be optimally mixed even before the drying step. The goal is to generate a core material mixed down to the micro or nano level already in the wet chemical manufacturing process. It should be noted that both this and subsequent steps would not be feasible with fumed silica, as it is synthesized in the gas phase. Due to the more homogeneous distribution of the opacifiers, compared

with dry mixing, an increased absorption capacity is additionally expected, which would lead to an improvement of the product properties and/or a possible reduction of the opacifier content. The purpose of opacifiers is to ensure the lowest possible penetration depth of thermal radiation in the wavelength relevant to the corresponding temperature range. Mostly magnetite, silicon carbide, and carbon black are used [86]. These substances could also be mixed directly into the liquid phase. Furthermore, it should be tested whether an irreversible bond between carbon black and silica can be induced by introducing, for example, carbon black particles directly into the reactor, even before the precipitation reaction is triggered by a pH shift. The type and number of functional groups that appear at defect sites on the surface of carbon black strongly depend on the manufacturing process [87]. Since only the functional groups, mostly consisting of hydrogen, oxygen, nitrogen, and sulfur, can induce polar behavior, suitable analytical techniques would have to be found to investigate the tendency to interact with silica particles.

Although the thermal properties of precipitated silica are already interesting for VIP in some applications, the low-cost alternative to fumed silica has not yet been established on the market. The main reason is the manufacturability of the boards. At present, it is impossible to produce stable plates from precipitated silica that can be handled in the further production process, because of the fractal dimension of the aggregates close to 3 and the associated spherical structure. This problem can also be addressed by admixing additives already in the liquid phase. It is expected that fibers added in the liquid phase will lead to a better cohesion of the compound not only due to their more homogeneous distribution but also due to a stronger bond to the silica particles. To further enhance this effect, fiber material and geometry could be adapted accordingly. In classic VIPs, the fiber diameter is significantly larger than the particles. However, if it is reduced to approximately the diameter of the aggregates (roughly 150 nm), the fibers could be incorporated into the agglomerates and have a stabilizing effect. Experiments with nanocellulose, for example, could be planned for this purpose. However, other auxiliaries could also have a positive effect on the aggregate structure. If, for example, small amounts of fumed silica are added to the stirred reactor before precipitation begins, this could have a positive effect on the attachment and structure formation of the aggregates, similar to that of a seed crystal. The author expects a similar effect from the addition of silica or glass fibers. Due to the chemical similarity, an attachment of the particles during precipitation is likely and could lead to a needle-shaped aggregate structure with embedded fibers.

9.3 Classification of aggregates in the liquid phase

It is already known that the pore size distribution of the core material is an important factor in the performance of VIPs. It directly influences the course of the thermal conductivity at different pressures. Therefore, the ability to influence or even specifically adjust the pore size distribution would be advantageous. Furthermore, it is known that the pore size distribution strongly depends on the aggregate size distribution of the silica. This gave rise to the idea of classifying the aggregates while they are still in the liquid phase, where they are present individually and have not agglomerated to form tertiary particles. By classifying them into specific size fractions, a reduction in the dispersion of the pores is expected. In addition, a narrower particle size distribution leads to an increase in the inter-grain volume, which would result in an increase in the intrinsic porosity of the agglomerates. A specific adjustment of the pore size allows for a selectable position of the thermal conductivity curve's inflection point. Different centrifuges, such as tubular or decanter centrifuges, could be used for the classification.

Chapter 11: Verification of the contribution from the co-authors

Paper 1:

Title: **Correlation of pore size distribution with thermal conductivity of precipitated silica and experimental determination of the coupling effect**

Journal: Applied Thermal Engineering

Authors: Sebastian Sonnick, Manuel Meier, Jesse Ross-Jones, Lars Erlbeck, Isabel Medina, Hermann Nirschl, Matthias Rädle

Position in the dissertation:

The content of this paper has been included in Chapter 4

Contribution of Sebastian Sonnick: Design and mechanical construction of the test facility, conception, thermal conductivity measurements, evaluation of the results, writing

Contribution of Manuel Meier: Measurements and evaluation of pore size distributions

Contribution of Lars Erlbeck: Thermal conductivity measurements, writing

Contribution of Jesse Ross-Jones: Discussions, proofreading, mathematical support

Contribution of Isabel Medina: Design and electrical construction of the test facility

Contribution of Hermann Nirschl: Supervision, funding, consulting

Contribution of Matthias Rädle: Supervision, funding, consulting

Signature of the authors:

Author	Signature
Sebastian Sonnick	
Manuel Meier	
Jesse Ross-Jones	
Lars Erlbeck	
Isabel Medina	
Hermann Nirschl	
Matthias Rädle	

Paper 2:

Title: **Thermal accommodation in nanoporous silica for vacuum insulation panels**

Journal: International Journal of Thermofluids

Authors: Sebastian Sonnick, Manuel Meier, Gamze Ünsal-Peter, Lars Erlbeck, Hermann Nirschl, Matthias Rädle

Position in the dissertation:

The content of this paper has been included in Chapter 5

Contribution of Sebastian Sonnick: Conception, thermal conductivity measurements, evaluation of the results, writing

Contribution of Manuel Meier: Measurements and evaluation of the solid materials

Contribution of Gamze Ünsal-Peter: Literature Review, Modification of the test facility, proofreading

Contribution of Lars Erlbeck: Thermal conductivity measurements, writing

Contribution of Hermann Nirschl: Supervision, funding, consulting

Contribution of Matthias Rädle: Supervision, funding, consulting

Signature of the authors:

Author	Signature
Sebastian Sonnick	
Manuel Meier	
Gamze Ünsal-Peter	
Lars Erlbeck	
Hermann Nirschl	
Matthias Rädle	

Paper 3:

Title: **Methodical selection of thermal conductivity models for porous silica-based media with variation of gas type and pressure**

Journal: International Journal of Heat and Mass Transfer

Authors: Sebastian Sonnick, Lars Erlbeck, Manuel Meier, Hermann Nirschl, Matthias Rädle

Position in the dissertation:

The content of this paper has been included in Chapter 6

Contribution of Sebastian Sonnick: Conception, Literature Review, measurements, Codewriting for evaluation of the results, writing

Contribution of Lars Erlbeck: Thermal conductivity measurements, writing

Contribution of Manuel Meier: Measurements regarding particle and pore sizes of the solid materials, Proofreading

Contribution of Hermann Nirschl: Supervision, funding, consulting

Contribution of Matthias Rädle: Supervision, funding, consulting

Signature of the authors:

Author	*Signature*
Sebastian Sonnick	
Lars Erlbeck	
Manuel Meier	
Hermann Nirschl	
Matthias Rädle	

Paper 4:

Title: **Silica-based core materials for thermal superinsulations in various applications**

Journal: International Journal of Energy Research

Authors: Sebastian Sonnick, Hermann Nirschl, Matthias Rädle

Position in the dissertation:

The content of this paper has been included in Chapter 7

Contribution of Sebastian Sonnick: Conception, measurements, calculations, evaluation of the results, writing

Contribution of Hermann Nirschl: Supervision, funding, consulting

Contribution of Matthias Rädle: Supervision, funding, consulting

Signature of the authors:

Author	*Signature*
Sebastian Sonnick	
Hermann Nirschl	
Matthias Rädle	

List of Figures

List of Publications

[1] Sebastian Sonnick et al. "Temperature stabilization using salt hydrate storage system to achieve thermal comfort in prefabricated wooden houses". In: *Energy and Buildings* 164 (Apr. 2018), pp. 48–60. ISSN: 0378-7788. DOI: 10.1016/j.enbuild.2017.12.063.

[2] Jesse Ross-Jones et al. "Conjugate heat transfer through nano scale porous media to optimize vacuum insulation panels with lattice Boltzmann methods". In: *Computers & Mathematics with Applications* (Oct. 2018). ISSN: 0898-1221. DOI: 10.1016/j.camwa.2018.09.023.

[3] Sebastian Sonnick et al. "Correlation of pore size distribution with thermal conductivity of precipitated silica and experimental determination of the coupling effect". In: *Applied Thermal Engineering* (Jan. 2019). ISSN: 1359-4311. DOI: 10.1016/j.applthermaleng.2019.01.074.

[4] Manuel Meier et al. "Multi-scale characterization of precipitated silica". In: *Powder Technology* 354 (Sept. 2019), pp. 45–51. ISSN: 0032-5910. DOI: 10.1016/j.powtec.2019.05.072.

[5] Maximilian Gaedtke et al. "Numerical study on the application of vacuum insulation panels and a latent heat storage for refrigerated vehicles with a large Eddy lattice Boltzmann method". en. In: *Heat and Mass Transfer* (Dec. 2019). ISSN: 1432-1181. DOI: 10.1007/s00231-019-02753-4.

[6] Sebastian Sonnick et al. "Passive room conditioning using phase change materials—Demonstration of a long-term real size experiment". en. In: *International Journal of Energy Research* 44.8 (2020), pp. 7047–7056. ISSN: 1099-114X. DOI: 10.1002/er.5406.

[7] Sebastian Sonnick et al. "Thermal accommodation in nanoporous silica for vacuum insulation panels". en. In: *International Journal of Thermofluids* 1-2 (Feb. 2020), p. 100012. ISSN: 2666-2027. DOI: 10.1016/j.ijft.2019.100012.

[8] Lars Erlbeck et al. "Impact of aeration and deaeration of switchable vacuum insulations on the overall heat conductivity using different core materials and filling gases". en. In: *International Journal of Energy and Environmental Engineering* 11.4 (Dec. 2020), pp. 395–404. ISSN: 2251-6832. DOI: 10.1007/s40095-020-00356-y.

[9]   Jesse Ross-Jones et al. "Pore-scale conjugate heat transfer simulations using lattice Boltzmann methods for industrial applications". en. In: *Applied Thermal Engineering* 182 (Jan. 2021), p. 116073. ISSN: 1359-4311. DOI: `10.1016/j.applthermaleng.2020.116073`.

[10] Sebastian Sonnick et al. "Methodical selection of thermal conductivity models for porous silica-based media with variation of gas type and pressure". en. In: *International Journal of Heat and Mass Transfer* 187 (May 2022), p. 122519. ISSN: 0017-9310. DOI: `10.1016/j.ijheatmasstransfer.2022.122519`.

[11] Sebastian Sonnick, Hermann Nirschl, and Matthias Rädle. "Silica-based core materials for thermal superinsulations in various applications". en. In: *International Journal of Energy Research* n/a.n/a (). ISSN: 1099-114X. DOI: `10.1002/er.8453`.

Bibliography

[1] Sibylle Wilke. *Energieverbrauch für fossile und erneuerbare Wärme*. de. Text. Publisher: Umweltbundesamt. Apr. 2016.

[2] Sebastian Sonnick et al. "Correlation of pore size distribution with thermal conductivity of precipitated silica and experimental determination of the coupling effect". In: *Applied Thermal Engineering* (Jan. 2019). ISSN: 1359-4311. DOI: 10.1016/j.applthermaleng.2019.01.074.

[3] Jesse Ross-Jones et al. "Conjugate heat transfer through nano scale porous media to optimize vacuum insulation panels with lattice Boltzmann methods". In: *Computers & Mathematics with Applications* (Oct. 2018). ISSN: 0898-1221. DOI: 10.1016/j.camwa.2018.09.023.

[4] Jesse Ross-Jones et al. "Pore-scale conjugate heat transfer simulations using lattice Boltzmann methods for industrial applications". en. In: *Applied Thermal Engineering* 182 (Jan. 2021), p. 116073. ISSN: 1359-4311. DOI: 10.1016/j.applthermaleng.2020.116073.

[5] Maximilian Gaedtke et al. "Application of a lattice Boltzmann method combined with a Smagorinsky turbulence model to spatially resolved heat flux inside a refrigerated vehicle". en. In: *Computers & Mathematics with Applications* 76.10 (Nov. 2018), pp. 2315–2329. ISSN: 0898-1221. DOI: 10.1016/j.camwa.2018.08.018.

[6] Chuan-Yong Zhu et al. "Numerical modeling of the gas-contributed thermal conductivity of aerogels". en. In: *International Journal of Heat and Mass Transfer* 131 (Mar. 2019), pp. 217–225. ISSN: 0017-9310. DOI: 10.1016/j.ijheatmasstransfer.2018.11.052.

[7] Timm Krüger et al. "Numerical Methods for Fluids". en. In: *The Lattice Boltzmann Method: Principles and Practice*. Ed. by Timm Krüger et al. Graduate Texts in Physics. Cham: Springer International Publishing, 2017, pp. 31–58. ISBN: 978-3-319-44649-3. DOI: 10.1007/978-3-319-44649-3_2.

[8] Derek W. Hengeveld et al. "Review of Modern Spacecraft Thermal Control Technologies". In: *HVAC&R Research* 16.2 (Mar. 2010), pp. 189–220. ISSN: 1078-9669. DOI: 10.1080/10789669.2010.10390900.

[9]   Ruben Baetens, Bjørn Petter Jelle, and Arild Gustavsen. "Aerogel insulation for building applications: A state-of-the-art review". en. In: *Energy and Buildings* 43.4 (Apr. 2011), pp. 761–769. ISSN: 0378-7788. DOI: `10.1016/j.enbuild.2010.12.012`.

[10] Ya-Ling He and Tao Xie. "Advances of thermal conductivity models of nanoscale silica aerogel insulation material". en. In: *Applied Thermal Engineering* 81 (Apr. 2015), pp. 28–50. ISSN: 1359-4311. DOI: `10.1016/j.applthermaleng.2015.02.013`.

[11] S. Q. Zeng, A. Hunt, and R. Greif. "Geometric Structure and Thermal Conductivity of Porous Medium Silica Aerogel". In: *Journal of Heat Transfer* 117.4 (Nov. 1995), pp. 1055–1058. ISSN: 0022-1481. DOI: `10.1115/1.2836281`.

[12] Ziyan Fu et al. "Critical review on the thermal conductivity modelling of silica aerogel composites". en. In: *Journal of Building Engineering* (June 2022), p. 104814. ISSN: 2352-7102. DOI: `10.1016/j.jobe.2022.104814`.

[13] Moran Wang and Ning Pan. "Predictions of effective physical properties of complex multiphase materials". en. In: *Materials Science and Engineering: R: Reports* 63.1 (Dec. 2008), pp. 1–30. ISSN: 0927-796X. DOI: `10.1016/j.mser.2008.07.001`.

[14] E Tsotsas and H Martin. "Thermal conductivity of packed beds: A review". en. In: *Chemical Engineering and Processing: Process Intensification* 22.1 (July 1987), pp. 19–37. ISSN: 0255-2701. DOI: `10.1016/0255-2701(87)80025-9`.

[15] P. Zehner and E. U. Schlünder. "Wärmeleitfähigkeit von Schüttungen bei mäßigen Temperaturen". de. In: *Chemie Ingenieur Technik* 42.14 (1970), pp. 933–941. ISSN: 1522-2640. DOI: `https://doi.org/10.1002/cite.330421408`.

[16] Evangelos Tsotsas. "M11 Wärmeleitfähigkeit von Schüttschichten". de. In: *VDI-Wärmeatlas: Fachlicher Träger VDI-Gesellschaft Verfahrenstechnik und Chemieingenieurwesen*. Ed. by Peter Stephan et al. Springer Reference Technik. Berlin, Heidelberg: Springer, 2019, pp. 1831–1843. ISBN: 978-3-662-52989-8. DOI: `10.1007/978-3-662-52989-8_30`.

[17] Stephan Parzinger. "Analytische Modellierung der temperatur- und gasdruckabhängigen effektiven Wärmeleitfähigkeit von Pulvern". de. PhD thesis.

[18] Matthias Neubronner et al. "D6 Properties of Solids and Solid Materials". en. In: *VDI Heat Atlas*. VDI-Buch. Berlin, Heidelberg: Springer, 2010, pp. 551–614. ISBN: 978-3-540-77877-6. DOI: `10.1007/978-3-540-77877-6_26`.

[19]   André Thess and Robert Kaiser. "Wärmeübertragung bei freier Konvektion: Innenströmungen". de. In: *VDI-Wärmeatlas*. Ed. by Peter Stephan et al. Springer Reference Technik. Berlin, Heidelberg: Springer, 2018, pp. 1–11. ISBN: 978-3-662-52991-1. DOI: `10.1007/978-3-662-52991-1_39-1`.

[20]   Peter Stephan. "Grundlagen der Berechnungsmethoden für Wärmeleitung, konvektiven Wärmeübergang und Wärmestrahlung". de. In: *VDI-Wärmeatlas*. Ed. by Peter Stephan et al. Springer Reference Technik. Berlin, Heidelberg: Springer, 2018, pp. 1–14. ISBN: 978-3-662-52991-1. DOI: `10.1007/978-3-662-52991-1_4-2`.

[21]   Harald Reiss. "Wärmestrahlung – Superisolierungen". de. In: *VDI-Wärmeatlas*. Ed. by Peter Stephan et al. Springer Reference Technik. Berlin, Heidelberg: Springer, 2019, pp. 1–83. ISBN: 978-3-662-52991-1. DOI: `10.1007/978-3-662-52991-1_73-1`.

[22]   Svein Rosseland. *Astrophysik: Auf atomtheoretischer grundlage*. Vol. 11. Springer-Verlag, 2013. ISBN: 3-662-26679-2.

[23]   R. Siegel and J. R. Howell. *Thermal radiation heat transfer*. NTRS Author Affiliations: NASA Lewis Research Center, Houston, University NTRS Document ID: 19720039380 NTRS Research Center: Legacy CDMS (CDMS). Jan. 1972.

[24]   Yee Kan Koh. "Thermal Conductivity and Phonon Transport". en. In: *Encyclopedia of Nanotechnology*. Ed. by Bharat Bhushan. Dordrecht: Springer Netherlands, 2012, pp. 2704–2711. ISBN: 978-90-481-9751-4. DOI: `10.1007/978-90-481-9751-4_277`.

[25]   Keith T. Regner et al. "Broadband phonon mean free path contributions to thermal conductivity measured using frequency domain thermoreflectance". en. In: *Nature Communications* 4.1 (Mar. 2013). Number: 1 Publisher: Nature Publishing Group, p. 1640. ISSN: 2041-1723. DOI: `10.1038/ncomms2630`.

[26]   "Thermal Conductivity of Nanostructured Thermoelectric Materials". In: *Thermoelectrics Handbook*. Ed. by D. M. Rowe. Num Pages: 16. CRC Press, 2006. ISBN: 978-1-315-22039-0.

[27]   Joseph Callaway. "Model for Lattice Thermal Conductivity at Low Temperatures". In: *Physical Review* 113.4 (Feb. 1959). Publisher: American Physical Society, pp. 1046–1051. DOI: `10.1103/PhysRev.113.1046`.

[28]   M. G. Holland. "Analysis of Lattice Thermal Conductivity". In: *Physical Review* 132.6 (Dec. 1963). Publisher: American Physical Society, pp. 2461–2471. DOI: `10.1103/PhysRev.132.2461`.

[29] Sumit Pramanik et al. "Current Advancements in Ceramic Matrix Composites". en. In: *Composite Materials*. Ed. by Kamal K. Kar. Berlin, Heidelberg: Springer Berlin Heidelberg, 2017, pp. 457–496. ISBN: 978-3-662-49512-4 978-3-662-49514-8. DOI: 10/f7vf.

[30] E. H. Ratcliffe. "Thermal conductivities of fused and crystalline quartz". en. In: *British Journal of Applied Physics* 10.1 (Jan. 1959), pp. 22–25. ISSN: 0508-3443. DOI: 10.1088/0508-3443/10/1/306.

[31] Heinrich Hertz. "Ueber die Berührung fester elastischer Körper". de. In: *Band 92*. De Gruyter, Feb. 2021, pp. 156–171. ISBN: 978-3-11-234240-4. DOI: 10.1515/9783112342404-004.

[32] Mikhail Grigorevich Kaganer. *Thermal insulation in cryogenic engineering*. Israel Program for Scientific Translations, 1969.

[33] Y. Ogniewicz and M. Yovanovich. "Effective conductivity of regularly packed spheres - Basic cell model with constriction". In: *15th Aerospace Sciences Meeting*. Aerospace Sciences Meetings. American Institute of Aeronautics and Astronautics, Jan. 1977. DOI: 10.2514/6.1977-188.

[34] W. van Antwerpen, P. G. Rousseau, and C. G. du Toit. "Multi-sphere Unit Cell model to calculate the effective thermal conductivity in packed pebble beds of mono-sized spheres". en. In: *Nuclear Engineering and Design* 247 (June 2012), pp. 183–201. ISSN: 0029-5493. DOI: 10.1016/j.nucengdes.2012.03.012.

[35] S. G Jennings. "The mean free path in air". In: *Journal of Aerosol Science* 19.2 (Apr. 1988), pp. 159–166. ISSN: 0021-8502. DOI: 10.1016/0021-8502(88)90219-4.

[36] Peter W. Atkins and Julio de Paula. "Wärmeleitung". de. In: *Physikalische Chemie*. Google-Books-ID: rSX3AAAACAAJ. John Wiley & Sons, Dec. 2006, pp. 672–673. ISBN: 978-3-527-31546-8.

[37] Ulrich Heinemann. "Influence of Water on the Total Heat Transfer in 'Evacuated' Insulations". en. In: *International Journal of Thermophysics* 29.2 (Apr. 2008), pp. 735–749. ISSN: 0195-928X, 1572-9567. DOI: 10.1007/s10765-007-0361-1.

[38] Jun-Jie Zhao et al. "Effects of solid–gas coupling and pore and particle microstructures on the effective gaseous thermal conductivity in aerogels". en. In: *Journal of Nanoparticle Research* 14.8 (July 2012), p. 1024. ISSN: 1572-896X. DOI: 10.1007/s11051-012-1024-0.

[39] J. Fricke, U. Heinemann, and H. P. Ebert. "Vacuum insulation panels—From research to market". In: *Vacuum*. The World Energy Crisis Part 2: Some More Vacuum-based Solutions 82.7 (Mar. 2008), pp. 680–690. ISSN: 0042-207X. DOI: 10.1016/j.vacuum.2007.10.014.

[40] Gilberto Medeiros Kremer. "Basic Principles of the Kinetic Theory". en. In: *An Introduction to the Boltzmann Equation and Transport Processes in Gases*. Ed. by Gilberto Medeiros Kremer. Interaction of Mechanics and Mathematics. Berlin, Heidelberg: Springer, 2010, pp. 1–35. ISBN: 978-3-642-11696-4. DOI: 10/bxj4j8.

[41] Paul A. Chambre and Samuel A. Schaaf. *Flow of Rarefied Gases*. en. Google-Books-ID: DIIrDgAAQBAJ. Princeton University Press, Mar. 2017. ISBN: 978-1-4008-8580-0.

[42] Karl Jousten. "Transporteigenschaften von Gasen". de. In: *Handbuch Vakuumtechnik*. Ed. by Karl Jousten. Springer Reference Technik. Wiesbaden: Springer Fachmedien, 2018, pp. 63–79. ISBN: 978-3-658-13386-3. DOI: 10.1007/978-3-658-13386-3_4.

[43] Sydney Chapman, T. G. Cowling, and D. Burnett. *The Mathematical Theory of Non-uniform Gases: An Account of the Kinetic Theory of Viscosity, Thermal Conduction and Diffusion in Gases*. en. Google-Books-ID: Cbp5JP2OTrwC. Cambridge University Press, 1990. ISBN: 978-0-521-40844-8.

[44] Martin Knudsen. "Die molekulare Wärmeleitung der Gase und der Akkommodationskoeffizient". In: *Annalen der Physik* 339.4 (Jan. 1911), pp. 593–656. ISSN: 0003-3804. DOI: 10.1002/andp.19113390402.

[45] W. Jitschin. "Wie gut stimmt die kinetische Gastheorie?" de. In: *Vakuum in Forschung und Praxis* 10.3 (1998), pp. 230–232. ISSN: 1522-2454. DOI: https://doi.org/10.1002/vipr.19980100313.

[46] Arnold Frohn, Norbert Roth, and Klaus Anders. "M10 Wärmeübertragung und Strömung in verdünnten Gasen". de. In: *VDI-Wärmeatlas*. VDI-Buch. Berlin, Heidelberg: Springer, 2013, pp. 1569–1588. ISBN: 978-3-642-19981-3. DOI: 10.1007/978-3-642-19981-3_105.

[47] Ralph K. Iler. *The Chemistry of Silica: Solubility, Polymerization, Colloid and Surface Properties and Biochemistry of Silica | Wiley*. en-us. Wiley, 1979. ISBN: 978-0-471-02404-0.

[48] Manuel Meier et al. "Multi-scale characterization of precipitated silica". In: *Powder Technology* 354 (Sept. 2019), pp. 45–51. ISSN: 0032-5910. DOI: 10.1016/j.powtec.2019.05.072.

[49] Katrin Heger. "Oberflächenfunktionalisierung synthetischer Kieselsäuren: Beitrag zur Erzeugung und Charakterisierung von Silan- und Phenylgruppen auf Siliciumdioxidoberflächen". PhD thesis. Technischen Universität Chemnitz, Mar. 1998.

[50] Otto W. Flörke et al. "Silica". en. In: *Ullmann's Encyclopedia of Industrial Chemistry*. American Cancer Society, 2008. ISBN: 978-3-527-30673-2.

[51] Constanze Setzer, Gonda van Essche, and Neil Pryor. "Silica". en. In: *Handbook of Porous Solids*. Wiley-Blackwell, 2008, pp. 1543–1591. ISBN: 978-3-527-61828-6. DOI: 10.1002/9783527618286.ch23a.

[52] Detlef Gysau. *Füllstoffe: Grundlagen und Anwendungen*. ger. Technologie des Beschichtens. Hannover: Vincentz Network, 2005. ISBN: 978-3-87870-793-6.

[53] M. Besbes, N. Fakhfakh, and M. Benzina. "Characterization of silica gel prepared by using sol–gel process". en. In: *Physics Procedia*. Proceedings of the JMSM 2008 Conference 2.3 (Nov. 2009), pp. 1087–1095. ISSN: 1875-3892. DOI: 10.1016/j.phpro.2009.11.067.

[54] Hartmut Tschritter et al. "Verfahren zur Herstellung von hochreinem mikronisiertem Silicagel". de. DE102006022685A1. Nov. 2007.

[55] May Yan Lee et al. "A Comparative Study of Production of Glass Microspheres by using Thermal Process". en. In: *IOP Conference Series: Materials Science and Engineering* 205 (June 2017), p. 012022. ISSN: 1757-8981, 1757-899X. DOI: 10.1088/1757-899X/205/1/012022.

[56] V. SPECCHIA, G. BALDI, and S. SICARDI. "Heat Transfer in Packed Bed Reactors with One Phase Flow". In: *Chemical Engineering Communications* 4.1-3 (Jan. 1980). Publisher: Taylor & Francis _eprint: https://doi.org/10.1080/00986448008935916, pp. 361–380. ISSN: 0098-6445. DOI: 10.1080/00986448008935916.

[57] J. E. Fesmire and S. D. Augustynowicz. "Thermal Performance Testing of Glass Microspheres under Cryogenic Vacuum Conditions". In: *AIP Conference Proceedings* 710.1 (June 2004). Publisher: American Institute of Physics, pp. 612–618. ISSN: 0094-243X. DOI: 10.1063/1.1774734.

[58] Seymour Lowell et al. *Characterization of Porous Solids and Powders: Surface Area, Pore Size and Density*. en. Particle Technology Series. Springer Netherlands, 2004. ISBN: 978-1-4020-2302-6.

[59] Jean Rouquerol et al. "Liquid intrusion and alternative methods for the characterization of macroporous materials (IUPAC Technical Report)". In: *Pure and Applied Chemistry* 84.1 (2011), pp. 107–136. ISSN: 0033-4545. DOI: 10.1351/PAC-REP-10-11-19.

[60] Manuel Meier. "Über den Entstehungsprozess poröser Strukturen am Beispiel der Partikelbildung von kolloidalem Silika und der Haufwerksbildung von gefällter Kieselsäure". de. PhD thesis. 2021. DOI: 10.5445/IR/1000129486.

[61] Andre Guinier. "Small-angle scattering of X-rays". en. In: *Structure of matter series*. Wiley, 1955, p. 276.

[62] Belynda Benane et al. "Multiscale structure of super insulation nano-fumed silicas studied by SAXS, tomography and porosimetry". en. In: *Acta Materialia* 168 (Apr. 2019), pp. 401–410. ISSN: 1359-6454. DOI: 10.1016/j.actamat.2019.02.024.

[63] Birgit M. Brunner. "Untersuchungen zur inneren Struktur von Hydrogelen aus N-Isopropylacrylamid mittels statischer Lichtstreuung". de. Accepted: 2006-01-23. PhD thesis. Universität Stuttgart, 2005.

[64] Günter Jakob Lauth and Jürgen Kowalczyk. "Messung der Diffusionskoeffizienten". de. In: *Einführung in die Physik und Chemie der Grenzflächen und Kolloide*. Ed. by Günter Jakob Lauth and Jürgen Kowalczyk. Berlin, Heidelberg: Springer, 2016, pp. 189–235. ISBN: 978-3-662-47018-3. DOI: 10.1007/978-3-662-47018-3_7.

[65] Tom Alexander Mulder. *Partikelgrößenanalyse mit Laserbeugung | Malvern Panalytical*. de. 2022.

[66] Alena Mudroch, José M. Azcue, and Paul Mudroch, eds. *Manual of Physico-Chemical Analysis of Aquatic Sediments*. New York: Routledge, Oct. 2017. ISBN: 978-0-203-74817-6. DOI: 10.1201/9780203748176.

[67] J. Kuhn et al. "Infrared-optical transmission and reflection measurements on loose powders". en. In: *Review of Scientific Instruments* 64.9 (Sept. 1993), pp. 2523–2530. ISSN: 0034-6748, 1089-7623. DOI: 10.1063/1.1143914.

[68] Deborah Herdt et al. "Malt roasting quality control by mid-infrared spectroscopy". In: *Journal of Brewing and Distilling* 10.1 (May 2021). Publisher: Academic Journals, pp. 1–16. ISSN: 2141-2197. DOI: 10.5897/JBD2021.0056.

[69] Khaled Raed. "Investigation of Knudsen and gas-atmosphere effects on effective thermal conductivity of porous media". eng. PhD thesis. Sept. 2013.

[70] G. Reichenauer, U. Heinemann, and H. -P. Ebert. "Relationship between pore size and the gas pressure dependence of the gaseous thermal conductivity". en. In: *Colloids and Surfaces A: Physicochemical and Engineering Aspects*. Proceedings of the Fourth International TRI/Princeton Workshop "Characterization of Porous Materials: from Angstroms to Millimeters" 300.1 (June 2007), pp. 204–210. ISSN: 0927-7757. DOI: 10.1016/j.colsurfa.2007.01.020.

[71] Frank Hemberger et al. "Thermal Transport Properties of Functionally Graded Carbon Aerogels". en. In: *International Journal of Thermophysics* 30.4 (Aug. 2009), pp. 1357–1371. ISSN: 1572-9567. DOI: 10.1007/s10765-009-0616-0.

[72] K. Swimm et al. "Coupling of gaseous and solid thermal conduction in porous solids". In: *Journal of Non-Crystalline Solids* 456 (Jan. 2017), pp. 114–124. ISSN: 0022-3093. DOI: `10.1016/j.jnoncrysol.2016.11.012`.

[73] K. Swimm et al. "Impact of the Backbone Connectivity on the Gas Pressure-Dependent Thermal Conductivity of Porous Solids". en. In: *International Journal of Thermophysics* 43.1 (Jan. 2022), p. 8. ISSN: 0195-928X, 1572-9567. DOI: `10.1007/s10765-021-02936-4`.

[74] Matthias Rottmann and Thomas Beikircher. "Pressure dependent effective thermal conductivity of pure and SiC-opacified expanded perlite between 293 K and 1073 K". en. In: *International Journal of Thermal Sciences* 179 (Sept. 2022), p. 107652. ISSN: 1290-0729. DOI: `10.1016/j.ijthermalsci.2022.107652`.

[75] J. R. Manson. "Simple Model for the Energy Accommodation Coefficient". In: *The Journal of Chemical Physics* 56.7 (Apr. 1972), pp. 3451–3455. ISSN: 0021-9606. DOI: `10.1063/1.1677719`.

[76] Kishore K. Kammara and Rakesh Kumar. "Development of empirical relationships for surface accommodation coefficients through investigation of nano-poiseuille flows using molecular dynamics method". en. In: *Microfluidics and Nanofluidics* 24.9 (Aug. 2020), p. 70. ISSN: 1613-4990. DOI: `10.1007/s10404-020-02375-x`.

[77] D. Bayer-Buhr et al. "Determination of thermal accommodation coefficients on CaSiO3 and SiO2 using molecular dynamics and experiments". en. In: *International Journal of Heat and Mass Transfer* 183 (Feb. 2022), p. 122219. ISSN: 0017-9310. DOI: `10.1016/j.ijheatmasstransfer.2021.122219`.

[78] Tianli Feng et al. "Molecular dynamics simulations of energy accommodation between gases and polymers for ultra-low thermal conductivity insulation". en. In: *International Journal of Heat and Mass Transfer* 164 (Jan. 2021), p. 120459. ISSN: 0017-9310. DOI: `10.1016/j.ijheatmasstransfer.2020.120459`.

[79] Hiroki Yamaguchi, Yu Matsuda, and Tomohide Niimi. "Molecular-dynamics study on characteristics of energy and tangential momentum accommodation coefficients". In: *Physical Review E* 96.1 (July 2017). Publisher: American Physical Society, p. 013116. DOI: `10.1103/PhysRevE.96.013116`.

[80] Lawrence W. Hrubesh and Richard W. Pekala. "Thermal properties of organic and inorganic aerogels". en. In: *Journal of Materials Research* 9.3 (Mar. 1994). Publisher: Cambridge University Press, pp. 731–738. ISSN: 2044-5326, 0884-2914. DOI: `10.1557/JMR.1994.0731`.

[81] Sebastian Sonnick et al. "Methodical selection of thermal conductivity models for porous silica-based media with variation of gas type and pressure". en. In: *International Journal of Heat and Mass Transfer* 187 (May 2022), p. 122519. ISSN: 0017-9310. DOI: `10.1016/j.ijheatmasstransfer.2022.122519`.

[82] B. Höhlein. *Die physikalischen Eigenschaften von Gasgemischen mit H2, CH4, H2O, N2, CO und CO2.* Tech. rep. 847. Institut für Reaktorbauelemente Jülich, Apr. 1972.

[83] Flávia A. Almeida et al. "Alternative low cost based core systems for vacuum insulation panels". en. In: *Ciência & Tecnologia dos Materiais.* Materiais 2015 29.1 (Jan. 2017), e151–e156. ISSN: 0870-8312. DOI: `10.1016/j.ctmat.2016.10.002`.

[84] Adam Gao et al. *Silicates and Silicas - Chemical Economics Handbook (CEH) | IHS Markit.* Tech. rep. Dec. 2017.

[85] E. Guesnet et al. "Why fumed and precipitated silica have different mechanical behavior: Contribution of discrete element simulations". In: *Journal of Non-Crystalline Solids* 524 (Nov. 2019), p. 119646. ISSN: 0022-3093. DOI: `10.1016/j.jnoncrysol.2019.119646`.

[86] H. Singh, M. Geisler, and F. Menzel. "Experimental investigations into thermal transport phenomena in vacuum insulation panels (VIPs) using fumed silica cores". en. In: *Energy and Buildings* 107 (Nov. 2015), pp. 76–83. ISSN: 0378-7788. DOI: `10.1016/j.enbuild.2015.08.004`.

[87] Holger Schmidt. "NMR-spektroskopische Untersuchungen an Carbon Black und Graphit". de. In: (Feb. 2003).